

**Structural Dynamics of Complex Molecules
by Ultrafast Electron Diffraction:
Concepts, Methodology and Applications**

Thesis by
Ramesh Srinivasan

In partial fulfillment of the requirements for the degree of
Doctor of Philosophy

California Institute of Technology
Pasadena, California
2005
(Defended December 1, 2004)

© 2005
Ramesh Srinivasan
All Rights Reserved

Dedicated with love and gratitude

to

Bhagawan Sri Sathya Sai Baba

and to

my dearest parents

Aruna and N.V. Srinivasan

Acknowledgements

In my native land of India, every person is regarded as having two births—the first, birth into the physical world, and the other, birth into the world of knowledge. Indian tradition emphasizes that for the former birth, we are eternally indebted to our parents, and for the latter, we are ever beholden to our teacher. It is in that spirit of my ancestors that I write these words of gratitude to my teacher and mentor, Prof. Ahmed Zewail. The human language, while a wondrously marvelous gift, often fails at times such as these to adequately express the whole gamut of one's emotions. Yet, standing as I am at the end of a long and arduous period of graduate school, it is but natural that I seek to acknowledge his profound influence on my growth as a scientist and as a human being. My entry into the Zewail group came about under very unusual circumstances, the details of which will have to wait for another day. Over the course of my studentship, I have been struck and inspired by his passion for science and his insatiable curiosity about the natural world. The award of the Nobel Prize in 1999 was certainly one of the high points of my tutelage under him. I am reminded of an anecdote that Isidor Isaac Rabi once shared, "My mother made me a scientist without ever intending to. Every other Jewish mother in Brooklyn would ask her child after school, 'So? Did you learn anything today?' But not my mother. 'Izzy,'

she would say, ‘did you ask a good question today?’ That difference—asking good questions—made me become a scientist.” It has been my singular fortune to learn from Prof. Zewail the art of asking the right questions. I have enjoyed our numerous discussions on the history of science, on the role of science and technology in bridging the gap between the ‘haves’ and the ‘have-nots’, on the cultural mores of our respective ancient civilizations, and on the art of communicating science to non-scientists and especially to young, budding scientists. While he has been a wonderful teacher, I hope I have been a worthy disciple. I am also grateful to his wife, Dema, and his sons, Hani and Nabeel, for giving me a home away from home, for many wonderful evenings of joy and laughter.

I have had the privilege of working with a team of brilliant and superbly accomplished colleagues over the years, not only in the diffraction sub-group but also in the larger Zewail group. My earliest foray into femtochemistry, albeit for an all-too-brief period, was with Chaozhi Wan and Spencer Baskin. I was soon lured into the challenging world of ultrafast diffraction. It was here that Udo Gomez and Vladimir Lobastov, two remarkable postdoctoral scholars, took me under their wings and taught me all I know about diffraction and equipment design. Vladimir, in particular, has been a tremendous mentor and colleague, and I will always cherish the experience of working with and learning from him. Hyotcherl Ihee and Jim

Cao, both members of the UED-2 team, shared generously from their wealth of experience and honed my skills in the theoretical analysis of the molecular diffraction signatures. The UED-3 team has, over the years, benefited from many outstanding personnel, each of whom brought their unique perspective and expertise to bear upon this discipline. Chong-Yu Ruan, Boyd Goodson, Jon Feenstra, Sang Tae Park, and Shoujun Xu have all been an integral part of this exciting endeavor. Jon and I have worked particularly closely for nearly 4 years, and it has been a wonderful experience having him as a colleague and as a friend. All of the work that is discussed in this dissertation bears their unmistakable imprint, and to each one of them, I owe many thanks.

All present and former members of the Zewail group not only provided me with a stimulating intellectual ambience, but they have also been wonderful friends. I can never forget the amazing secretaries we have had over the years, who made life in the sub-basement far easier than it otherwise might have been. Mary Sexton, Sylvia Jacoby, Janet Davis, and De Ann Lewis have all been an inexhaustible source of cheer and comfort.

I also wish to thank all the faculty of the Chemistry and Chemical Engineering Division for their formal and informal guidance over the years. In particular, I wish to thank Prof. George Gavalas for his mentorship during my master's thesis. Prof. Vince McKoy always evinced great personal interest

in my research, and his constant encouragement has been one of the abiding memories of my graduate career.

The National Science Foundation and the Air Office of Scientific Research are gratefully acknowledged for their generous financial support of this work.

To my parents, I owe all that I am and hope to be. Their unstinting support, words of comfort and wisdom, and their unshakable belief in me helped me push myself harder when I didn't think I could do any better. This dissertation is more a testimony to their love than to my abilities. To Bhagawan Sri Sathya Sai Baba, my dearest friend and guide, I offer this labor of love in a spirit of humble dedication.

Ramesh Srinivasan

Pasadena, California

November 23, 2004

Abstract

The central theme in ultrafast electron diffraction (UED) is the elucidation of the structural dynamics of *transient* molecular entities. With properly timed sequences of ultrafast electron pulses, it is now possible to image complex molecular structures in the four dimensions of space and time with resolutions approaching 0.01 Å and 1 ps, respectively. Reaching this spatiotemporal resolution on the atomic scale has been the driving force behind the development and application of the third generation UED instrument—the subject of this dissertation. The current state-of-the-art in resolutions and sensitivity, together with theoretical advances, has made possible the *direct* determination of transient structures, leading to studies of diverse molecular phenomena hitherto not accessible to other techniques. By freezing structures on the ultrafast timescale, we are able to develop concepts that correlate *structure* with *dynamics*. Examples include structure-driven radiationless processes, dynamics-driven reaction stereochemistry, and non-equilibrium structures exhibiting negative temperature, bifurcation, or selective energy localization in bonds. These successes in the studies of complex molecular systems, even without heavy atoms, establish UED as a powerful method for mapping out temporally changing molecular structures in chemistry, and potentially, in biology.

Table of Contents

<i>Acknowledgements</i>	iv
<i>Abstract</i>	viii
<i>List of Figures</i>	xiv
<i>List of Schemes</i>	xxiii
<i>List of Tables</i>	xxiv
1. Introduction.....	1
Figures.....	10
References.....	12
2. UED Theory.....	18
2.1 Introduction.....	18
2.2 The Diffraction-Difference Method: Transient Structures.....	22
2.3 Ground-State Structures.....	27
2.4 Structure Search and Refinement.....	28
Figures.....	32
References.....	35
3. Third Generation UED Instrumentation.....	36
3.1 Introduction.....	36
3.2 Femtosecond Laser System.....	37
3.3 Vacuum Chambers and Molecular Beams.....	39
3.4 Electron Gun.....	40
3.5 CCD Camera System.....	41
3.6 Time-of-Flight Mass Spectrometer.....	44
References.....	45
Figures.....	46

4. UED Methodology.....	64
4.1 Introduction.....	64
4.2 Streaking: Electron Pulse Characterization.....	65
4.3 Clocking: Zero of Time.....	70
4.4 Temporal and Spatial Overlap: Velocity Mismatch.....	73
4.5 Calibration of CCD Camera.....	76
4.6 CCD Image Processing.....	76
4.7 Normalization of Time-Dependent Diffraction Signals.....	81
4.8 Analysis of 1D Diffraction Data: Ground-State Structures.....	82
4.9 Time-Resolved Experiments: The Diffraction-Difference Method.....	84
4.10 Least-Squares Fitting.....	88
4.11 Estimation of Spatial Coherence.....	90
References.....	91
Figures.....	92
5. Reactive Intermediate Structures: A Case Study.....	111
5.1 Introduction.....	111
5.2 Experimental.....	114
5.3 Results and Discussion	
A. Ground-State Structures of $C_2F_4I_2$	115
B. Structural Dynamics of the $C_2F_4I_2$ Reaction.....	116
C. Structural Change, Intermediate to Product: The $C_2F_4I \rightarrow$ $C_2F_4 + I$ Process.....	122
D. Structure of the C_2F_4I Radical Intermediate.....	124
5.4 Conclusions.....	132
Figures.....	133
References.....	146

6. Dark Structures in Nonradiative Processes.....	148
6.1 Introduction.....	148
6.2 Ground-State Structures	
A. Pyridine.....	158
B. 2-Picoline.....	160
C. 2,6-Lutidine.....	160
6.3 Transient Structures	
A. Pyridine.....	161
B. 2-Picoline.....	165
C. 2,6-Lutidine.....	166
6.4 Photochemistry	
A. Pyridine.....	166
B. 2-Picoline.....	174
C. 2,6-Lutidine.....	177
6.5 Photophysics.....	178
6.6 Conclusions.....	182
Figures.....	184
References.....	210
7. Non-Equilibrium Structures.....	216
7.1 Introduction.....	216
7.2 Concepts of Equilibrium <i>vs.</i> Non-equilibrium Structures.....	217
7.3 Experimental Methodology.....	220
7.4 Data Processing and Analysis	
A. Background Subtraction.....	220
B. Generation of “Product-Isolated” Curves from Diffraction Difference Signals.....	221
C. Novel Aspects of the Product Structure Analysis Used for “Hot” HT Product.....	224

D. The Generalized Monte Carlo Method: A Complementary Analysis.....	229
7.5 Results and Discussion	
A. Ground States of CHT and CHD.....	231
B. Structural Dynamics of CHT.....	232
C. Structural Dynamics of CHD.....	234
7.6 Review of Previous Studies in Light of Our UED Results	
A. The Resonance Raman Studies of Mathies and co-workers...	243
B. The Initial Work of Sension and co-workers.....	246
C. The Work of Fuss, Kompa, and co-workers.....	248
7.7 Implications of UED Studies on Understanding IVR.....	251
7.8 Conclusions.....	258
Figures.....	259
References.....	277
8. Conformational Dynamics on Complex Energy Landscapes.....	280
8.1 Introduction.....	280
8.2 Methodology.....	282
8.3 Structure Refinement.....	283
8.4 DFT Calculations.....	284
8.5 Monte Carlo Global Structural Optimization.....	285
8.6 Results and Discussion	
A. Structures of Cope Rearrangement.....	285
B. Ring Opening Reactions.....	289
C. The Observation of Non-equilibrium Configurations in OT....	291
8.7 Conclusions.....	299
Figures.....	301
References.....	313

9. Hydrogen-Bonding in Acetylacetone.....	315
9.1 Introduction.....	315
9.2 Experimental.....	318
9.3 Ground State.....	318
9.4 Structural Dynamics.....	322
9.5 Results and Discussion.....	323
9.6 Conclusions.....	329
Figures.....	330
References.....	343
10. Conclusions and Future Directions.....	347
Figures.....	351
References.....	352

List of Figures

1-1	Example of diffraction with two scattering centers.....	10
1-2	The UED experiment.....	11
2-1	Concept of ultrafast electron diffraction	32
2-2	The diffraction-difference method.....	33
2-3	Isolation of transient species through choice of t_{ref}	34
3-1	Third-generation UED-3 apparatus.....	46
3-2	Layout of beam path for the femtosecond laser pulses	47
3-3a	Schematic front view of the UED-3 apparatus.....	48
3-3b	Schematic side view of UED-3 apparatus.....	49
3-4	Schematic of UED-3 electron gun assembly	50
3-5	Detailed view of the electron generation and acceleration assembly	51
3-6	Equipotential lines in extraction region of electron gun.....	52
3-7	Detailed view of magnetic lens assembly	53

3-8	Detailed view of the electron streaking and deflection assembly	54
3-9	UED-3 detector assembly	55
3-10	Individual components of the custom-made detector assembly.....	56
3-11	Photographs of selected detector components	57
3-12	Schematic of time-of-flight mass spectrometry apparatus	58
3-13	The linear TOF-MS chamber	59
3-14	Acceleration and detector assembly for time-of-flight apparatus.....	60
3-15	Geometry of time-of-flight mass spectrometer	61
3-16	Arrangement and synchronization of electrical pulses in TOF-MS	62
3-17	Typical mass spectrum obtained in the TOF-MS apparatus	63
4-1	Calibration of electron gun via streaking experiments.....	92
4-2	Typical X-Y profile of the nearly circular electron beam	93
4-3	Results of <i>in situ</i> streaking experiment for electron pulse measurement	94
4-4	Calibration of electron pulse width.....	95
4-5	Improvement in electron gun performance	96

4-6	Pulse-to-pulse stability of the electron gun	97
4-7	Lensing experiment to determine <i>in situ</i> the zero-of-time.....	98
4-8	Photoionization-induced ‘lensing’ effect for measuring time-zero	99
4-9	Geometry of crossed-beam experiment	100
4-10	Angular dependence of temporal broadening due to velocity mismatch	101
4-11	Overall temporal resolution (including velocity mismatch) as a function of spatial and temporal width of the electron pulses	102
4-12	Calibration of pixel size on phosphor screen using Group 0, Element 1 of the USAF-1951 resolution target.....	103
4-13	Determination of mean pixel size on phosphor screen.....	104
4-14	Modulation Transfer Function for the ICCD camera.....	105
4-15	Calibration of single electron events on the detector	106
4-16	Inverse atomic ratio method.....	107
4-17	Processing procedure for 2-D diffraction images and ground-state data analysis.....	108
4-18	Diffraction-difference analysis for time-resolved experiments.....	109

4-19	Divergence of electron beam.....	110
5-1	Ground-state molecular diffraction image of $C_2F_4I_2$	135
5-2	Refined ground-state structure of $C_2F_4I_2$	136
5-3	Time-resolved 2D diffraction-difference images of $C_2F_4I_2$	137
5-4	Effect of Fourier filtering on raw diffraction-difference curves	138
5-5	Time-resolved structural changes in the elimination of iodine from $C_2F_4I_2$	139
5-6	Time-resolved structural changes involving only the $C_2F_4I \rightarrow$ $C_2F_4 + I$ contribution to the diffraction-difference signal	140
5-7	Time dependence of the formation of C_2F_4 molecules from the decay of C_2F_4I transient structures	141
5-8	Structural determination of the transient C_2F_4I intermediate	142
5-9	Refinement of the C_2F_4I radical structure	143
5-10	Complete structural determination of the $C_2F_4I_2$ elimination reaction	144
6-1	Ground-state molecular diffraction image of pyridine	185
6-2	Comparison between experimental and refined theoretical $sM(s)$ and $f(r)$ curves for ground-state pyridine	186

6-3	Refined ground-state structural parameters of pyridine	187
6-4	Ground-state molecular diffraction image of picoline	188
6-5	Refined ground-state structural parameters of picoline	189
6-6	Ground-state molecular diffraction image of 2,6-lutidine.....	190
6-7	Comparison of ground-state structures of the three azines.....	191
6-8	Refined ground-state structural parameters of lutidine.....	192
6-9	Time-resolved 2D diffraction-difference images of pyridine	193
6-10	Time-resolved 1D radial distribution curves for pyridine.....	194
6-11	Possible structures from reaction of pyridine.....	195
6-12	Comparisons of the experimental radial distribution curve with normalized theoretical curves for possible pyridine channels.....	196
6-13	Structural parameters of the pyridine ring-opened product.....	197
6-14	Refinement of ring-opened pyridine structure	198
6-15	Pyridine structure and population change with time	199
6-16	Temporal dependence of the pyridine product fraction.....	200
6-17	Possible structures from reaction of picoline.....	201

6-18	Structural parameters for the picoline ring-opened product	202
6-19	Temporal dependence of the picoline product fraction.....	203
6-20	Time-resolved 1D radial distribution curves for lutidine	204
6-21	Possible structures from reaction of lutidine.....	205
6-22	Comparisons of the experimental radial distribution curve with normalized theoretical curves for possible lutidine channels	206
6-23	Lutidine structure and population change with time	207
6-24	Temporal dependence of the lutidine product fraction	208
6-25	Photochemistry of azines elucidated by UED.....	209
7-1	Calculated diffraction curves for a single bond in the equilibrium regime	261
7-2	Calculated diffraction curves for a single bond in the non- equilibrium regime	262
7-3	Observed ground-state diffraction image and corresponding $f(r)$ curve for CHT.....	263
7-4	Observed ground-state diffraction image and corresponding $f(r)$ curve for CHD.....	264
7-5	Refined structural parameters of ground-state CHT.....	265

7-6	Refined structural parameters of ground-state CHD.....	266
7-7	Non-equilibrium ‘negative temperature’ in CHT as reflected in the transient-only sM(s) curves	267
7-8	Non-equilibrium ‘negative temperature’ in CHT	268
7-9	Evolution of transient non-equilibrium structure in CHT.....	269
7-10	Time-resolved 2D diffraction-difference images of CHD.....	270
7-11	Time-resolved formation of hot HT structures after CHD ring opening.....	271
7-12	Temporal evolution of hot HT structures following ring opening of CHD	272
7-13	Structural refinement of ring-opened HT structure.....	273
7-14	Evolution of transient far-from-equilibrium structure in CHD.....	274
7-15	Potential energy landscape relevant to the formation of HT.....	275
8-1	Diffraction of ground-state COT3 and BCO structures in thermal equilibrium	304
8-2	Ground-state molecular scattering curves for COT3 and BCO	305
8-3	Ground-state radial distribution curves for COT3 and BCO.....	306

8-4	Diffraction-difference images of light-mediated reaction of COT3.....	307
8-5	COT3 molecular scattering diffraction-difference curves	308
8-6	COT3 radial distribution diffraction-difference curves.....	309
8-7	Potential energy landscape for OT conformer structures	310
8-8	Refined transient-only OT structures	311
9-1	2D ground-state diffraction image of acetylacetone	332
9-2	Structural refinement of ground-state acetylacetone	333
9-3	Refined structural parameters of the AcAc enol tautomer	334
9-4	Observed structural dynamics of acetylacetone	335
9-5	Experimental and theoretical diffraction-difference data for different reaction pathways of acetylacetone.....	336
9-6	Refinement of “product only” data in acetylacetone.....	337
9-7	Refined structural parameters of the 2-penten-4-on-3-yl radical.....	338
9-8	Evolution of OH loss products for all experimental time slices.....	339
9-9	Difference-difference data to discriminate between singlet and triplet structures	340

9-10 Structures involved in the dynamics of the OH elimination reaction	341
9-11 Power-dependence studies of acetylacetone photochemistry	342
10-1 Phenomena and concepts elucidated by UED	351

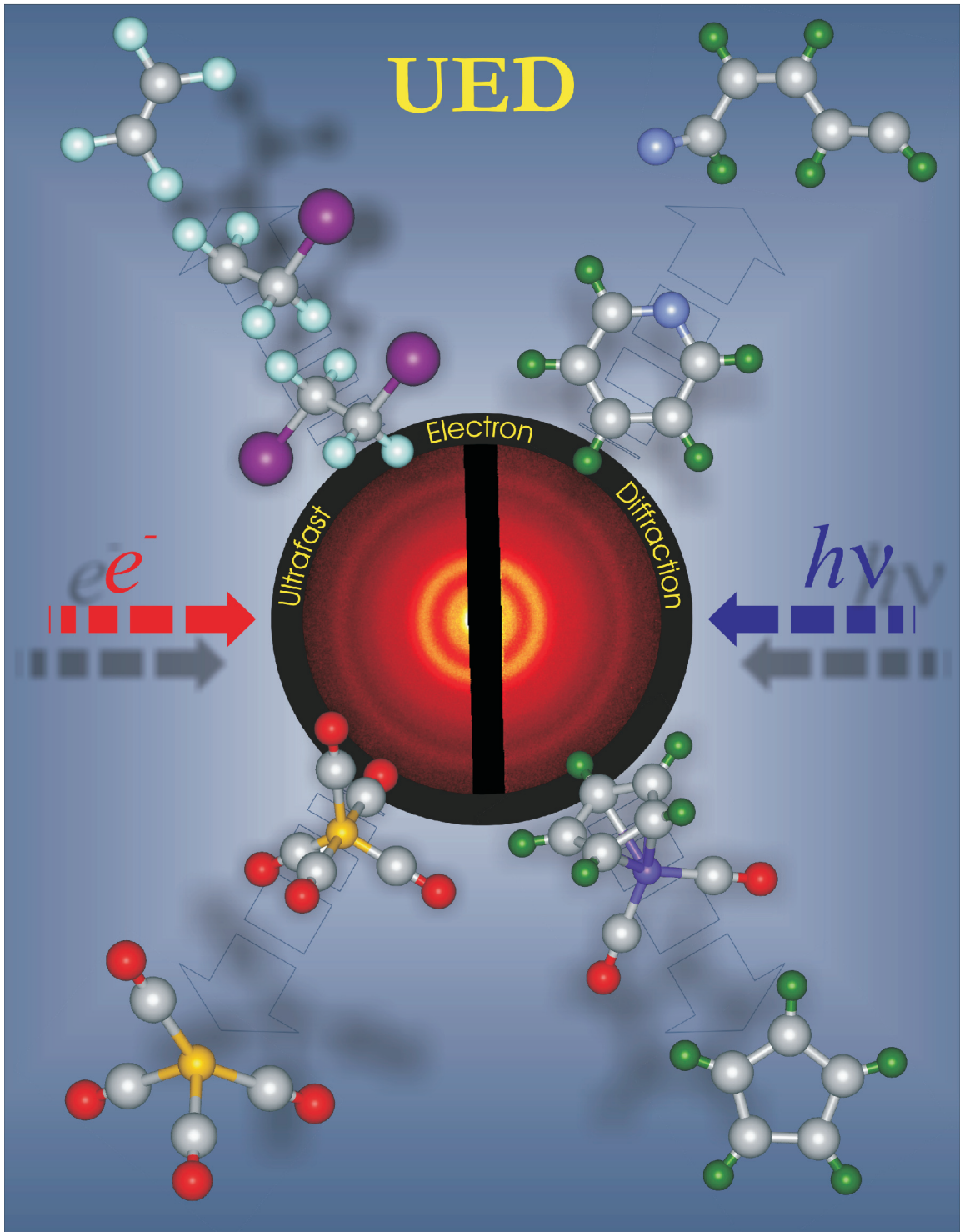
List of Schemes

5-1	Non-concerted elimination reaction of $C_2F_4I_2$ with the hitherto unknown reaction intermediate.....	133
5-2	Dihalide elimination reactions involving C_2R_4X radical intermediates.....	134
6-1	Pyridine reaction with multiple reaction pathways.....	184
7-1	Nonradiative decay of excited 1,3,5-cycloheptatriene to 'vibrationally hot' ground state.....	259
7-2	Ring opening of 1,3-cyclohexadiene to form 1,3,5-hexatriene.....	260
8-1	Thermal Cope rearrangement of 1,3,5-cyclooctatriene to bicyclo[4.2.0]octa-2,4-diene	301
8-2	Light-mediated electrocyclic ring opening of 1,3,5-cyclooctatriene to 1,3,5,7-octatetraene.....	302
8-3	Thermal equilibrium of 1,3,6-cyclooctatriene, 1,3,5-cyclooctatriene, and bicyclo[4.2.0]octa-2,4-diene	303
9-1	Structures of enolic acetylacetone.....	330
9-2	Acetylacetone enol-keto tautomerization by hydrogen shift.....	330
9-3	Possible reactions of acetylacetone following UV excitation.....	331

List of Tables

5-1	Experimental and theoretical values of structural parameters for the classical C_2F_4I radical intermediate.....	145
7-1	Refined structural parameters of the far-from-equilibrium HT structure	276
8-1	Structural coordinates of COT3 obtained from least-squares partial refinement of UED data.....	312

UED



1

INTRODUCTION*

The twentieth century has been witness to major advances in our ability to peer into the microscopic world of molecules, thereby giving us unparalleled insights into their static and temporal behavior.¹ Beginning with X-rays at the turn of the 20th century, diffraction techniques have allowed determination of *equilibrium* three-dimensional structures with atomic resolution, in systems ranging from diatoms (NaCl) to DNA, proteins, and complex assemblies such as viruses.² For dynamics, the time resolution has similarly reached the fundamental atomic-scale of motion. With the

* From Srinivasan, R.; Lobastov, V.A.; Ruan, C.-Y.; Zewail, A.H., *Helv. Chim. Acta*, **2003**, *86*, 1762.

advent of femtosecond time resolution nearly two decades ago, it has become possible to study—in real time—the dynamics of *non-equilibrium* molecular systems, also from the very small (NaI) to the very large (DNA, proteins, and their complexes).³

Armed with this ability to capture both the static architecture as well as the temporal behavior of the chemical bond, a tantalizing goal that now stimulates researchers the world over is the potential to map out, in real time, the coordinates of all individual atoms in a reaction, as, for example, when a molecule unfolds to form selective conformations, or when a protein docks onto the cell surface. These transient structures provide important insights into the function of chemical and biological molecules. As function is intimately associated with intrinsic conformational dynamics, knowing a molecule's static structure is often only the first step toward unraveling how the molecule functions, especially in the world of biology. Thus, elucidating the real-time 'structural dynamics' of *far-from-equilibrium* conformations at atomic scale resolution is vital to understanding the fundamental mechanisms of complex chemical and biological systems.

Time-resolved experiments with femtosecond time resolution have been performed in the past with probe wavelengths ranging from the ultraviolet to the infrared and far-infrared. On this time scale, one is able to freeze localized structures in space (wave packets) and observe their

evolution in time—thus elucidating the elementary processes of bond transformation via transition states, in chemistry and biology.³⁻⁹ Recent advances have been made in multidimensional spectroscopy to correlate frequencies of optical transitions with temporal evolution, thereby probing structural changes in different relaxation processes.^{10, 11} For complex molecular structures, however, the positions of all atoms at a given time can only be obtained if the probe is able to ‘see’ interferences of all atoms. Diffraction methods using X-rays or electrons have the unique ability of revealing all internuclear coordinates with very high spatial resolution, thus providing a global picture of structural change on the ultrafast time scale with atomic level detail.

Electron or X-ray pulses can, in principle, be used to obtain time-varying molecular structures. These pulses must be short enough to freeze the atomic motions, yet bright enough to provide a discernible diffraction pattern. In the case of X-rays, photons are scattered by electrons in the molecular sample, so the diffracted intensity depends directly on the electronic density. Because most electrons are centered on atoms, these electron densities reflect the positions of nuclei, especially for heavy atoms. At present, ultrafast pulsed X-ray sources¹² include third-generation synchrotron radiation, laser-produced plasma sources, high-order harmonics production in gases and on solid surfaces, and free-electron lasers. While

high-flux X-ray pulses from synchrotron sources are relatively long (tens of picoseconds; dictated by the duration of electron bunches in a storage ring), the sub-picosecond X-ray pulses from other generation schemes suffer from rather low fluxes.¹³ As a result, ultrafast X-ray diffraction studies have primarily focused on solid samples¹⁴ where the intrinsic long-range order enhances the signal-to-noise ratio of the interference patterns. X-ray absorption spectroscopy (XAS) techniques such as extended X-ray absorption fine structure (EXAFS) and X-ray absorption near-edge structure (XANES) spectroscopies have been used to obtain local structural information in solutions on the nanosecond timescale,^{15, 16} and on the ultrafast timescale, in gases¹⁷ and liquids.¹⁸

The method of choice in our laboratory has been ultrafast electron diffraction (UED), which has unique advantages. First, unlike X-ray photons, which are scattered by the electron distribution (Thompson scattering), electrons are scattered by both the atomic nuclei and the electron distribution (Fig. 1–1). Because of Coulomb scattering, electron-scattering cross-section is some six orders of magnitude stronger than X-ray scattering from molecules.¹⁹ It was this feature of electron–matter interaction that prompted Mark and Wierl in 1930 to use electrons (instead of X-rays) to study gas-phase molecular structures; they produced a diffraction pattern²⁰ from CCl₄ that was more distinct than similar X-ray scattering exposures obtained

earlier by Debye and co-workers²¹ and required a fraction of the exposure time (1 s compared to 20 h for the X-ray pattern). Second, UED experiments are ‘tabletop’ scale and can be implemented with ultrafast laser sources. Third, electrons are less damaging to specimens per useful scattering event. For example, using electrons in microscopy²² has shown²³ that the ratio of inelastic/elastic scattering events for 80–500 keV electrons is 3, and that for 1.5-Å X-rays is 10. The energy deposited per inelastic scattering event for 1.5-Å X-rays is 400 times that of electrons, thus implying that the energy deposited per useful (elastic) scattering event is 1000 times smaller for 80–500 keV electrons. Fourth, electrons, because of their short penetration depth arising from strong interaction with matter, are well-suited for surface characterization, gases, and thin samples.

Imaging transient molecular structures on ultrafast time scales demands not only the marriage of ultrafast probing techniques with those of conventional diffraction, but also the development of new concepts for reaching simultaneously the temporal and spatial resolutions of atomic scale. Following the development of femtochemistry in the mid 1980s, the Zewail group embarked upon the challenge of achieving time-resolved electron diffraction in the sub-picosecond and picosecond regime. In 1991, it was proposed that replacing the ‘probe’ laser pulse in femtochemistry experiments with an electron pulse (Fig. 1–2) would open up new vistas in our

understanding of structural dynamics.^{24, 25} A year later, diffraction patterns with picosecond electron pulses were reported, but without recording the temporal evolution of the reaction.²⁶ Since those first images, technical and theoretical advances in our laboratory²⁷⁻⁴⁵ have culminated in the third-generation UED apparatus (UED-3) with spatial and temporal resolution of 0.01 Å and 1 ps, respectively. Moreover, we can now detect chemical change as low as 1%. As a result of these advances, a wide variety of phenomena has been studied in our laboratory.²⁷⁻⁴⁵

Historically, the first gas-phase electron diffraction (GED) investigation of a molecular structure, that of CCl₄, was reported by Mark and Wierl in 1930,²⁰ only three years after the discovery of electron diffraction by Davisson and Germer for a crystal of nickel,⁴⁶ and by Thomson and Reid for a thin film of celluloid.⁴⁷ The utility of gas-phase electron diffraction was recognized by several research groups, beginning with that of Linus Pauling and his graduate student, Lawrence Brockway,⁴⁸ at Caltech. GED was further refined to elucidate the precise arrangement of atoms in molecules for understanding the *static* nature of the chemical bond.^{19, 49, 50} The original method for analyzing GED data, initiated by Mark and Wierl, and further developed by Pauling and Brockway, was called the ‘visual method’ because the patterns were analyzed simply by measuring the positions of maxima and minima, and by estimating their relative height and

depth by eye, thanks to the extraordinary ability of the human eye to correct for the steeply falling background. Soon, however, a more direct method of determining bond distances was proposed by Pauling and Brockway⁵¹—the so-called radial distribution method—that invoked the Fourier transform of the estimated intensity data.

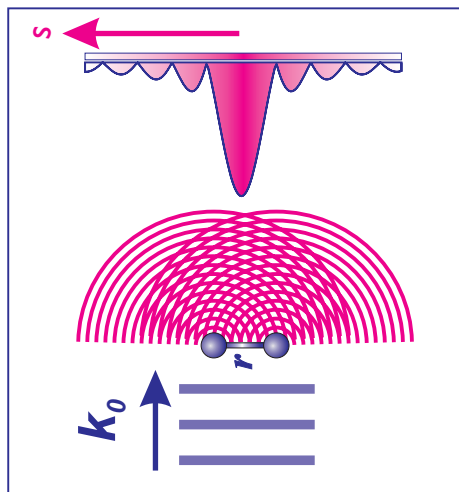
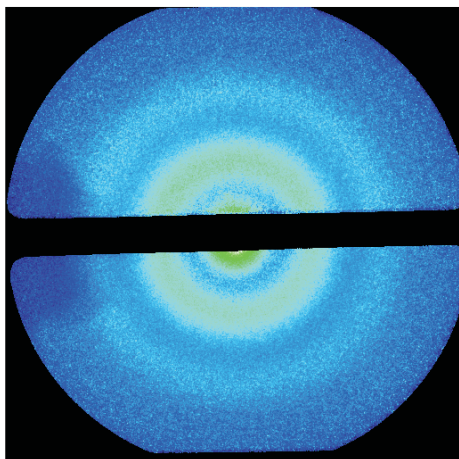
A significant advance in the quantitative measurement of the intensity distribution was the introduction of the ‘rotating sector’ into the diffraction apparatus, proposed by Trendelenbur,⁵² Finbak,⁵³ and Debye⁵⁴ in the 1930s, which obviated the use of visual estimates. This rotating sector (a metallic disk of special shape)—which attenuates the inner, more intense part of the pattern, effectively enhancing the outer, weaker signals—was a crucial step in the development of what came to be known as the ‘sector-microphotometer’ method. Until the early 1970s, diffraction patterns were recorded exclusively with photographic film. The replacement of these film-based detectors with an electronic detector by Fink and Bonham⁵⁵ was a turning point towards electronic microdensitometry—evolving from scintillator-photomultipliers^{56, 57} to linear array detectors.⁵⁸ The introduction of 2D area detectors—charge-coupled device (CCD) with fiber optic coupling and image intensification—in our laboratory^{26, 30, 35} represents the current state-of-the-art in digital diffraction imaging.

It is not surprising that the earliest attempts at introducing time resolution into electron diffraction mirrored the development of digital detection techniques. Ischenko *et al.*⁵⁹ created microsecond electron pulses by chopping a continuous electron beam with an electromagnetic chopper to study the IR multiphoton dissociation of CF₃I (see ref.⁵⁰ for a critique). Rood and Milledge⁶⁰ conducted diffraction studies on the decomposition of ClO₂ with 100- μ s electron pulses, while Bartell and Dibble⁶¹ studied phase change in clusters produced in supersonic jets, with a time-of-flight resolution of *ca.* 1 μ s. Ewbank *et al.*⁶² advanced the temporal resolution to nanoseconds (and later shorter⁶³) by combining a laser-initiated electron source with a linear diode array detector and investigated the photofragmentation of small molecules (e.g., CS₂). Mourou and Williamson⁶⁴ pioneered the use of a modified streak camera to generate 100-ps electron pulses to record diffraction images from thin aluminum films in transmission mode; they subsequently produced 20-ps electron pulses to study the phase transformation in these films before and after irradiation with a laser.⁶⁵ Elsayed-Ali and co-workers succeeded in using 200-ps (and later shorter) electron pulses to investigate surface melting with reflection high-energy electron diffraction (RHEED).^{66, 67}

In the field of ultrafast electron diffraction, for the studies of isolated structures *evolving with time*, the leap forward came from the use of digital

processing with CCD cameras, generation of ultrashort electron packets using femtosecond lasers and high extraction fields, and *in situ* pulse sequencing and clocking—all of which gave us unprecedented levels of sensitivity and spatiotemporal resolution. Using these developments, we have studied a variety of complex molecular structures and resolved the temporal evolution of different classes of reactions, as discussed in this thesis. More recently, Weber and co-workers have succeeded in obtaining ultrafast diffraction images of cyclohexadiene,⁶⁸ a system we have studied both theoretically and experimentally. Theoretical analysis of the diffraction signatures of individual vibrational modes in polyatomic molecules prepared in a specific vibrational state was also reported.^{69, 70}

Atomic-Scale Diffraction

 N_2 Diffraction Image

N–N Bond Length

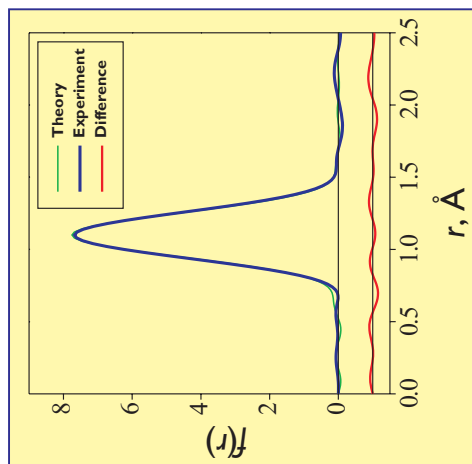


Figure 1-1. Example of diffraction with two scattering centers. (*Left*) Just as in Young’s classic double-slit experiment, interference patterns are created when an electron beam with wavelength on the order of 1 Å scatters from two atoms. (*Middle*) Diffraction image of diatomic nitrogen recorded in UED-3. (*Right*) Radial distribution curve, $f(r)$, for nitrogen calculated from the diffraction image. The peak of the $f(r)$ curve corresponds to the average N–N bond length, and the FWHM of the peak is related to the mean amplitude of vibration, l .

The UED Experiment

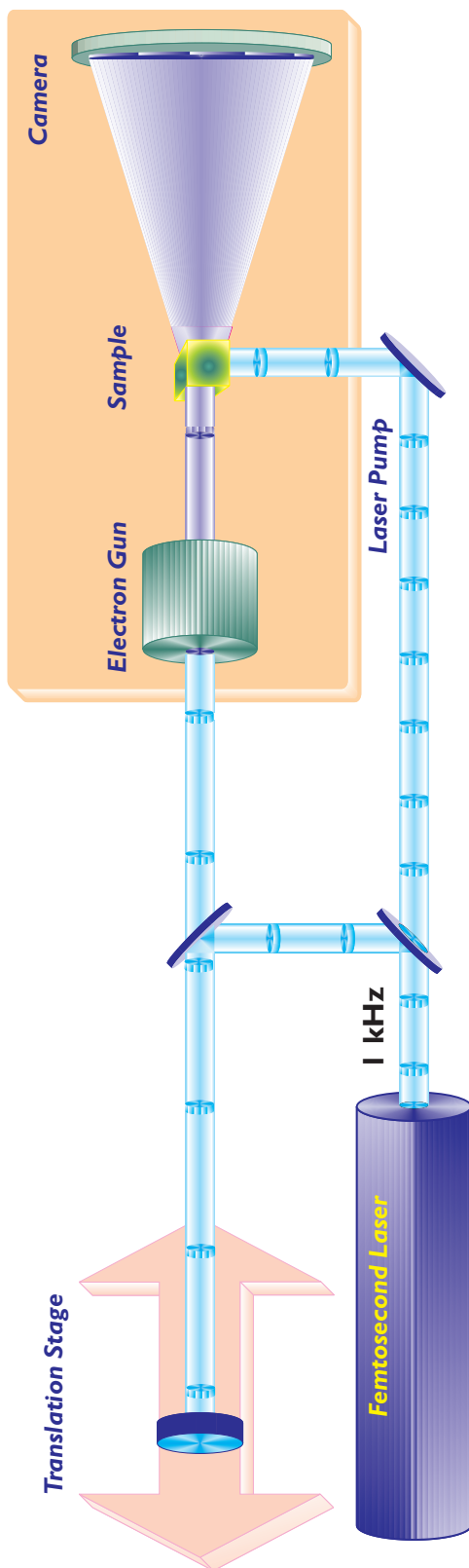


Figure 1-2. The UED Experiment. Properly timed sequences of ultrafast pulses are employed—femtosecond laser pulse to initiate the reaction and ultrashort electron pulses to probe the ensuing structural change in the molecular sample. The resulting electron diffraction patterns are then recorded on a CCD camera.

References

1. Zewail, A. H., *The Chemical Bond: Structure and Dynamics*. Academic Press: San Diego, California, 1992.
2. Kojic-Prodic, B.; Kroon, J., *Croat. Chem. Acta* **2001**, *74*, 1.
3. Zewail, A. H., *Femtochemistry: Atomic-Scale Dynamics of the Chemical Bond Using Ultrafast Lasers*. In *Les Prix Nobel: The Nobel Prizes 1999*, Frängsmyr, T., Ed., Almqvist & Wiksell: Stockholm, 2000.
4. Zewail, A. H., *Femtochemistry: Ultrafast Dynamics of the Chemical Bond*. World Scientific: Singapore, 1994.
5. Manz, J.; Wöste, L., *Femtosecond Chemistry*. VCH: Weinheim, 1995.
6. Chergui, M., *Femtochemistry: Ultrafast Chemical and Physical Processes in Molecular Systems*. World Scientific: Singapore, 1996.
7. Sundström, V., *Femtochemistry and Femtobiology: Ultrafast Reaction Dynamics at Atomic-Scale Resolution*. Imperial College Press: London, 1997.
8. De Schryver, F. C.; De Feyter, S.; Schweitzer, G., *Femtochemistry*. Wiley-VCH: Weinheim, 2001.
9. Douhal, A.; Santamaria, J., *Femtochemistry and Femtobiology: Ultrafast Dynamics in Molecular Science*. World Scientific: Singapore, 2002.
10. Zanni, M. T.; Hochstrasser, R. M., *Curr. Opin. Struc. Biol.* **2001**, *11*, 516.

11. Mukamel, S., *Principles of Nonlinear Optical Spectroscopy*. Oxford University Press: New York, 1995.
12. Gauthier, J. C.; Rouse, A., *J. Phys. IV* **2002**, *12*, 59.
13. Siders, C. W.; Cavalleri, A., *Science* **2003**, *300*, 591.
14. Rouse, A.; Rischel, C.; Gauthier, J.-C., *Rev. Mod. Phys.* **2001**, *73*, 17.
15. Chen, L. X.; Jäger, W. J. H.; Jennings, G.; Gosztola, D. J.; Munkholm, A.; Hessler, J. P., *Science* **2001**, *292*, 262.
16. Ouïlanov, D. A.; Tomov, I. V.; Dvornikov, A. S.; Rentzepis, P. M., *Proc. Natl. Acad. Sci. USA* **2002**, *99*, 12556.
17. Ráksi, F.; Wilson, K. R.; Jiang, Z.; Ikhlef, A.; Côté, C. Y.; Kieffer, J.-C., *J. Chem. Phys.* **1996**, *104*, 6066.
18. Saes, M.; Bressler, C.; Abela, R.; Grolimund, D.; Johnson, S. L.; Heimann, P. A.; Chergui, M., *Phys. Rev. Lett.* **2003**, *90*, 0474031.
19. Hargittai, I.; Hargittai, M., *Stereochemical Applications Of Gas-Phase Electron Diffraction*. VCH: New York, 1988.
20. Mark, H.; Wierl, R., *Naturwissenschaften* **1930**, *18*, 205.
21. Debye, P.; Bewilogua, L.; Ehrhardt, F., *Phys. Z.* **1929**, *30*, 84.
22. Klug, A., In *Les Prix Nobel: The Nobel Prizes 1982*, Odelberg, W., Ed., Almqvist & Wiksell: Stockholm, 1983.
23. Henderson, R., *Q. Rev. Biophys.* **1995**, *28*, 171.
24. Zewail, A. H., *Farad. Discuss.* **1991**, *91*, 207.

-
25. Williamson, J. C.; Zewail, A. H., *Proc. Natl. Acad. Sci. USA* **1991**, *88*, 5021.
 26. Williamson, J. C.; Dantus, M.; Kim, S. B.; Zewail, A. H., *Chem. Phys. Lett.* **1992**, *196*, 529.
 27. Williamson, J. C.; Zewail, A. H., *Chem. Phys. Lett.* **1993**, *209*, 10.
 28. Williamson, J. C.; Zewail, A. H., *J. Phys. Chem.* **1994**, *98*, 2766.
 29. Dantus, M.; Kim, S. B.; Williamson, J. C.; Zewail, A. H., *J. Phys. Chem.* **1994**, *98*, 2782.
 30. Williamson, J. C.; Cao, J. M.; Ihee, H.; Frey, H.; Zewail, A. H., *Nature* **1997**, *386*, 159.
 31. Ihee, H.; Cao, J.; Zewail, A. H., *Chem. Phys. Lett.* **1997**, *281*, 10.
 32. Cao, J.; Ihee, H.; Zewail, A. H., *Chem. Phys. Lett.* **1998**, *290*, 1.
 33. Cao, J.; Ihee, H.; Zewail, A. H., *Proc. Natl. Acad. Sci. USA* **1999**, *96*, 338.
 34. Ihee, H.; Zewail, A. H.; Goddard III, W. A., *J. Phys. Chem. A* **1999**, *103*, 6638.
 35. Ihee, H.; Lobastov, V. A.; Gomez, U.; Goodson, B. M.; Srinivasan, R.; Ruan, C.-Y.; Zewail, A. H., *Science* **2001**, *291*, 458.
 36. Ihee, H.; Cao, J. M.; Zewail, A. H., *Angew. Chem.-Int. Edit.* **2001**, *40*, 1532.
 37. Ihee, H.; Kua, J.; Goddard III, W. A.; Zewail, A. H., *J. Phys. Chem. A* **2001**, *105*, 3623.

-
38. Ruan, C. Y.; Lobastov, V. A.; Srinivasan, R.; Goodson, B. M.; Ihee, H.; Zewail, A. H., *Proc. Natl. Acad. Sci. USA* **2001**, *98*, 7117.
39. Lobastov, V. A.; Srinivasan, R.; Goodson, B. M.; Ruan, C. Y.; Feenstra, J. S.; Zewail, A. H., *J. Phys. Chem. A* **2001**, *105*, 11159.
40. Ihee, H.; Feenstra, J. S.; Cao, J. M.; Zewail, A. H., *Chem. Phys. Lett.* **2002**, *353*, 325.
41. Ihee, H.; Goodson, B. M.; Srinivasan, R.; Lobastov, V.; Zewail, A. H., *J. Phys. Chem. A* **2002**, *106*, 4087.
42. Goodson, B. M.; Ruan, C. Y.; Lobastov, V. A.; Srinivasan, R.; Zewail, A. H., *Chem. Phys. Lett.* **2003**, *374*, 417.
43. Srinivasan, R.; Lobastov, V. A.; Ruan, C. Y.; Zewail, A. H., *Helv. Chim. Acta* **2003**, *86*, 1763.
44. Srinivasan, R.; Feenstra, J. S.; Park, S. T.; Xu, S. J.; Zewail, A. H., *J. Am. Chem. Soc.* **2004**, *126*, 2266.
45. Xu, S. J.; Park, S. T.; Feenstra, J. S.; Srinivasan, R.; Zewail, A. H., *J. Phys. Chem. A* **2004**, *108*, 6650.
46. Davisson, C. J.; Germer, L. H., *Phys. Rev.* **1927**, *30*, 705.
47. Thomson, G. P.; Reid, A., *Nature* **1927**, *119*, 890.
48. Brockway, L. O., *Rev. Mod. Phys.* **1936**, *8*, 231.
49. Goodman, P., *Fifty Years of Electron Diffraction*. D. Reidel Publishing: Dordrecht, 1981.

-
50. Mastryukov, V. S., *Vibrational Spectra and Structure* **2000**, *24*, 85.
51. Pauling, L.; Brockway, L. O., *J. Am. Chem. Soc.* **1935**, *57*, 2684.
52. Trendelenburg, F., *Naturwissenschaften* **1933**, *21*, 173.
53. Finbak, C., *Avh. Norsk Vidensk.-Akad. Oslo* **1937**, 13.
54. Debye, P. P., *Phys. Z.* **1939**, *66*, 404.
55. Fink, M.; Bonham, R. A., *Rev. Sci. Instrum.* **1970**, *41*, 389.
56. Bonham, R. A.; Fink, M., *High Energy Electron Scattering*. Van Nostrand Reinhold: New York, 1974.
57. Fink, M.; Moore, P. G.; Gregory, D., *J. Chem. Phys.* **1979**, *71*, 5227.
58. Ewbank, J. D.; Schäfer, L.; Paul, D. W.; Benston, O. J.; Lennox, J. C., *Rev. Sci. Instrum.* **1984**, *55*, 1598.
59. Ischenko, A. A.; Golubkov, V. V.; Spiridonov, V. P.; Zgurskii, A. V.; Akhmanov, A. S.; Vabischevich, M. G.; Bagratashvili, V. N., *Appl. Phys. B* **1983**, *32*, 161.
60. Rood, A. P.; Milledge, J., *J. Chem. Soc., Faraday Trans. 2* **1984**, *80*, 1145.
61. Bartell, L. S.; Dibble, T. S., *J. Am. Chem. Soc.* **1990**, *112*, 890.
62. Ewbank, J. D.; Faust, W. L.; Luo, J. Y.; English, J. T.; Monts, D. L.; Paul, D. W.; Dou, Q.; Schäfer, L., *Rev. Sci. Instrum.* **1992**, *63*, 3352.
63. Ischenko, A. A.; Schäfer, L.; Ewbank, J. D., In *Time-resolved Diffraction*, Helliwell, J. R.; Rentzepis, P. M., Eds., Oxford University Press: New York, 1997.

-
64. Mourou, G.; Williamson, S., *Appl. Phys. Lett.* **1982**, *41*, 44.
65. Williamson, S.; Mourou, G.; Li, J. C. M., *Phys. Rev. Lett.* **1984**, *52*, 2364.
66. Elsayed-Ali, H. E.; Mourou, G. A., *Appl. Phys. Lett.* **1988**, *52*, 103.
67. Aeschlimann, M.; Hull, E.; Cao, J.; Schmuttenmaer, C. A.; Jahn, L. G.; Gao, Y.; Elsayed-Ali, H. E.; Mantell, D. A.; Scheinfein, M. R., *Rev. Sci. Instrum.* **1995**, *66*, 1000.
68. Dudek, R. C.; Weber, P. M., *J. Phys. Chem. A* **2001**, *105*, 4167.
69. Ryu, S.; Stratt, R. M.; Baeck, K. K.; Weber, P. M., *J. Phys. Chem. A* **2004**, *108*, 1189.
70. Geiser, J. D.; Weber, P. M., *J. Chem. Phys.* **1998**, *108*, 8004.

2

UED THEORY*

2.1 Introduction

The general theory of GED is well-established;^{1, 2} here, we summarize the basic equations used in the analysis of scattering patterns and the subsequent extraction of internuclear separations. Electron scattering intensity is typically expressed as a function of s , the magnitude of momentum transfer between an incident electron and an elastically scattered electron:

$$s = \frac{4\pi}{\lambda} \sin\left(\frac{\theta}{2}\right) \quad (2-1)$$

* Parts of this chapter have been adapted from Srinivasan, R.; Lobastov, V.A.; Ruan, C.-Y.; Zewail, A.H., *Helv. Chim. Acta*, **2003**, 86, 1762.

where λ is the de Broglie wavelength of the electrons (0.067 Å at 30 keV) and θ is the scattering angle.

The total scattering intensity, I , is a sum of contributions from individual atoms (atomic scattering, I_A) superimposed with interference terms from all atom–atom pairs (molecular scattering, I_M):

$$I(s) = I_A(s) + I_M(s) \quad (2-2)$$

In the independent-atom model, where the independence of the electronic potentials of each atom in the molecule is assumed, the atomic scattering intensity can be written as a sum of elastic and inelastic scattering contributions:

$$I_A(s) = C \sum_{i=1}^N \left(|f_i(s)|^2 + 4 \frac{S_i(s)}{a_0^2 s^4} \right) \quad (2-3)$$

where N is the number of atoms in the molecule; f_i and S_i are, respectively, the elastic and inelastic scattering amplitudes for atom i , respectively; a_0 is the Bohr radius; and C is a proportionality constant. The contributions from spin-flip scattering amplitudes (g_i) have not been included as they are generally neglected for high-energy electron diffraction experiments.³

For the purpose of structural determination, only I_M is of interest because it contains the information regarding internuclear separations. The molecular scattering intensity of an isotropic sample can be written as a double sum over all N atoms in the molecule:

$$I_M(s) = C \sum_i^N \sum_{j \neq i}^N |f_i| |f_j| \exp\left(-\frac{1}{2} l_{ij}^2 s^2\right) \cos(\eta_i - \eta_j) \frac{\sin(sr_{ij})}{sr_{ij}} \quad (2-4)$$

where f_i is the elastic scattering amplitude for the i th atom, η_i is the corresponding phase term, r_{ij} is the internuclear separation between atoms i and j , l_{ij} is the corresponding mean amplitude of vibration, and C is a proportionality constant. The atomic scattering factors f and η depend on s and atomic number Z ; tables of f and η are available in the literature⁴ with f scaling as Z/s^2 (*Rutherford* scattering). The relative contribution of each atomic pair to the total molecular scattering intensity (from Eqn. 2-4) is, therefore, roughly proportional to $(Z_i Z_j)/r_{ij}$. Since $I_M(s)$ decays approximately as s^{-5} , the modified molecular scattering intensity, $sM(s)$, is often used instead of $I_M(s)$ in order to highlight the oscillatory behavior ($\sin(sr_{ij})/r_{ij}$) of the diffraction signal at higher values of s ; note that the $\sim s^{-5}$ dependence arises from the s^{-2} contribution from f_i and similarly from f_j , along with the $1/s$ term of the sinc function, which results from isotropic averaging in the gas sample.

The modified molecular scattering intensity can be defined either as:

$$sM(s) = s \frac{I_M(s)}{I_A(s)} \quad (2-5a)$$

or

$$sM(s) = s \frac{I_M(s)}{|f_a||f_b|} \quad (2-5b)$$

where a and b correspond to two chosen atoms in the molecule (usually atoms with relatively high Z). Note that the experimental $I_M^E(s)$ can be transformed into $sM^E(s)$ by simply dividing by an atomic reference signal (xenon gas, in our case) and multiplying by s (obtained from measured θ through the known camera length).

Although the molecular scattering function contains all of the structural information about the molecule, a more intuitive interpretation of experimental results is achieved by taking the Fourier (sine) transform of $sM(s)$ and examining $f(r)$, the radial distribution function:

$$f(r) = \int_0^{s_{\max}} sM(s) \sin(sr) \exp(-ks^2) ds \quad (2-6)$$

where k is a damping constant. The exponential damping term filters out the artificial high frequency oscillations in $f(r)$ caused by the cutoff at s_{\max} . The radial distribution curve reflects the relative density of internuclear distances

in the molecule. In our UED-3 experiments, the available experimental scattering intensity, $sM^E(s)$, typically ranges from $s_{\min} = 1.5 \text{ \AA}^{-1}$ to $s_{\max} = 18.5 \text{ \AA}^{-1}$ (θ from 0.9° to 11.3°). For the range from 0 to s_{\min} , the theoretical scattering intensity, $sM^T(s)$, is appended to avoid distortions of the radial distribution baseline. It should be noted that all data analyses and structural refinements are performed on $sM^E(s)$ and not $f(r)$ because of inaccuracies that could potentially be introduced into $f(r)$ through improper choice of k .

2.2 The Diffraction-Difference Method: Transient Structures

To follow the structural changes that occur over the course of a given reaction, a series of averaged 2D diffraction images are recorded—with varying time delay, t (see Fig. 2–1). Before analyzing the time-dependent diffraction signals, we normalize the intensity of each time-dependent 2D image to the total number of electrons detected on the CCD. This normalization procedure accounts for any systematic variation (1% or less) in electron scattering intensity as a function of temporal delay. Each of these normalized, averaged images, thus, reflects the transient behavior of the molecular structures at a particular temporal delay following excitation. Unlike the ground-state data, the scattering intensity at time $t > 0$, $I(t > 0; s)$, contains contributions from more than one type of molecular species—not just the reactant structures, but also the transient, intermediate, and product

structures of the reaction.

Structural dynamics of a species involves two important changes: *population* change and *structural* change. Consider the following reaction:



where there is a change of species from reactant (S_R) through intermediate (S_I) to product (S_P). A species is defined as a molecular entity with a particular chemical formula. The time-resolved scattering intensity $I(t; s)$ can be written as a sum of the individual scattering intensities from each species, $I_\alpha(t; s)$, at time t :

$$I(t; s) = \sum_\alpha I_\alpha(t; s) = \sum_\alpha p_\alpha(t) \cdot \sigma_\alpha(t; s) \quad (2-8)$$

where α indexes all possible species (reactant, intermediate, or product) occurring over the course of the reaction, $p_\alpha(t)$ is the normalized probability, henceforth referred to as the population of a given species, α , and $\sigma_\alpha(t; s)$ is the effective scattering cross-section from that species. Depending on the time resolution of the diffraction experiment, we can resolve either the temporal change in species population, $p_\alpha(t)$, or the temporal change in species structure—manifested as a change in the effective scattering cross-section,

$\sigma_a(t; s)$ —or both.

In UED, all species present will scatter the incident electrons regardless of their participation in the reaction. Thus, in most cases, the vast majority (>85–90%) of the diffracting media is comprised of non-reacting parent molecules: $p_{\text{reactant}} \gg p_{\text{intermediate}} \text{ or } p_{\text{product}}$. Furthermore, the molecular scattering intensity from a reaction fragment is usually weaker than that from the parent molecule because it has fewer internuclear pairs. Therefore, to accentuate the diffraction signal arising from structural changes occurring over the course of the reaction, we employ the diffraction-difference method,⁵ wherein we use a reference image to obtain the diffraction-difference signal, $\Delta I(t; t_{\text{ref}}; s)$, from the relation:

$$\Delta I(t; t_{\text{ref}}; s) = I(t; s) - I(t_{\text{ref}}; s) \quad (2-9)$$

where t_{ref} refers to the reference time (e.g., prior to the arrival of the reaction-initiating laser pulse). Combining Eqns. 2-8 and 2-9 gives

$$\Delta I(t; t_{\text{ref}}; s) = \sum_{\alpha} p_{\alpha}(t) \cdot \sigma_{\alpha}(t; s) - \sum_{\alpha} p_{\alpha}(t_{\text{ref}}) \cdot \sigma_{\alpha}(t_{\text{ref}}; s) \quad (2-10)$$

The experimental diffraction intensity curve is a sum of the desired structural information, $I_M^E(s)$, and a background intensity profile, $I_B^E(s)$:

$$I^E(s) = I_B^E(s) + I_M^E(s) \quad (2-11)$$

where $I_B^E(s)$ contains contributions from atomic scattering, $I_A(s)$, and the experimental background response. It follows from this definition that the experimental difference curve is given by:

$$\Delta I^E(t; t_{\text{ref}}; s) = \Delta I_M^E(t; t_{\text{ref}}; s) + \Delta I_B^E(t; t_{\text{ref}}; s) \quad (2-12)$$

Because I_B^E is comprised mostly of atomic scattering, which is unchanged over the course of a chemical reaction, $\Delta I_B^E(t; t_{\text{ref}}; s)$ should be nearly zero. Thus, whereas the total diffraction signal, $I(t; s)$, is dominated by the background intensity, $I_B^E(t; s)$, the diffraction-difference curve is dominated by the molecular scattering intensity, $I_M^E(t; s)$:

$$\Delta I^E(t; t_{\text{ref}}; s) \approx \Delta I_M^E(t; t_{\text{ref}}; s) \quad (2-13)$$

Thus, Eqn. 2-13, which is a direct consequence of the diffraction-difference approach, allows us to obtain transient molecular structures even if their population is small relative to the unchanging background (Fig. 2-2). It may be noted that the diffraction-difference method does not depend on the

specific formulae used to express I_M . While the well-known description, Eqn. 2–4, is usually used, formulae more sophisticated than Eqn. 2–4 have been used in our UED studies.

One of the most important features of the diffraction-difference method is the control over t_{ref} . The choice of t_{ref} —the sequence of the electron pulses—allows us to isolate structures of different species evolving with time:

(1) By choosing t_{ref} to be at negative time, we can obtain the ground-state diffraction pattern. Also, by recording diffraction images at two different negative times (probing the same reactant structure at each of these times), we can obtain a control diffraction-difference image to verify the absence of rings.

(2) By choosing t_{ref} to be at a specific positive time, we can isolate different transient species in, say, non-concerted reactions based on the relevant timescales of the non-concerted bond breaking, as described for the case of $\text{C}_2\text{F}_4\text{I}_2$ in Chapter 5 (see Fig. 2–3).

(3) Finally, we can also extract the molecular diffraction signal resulting only from the transient species via the ‘transient-only’ or the ‘transient-isolated’ method. In this case, the reactant diffraction signal ($I_{\text{reactant}}(s)$, obtained at a negative time) is scaled by the fractional change, $\Delta p_{\text{reactant}}(t; t_{\text{ref}})$, and added to the diffraction difference signals obtained at positive times, thereby canceling out the parent contribution:

$$\Delta I(t; t_{\text{ref}}; s) + \Delta p_{\text{reactant}}(t; t_{\text{ref}}) \cdot I_{\text{reactant}}(s) = \sum_{\alpha \neq \text{reactant}} \Delta p_{\alpha}(t; t_{\text{ref}}) \cdot \sigma_{\alpha}(t; s) \quad (2-14)$$

2.3 Ground-State Structures

Ground-state diffraction patterns are obtained by timing the electron pulse to arrive at the molecular sample before the laser pulse (negative time; see Fig. 2-1) or by completely blocking the laser arm (to reduce the noise due to laser light). From Eqn. 2-5, the modified experimental molecular scattering intensity of the ground-state is given by:

$$sM^E(s) = s \frac{I^E(s) - I_B^E(s)}{I_A(s)} \quad (2-15a)$$

or

$$sM^E(s) = s \frac{I^E(s) - I_B^E(s)}{|f_a||f_b|} \quad (2-15b)$$

We do not obtain the curve for $I_B^E(s)$ by merely calibrating the detector because the amount of scattered laser light and other factors vary from experiment to experiment and with each molecular system. Instead, background curves are independently obtained for each experiment. Such background curves may be ascertained by different methods, three of which

are described: (1) A crude yet often effective approximation is a low-order polynomial curve fit through all the data points of $I^E(s)$; (2) A more rigorous way of obtaining $I_B^E(s)$ exploits the sinusoidal nature of $I_M(s)$, cycling above and below zero several times over the experimental detection range. This approach introduces a set of zero-positions, s_n , of s where the theoretical molecular intensity curve, $I_M^T(s)$, crosses zero, *i.e.*, $I_M^T(s_n) = 0$. If $I_M^T(s)$ approaches $I_M^E(s)$, it should then hold from Eqn. 2-2 that $I^E(s_n) = I_B^E(s_n)$ at the zero-positions, s_n . Therefore, $I_B^E(s)$ can be approximated by fitting a polynomial curve through $[s_n, I^E(s_n)]$; (3) A third way to obtain $I_B^E(s)$ is to express $I_B^E(s)$ independently as a polynomial curve defined by the variable coefficients of each order, and to optimize these variables by minimizing the difference (more precisely, χ^2) between $I_M^T(s)$ and $I_M^E(s)$. This method should produce the same background curve obtained with the second method if there is no systematic error. The three methods can also be applied to the time-resolved diffraction data. Currently, method (3) as described above is the method of choice in UED-3.

2.4 Structure Search and Refinement

UED utilizes quantum-chemical calculations as a starting point for the global conformational search. In UED-3, the structure parameters are constructed with internal coordinates of a geometrically consistent structural

model for the molecule—the so-called Z -matrix of quantum chemistry—to facilitate easier comparison between theory and experiment. To ensure that all possible structures are considered in the refinements, Monte Carlo sampling procedures are applied to search all possible good fits to the data (in terms of χ^2) in a configuration space set up by the Z -matrix coordinates. The distance between any two given structures is defined as the square root of the sum of the squared displacements between all corresponding nuclear coordinates of the two structures. Based on the distance between randomly sampled structures to a starting structure, the configuration hyperspace is first partitioned and then searched for local minima. When the sampling within the partitioned subspace is found to converge to a local χ^2 minimum, the radius of convergence is determined along each adjustable internal coordinate to give the size of local minimum basin. Finally, lowest-local-minima structures are statistically analyzed to reveal the ensemble distribution of a global minimum structure. The Monte Carlo sampling algorithm, coupled with the internal coordinate representation, allows the fit structure to be vastly different from the starting model provided by quantum calculations. This forms the basis of the UED-3 structural search in large conformational space guided by experiment.

Refinement of the diffraction data is performed with software developed in our laboratory at Caltech using a procedure that iteratively

minimizes the statistical χ^2 . For example, for a given difference curve, $\Delta I^E(t; t_{\text{ref}}; s)$, the determination of the relative fractions or structural parameters of each molecular species is made by minimizing

$$\chi^2 = \sum_{s_{\text{min}}}^{s_{\text{max}}} \frac{[S_c \cdot \Delta s M^T(t; t_{\text{ref}}; s) - \Delta s M^E(t; t_{\text{ref}}; s)]^2}{[\delta(s)]^2} \quad (2-16)$$

where the $\Delta s M(s)$ is the difference-modified molecular-scattering intensity, $\delta(s)$ is the standard deviation of $\Delta s M^E(t; t_{\text{ref}}; s)$ at each s position (over the available range), and S_c is a scaling factor (whose magnitude is determined by the amplitude of the ground-state signal). $\Delta s M^E(t; t_{\text{ref}}; s)$ is obtained from $\Delta I^E(t; t_{\text{ref}}; s)$ by Eqn. 2-15, and the $\delta(s)$ values are calculated from the corresponding values of $\delta(\text{pix})$ (the standard deviation of the scattering intensity at each pixel radius) with appropriate error propagation.

Beginning with an assumed initial species distribution and the starting structural parameters for each species, the software first fits the residual background, $\Delta I_B^E(t; t_{\text{ref}}; s)$, as a polynomial curve by optimizing the variable coefficients in order to minimize the difference (more precisely, χ^2) between $I_M^T(s)$ and $I_M^E(s)$. Then the experimental $\Delta s M^E(t; t_{\text{ref}}; s)$ curve is obtained with the background-free ΔI by Eqn. 2-15, and χ^2 is calculated to evaluate the quality of the fit. This procedure is repeated until the best least-

squares fit between theoretical and experimental $\Delta sM(s)$ curves is reached (*i.e.*, until χ^2 is minimized).

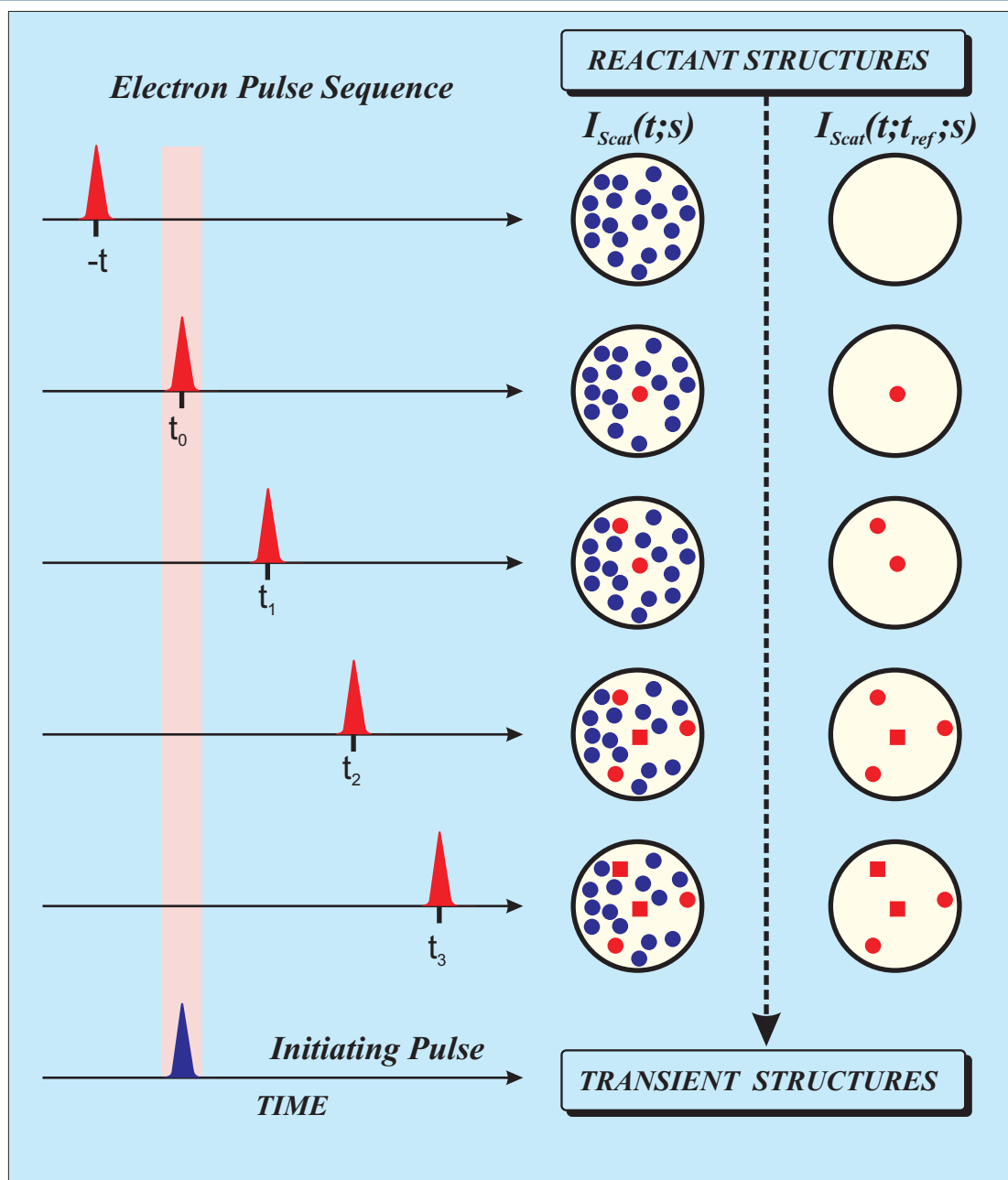


Figure 2-1. Concept of Ultrafast Electron Diffraction. An ultrafast initiation pulse (shown in blue) triggers the reaction and a second ultrashort electron pulse (shown in red) probes the resulting structural change. The electron pulse can be timed to arrive before the initiating pulse (negative time) thus probing the parent (shown as blue filled circles) or after the laser pulse (positive time), now probing the transient structures also (shown as red filled circles and squares). The time at which the light and electron pulses arrive simultaneously at the molecular sample is the zero-of-time (t_0). With increasing time lapse after the initiation pulse, the transient species undergoes a population change (indicated by the growth of the red filled units at the expense of the blue filled circles) and a structural change (shown as the transformation of red circles into red squares). The Diffraction-Difference Method dramatically enhances the significance of the transient species contribution in the diffraction-difference patterns; $I_{Scat}(t; t_{ref}; s)$. The small residual contribution of unreacted parents is not shown here.

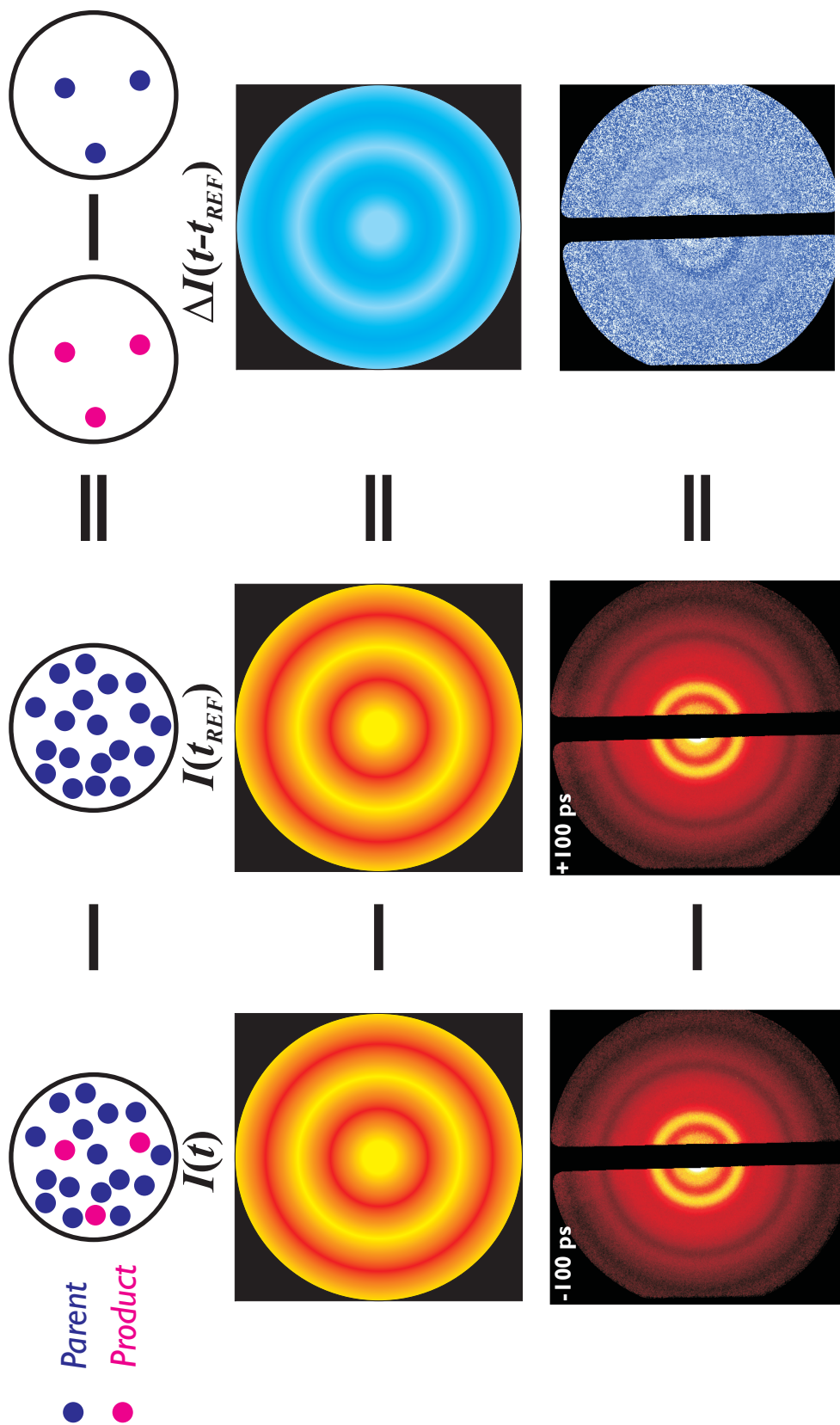


Figure 2-2. The diffraction-difference method. (*Top*) The difference of each time-resolved diffraction pattern from a reference pattern, t_{ref} (chosen at negative or at positive time), allows the extraction of the small population of time-evolving structures embedded in the large background signal of unreacted parents. (*Middle*) Note that this dramatically enhances the significance of the transient species contribution in the diffraction-difference patterns. (*Bottom*) The time-resolved patterns of pyridine at -100 ps and $+100$ ps are nearly identical; however their difference reveals the diffraction signature of the transient structure.

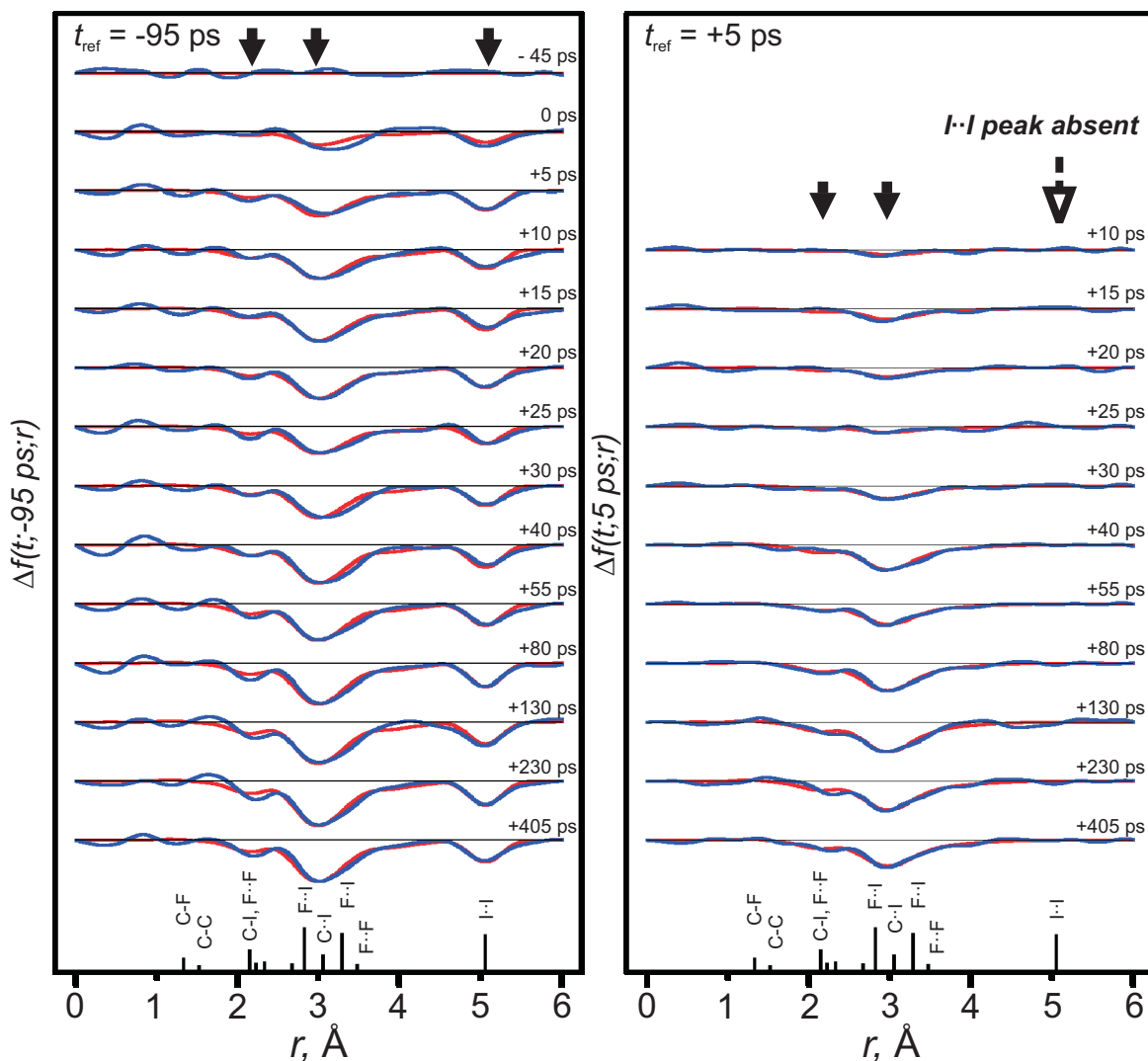
Isolation of Transient Structures: Choice of t_{ref} 

Figure 2-3. Isolation of transient species through choice of t_{ref} . Blue experimental $f(t; -95 \text{ ps}; r)$ curves (left) and $f(t; 5 \text{ ps}; r)$ curves (right) obtained at varying time delays with subsequent Fourier filtering (the Fourier cutoff was 9 \AA); theoretical curves are shown in red. Note that the negative peak at $\sim 5 \text{ \AA}$ is absent in the difference curves referenced to $+5 \text{ ps}$. Internuclear distances of the ground state *anti* conformer are indicated below the two panels for reference.

References

1. Hargittai, I.; Hargittai, M., *Stereochemical Applications Of Gas-Phase Electron Diffraction*. VCH: New York, 1988.
2. Williamson, J. C. Ultrafast Gas-Phase Electron Diffraction. Ph.D. Thesis, California Institute of Technology, Pasadena, 1998.
3. Yates, A. C., *Phys. Rev.* **1968**, *176*, 173.
4. Wilson, A. J. C.; Prince, E., *International Tables for Crystallography*. 2nd. ed.; Kluwer Academic Press: Dordrecht, 1999.
5. Ihee, H.; Cao, J.; Zewail, A. H., *Chem. Phys. Lett.* **1997**, *281*, 10.

3

THIRD GENERATION UED INSTRUMENTATION*

3.1 Introduction

Ultrafast electron diffraction combines several disparate fields of study: femtosecond pulse generation, electron beam optics, CCD detection systems, and GED. Output from a femtosecond laser is split into a pump path and an electron-generation path. The pump laser proceeds directly into the vacuum chamber and excites a beam of molecules. The probe laser is directed toward a back-illuminated photocathode, where the laser generates electron pulses via the photoelectric effect; the electrons are accelerated, collimated,

* Parts of this chapter have been adapted from Srinivasan, R.; Lobastov, V.A.; Ruan, C.-Y.; Zewail, A.H., *Helv. Chim. Acta*, **2003**, *86*, 1762.

focused, and scattered by the isolated molecules. The time delay between the arrival of the pump laser pulse and the probe electron pulse is controlled with a computer-driven translation stage. The resulting diffraction patterns are detected with a CCD camera, and the images are stored on a computer for later analysis. The UED-3 apparatus (Fig. 3–1) is also equipped with a time-of-flight mass spectrometer (MS-TOF) to aid in the identification of species generated during the course of chemical reactions. The following sections describe the individual components of the apparatus in more detail.

3.2 Femtosecond Laser System

The laser system can be divided into three stages: (1) ultrashort pulse generation, (2) pulse amplification, and (3) wavelength selection. In the first and second generations of UED, femtosecond laser pulses centered at 620 nm were generated with a home-built colliding-pulse, mode-locked ring dye laser (CPM) similar to the original system built for femtochemistry studies.^{1, 2} Output from the CPM (100 MHz, 200 pJ) was amplified to 2 mJ in a 30-Hz, homebuilt, four-stage, NdYAG-pumped dye amplifier (PDA). The pump wavelength was either maintained at 620 nm or converted to 310 nm through second harmonic generation with a KD*P crystal. A wavelength of 258 nm was required to create photoelectrons from the gold photocathode. Therefore, part of the pump laser was focused into a quartz crystal to generate

continuum, and 516 nm was selected with a 10-nm bandpass filter. The energy of these pulses was then boosted to microjoules in a two-state, transversely-pumped dye amplifier. The amplified output was frequency-doubled with a BBO crystal to form ultraviolet light at 258 nm, and the final laser output was focused and directed toward the photocathode.

The femtosecond laser path in UED-3 is shown in Fig. 3–2. Femtosecond laser pulses (82 MHz, 8 nJ) centered at 800 nm are generated with a Ti:sapphire oscillator (Tsunami, Spectra-Physics). These pulses are then amplified in a 1-kHz two-stage Ti:sapphire amplifier (SuperSpitfire, Spectra-Physics) to yield an output pulse energy of 3 mJ. Both stages are pumped by 1-kHz intra-cavity doubled Nd:YLF lasers (Merlin, Spectra-Physics). Single-shot autocorrelation of the amplified pulses yields a pulse duration full-width at half-maximum (fwhm) of 120 fs. These pulses are frequency-tripled in a femtosecond third-harmonic generator (Uniwave Technology) to give UV femtosecond pulses (350 μ J, 267 nm). An optical beam splitter is used to split this UV output into two arms to form the pump beam and the electron generation beam. Most (90%) of the UV beam is directed into the scattering chamber to initiate the chemical reaction, whereas a smaller fraction of the laser power is directed into a delay line with a computer-controlled translation stage and then focused onto the photocathode in the electron gun.

3.3 Vacuum Chambers and Molecular Beams

The first-generation UED apparatus housed the electron gun, molecular beam, and the CCD detector in the same chamber. However, the electron gun was prone to arcing if the background pressure rose much above 1×10^{-4} Torr, and on at least one occasion, an electrical arc was strong enough to destroy a CCD. Keeping the electron gun clean and free from arcing was the motivation for introducing differential pumping in the second-generation apparatus, so that the electron-gun-chamber pressure could be kept below 1×10^{-6} Torr even while running sample gas in the scattering chamber at 1×10^{-4} Torr or higher.

The UED-3 apparatus (Figs. 3-3a and 3-3b) consists of four separate vacuum chambers—the electron gun, the scattering chamber, the detection chamber and the time-of-flight mass spectrometry chamber—in order to protect sensitive instruments from potentially corrosive sample molecules. Pressures below 1×10^{-7} Torr are attained in the scattering chamber in the absence of the molecular beam and are as high as 10^{-4} Torr when the molecular beam is operating. The pressure in the detection chamber is kept at 10^{-2} Torr to avoid condensation on thermoelectrically cooled surfaces. In an effort to minimize scattered light, the laser pulses enter the scattering chamber through a series of baffles attached to the light entrance port and exit through a Wood's horn sealed by a quartz window at Brewster's angle.

Care is taken to avoid any stray electric or magnetic fields that might distort the path of the scattered electrons.

The sample molecules enter the vacuum chamber in a free-jet expansion through a 125- μm diameter needle tip; the sample inlet manifold being mounted on a high-precision *xyz* positioning stage. The needle and inlet tube are wrapped with a resistive heating element to prevent condensation and clogging, while the sample bulb is warmed with heating tapes to provide sufficient vapor pressure of less volatile samples inside the chamber.

3.4 Electron Gun

In UED-3, the cylindrically symmetric gun consists of a negatively-biased photocathode, a gold extraction mesh, an aperture, and a magnetic focusing lens (Fig. 3–4). The electron gun, powered by a variable high-voltage power supply, is designed to operate at 30 kV (compared to 18 kV in UED-2). The photocathode is back-illuminated in this design: a thin, 450- \AA silver film was deposited on one side of a sapphire window using a home-built metal evaporation chamber. A grounded gold extraction mesh, located 5 mm from the cathode surface, provides a very high extraction field of 6 kV/mm (compared to 2.7 kV/mm in UED-2) (see Fig. 3–5). The extracted electrons are then sent through a Pt:Ir aperture (150- μm diameter), which assists in cleaning the electron beam profile. The resulting equipotential lines in the

electron gun are shown in Fig. 3–6. In UED-2, a series of electrostatic lenses focused the electron beam by reducing the electron velocity over a region of several centimeters. However, replacing the electrostatic lens by a magnetic lens assembly (Fig. 3–7) in UED-3 successfully avoids this velocity reduction so that the electron velocity remains large and constant after the initial extraction, thereby reducing the transit time to the interaction region and concomitantly reducing the broadening of the electron pulse. Temporal characterization of the electron gun via a streak experiment is discussed in the next chapter. Two pairs of deflection plates provide x and y axis control of the electron beam, while a third pair of aluminum plates is used for streak measurements (Fig. 3–8).

3.5 CCD Camera System

A component critical to the success of UED is the detection system. The electron flux has to be maintained very low in order to keep the temporal resolution ultrafast. Early on, it was recognized that all of the scattered electrons must be detected for the experiment to succeed, and the two-dimensional CCD was introduced as a detector in direct electron bombardment mode in UED-1. To increase the longevity and flexibility of the detection system, UED-2 employed two CCDs: a small, direct-bombardment device installed in the scattering chamber for time-zero measurements, and

another large, scientific-grade device mounted in a separate chamber at the end of a phosphor scintillator/fiber optic/image intensifier chain for recording diffraction patterns.

In UED-3, we designed an improved low-noise, two-dimensional CCD camera assembly with the same elements as in UED-2, but without the small CCD (see Figs. 3–9 and 3–10). The camera has high detective quantum efficiency and principally comprises (Fig. 3–11) a phosphor scintillator (P-47), a fiber optic taper, a proximity-focused image intensifier (Hamamatsu), and finally the scientific-grade CCD camera (Photometrics, KAF-1000). Because the scattering intensity in electron diffraction decays rapidly with increasing scattering angle (usually varying over 6-8 orders of magnitude), we introduced a radially symmetric, variable neutral-density apodizing optical filter coated onto the backside of the scintillator—the rotating sector analog in our digital detection system, albeit with no mechanical moving parts. This filter allows the simultaneous measurement of diffracted intensities varying over 7 orders of magnitude, thereby effectively extending the dynamic range of detected intensities and consequently improving the precision of internuclear distance measurements in comparison with previous generations of UED. To block the scattered light and yet still permit single-electron detection, the phosphor screen is coated with 500-nm of aluminum.

The CCD chip consists of an array of 1024 x 1024 individual pixel elements (compared to 512 x 512 pixels in UED-2), each pixel being 24 μm on a side. The scattered electrons impinge upon a phosphor screen, thereby generating photons that are then transferred via a fiber-optic taper to a proximity-focused image intensifier. The photons are reconverted back to electrons at the photocathode on the front end of the image intensifier; the resulting electron signal is amplified and then reconverted back to photons at the back end of the intensifier. These photons are then transferred via a second fiber-optic taper onto the CCD chip.

Experiments showed that a single electron generates 20–30 counts, and saturation occurs above 65535 counts. The response of the CCD is linear over this range. The undiffracted beam, containing 99% of the electron intensity over a small area, is trapped by an aluminum beam stop mounted in front of the phosphor screen, in order to prevent damage. To enhance low-light sensitivity by reducing dark current, the CCD is cooled to -40°C by a three-stage thermoelectric cooler, which is coupled to a liquid circulation heat exchanger to draw heat away from the thermoelectric cooler. The CCD chip is controlled with a camera electronics unit and a computer-driven digital imaging system (Roper Scientific, V++). The analog–digital conversion process operates with 16-bit resolution, and the readout rate is kept at 200 kHz to minimize digital noise. At this rate, a 512 x 512 pixel image (obtained

by operating the CCD in 2 x 2 binning mode) requires *ca.* 1 s for readout. The images are stored on a computer for subsequent data analysis. A typical experiment involves recording 1000 frames per second (kHz repetition rate) on the CCD over 240 s to give a single image that is readout in 1 s; *ca.* 100 such images are then averaged to produce the diffraction pattern at a specific time delay. The digital nature of our data acquisition permits the use of a variety of powerful image processing techniques that aid in the isolation of molecular diffraction signals, as detailed in the next chapter.

3.6 Time-of-Flight Mass Spectrometer

Unlike the previous generations of UED, UED-3 was also equipped with a time-of-flight mass spectrometer (TOF-MS), which could be used either in a linear arrangement or in a reflectron design. The schematic for the TOF-MS is shown in Fig. 3–12, while Fig. 3–13 shows the TOF-MS chamber. As UED-3 was designed to handle large and complex chemical and biological molecules, the TOF-MS was included in the design to help identify the different species that were being generated in the interaction volume, and hence to potentially narrow the search space for structural determination. As seen in Fig. 3–14, the TOF-MS consists of a set of retractable field plates and an MCP detector. The SIMION calculations of equipotential lines along the center plane are displayed in Fig. 3–15. Figure 3–16 shows the

synchronization of electrical pulses in the UED-3 TOF-MS setup and a typical mass spectrum for the $C_2F_4I_2$ is shown in Fig. 3–17. Note, however, that for all the systems reported in this thesis, the diffraction patterns alone were able to identify the structural species, and hence, there was no need to record the mass spectra. However, current efforts in UED-3 are focused on biological molecules, and the mass spectral information could play an important role in species identification in such cases.

References

1. Zewail, A. H., *J. Phys. Chem. A* **2000**, *104*, 5660.
2. Williamson, J. C. Ultrafast Gas-Phase Electron Diffraction. Ph.D. Thesis, California Institute of Technology, Pasadena, 1998.

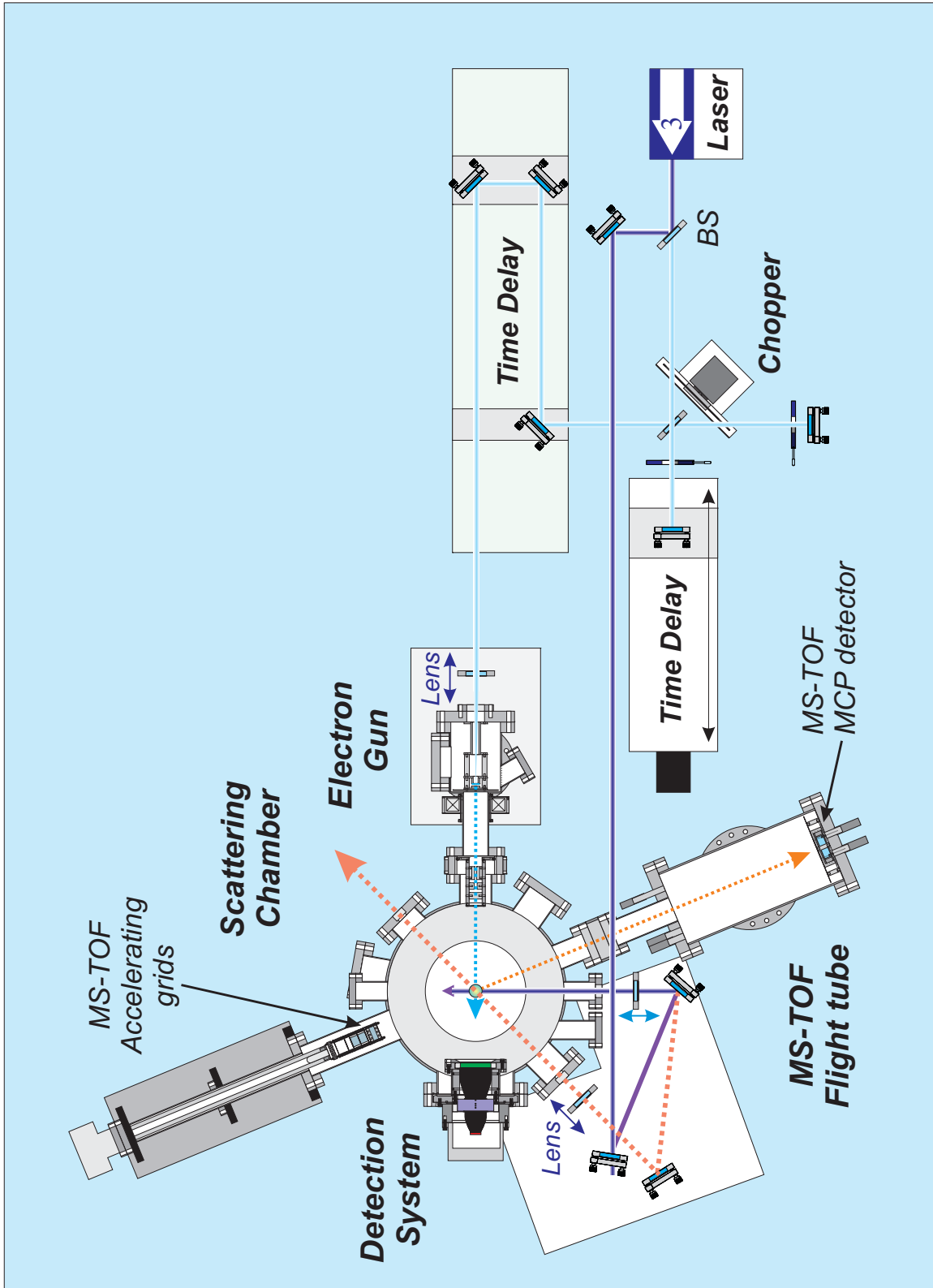


Figure 3-1. Third-generation UED-3 apparatus schematic, with the time-of-flight mass spectrometer (MS-TOF).

Femtosecond Laser Beam Path

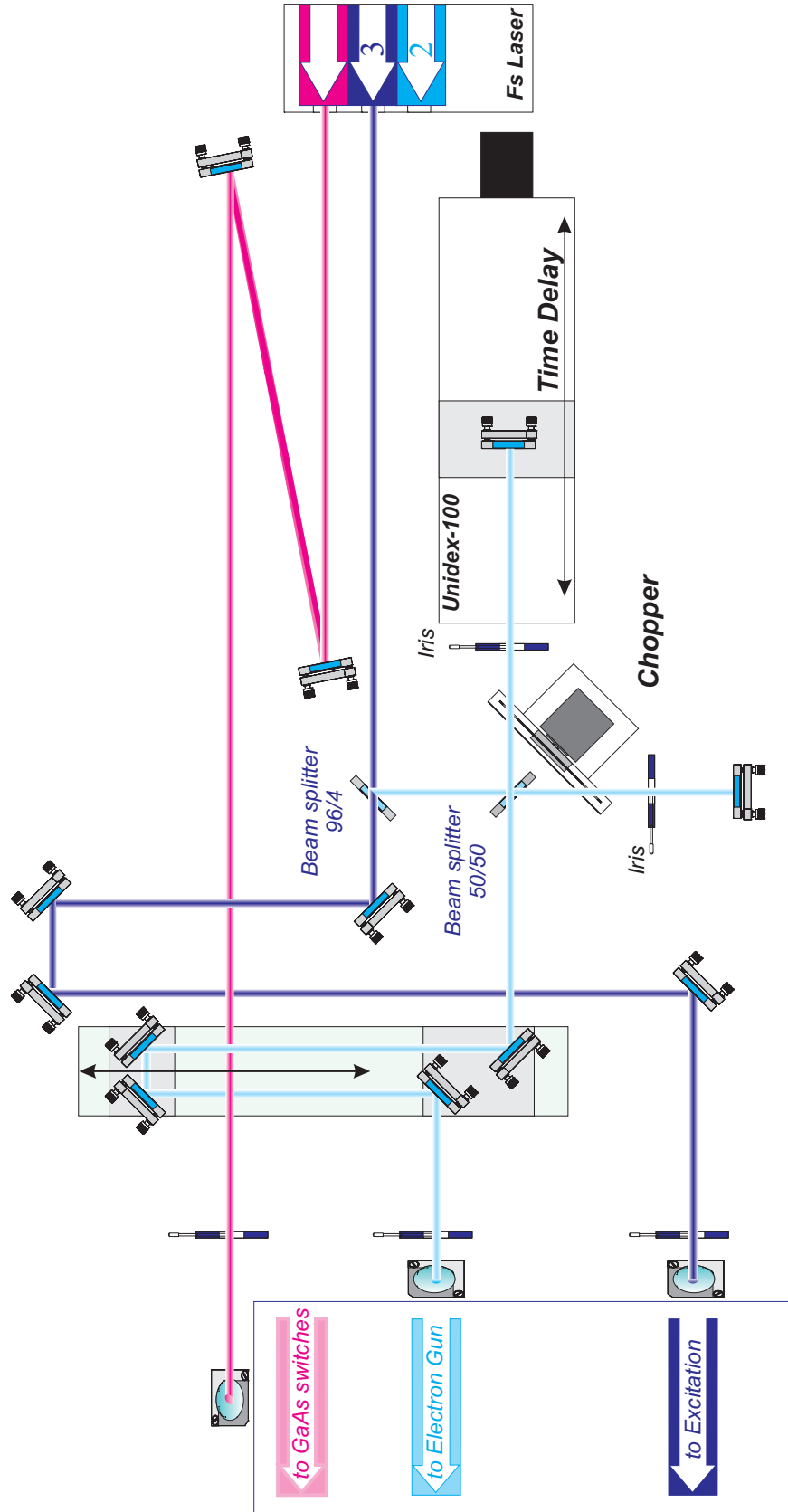


Figure 3-2. Layout of the beam path for the femtosecond laser pulses.

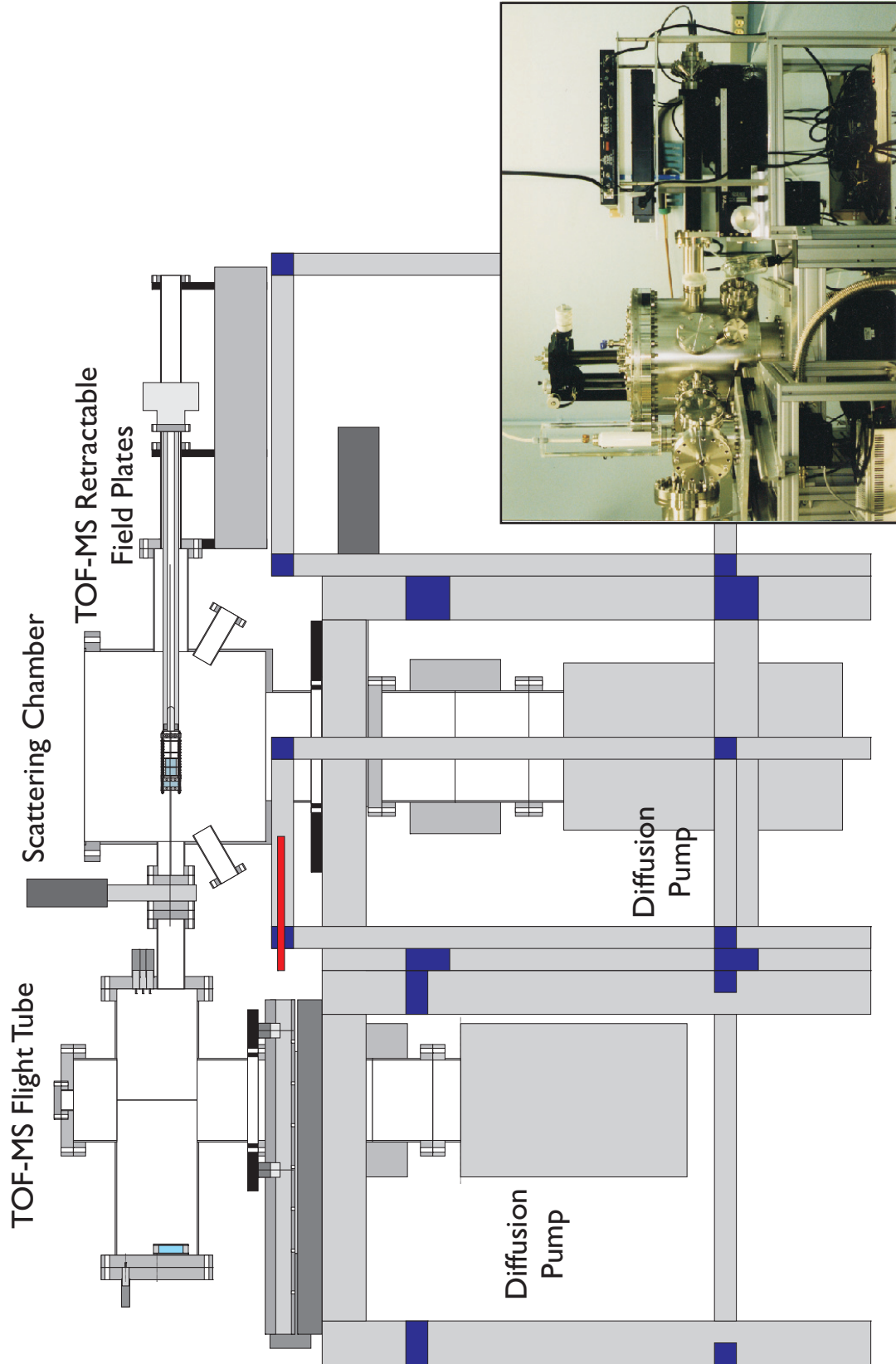


Figure 3-3a. Schematic front view of the UED-3 apparatus. Inset shows the photograph of the actual machine.

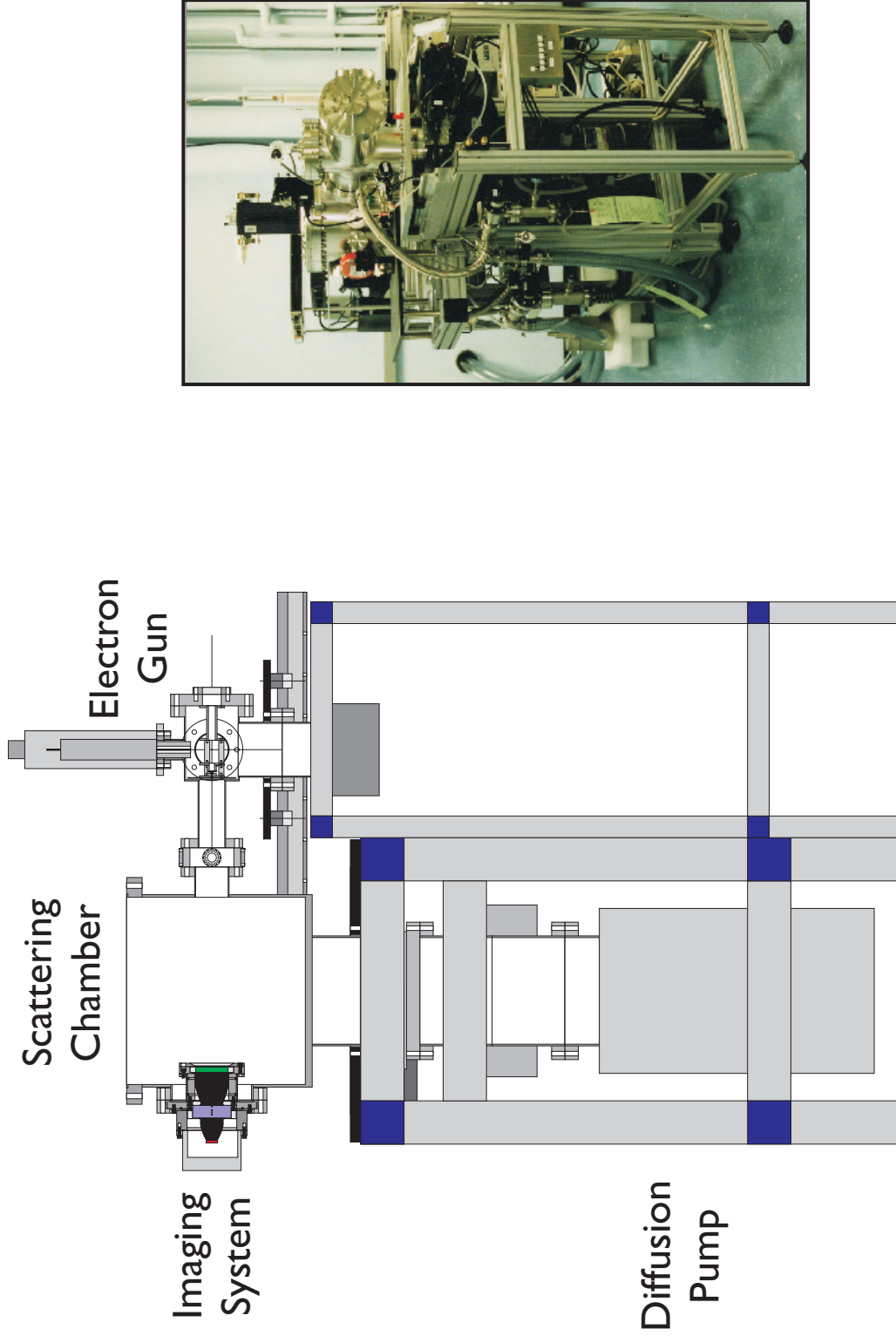


Figure 3-3b. Schematic side view of UED-3 apparatus. Also shown is the photograph of the diffraction machine.

Electron Gun Assembly

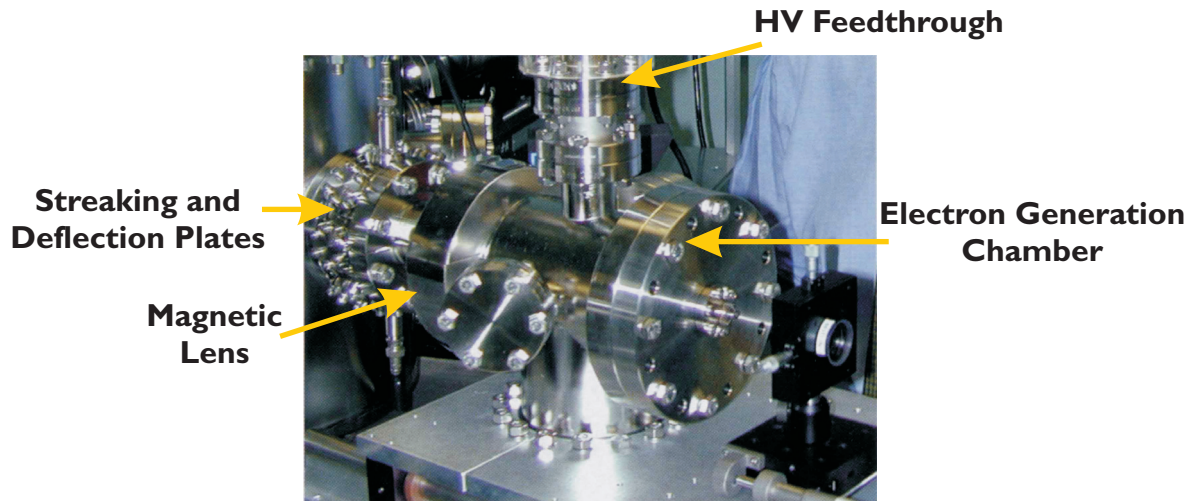
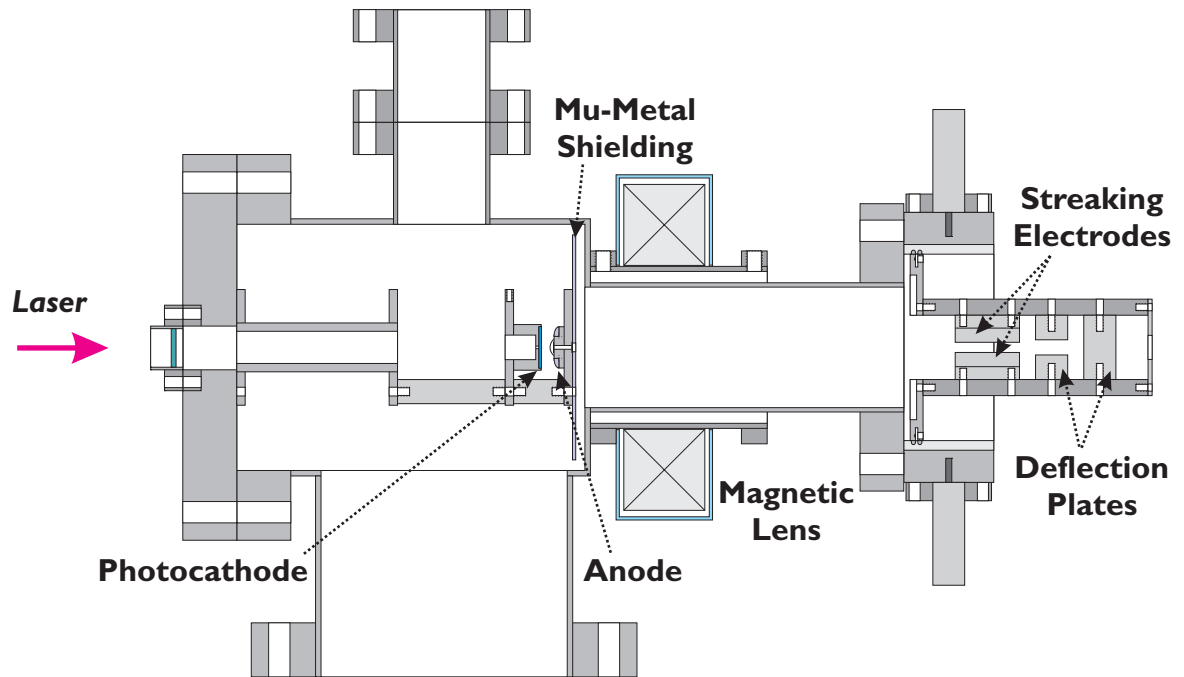


Figure 3-4. Schematic of UED-3 electron gun assembly. Also shown is a photograph of the electron generation chamber.

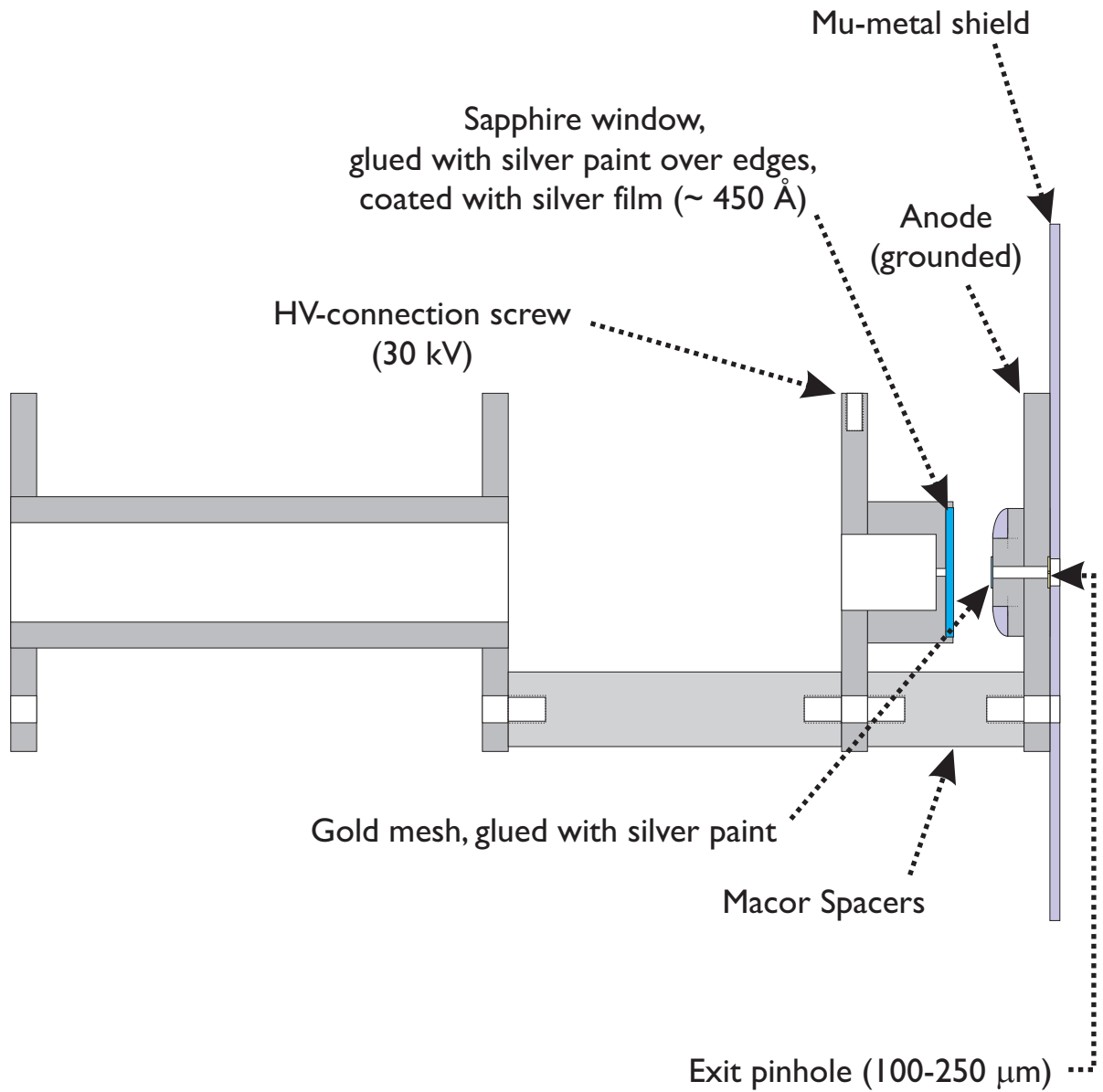


Figure 3-5. Detailed view of the electron generation and acceleration assembly.

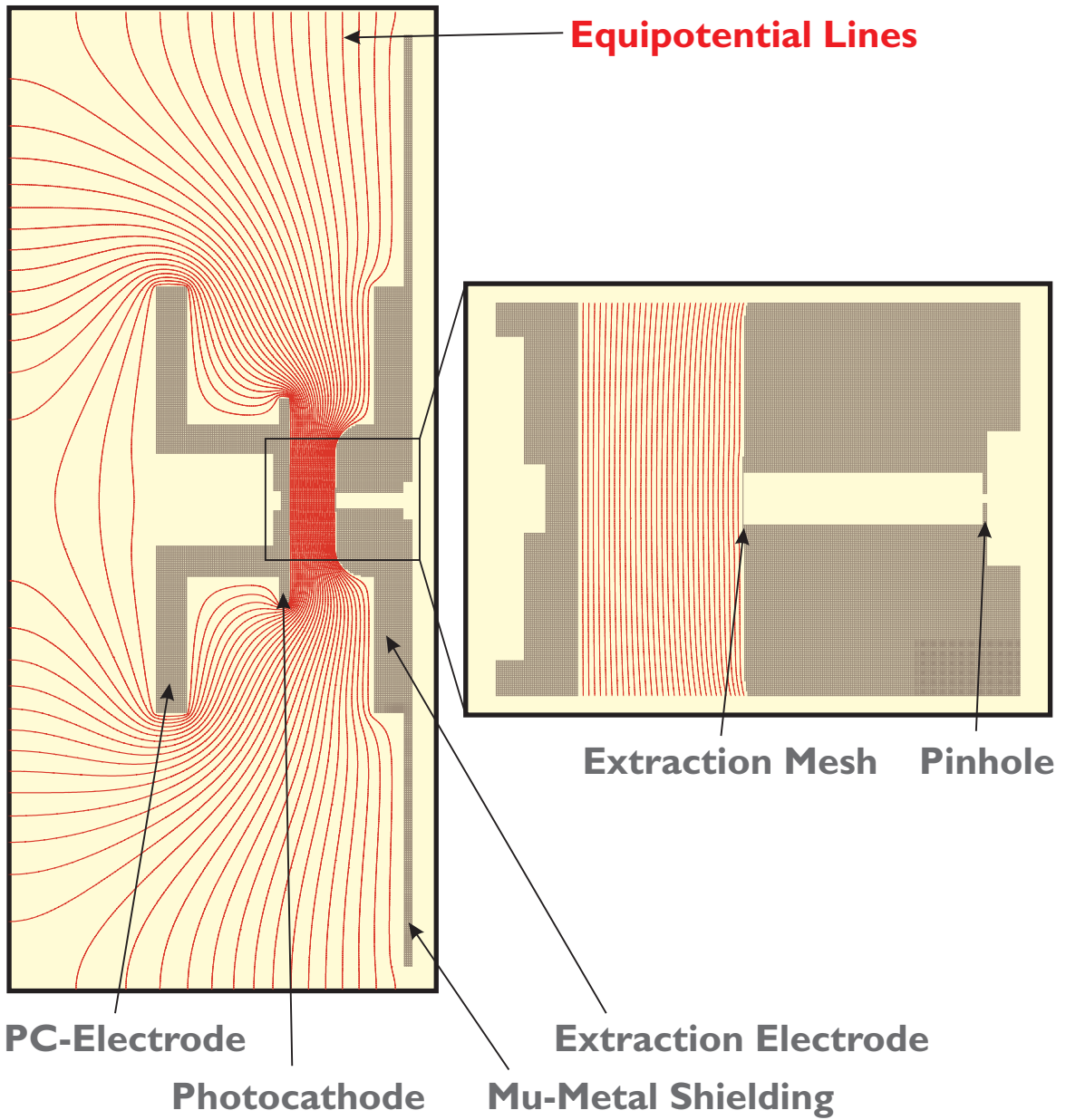


Figure 3-6. Equipotential lines in the extraction region of the UED-3 electron gun at 30 kV accelerating voltage.

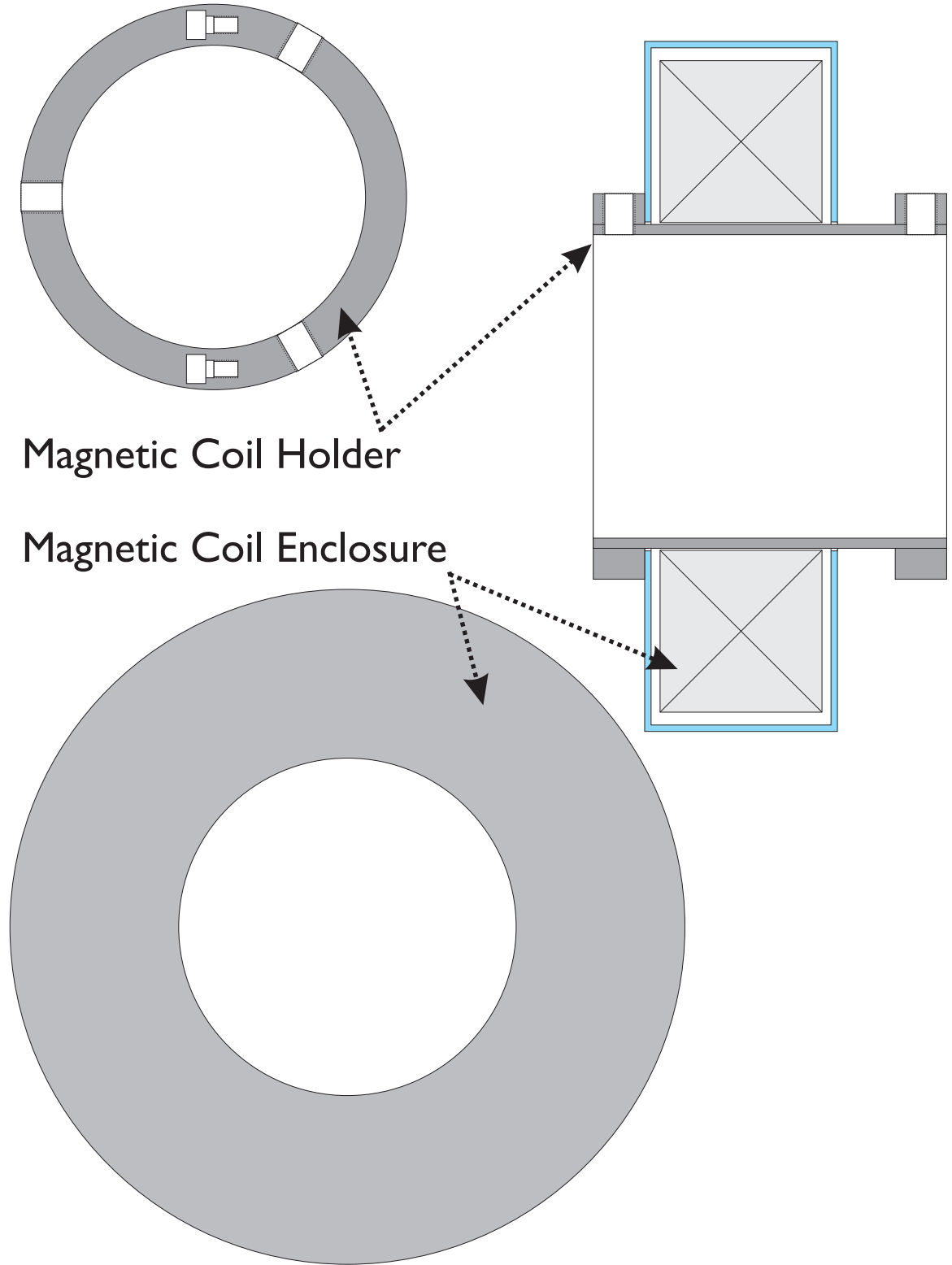


Figure 3-7. Detailed view of magnetic lens assembly.

Streaking and Deflection Assembly

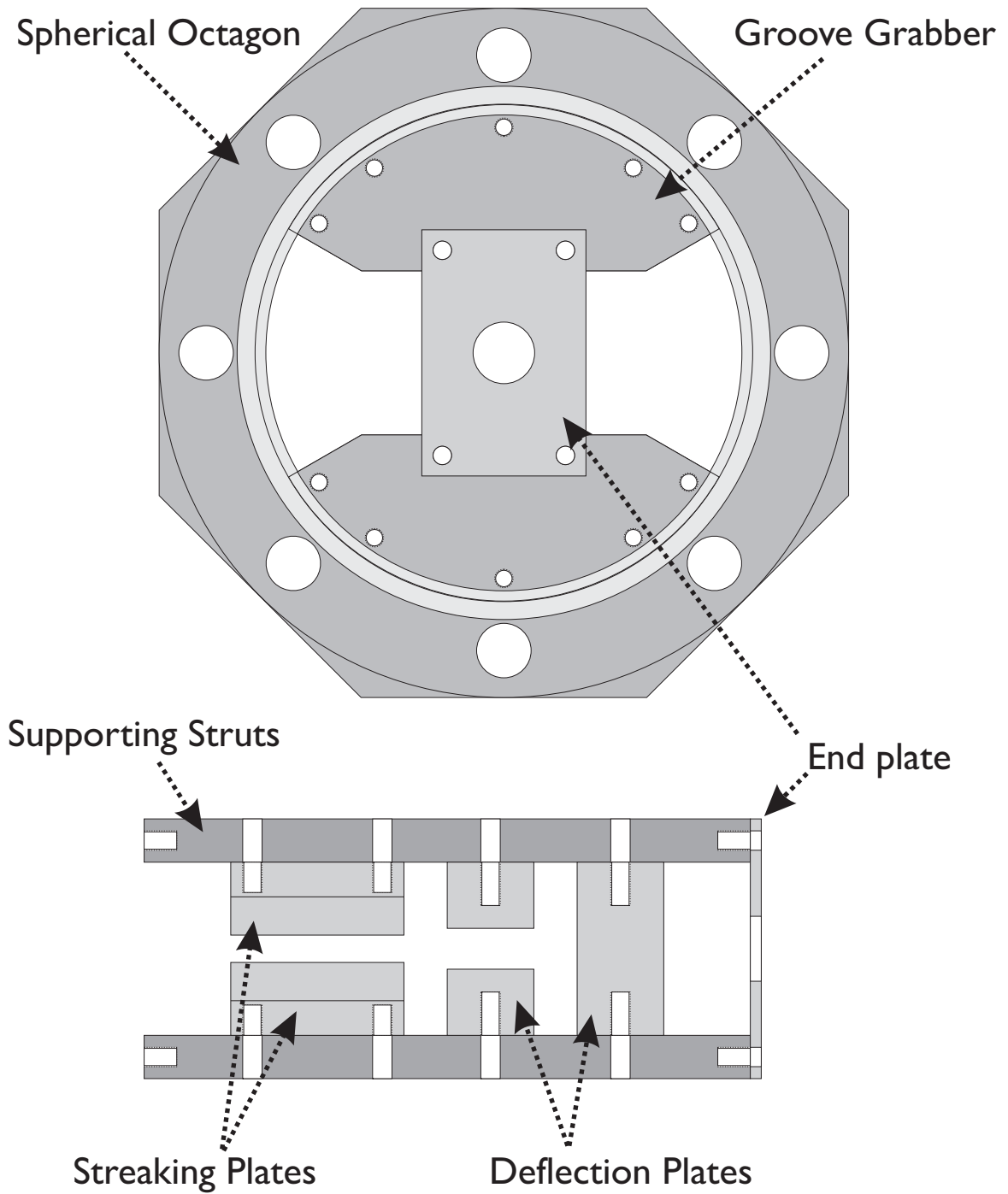


Figure 3-8. Detailed view of the electron streaking and deflection assembly.

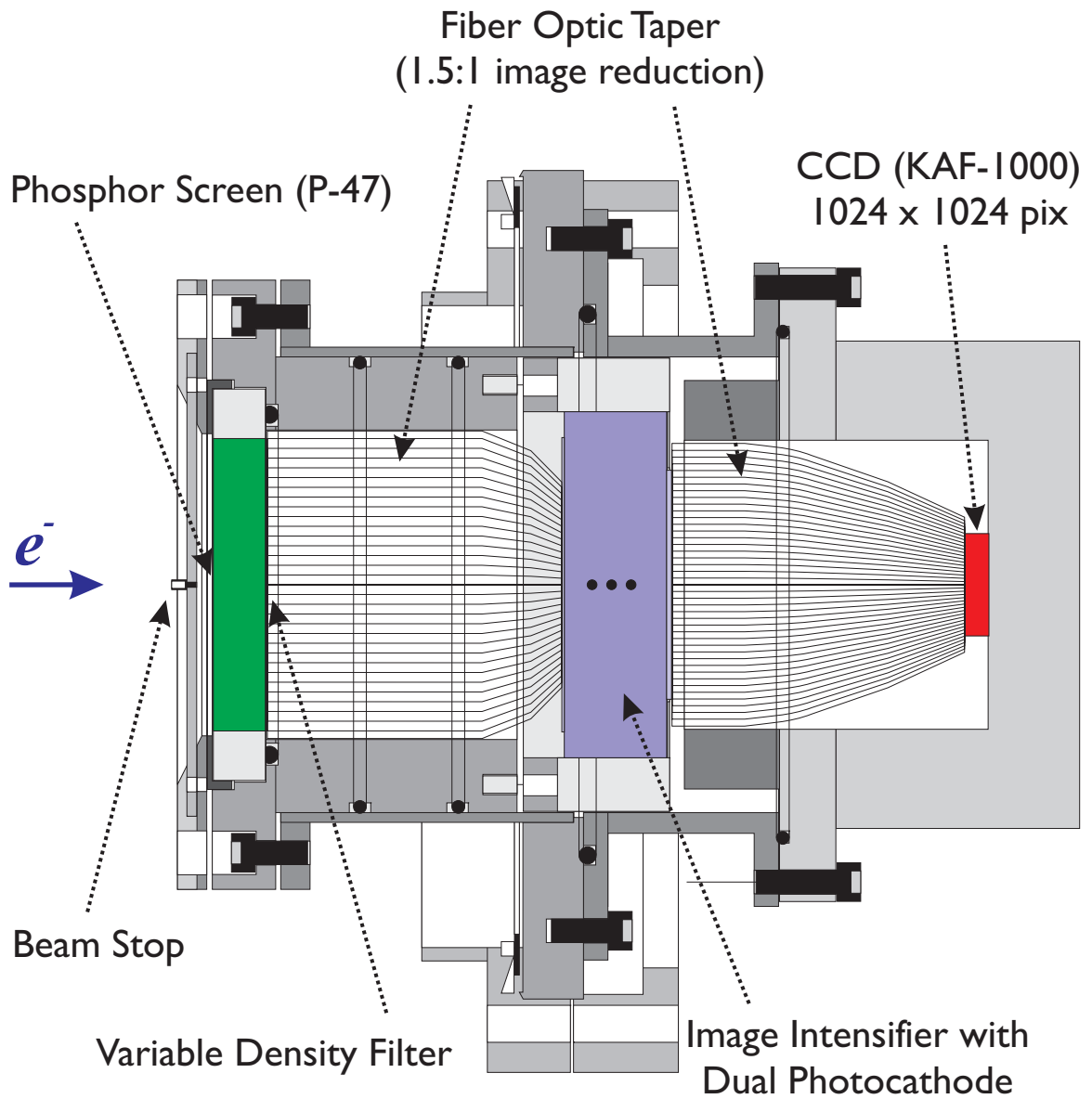
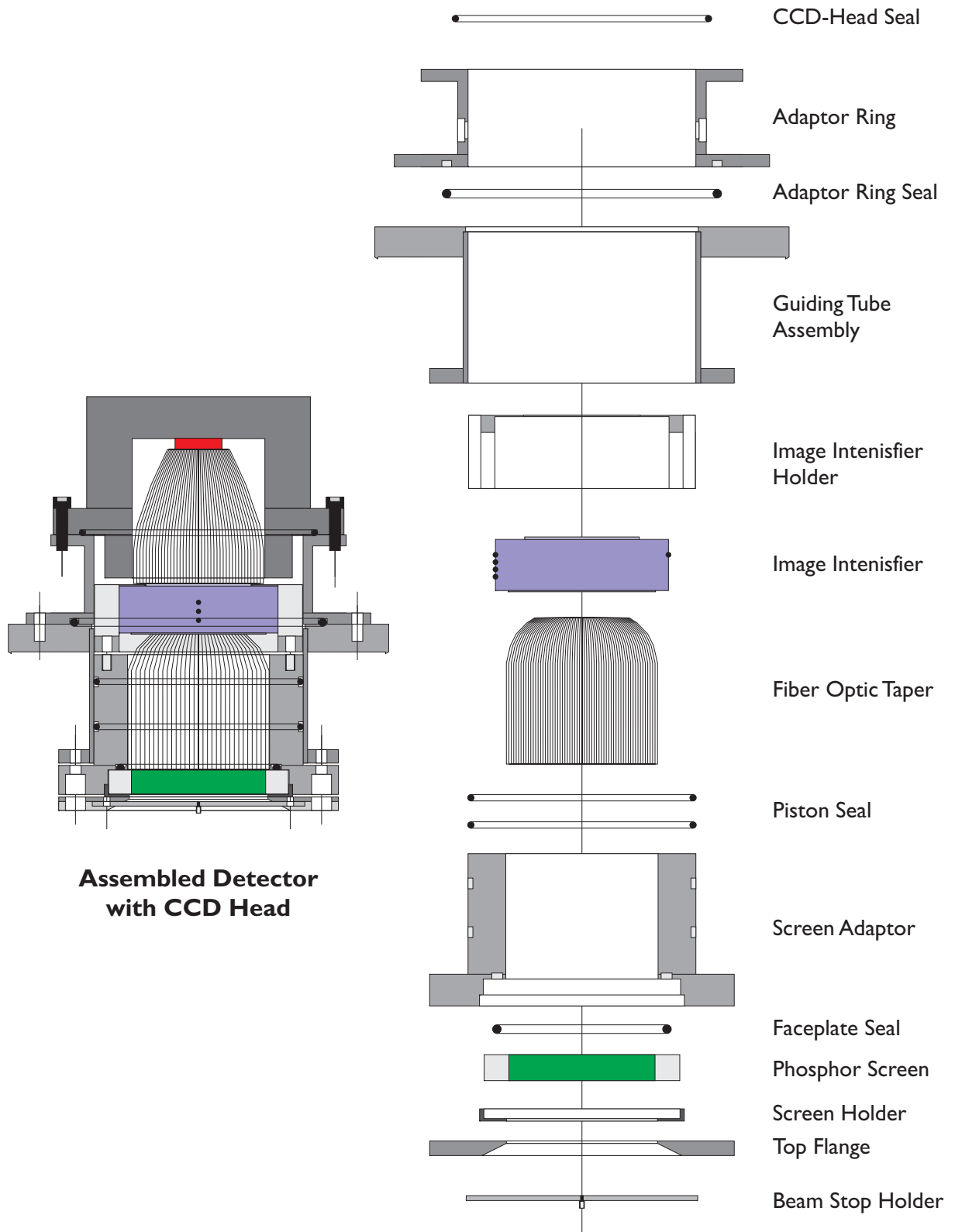


Figure 3-9. UED-3 Detector Assembly.



Assembled Detector with CCD Head

Figure 3-10. Individual components of the custom-made detector assembly.



Image Intensifier



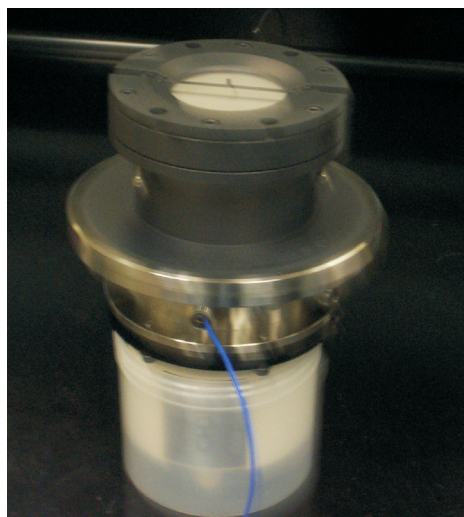
Fiber Optic Taper



CCD Head



Phosphor Screen



Fully Assembled Detector

Figure 3-11. Photographs of selected detector components.

Time-of-Flight Mass Spectrometry

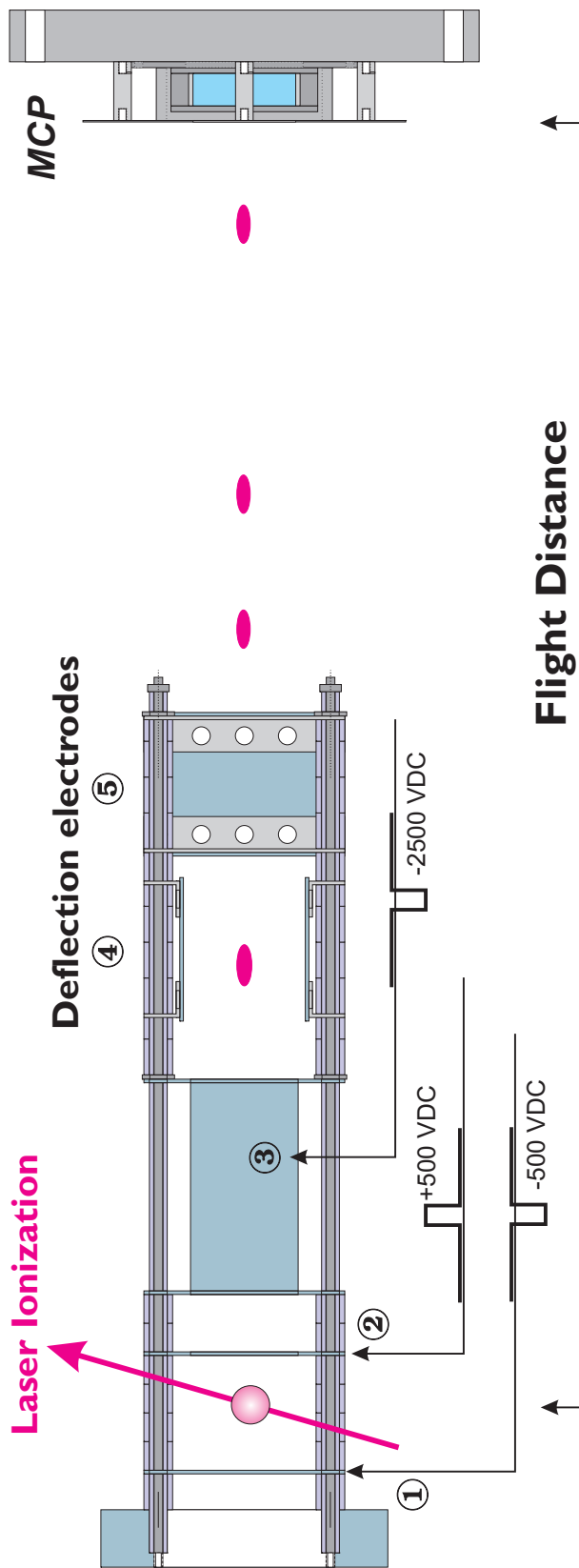


Figure 3-12. Schematic of time-of-flight mass spectrometry apparatus in UED-3. Also indicated are the applied electrical pulses; for details of the electrical arrangement and synchronization, see Figure 3-16.

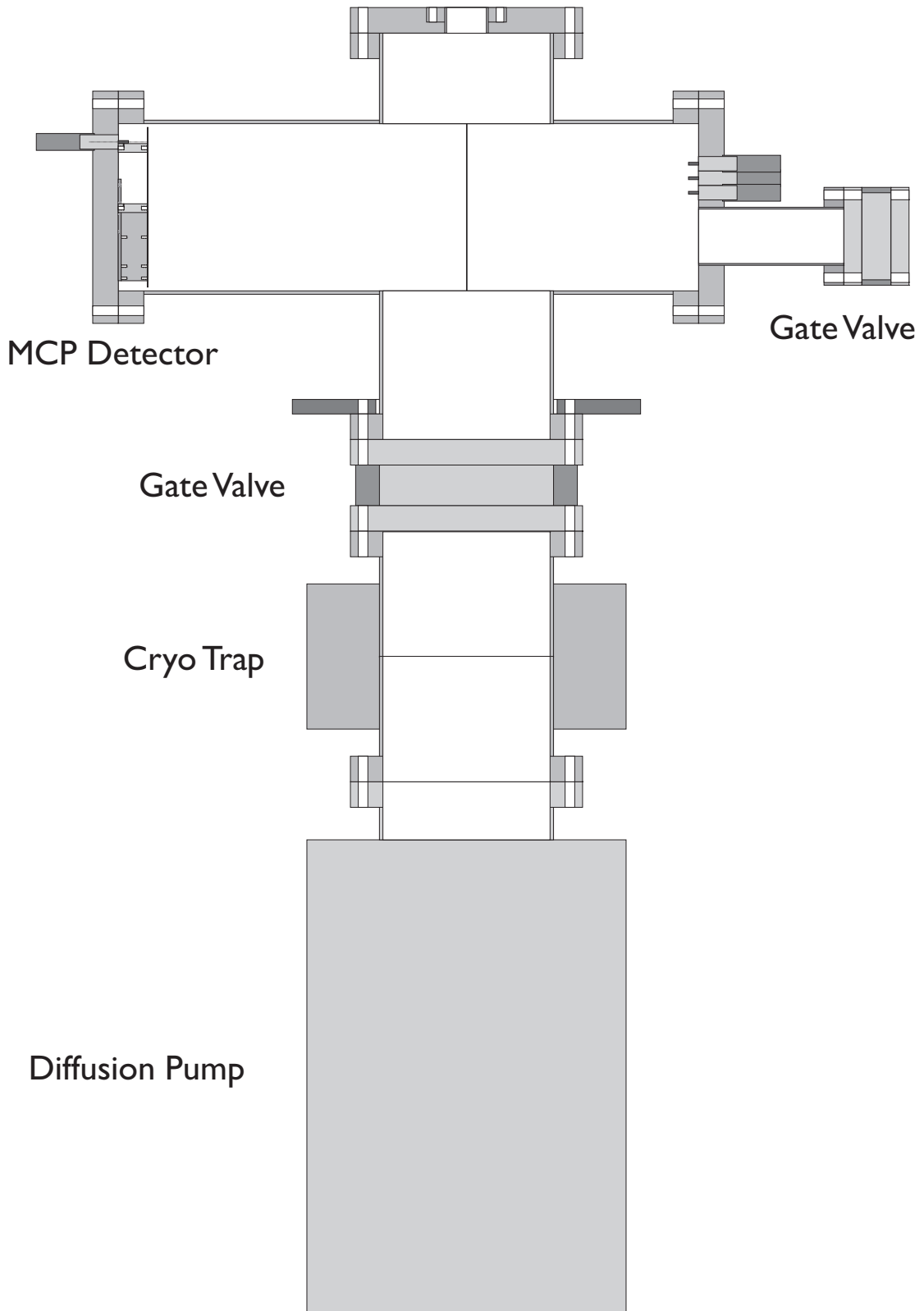
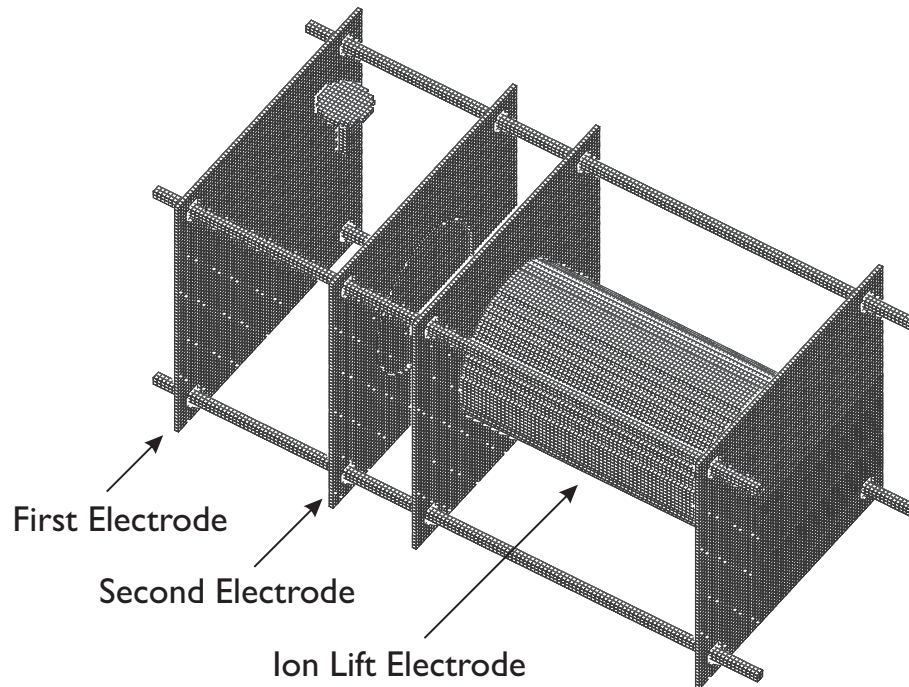


Figure 3-13. The linear TOF-MS chamber.

TOF Acceleration Assembly



MCP Detector Assembly

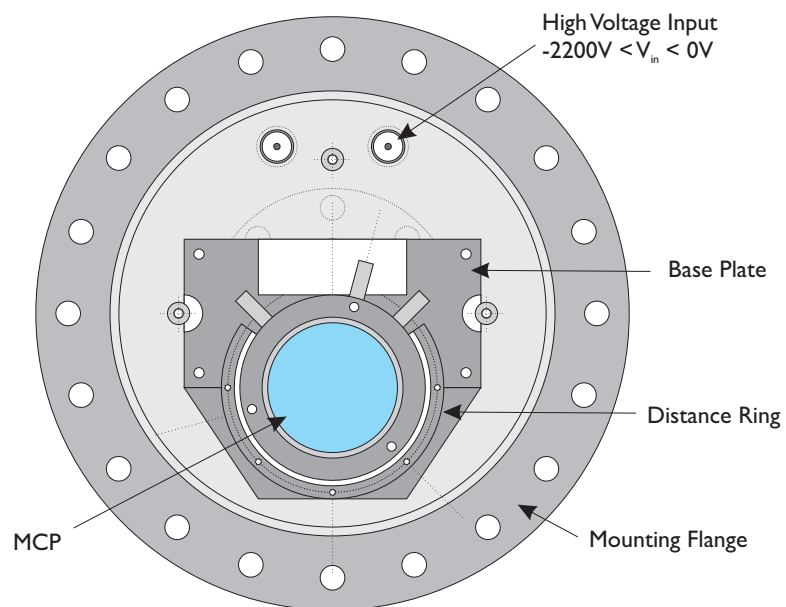


Figure 3-14. Acceleration assembly (top) and detector assembly (bottom) for time-of-flight apparatus.

UED-3 TOF-MS

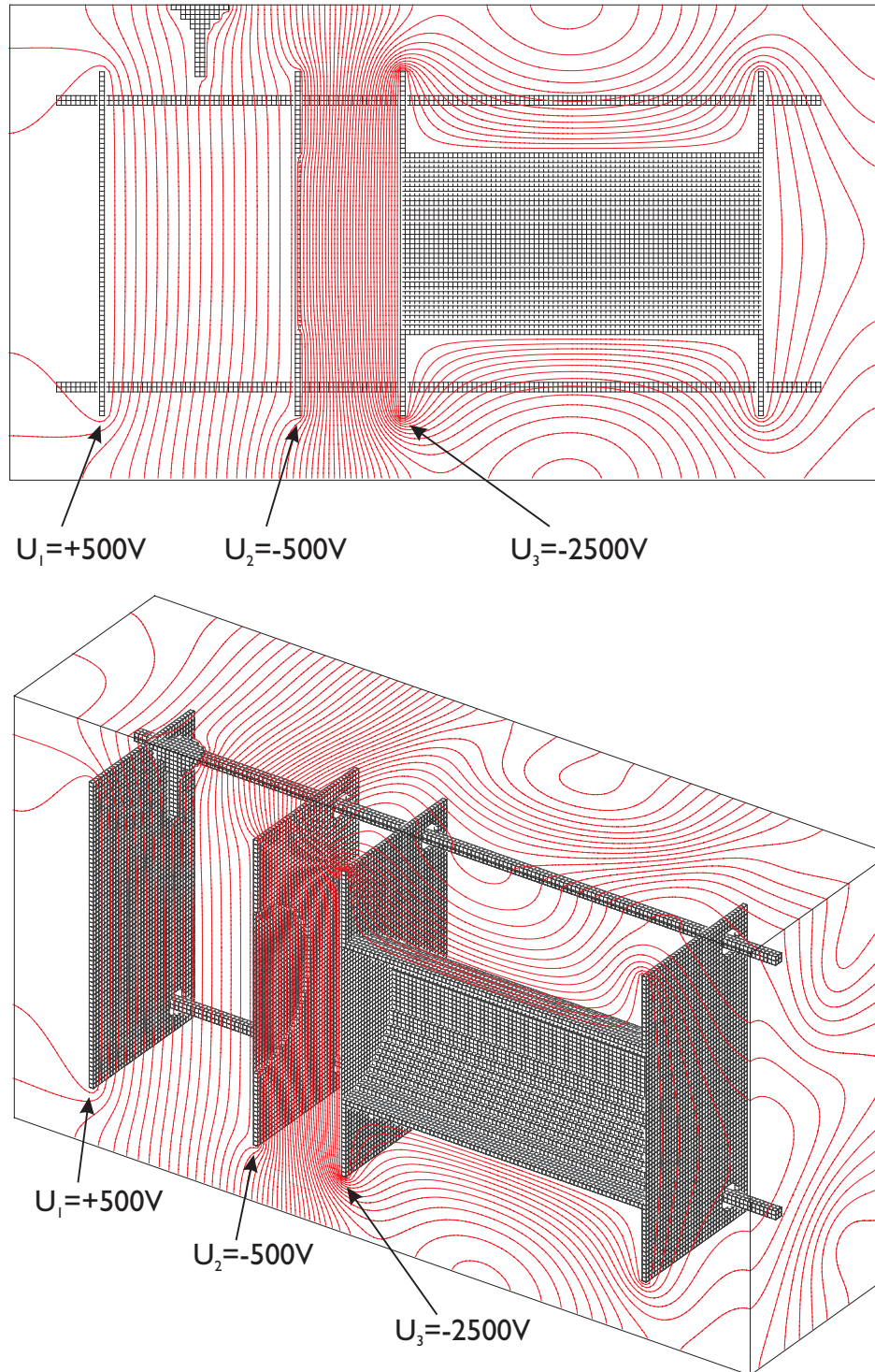


Figure 3-15. UED-3 geometry of time-of-flight mass spectrometry. Shown are equipotential lines along the center plane. Note the applied uniform acceleration fields and the nearly parallel equipotential surfaces.

MS-TOF Acceleration Assembly

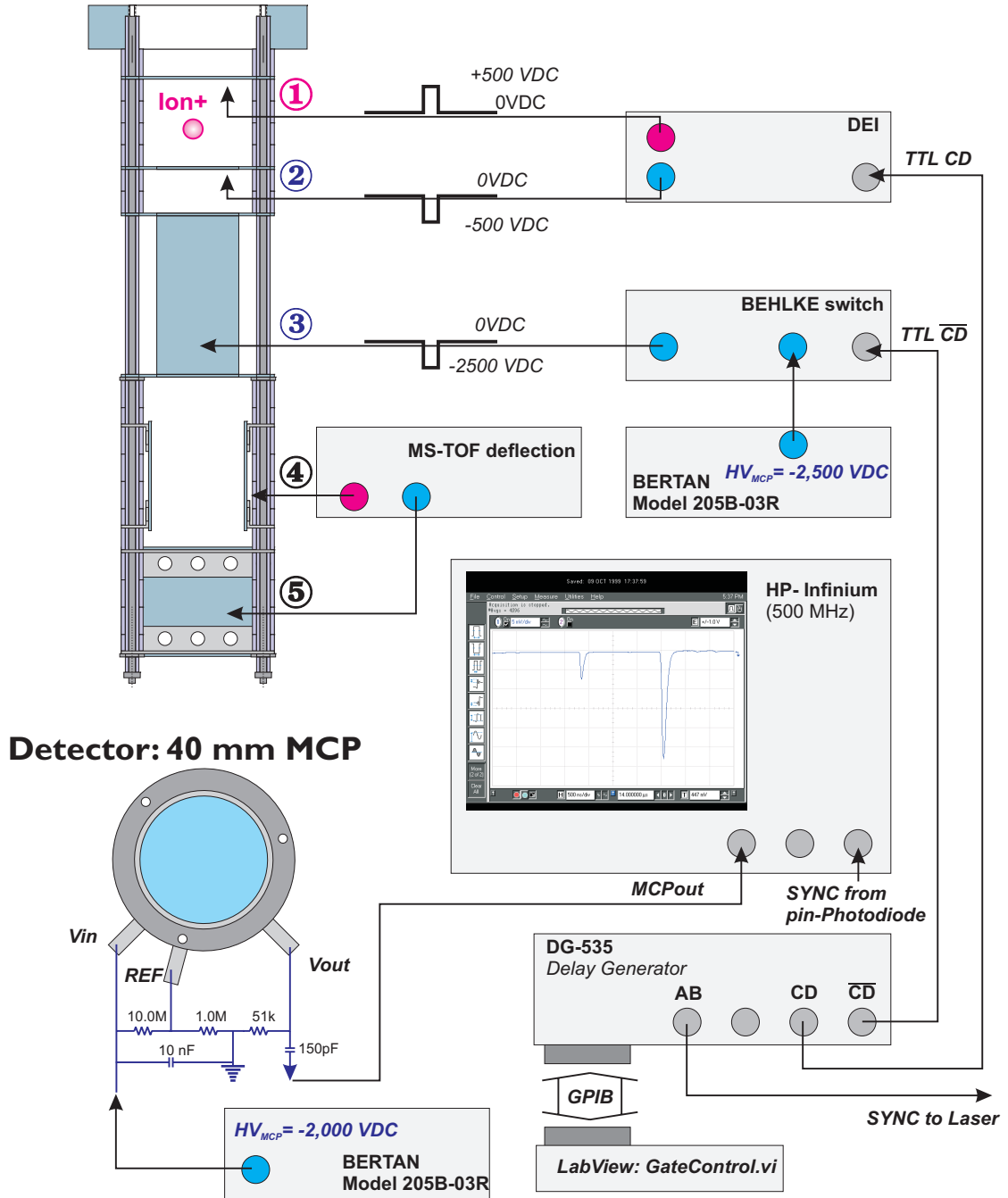


Figure 3-16. Arrangement and synchronization of electrical pulses in UED-3 time-of-flight mass spectrometry.

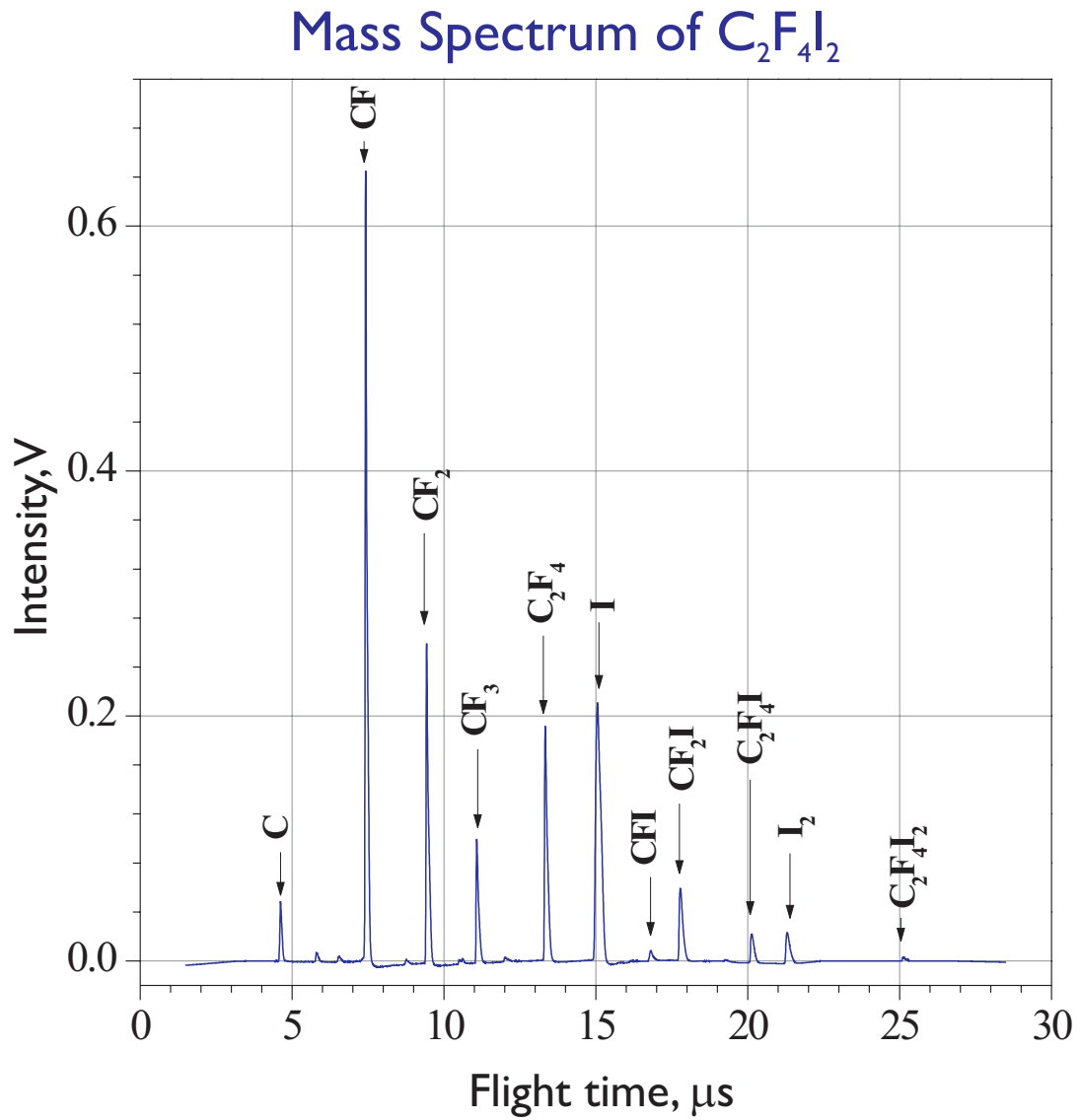


Figure 3-17. Typical mass spectrum obtained in the UED-3 time-of-flight mass spectrometry apparatus.

4

UED METHODOLOGY*

4.1 Introduction

The total temporal resolution of UED, Δt_{total} , depends on the durations of the pump pulse ($\Delta t_{\text{p-laser}}$) and electron pulses ($\Delta t_{\text{electron}}$) and on temporal broadening caused by velocity mismatch between photons and electrons (Δt_{VM}):

$$\Delta t_{\text{total}}^2 = \Delta t_{\text{p-laser}}^2 + \Delta t_{\text{electron}}^2 + \Delta t_{\text{VM}}^2 \quad (4-1)$$

* Parts of this chapter have been adapted from Srinivasan, R.; Lobastov, V.A.; Ruan, C.-Y.; Zewail, A.H., *Helv. Chim. Acta*, **2003**, 86, 1762.

Eqn. 4–1 is based on the assumption that the laser and electron beams have Gaussian spatial and temporal profiles and that the density profile of the molecular beam cross-section is Gaussian. The fwhm of the pump laser pulse ($\Delta t_{\text{p-laser}}$) is 120 fs, which is smaller than the contributions from the other two terms. Consequently, the laser pulse contribution to the total experimental temporal resolution is relatively small, and this section will focus primarily on the duration of the electron pulse and the impact of velocity mismatch.

4.2 Streaking: Electron Pulse Characterization

Several different factors contribute to temporal broadening in the formation of short electron pulses, and these factors have been extensively examined in the streak camera literature. The total streak camera resolution, Δt_{R} , is often defined as a function of three different pulse-broadening sources:¹

$$\Delta t_{\text{R}}^2 = \Delta t_{\text{e-laser}}^2 + \Delta t_{\text{D}}^2 + \Delta t_{\text{S}}^2 \quad (4-2)$$

where $\Delta t_{\text{e-laser}}$ is the temporal duration of the laser pulse, which creates the photoelectrons, Δt_{D} is the broadening of the electron pulse from its generation until it strikes the detector, and Δt_{S} is related to the detector geometry and spatial resolution. Eqn. 4–2 is based on the assumption that the electron

pulses have a Gaussian temporal distribution. The first term of Eqn. 4–2 corresponds to the temporal fwhm of the laser pulse, in this case 120 fs. The second term in Eqn. 4–2, Δt_D , represents broadening of the electron pulse as it travels from the photocathode to the detector. The broadening of the electron pulse can be classified into three regimes: initial broadening at the photocathode caused by the angular and energetic spread of the ejected photo-electrons; subsequent broadening of the pulse in the region of high electron density between the photocathode and anode due to space–charge effects; and broadening over the rest of the travel distance mainly due to non-uniform electron velocity distribution. For our current time resolution of 1 ps, the initial temporal broadening and the space–charge effects dominate the pulse broadening.

The initial temporal broadening of the photoelectrons is given by:¹

$$\Delta t_{D(\text{initial})} = \frac{\sqrt{2m_e \Delta \mathcal{E}}}{eE_{\text{PC}}} \quad (4-3)$$

where $\Delta \mathcal{E}$ is the fwhm of the ejected photoelectron energy distribution, e is the electron charge, m_e is the electron mass, and E_{PC} is the electric field near the photocathode. Both E_{PC} and $\Delta \mathcal{E}$ may be controlled experimentally. The energy distribution, $\Delta \mathcal{E}$, which is related to the amount of excess energy in the

photoemission process, can be minimized by proper selection of the photocathode material (hence its work function) and the incident laser wavelength. We have chosen to work with thin (*ca.* 450 Å) silver photocathodes, which have proved durable under our operating conditions and are easy to prepare. With a work function of 3.65 eV reported for a 450-Å Ag film, barring thermal effects and surface contamination, the photoelectron energy distribution is expected to be narrow (*ca.* 0.6 eV for a one-photon and *ca.* 2.5 eV for a two-photon emission process); note that the energy distribution of the laser pulse is only ~ 0.1 eV. Eqn. 4–3 shows that the initial temporal broadening also depends on the electric field E_{PC} between the photocathode and the extraction mesh. Our present electron gun design sets $E_{PC} = 6$ kV/mm, which is similar to that used in state-of-the-art streak cameras. Under these conditions, we estimate $\Delta t_{D(\text{initial})}$ to be *ca.* 350 to 900 fs.

Once the electrons are extracted, the pulse undergoes collimation and deflection until it strikes the detector. From the instant the electrons are generated, electron–electron Coulombic repulsion causes pulse broadening, and the effects of this repulsion on the spatial and temporal characteristics of an electron pulse have been collectively called the space–charge effect. The influence of space–charge effects on temporal broadening can be understood by considering electrons at the front and back of an electron pulse. The front electrons are accelerated forward by repulsion from the electrons behind

them, while the trailing electrons are decelerated by the charges in front. The net result is that the entire pulse broadens in all directions over time. Due to the inverse-square dependence of Coulombic repulsion on distance, space-charge effects are very sensitive to the electron density of the pulse and are greatly reduced when the electron density is low. One method for reducing the broadening is to accelerate the electrons to a high velocity within a very short distance; not only does this spread the electron pulse out over a greater distance, but it also reduces the time during which the electron pulse may broaden before intersecting the molecular beam or striking the detector. To reach sub-picosecond performance, the electron density must be reduced by limiting the number of electrons per pulse, which means that successful electron diffraction experiments require a high quantum efficiency detector such as a specially designed CCD camera.

The third term in Eqn. 4-2, Δt_s , contains broadening effects due to the detector. This *does not* reflect the temporal response of the detector itself, but rather how the spatial resolution and the position of the detector (with respect to the electron gun) influence streak measurements. When recording electron diffraction patterns, the electrons are not streaked, and, therefore, Δt_s does not apply to the UED experimental time resolution. We must, however, consider Δt_s when conducting streak experiments to measure the electron pulse length.

In the measurement of electron-pulse durations with streaking techniques, a time-dependent electric field is ramped across the first deflector pair such that an electron pulse traveling between the plates experiences a dispersive effect (Fig. 4–1). Very fast rates of voltage change ($\partial V/\partial t$) are required to disperse single picosecond pulses. To synchronize the arrival of the electron pulse with the maximum voltage gradient ($\partial V/\partial t$) at the streaking plates, an optical delay line was constructed to control the firing time of the photoconductive switch. Of the two optical arms, one is directed toward the switch and the other toward the photocathode on the electron gun. The arm leading to the electron gun incorporates a Michelson interferometer to generate laser pulse pairs with a well-defined pulse separation Δt_{sp} ; Δt_{sp} is adjusted with a second optical delay. This laser pulse pair generates a pair of electron pulses with the same time separation Δt_{sp} at the photocathode.

After streaking, the two electron pulses are separated by a distance D_{pix} (in pixels) on the CCD detector. The streak velocity, in pixels per ps, is calculated from Δt_{sp} and D_{pix} . Single-shot streak image pairs are typically taken for a wide range of laser intensities in order to observe the effect of current density on the electron pulse length. By measuring the center position of each electron pulse on the CCD, the streak speed is readily calculated in units of pixels per picosecond. The pulse width of each electron

pulse is then calculated by dividing the spatial fwhm of the pulse (pix) by the streak speed (pix/s).

The unstreaked electron beam profile is shown in Fig. 4–2, while a typical set of low-intensity electron pulse pairs obtained in UED-3 is shown in Fig. 4–3. After analyzing such pulse pairs, we obtain a curve that describes the temporal behavior of the electron gun as a function of the number of generated electrons (Fig. 4–4). It is clear from this curve that there is little or no broadening by space–charge effects at low numbers of electrons. Moreover, Fig. 4–5 also highlights the dramatic improvement in the electron gun performance in UED-3 as compared to UED-2—a 5-ps pulse in UED-2 contained only 3000 electrons, while in UED-3, an electron pulse of the same width contains nearly 100,000 electrons. The remarkable stability of the electron gun from pulse-to-pulse is depicted in Fig. 4–6, with measurements made on both sides of the detector.

4.3 Clocking: Zero of Time

In a UED experiment, the time coordinate for a reaction can only be established if there is a point of reference for the relative time delay between the initiation pulse and the electron pulse. This reference point is called time-zero (t_0), the time when both pulses simultaneously intersect in the sample. Careful measurement of laser and electron beam paths can narrow the time-

zero window to within 100 ps. Another approach is to rely on the changes in the diffraction pattern of the system under investigation, but this is not an independent means of finding t_0 . More importantly, this method is simply not practical for gas-phase work because of the long integration times required to obtain a single data point.

In the clocking technique developed for UED,¹ we use the crossed-beam geometry of the actual diffraction experiment to determine time-zero via the 'lensing effect'. During CF_3I dissociation reaction studies, a dramatic change had been observed in the undiffracted electron beam profile when the excitation laser was present. The beam spot intensified along one axis, with a corresponding subtle decrease in the overall width (see Fig. 4–7). This effect only occurred when both the excitation laser and the molecular beam were present. The intensified strip was parallel to the laser axis and could be shifted up and down within the beam spot by adjusting the vertical tilt of the excitation laser entrance lens. Defocusing the laser reduced the stripe intensity. This phenomenon was termed photoionization-induced lensing. The effect is analogous to plasma lensing, a technique in which the high-energy charged beams in particle accelerators are focused by passing through a plasma field.

In our experiment, the pump laser photoionizes a fraction of the molecular beam sample, producing a mixture of positive ions and ejected electrons. The ejected electrons have an excess kinetic energy KE of

$$\text{KE} = nh\nu - \Phi_{\text{IP}} \quad (4-4)$$

where n is the number of photons involved in the excitation, ν is the photon frequency, and Φ_{IP} is the ionization potential of the molecules. These ejected electrons begin to diffuse with their excess kinetic energy, resulting in net charge redistribution within the plasma. The ions remain more or less stationary on the picosecond time scale, so the net effect is the formation of a cylindrically symmetric charge gradient and a radial electric field about the initiation laser axis that focuses the charged electron beam. With less than 1% ionization, the radial electric field in the interaction region may be as high as 10 kV/m, which is sufficient to perturb the path of the incoming high-energy electron beam, and the effects are seen directly in the beam spot profile.

We exploited this phenomenon to obtain the time-zero for UED experiments. Time-resolved studies of photoionization-induced lensing were conducted on CF_3I gas, which has an ionization energy of 10.23 eV. For a three-photon process with 4.66-eV photons, the excess kinetic energy of the

ejected electrons is *ca.* 3.7 eV, which corresponds to the electrons traveling *ca.* 1 μm in 1 ps. Fig. 4–8 shows the degree of lensing *vs.* time; the lensing is a maximum when the focused laser and electron pulses are temporally overlapped. The time at which the ellipticity of the electron beam begins to deviate from that of a symmetric profile is defined to be the reaction zero-of-time. The results elucidate t_0 precisely and, hence, allow a direct clocking of changes in the diffraction experiment with picosecond or shorter resolution.

4.4 Temporal and Spatial Overlap: Velocity Mismatch

The velocity of 30-keV electrons is approximately one-third the speed of light. This velocity mismatch causes different molecules across the laser-electron intersection region to experience different time delays between the two pulses. For example, if the laser pulse and the electron pulse copropagate, and if both reach the near edge of the molecular beam at the same instant, then the electron beam (on account of its lower velocity) will encounter molecules at the farther edge of the sample at much later times after the light pulse has passed through. Since the time required for the electrons to cross the molecular beam sample is on the order of picoseconds, the temporal broadening due to velocity mismatch is a significant contributor to the total experimental resolution. In principle, temporal broadening due to velocity mismatch might be large enough that the total experimental

resolution does not improve when shorter electron pulses or shorter laser pulses are introduced. To estimate the importance of velocity mismatch, we used a geometrical model¹ to represent the temporal broadening with an analytical function in terms of experimental parameters (Fig. 4–9).

Our theoretical model of velocity mismatch encompasses several factors: (1) the ratio of the photon velocity to the electron velocity, κ ; (2) the spatial fwhm of the laser pulse, w_L ; (3) the spatial fwhm of the electron pulse, w_e ; (4) the cross-sectional fwhm of the molecular beam, w_M ; (5) the angle of intersection θ between the laser pulse and the electron pulse. When the two beams copropagate, the fwhm of the temporal broadening is given by:

$$\Delta t_{\text{VM}}(\theta=0) = \frac{w_M(\kappa-1)}{c} \quad (4-5)$$

As expected, if the laser and electron pulses have identical velocities ($\kappa = 1$), and are co-propagating ($\theta = 0$), then there is no velocity mismatch. Note that thin molecular samples reduce Δt_{VM} , and there is negligible broadening when the electron velocity approaches the speed of light ($\kappa \rightarrow 1$).

If the spatial width of the laser pulse is sufficiently small relative to w_M :

$$w_L \leq w_M \sqrt{\kappa - 1} \quad (4-6)$$

then the minimum temporal broadening actually occurs at a nonzero angle, θ_{\min} , where

$$\theta_{\min} = \arccos\left(\frac{w_L^2 + w_M^2}{\kappa w_M^2}\right) \quad (4-7)$$

The temporal broadening at this angle is:

$$\Delta t_{\text{VM}}(\theta_{\min}) = \frac{w_L}{c} \sqrt{\frac{(\kappa^2 - 1) - \frac{w_L^2}{w_M^2}}{1 + \frac{w_L^2}{w_M^2}}} \approx \frac{w_L}{c} \sqrt{\kappa^2 - 1} \quad (4-8)$$

which is independent of the spatial width of the electron pulse.

For our UED apparatus, $\kappa \approx 3$ and typical beam fwhm values are $w_e = 350 \mu\text{m}$ and $w_L = w_M = 250 \mu\text{m}$. Fig. 4-10 displays the dependence of Δt_{VM} on the laser–electron beam intersection angle, and it can be seen that temporal broadening is minimized when the electron and laser beams are nearly perpendicular. In this manner, the overall temporal resolution of the experiment (which includes contributions from the electron pulse width, the laser pulse width, and the group velocity mismatch) is calculated as a

function of the electron beam parameters (Fig. 4–11). For an electron beam condition of 300- μm diameter, the overall temporal resolution increases to only 4 ps for a pulse of 3.5 ps. As is readily seen from Eqn. 4–8, velocity mismatch can be further reduced by decreasing the ratio of the beam velocities, κ , which in turn implies higher accelerating voltages to increase the velocity of electrons. A decrease in the laser beam and molecular beam widths and reducing the laser-electron intersection angle from the present 90° to θ_{\min} (60°) (Fig. 4–10) will also serve to reduce velocity mismatch.

4.5 Calibration of CCD Camera

Figures 4–12 and 4–13 show the calibration of the pixel size on the CCD camera based on measurement of the intensity distribution and the estimation of the edge spread function. The USAF-1951 resolution target is used for this purpose. The calibration of the Modulation Transfer Function of the intensified CCD system is shown in Fig. 4–14 while Fig. 4–15 displays the single-electron-event statistics on the detector.

4.6 CCD Image Processing

The digital nature of our data acquisition permits the use of a variety of powerful image processing techniques that aid in the isolation of molecular diffraction signals. At each given time delay between pump (laser) and probe

(electron) pulses, a series of 2-D diffraction images (\mathbf{A}_i , $i = 1, 2, \dots, n$) are acquired with the CCD camera (here, bold characters denote 2-D images). The first step in the image processing is to generate an averaged 2-D image, from which unwanted random events have been removed; such events may be caused, for example, by spontaneous emission and cosmic rays. The averaged image, $\overline{\mathbf{A}}$, is created according to the iterative procedure described below (Fig. 4–16).

A key trait of our 2-D data is the accessibility of the individual pixels in the digitized images, which allows us to treat each pixel as an independent detector statistically characterized by its own mean intensity and standard deviation. For each \mathbf{A}_i , a corresponding binary “mask” image, \mathbf{M}_i , is created. For example, a given pixel with coordinates (x,y) in each \mathbf{M}_i has a value of *one* if the corresponding pixel in the diffraction image \mathbf{A}_i is valid (the conditions for validity are outlined below) or has a value of *zero* otherwise. We define $M_i(x,y)$ as that pixel in a given \mathbf{M}_i with coordinates (x,y) ; initially, $M_i(x,y) = 1$ for all pixels in all n mask images.

In the first step of each processing loop, an average value for the signal intensity at each pixel, $\overline{A}(x,y)$, is obtained over the n raw diffraction images:

$$\overline{A}(x,y) = \frac{\sum_i^n M_i(x,y) \cdot A_i(x,y)}{\sum_i^n M_i(x,y)} \quad (4-9)$$

where $A_i(x,y)$ is the signal intensity for the pixel with coordinates (x,y) in the i th diffraction image (A_i), and the sum $\sum_i^n M_i(x,y)$ gives the number of valid pixels over all A_i with coordinates (x,y) . During this step $\bar{A}(x,y)$ and $\sigma(x,y)$ (the standard deviation of the averaged scattering intensity) are calculated for each pixel in the average image \bar{A} . In order to remove the signal spikes from random events, each diffraction image A_i is then submitted to a pixel-by-pixel rejection criterion requiring that the value of given pixel $A_i(x,y)$ lies within four standard deviations of the average value for that pixel (i.e., that $\bar{A}(x,y) - 4\sigma(x,y) \leq A_i(x,y) \leq \bar{A}(x,y) + 4\sigma(x,y)$). If a given value for $A_i(x,y)$ does not meet this criterion, then this pixel is declared invalid, and the value of $M_i(x,y)$ in the corresponding mask image M_i is set to zero—thereby preventing this pixel from contributing to the averaged signal in the next processing loop. This cycle is typically repeated three times, with the $\bar{A}(x,y)$ values, $\sigma(x,y)$ values, and the M_i mask images updated after each cycle.

At the conclusion of the last cycle, the final 2-D binary mask (M') is generated. Pixels in M' corresponding to inactive regions of the CCD camera (and pixels manually removed due to systematic problems) are set to zero, thereby ensuring that these regions do not contribute to the final diffraction signal when the averaged \bar{A} image is multiplied by this final mask. This

process yields the final, processed averaged image, \overline{A}' , which is now used for all further analysis. All averaged images, including background images and the reference gas images, were generated by this procedure.

Next, an averaged background image (\overline{B}'), obtained under identical conditions as the molecular diffraction image (e.g., exposure time, laser light scattering, etc.)—except *without* the presence of the gas sample under study—is then subtracted from \overline{A}' . After this background subtraction, the 2-D diffraction image is then divided by a corresponding reference 2-D image, \overline{X}' , obtained from a monatomic gas (xenon):

$$\mathbf{R}^{2D} = \frac{\overline{A}' - \overline{B}'}{\overline{X}' - \overline{B}_x'} \quad (4-10)$$

where \overline{B}_x' is the corresponding background image for \overline{X}' . This division by the smoothly decaying diffraction intensity of the atomic reference gas not only permits the direct visualization of molecular interferences (rings) in the 2-D “ratio” images, \mathbf{R}^{2D} , but also removes most of the systematic errors associated with the apparatus function of the detector. Each \mathbf{R}^{2D} is then converted to an experimental 1-D total intensity curve, $R^E(\text{pix})$, by calculating the average intensity as a function of pixel radius, $\rho(\text{pix})$, from the electron beam center, according to the relation:

$$\sqrt{x^2 + y^2} < \rho < \sqrt{(x+1)^2 + (y+1)^2} \quad (4-11)$$

Corresponding values for the standard deviation of the scattering intensity at each pixel radius, $\sigma(\text{pix})$, are also calculated, permitting an additional round of spike rejection in the final calculation of $R^E(\text{pix})$. The $\sigma(\text{pix})$ values are then used later as the weighting function in least-squares refinements (see below). Finally, $R^E(\text{pix})$ is converted to $R^E(s)$ by calculating the scattering angle θ from the pixel dimensions and the camera length L (which is defined as the distance between the scattering volume beneath the sample nozzle and the detection screen). The camera length for these experiments was calibrated by comparing experimentally derived diffraction data obtained from high-purity nitrogen gas with literature values. The division by the reference gas scattering intensity is accounted for by multiplying $R^E(s)$ by the theoretical scattering intensity of the reference gas, $I_{ref}^T(s)$:

$$I^E(s) = R^E(s) \times I_{ref}^T(s) \quad (4-12)$$

The experimental 1-D diffraction curves, $I^E(s)$, may then be analyzed to generate the $sM^E(s)$ and $f(r)$ curves that reflect the structural features of the molecules under study.

4.7 Normalization of Time-Dependent Diffraction Signals

Before analyzing time-dependent diffraction signals, we normalize the total intensity of each time-dependent 2-D image, $\bar{A}'(t)$. This normalization procedure removes any systematic variation ($\sim 1\%$ or less) in electron scattering intensity as a function of temporal delay (e.g., resulting from minuscule changes in photon flux at the photocathode as the delay line retroreflector is placed at different positions). The normalization is performed by first calculating the mean intensity of each image, $\langle \bar{A}'(t) \rangle$, according to the relation:

$$\langle \bar{A}'(t) \rangle = \frac{\sum_{x,y}^{512} M'(x,y;t) \cdot \bar{A}'(x,y;t)}{\sum_{x,y}^{512} M'(x,y;t)} \quad (4-13)$$

where $\bar{A}'(x,y;t)$ is the signal intensity at the pixel with coordinates (x,y) in the averaged 2-D image acquired at time delay t , $M'(t)$ is the binary mask image corresponding to the diffraction image $\bar{A}'(t)$, and 512 is the effective

number of pixels along both x and y (our CCD camera has 1024×1024 pixels, but 2×2 binning is typically employed). The quantity $\langle \bar{A}'(t) \rangle^{-1}$ obtained at each time delay is then used as the normalization constant for the corresponding averaged 2-D image. Once normalization has been performed, the diffraction difference method can be employed.

4.8 Analysis of 1D Diffraction Data: Ground-State Structures

The procedure for processing our diffraction data is illustrated in Fig. 4-17. The experimental diffraction intensity curve is a sum of the desired structural information, $I_M^E(s)$, and a background intensity profile, $I_B^E(s)$:

$$I^E(s) = I_B^E(s) + I_M^E(s) \quad (4-14)$$

where $I_B^E(s)$ contains contributions from atomic scattering, $I_A(s)$, and the experimental background response. Thus, the modified experimental molecular scattering intensity is given by:

$$sM^E(s) = s \frac{I^E(s) - I_B^E(s)}{I_A(s)} \quad (4-15)$$

or

$$sM^E(s) = s \frac{I^E(s) - I_B^E(s)}{|f_a||f_b|} \quad (4-16)$$

We did not obtain the curve for $I_B^E(s)$ by merely calibrating the detector because the amount of scattered laser light and other factors varied from experiment to experiment and with each molecular system. Instead, background curves were independently estimated for each experiment. Such background curves may be ascertained using different methods, three of which are described: (1) A crude yet often effective approximation is a low-order polynomial curve fit through all the data points of $I^E(s)$; (2) A more rigorous way of obtaining $I_B^E(s)$ exploits the sinusoidal nature of $I_M(s)$, cycling above and below zero several times over the experimental detection range. This approach introduces a set of zero-positions, s_n , of s where the theoretical molecular intensity curve, $I_M^T(s)$, crosses zero: i.e., $I_M^T(s_n) = 0$. If $I_M^T(s)$ approaches $I_M^E(s)$, it should then hold from Eqn. 4-14 that $I^E(s_n) = I_B^E(s_n)$ at the zero-positions, s_n . Therefore, $I_B^E(s)$ can be approximated by fitting a polynomial curve through $[s_n, I^E(s_n)]$; (3) A third way to estimate $I_B^E(s)$ is to express $I_B^E(s)$ independently as a polynomial curve defined by the variable coefficients of each order, and to optimize these variables by minimizing the difference (more precisely, χ^2) between $I_M^T(s)$ and $I_M^E(s)$. This method should produce the same background curve obtained with the second method if there

is no systematic error. These three methods can also be applied to the time-resolved diffraction data, as explained later.

4.9 Time-Resolved Experiments: The Diffraction-Difference Method

In order to follow the structural changes that occur over the course of a given chemical reaction, we recorded a series of averaged 2-D diffraction images with varying time delay, t , between the pump (laser) and probe (electron) pulses. Each of these images thus reflects the transient behavior of the molecular structures at the corresponding temporal delay following laser excitation. Unlike the ground-state data, the scattering intensity at a time $t > 0$, $I(t > 0; s)$ contains contributions from more than one type of molecular species—not just the parent molecules, but also intermediates and products of the reaction. Therefore, the time-resolved scattering intensity $I(t; s)$ can be written as a sum of the individual scattering intensities from each species at time t , $I_\alpha(t; s)$:

$$I(t; s) = \sum_{\alpha} I_{\alpha}(t; s) \quad (4-17)$$

where α indexes all possible structures occurring over the course of the reaction. If the molecular structures of the species formed (transient or otherwise) do not change significantly over the time window that defines the

species α , we may partition the time dependence of $I_\alpha(t; s)$ into the relative concentration of structure α by writing:

$$I(t; s) = \sum_{\alpha} I_{\alpha}(t; s) \approx \sum_{\alpha} p_{\alpha}(t) \cdot I_{\alpha}(s) \quad (4-18)$$

where $p_{\alpha}(t)$ is the population (or mole fraction) of a given structure α and $I_{\alpha}(s)$ is the time *independent* scattering intensity from that structure. In the present case, we will consider α to refer to parent, intermediate, and product structures.

In UED, all species present will scatter the incident electrons regardless of their participation in the chemical reaction. Thus, in most cases the vast majority (>85–90%) of the diffracting media is comprised of non-reacting parent molecules: $p_{\text{parent}} \gg p_{\text{intermediate}}$ or p_{product} . Furthermore, the molecular scattering intensity from a reaction fragment is usually weaker than that from a parent molecule because it has fewer internuclear pairs. Therefore, in order to accentuate the diffraction signal arising from structural changes occurring over the course of the reaction, we employed the so-called diffraction-difference method (Fig. 4–18), whereby we use a reference image to obtain the diffraction-difference signal, $\Delta I(t; t_{\text{ref}}; s)$, from the relation:

$$\Delta I(t; t_{\text{ref}}; s) = I(t; s) - I(t_{\text{ref}}; s) \quad (4-19)$$

where t_{ref} refers to the reference time (e.g., prior to the arrival of the reaction-initiating laser pulse). Combining Eqns. 4-18 and 4-19 gives:

$$\Delta I(t; t_{\text{ref}}; s) \approx \sum_{\alpha} p_{\alpha}(t) \cdot I_{\alpha}(s) - \sum_{\alpha} p_{\alpha}(t_{\text{ref}}) \cdot I_{\alpha}(s) = \sum_{\alpha} \Delta p_{\alpha}(t; t_{\text{ref}}) \cdot I_{\alpha}(s) \quad (4-20)$$

Equation (4-20) thus presents $\Delta I(t; t_{\text{ref}}; s)$ in terms of the *changing populations* of the molecular structures involved—if the molecular structure of a given species *does* undergo significant structural change during the time window of the experiment, it may be necessary to refine its structural parameters at each point in time.

The diffraction-difference method has several general advantages. First, the large (unwanted) background signal from atomic scattering is a common contribution to all images—regardless of the temporal delay and the nature of the reaction—and can, therefore, be essentially removed by the subtraction. It follows from the definition of the total scattering intensity, I^E ($= I_{\text{M}}^E + I_{\text{B}}^E$), that the experimental difference curve is given by:

$$\Delta I^E(t; t_{\text{ref}}; s) = \Delta I_{\text{M}}^E(t; t_{\text{ref}}; s) + \Delta I_{\text{B}}^E(t; t_{\text{ref}}; s) \quad (4-21)$$

Because I_B^E is comprised mostly of atomic scattering, which is unchanged over the course of a chemical reaction, $\Delta I_B^E(t; t_{\text{ref}}; s)$ should be nearly zero. Thus, whereas the total diffraction signal, $I(t; s)$, is dominated by the background intensity, $I_B^E(t; s)$, the diffraction-difference curve is dominated by the molecular scattering intensity, $I_M^E(t; s)$:

$$\Delta I^E(t; t_{\text{ref}}; s) \approx \Delta I_M^E(t; t_{\text{ref}}; s) \quad (4-22)$$

Second, any intrinsic systematic error of the detection system will be greatly reduced (or effectively eliminated) by the subtraction. Third, each diffraction-difference curve reflects comparable contributions from the parent and product structures—in contrast to the original raw data, wherein only a relatively small fraction of the signal comes from products (and/or intermediates), with the vast majority of the signal originating from the parent. Therefore, the significance of the product contribution is dramatically enhanced in $\Delta I(t; t_{\text{ref}}; s)$: $|\Delta p_{\text{parent}}| \approx |\Delta p_{\text{intermediate}}| \approx |\Delta p_{\text{product}}|$ (Note that the diffraction-difference method does not depend on the specific formulae used to express I_M).

If desired, knowledge of the fractional changes of the species involved in the reaction, $\Delta p_\alpha(t; t_{\text{ref}})$, can be used to extract the molecular diffraction signal resulting only from the reaction's products. The parent diffraction

signal ($I_{parent}(s)$, obtained at a negative time) is scaled by $\Delta p_{parent}(t; t_{ref})$ and added to the diffraction difference signals obtained at positive times, thereby canceling out the parent contribution:

$$\Delta I(t; t_{ref}; s) - \Delta p_{parent}(t; t_{ref}) \cdot I_{parent}(s) = \sum_{\alpha \neq parent} \Delta p_{\alpha}(t; t_{ref}) \cdot I_{\alpha}(s) \quad (4-23)$$

(Note that $\Delta p_{\alpha}(t; t_{ref})$ is typically a negative number). This procedure, which we have referred to as the “product-isolated” or “product-only” method, has been utilized frequently in our more recent work.

Prior to analyzing the diffraction-difference signals, high-frequency noise was reduced with low-pass Fourier filtering (performed via convolution with a parabolic cut-off function valued 1.0 at 0.0 Å and 0.0 at ≈ 8.7 Å). This filter, which was carefully chosen to prevent any significant damping of higher-frequency components of the diffraction signal, reduced the standard deviation values resulting from least-squares fitting by about half compared to similar analyses of unfiltered data but did not significantly alter the results of the fits.

4.10 Least-Squares Fitting

Refinements of the diffraction data were performed with software developed in-house using a procedure (similar to that used in conventional gas-phase electron diffraction) that iteratively minimizes the statistical χ^2 . For example, for a given difference curve, $\Delta I^E(t; t_{ref}; s)$, the determination of

the relative fractions or structural parameters of each molecular species was made by minimizing:

$$\chi^2 = \sum_{s_{\min}}^{s_{\max}} \frac{[S_c \cdot \Delta s M^T(t; t_{\text{ref}}; s) - \Delta s M^E(t; t_{\text{ref}}; s)]^2}{[\sigma(s)]^2} \quad (4-24)$$

where the $\Delta s M(s)$ is the difference modified molecular scattering intensity, $\sigma(s)$ is the standard deviation of $\Delta s M^E(t; t_{\text{ref}}; s)$ at each s position (over the available range), and S_c is a scaling factor (whose magnitude is determined by the amplitude of the ground-state signal). $\Delta s M^E(t; t_{\text{ref}}; s)$ is obtained from $\Delta I^E(t; t_{\text{ref}}; s)$, and the $\sigma(s)$ values are calculated from the corresponding values of $\sigma(\text{pix})$ (the standard deviation of the scattering intensity at each pixel radius) with appropriate error propagation.

Beginning with an assumed initial product distribution and the starting structural parameters for each species, the software first fits the residual background, $\Delta I_B^E(t; t_{\text{ref}}; s)$, with the experimental $\Delta I^E(t; t_{\text{ref}}; s)$ values at the zero-positions (s_n) of the theoretical $\Delta I_M^T(t; t_{\text{ref}}; s)$ curve. Then the experimental $\Delta s M^E(t; t_{\text{ref}}; s)$ curve is obtained with the background-free ΔI , and χ^2 is calculated to evaluate the quality of the fit. This procedure is repeated until the best least-squares fit between theoretical and experimental $\Delta s M(s)$ curves is reached (i.e, until χ^2 is minimized). In the

fitting algorithm, the absolute amplitude of the diffraction-difference signal may then be scaled to that of the ground-state signal to give the relative number densities of every structure at each time delay over the course of the experiment.

4.11 Estimation of Spatial Coherence

The primary purpose of the electron beam being to record diffraction images, the electron beam has to maintain spatial as well as temporal coherence. Spatial coherence describes the phase correlation between different points in the electron beam; if phase correlation is lost over a distance X , then two atoms separated by X will not contribute interference terms to the scattered intensity. Estimates of coherence are estimated below for transverse (lateral) dimensions and longitudinal (chromatic) dimensions. The lateral coherence length, X_L , for a circular, uniform, and monochromatic source is calculated from:

$$X_L = \lambda/\alpha \quad (4-25)$$

where α is the angular divergence of the beam.

In order to measure the divergence of the electron beam in UED-3, we measured the size of the electron beam at the detector. We also measured the edge spread function of the e-beam at an earlier position along its trajectory by using a knife edge. The edge spread function was measured by introducing

a secondary Al target into the path of the e-beam at a distance of $L = 143$ mm from the phosphor screen and with steps of 0.125 mm. The resultant integral intensity measured on the screen is plotted against the position of the Al edge, as shown in Fig. 4–19. Using the geometrical constraints as depicted in the figure, the divergence of our electron beam has been estimated to be 0.35 mrad. Using the relativistic wavelength for 30 keV electrons, the lateral coherence length of the UED-3 electron beam is estimated to be 100 Å. Non-monochromaticity corrections have not been included in this estimation.

References

1. Williamson, J. C. Ultrafast Gas-Phase Electron Diffraction. Ph.D. Thesis, California Institute of Technology, Pasadena, 1998.

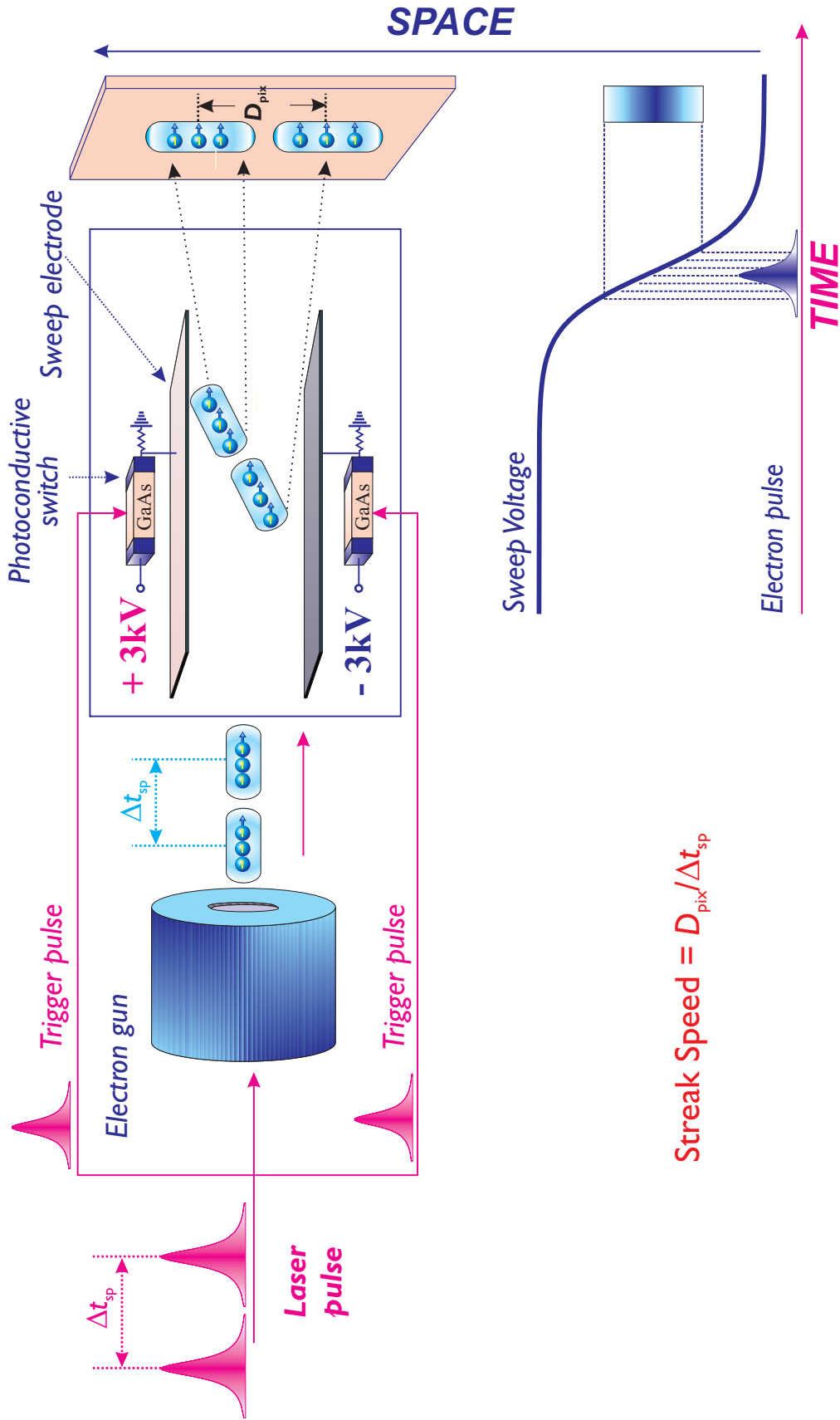


Figure 4-1. Calibration of electron gun via streaking experiments. Two electrons separated in time by Δt_{sp} enter a pair of streak plates. A fast voltage gradient across the streak plates causes the electrons to be separated by a distance D_{pix} at the detector.

Electron Beam Spatial Profile

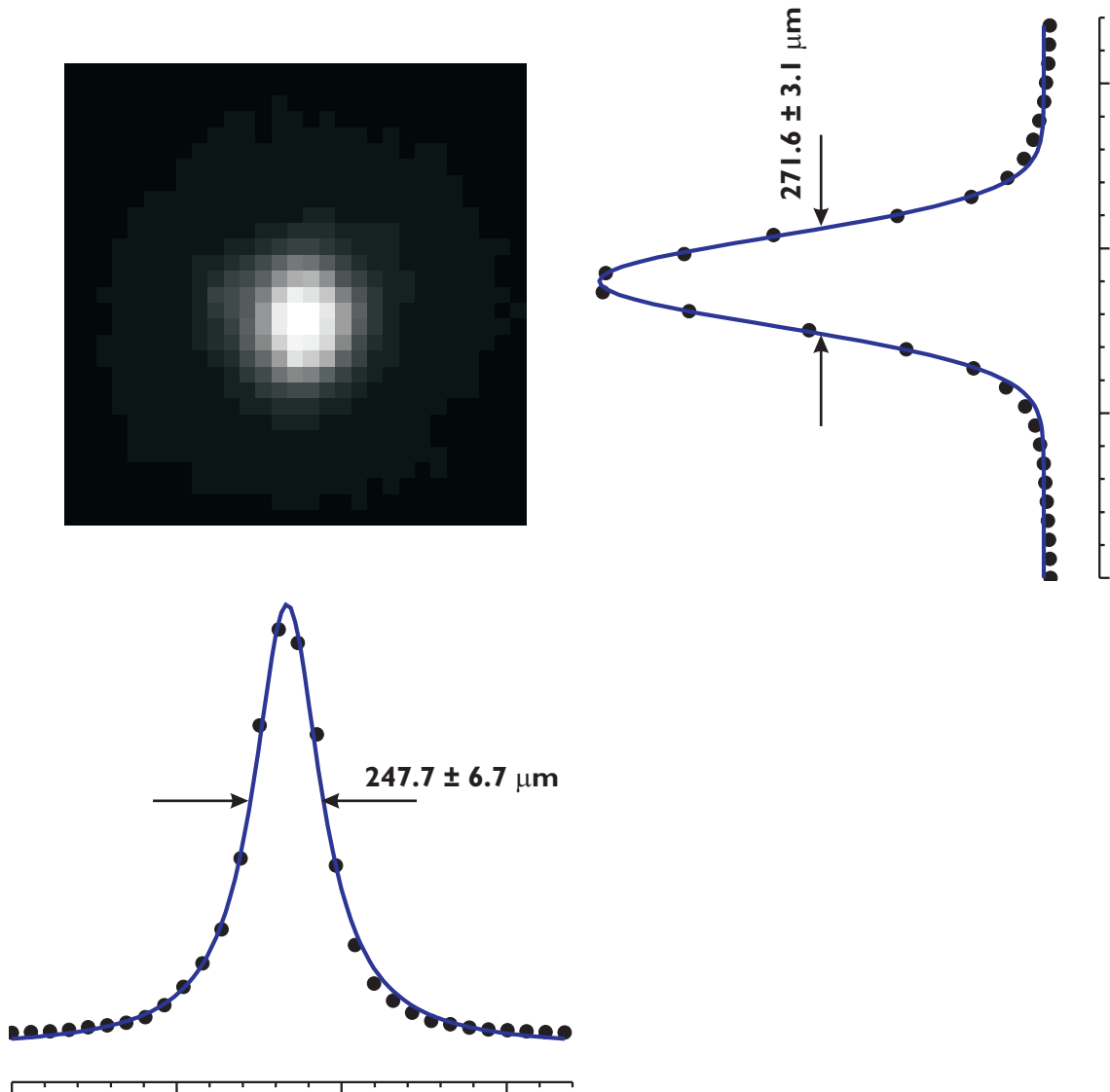


Figure 4-2. Typical X-Y profile of the nearly circular electron beam comprising ~ 4 ps pulses with ~ 25000 electrons/pulse. The image intensifier gain is 775V.

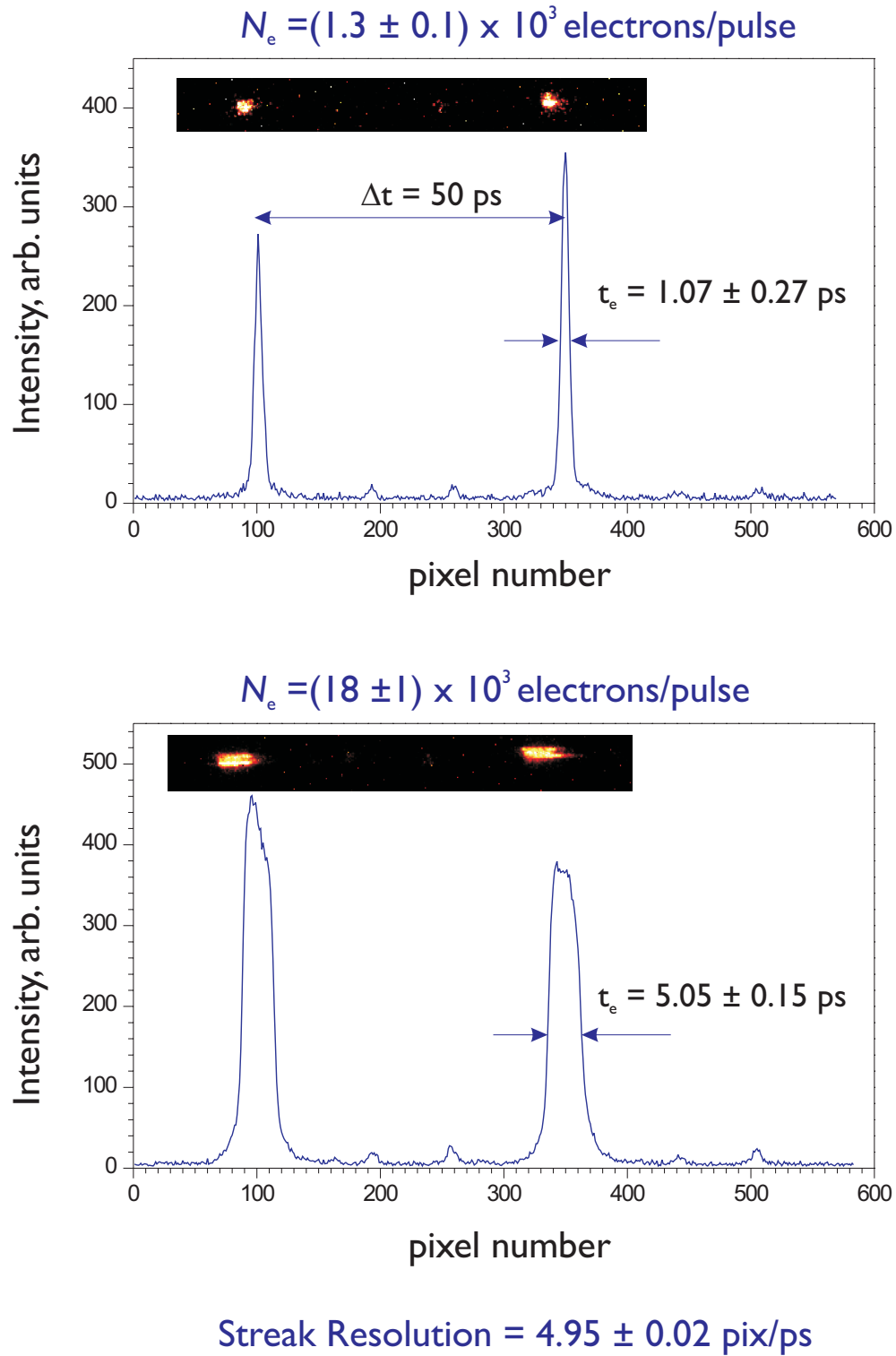


Figure 4-3. Results of an *in situ* streaking experiment showing ultrafast precision for electron pulse measurement in UED-3. The images of the streaked electron pulses separated by 50 ps are shown above the peaks of their respective profiles.

Calibration of Electron Gun

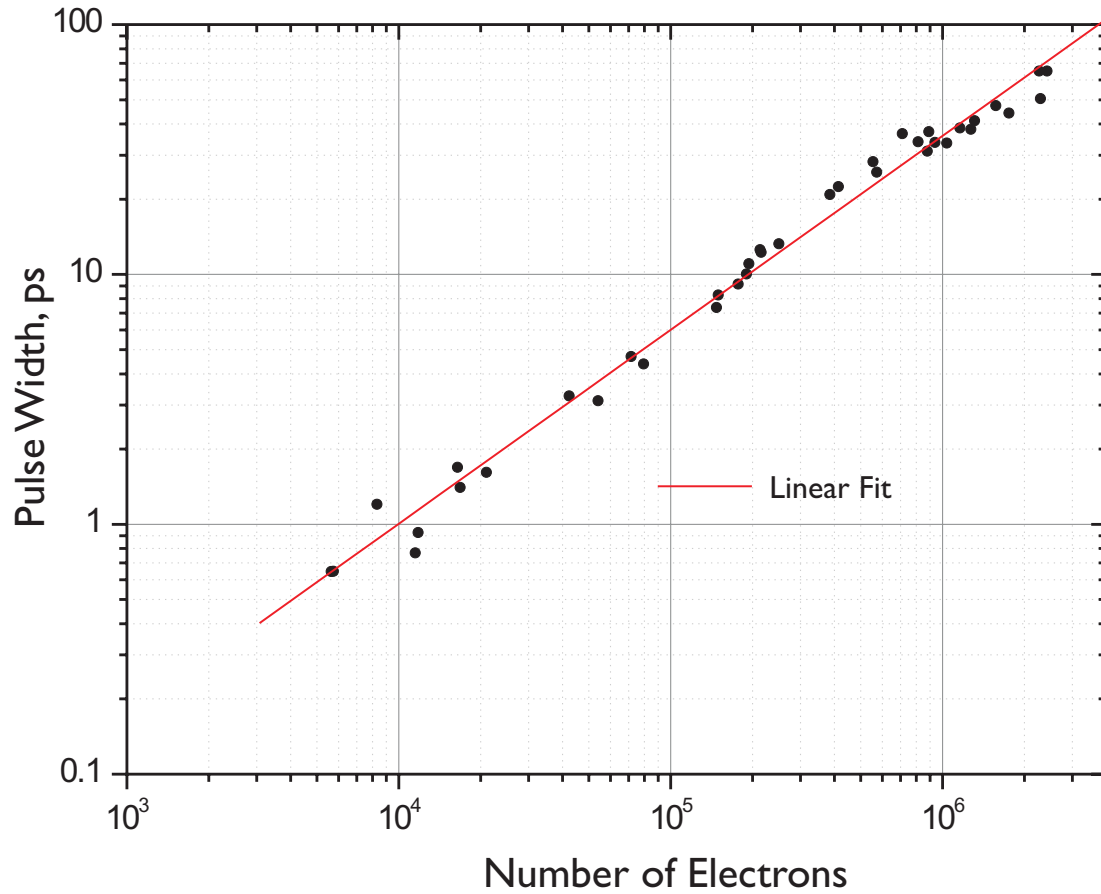


Figure 4-4. Calibration of electron pulse width as a function of the number of electrons per pulse.

Improvement in Electron Gun Performance

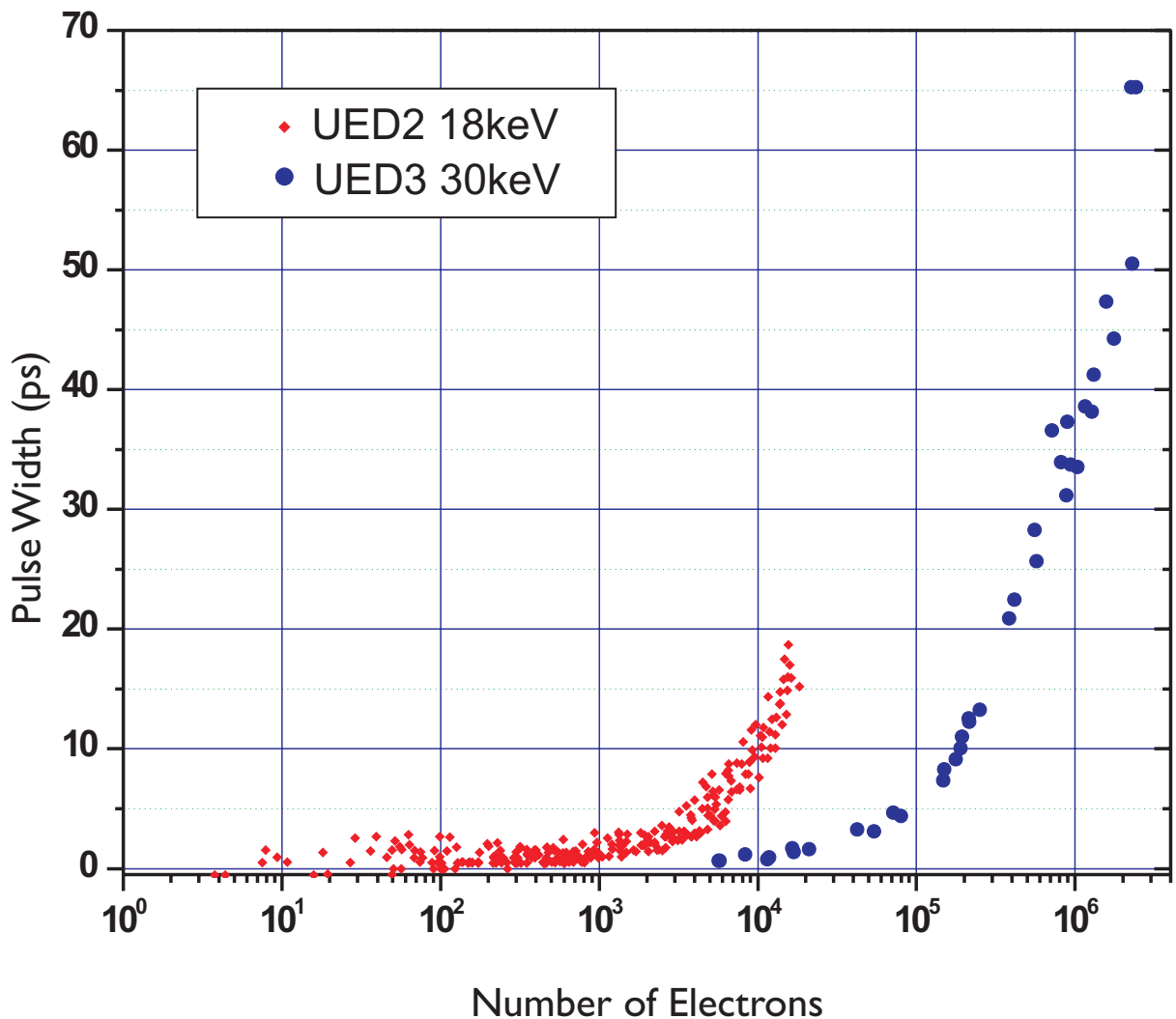


Figure 4-5. Measured electron pulse widths as a function of the number of electrons. The blue curve (UED-3) shows more than an order-of-magnitude improvement in the electron gun performance in comparison to the red curve (UED-2).

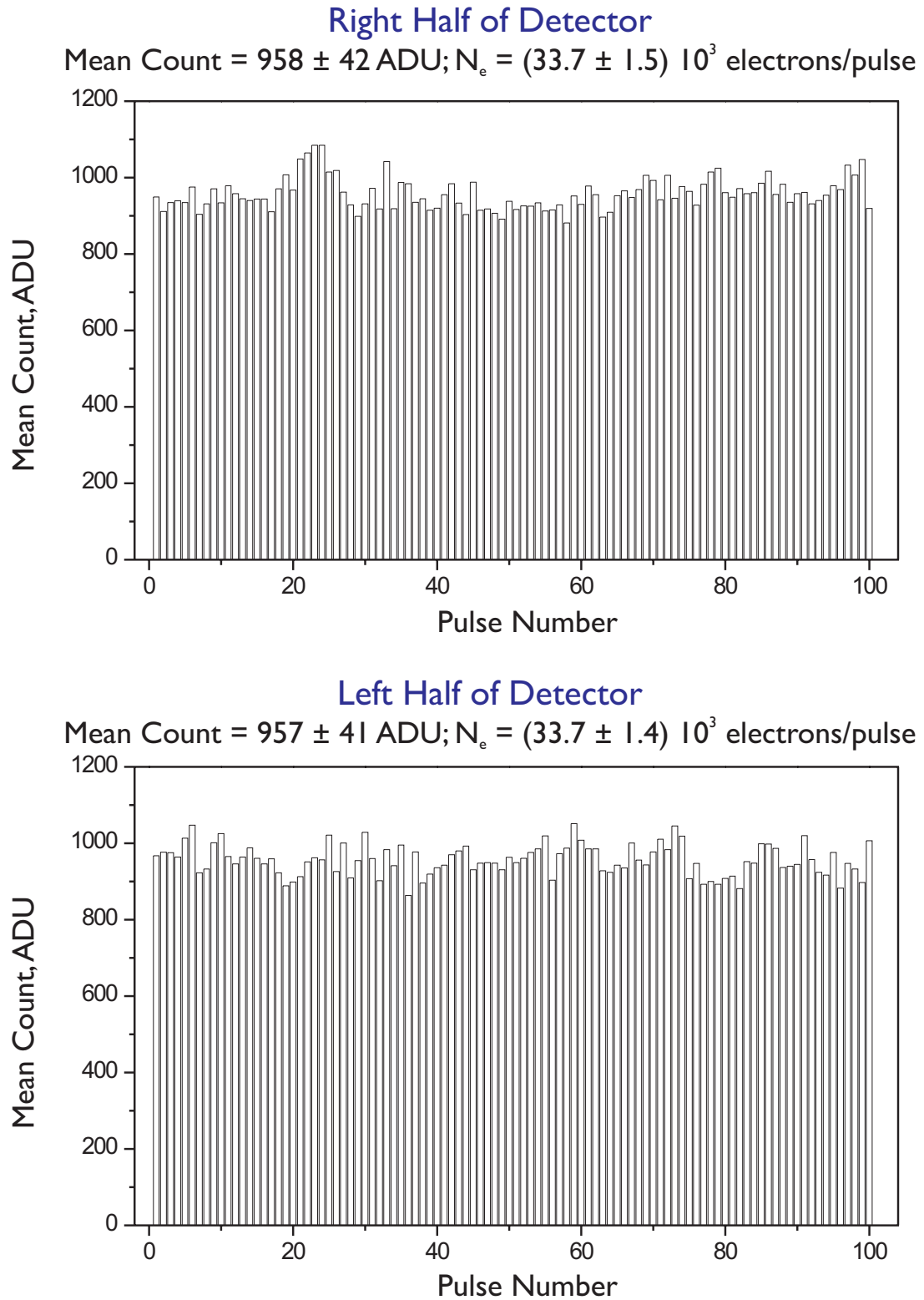


Figure 4-6. Pulse-to-pulse stability of the electron gun measured for 100 pulses on both sides of the detector. The measured statistics indicates the low variation in the average number of electrons/pulse.

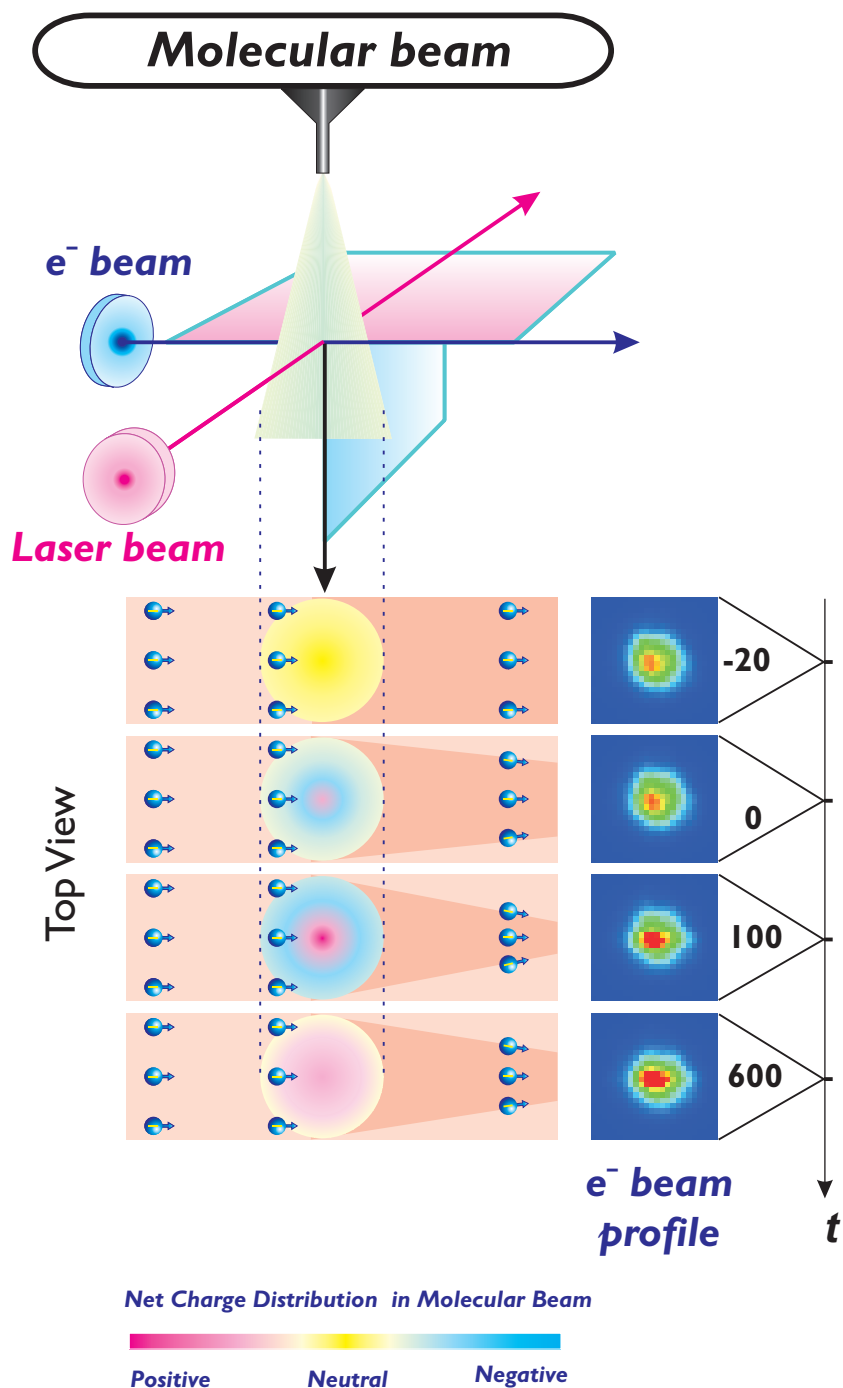


Figure 4-7. Schematic of the lensing experiment to determine *in situ* the zero-of-time. (*Top*) Excitation laser is incident on the molecular beam. (*Bottom*) Sequence of ionization-induced lensing. Excitation laser ionizes molecules within the sample through multiphoton absorption. The nascent electrons (depicted as a light blue cloud) exit the interaction region within picoseconds, while the positive ions (shown as a pink cloud) remain behind. The incident electron beam (shown as dark blue circles) is deflected by the resulting positively-charged ion lens, and the altered beam shape is detected on the CCD.

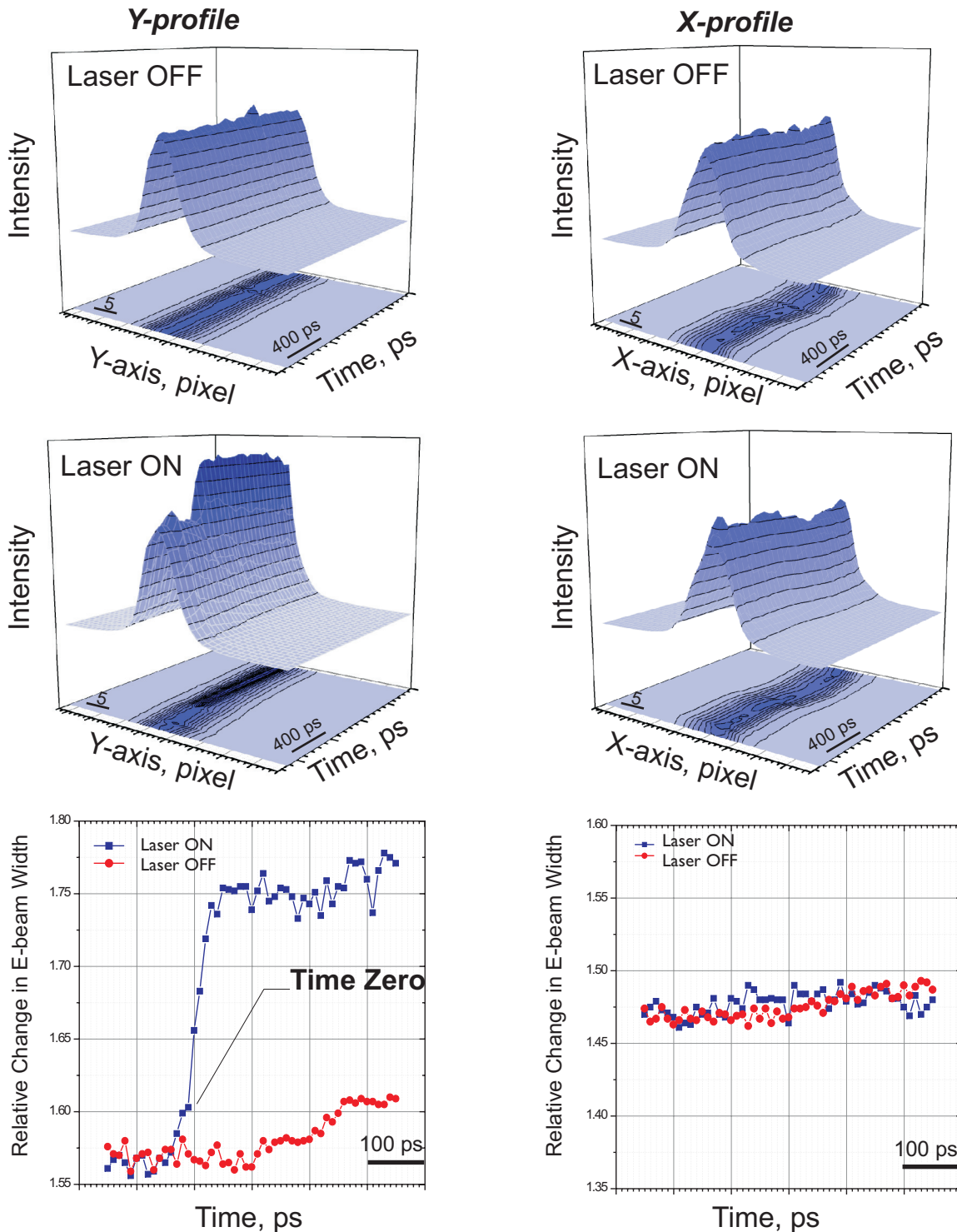


Figure 4-8. Photoionization-induced 'lensing' effect for measuring zero-of-time. A molecular beam of CF_3I was used. Left panel shows the vertical profile of the electron beam while the right panel shows the horizontal profile in absence (*top*) and presence (*middle*) of the laser. The *bottom* panel shows the variation of the fwhm of the electron beam profile as a function of the relative delay between the laser and electron pulses.

Velocity Mismatch

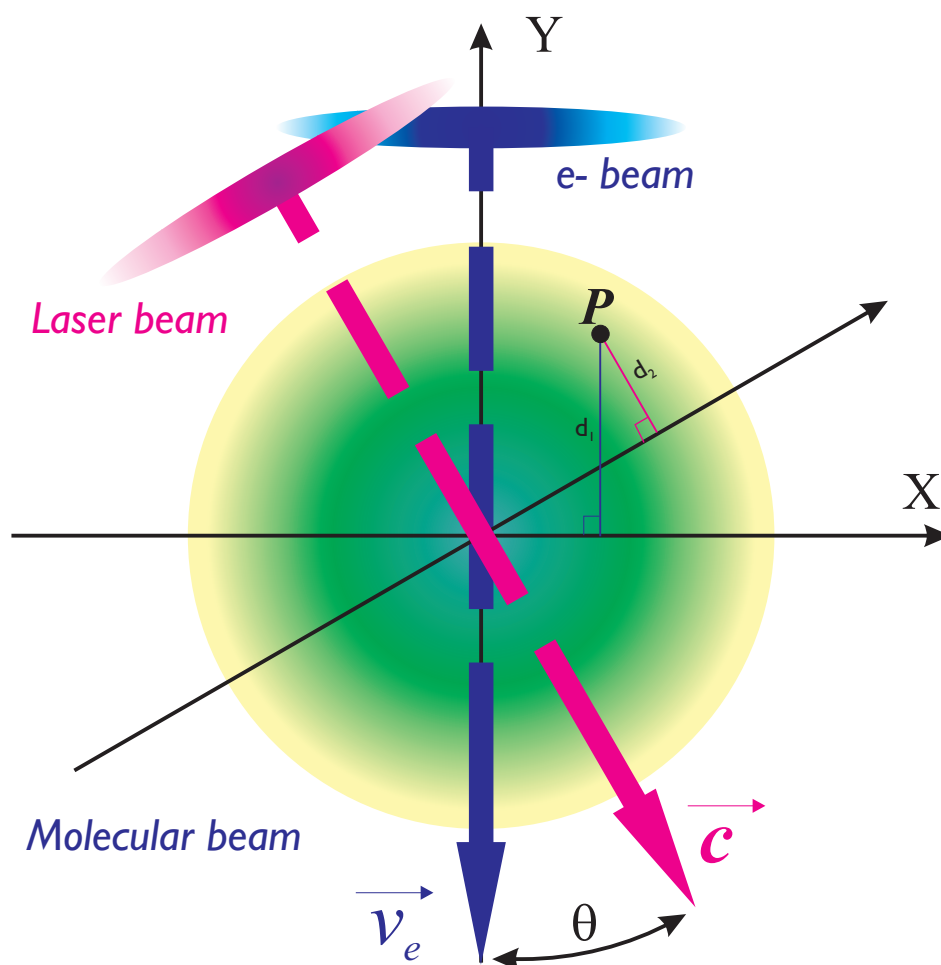
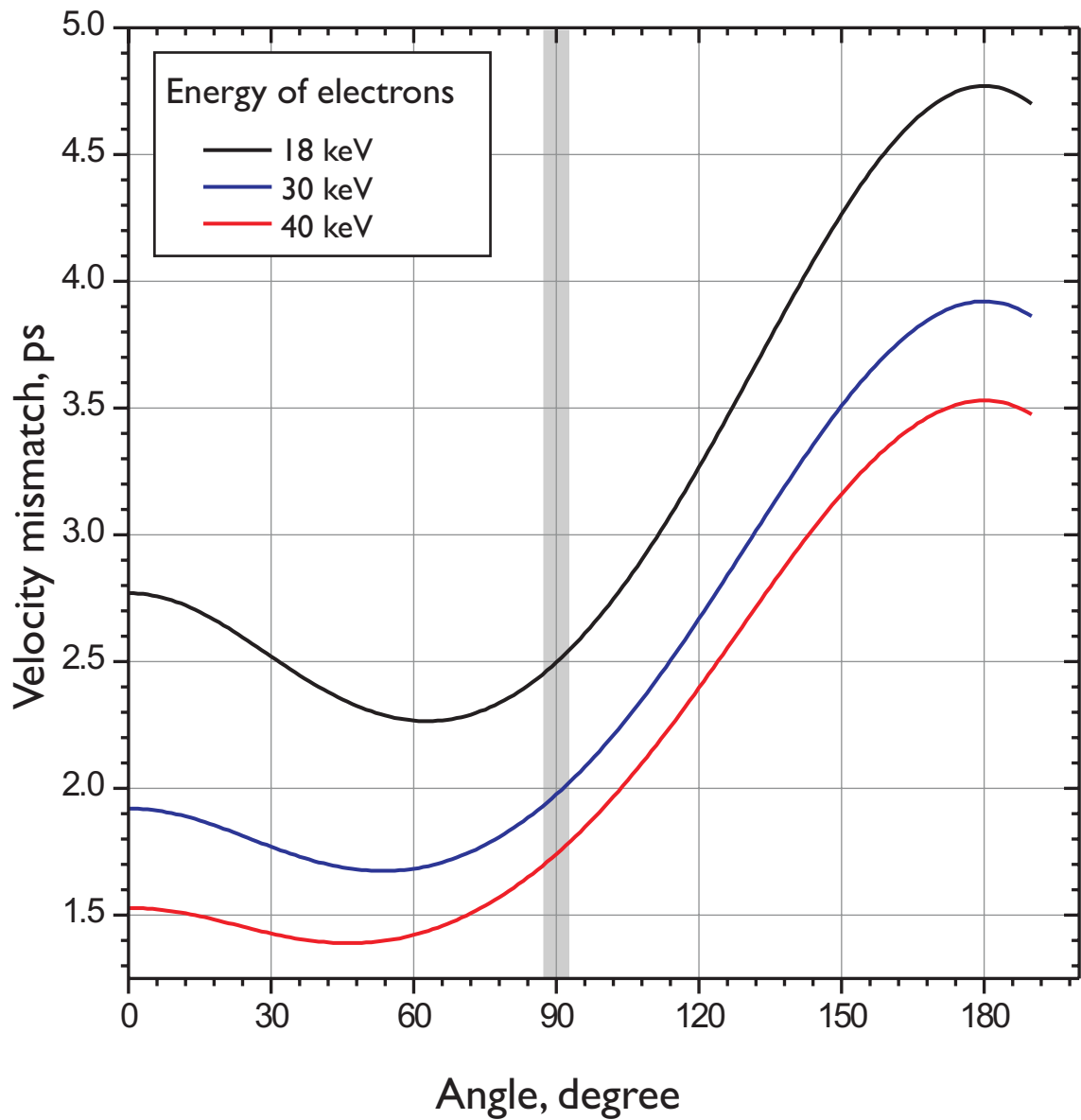
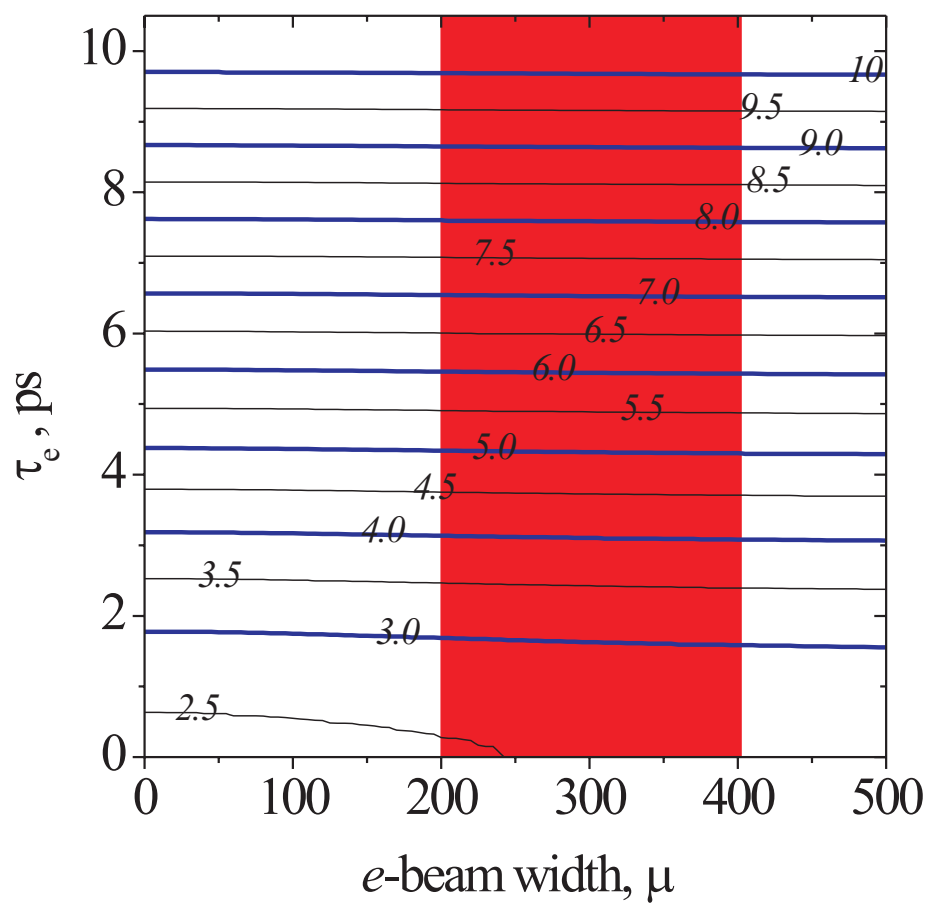


Figure 4-9. Geometry of a crossed-beam experiment. The trajectories of the laser and electron beams intersect at angle θ within the center of a molecular beam. The molecular beam flow is normal to the page, and a cross section of the beam is represented by the shaded coincident circles. If time zero is defined at the origin, then a molecule at point P observes a time delay t between the laser and electron pulses of $d_1/v_e - d_2/c$.



Molecular beam diameter, $w_M = 300 \mu\text{m}$
Electron beam diameter, $w_e = 250 \mu\text{m}$
Laser beam diameter, $w_L = 250 \mu\text{m}$

Figure 4-10. Angular dependence of the temporal broadening due to velocity mismatch (see text).



e-Gun Voltage, $U = 30$ kV
Molecular beam diameter, $w_M = 300$ μm
Laser beam diameter, $w_M = 250$ μm
Laser pulse width, $t_L = 120$ fs

Figure 4-11. Overall temporal resolution of UED-3 (including velocity mismatch) as a function of spatial and temporal width of the electron pulses.

Calibration of Pixel Size

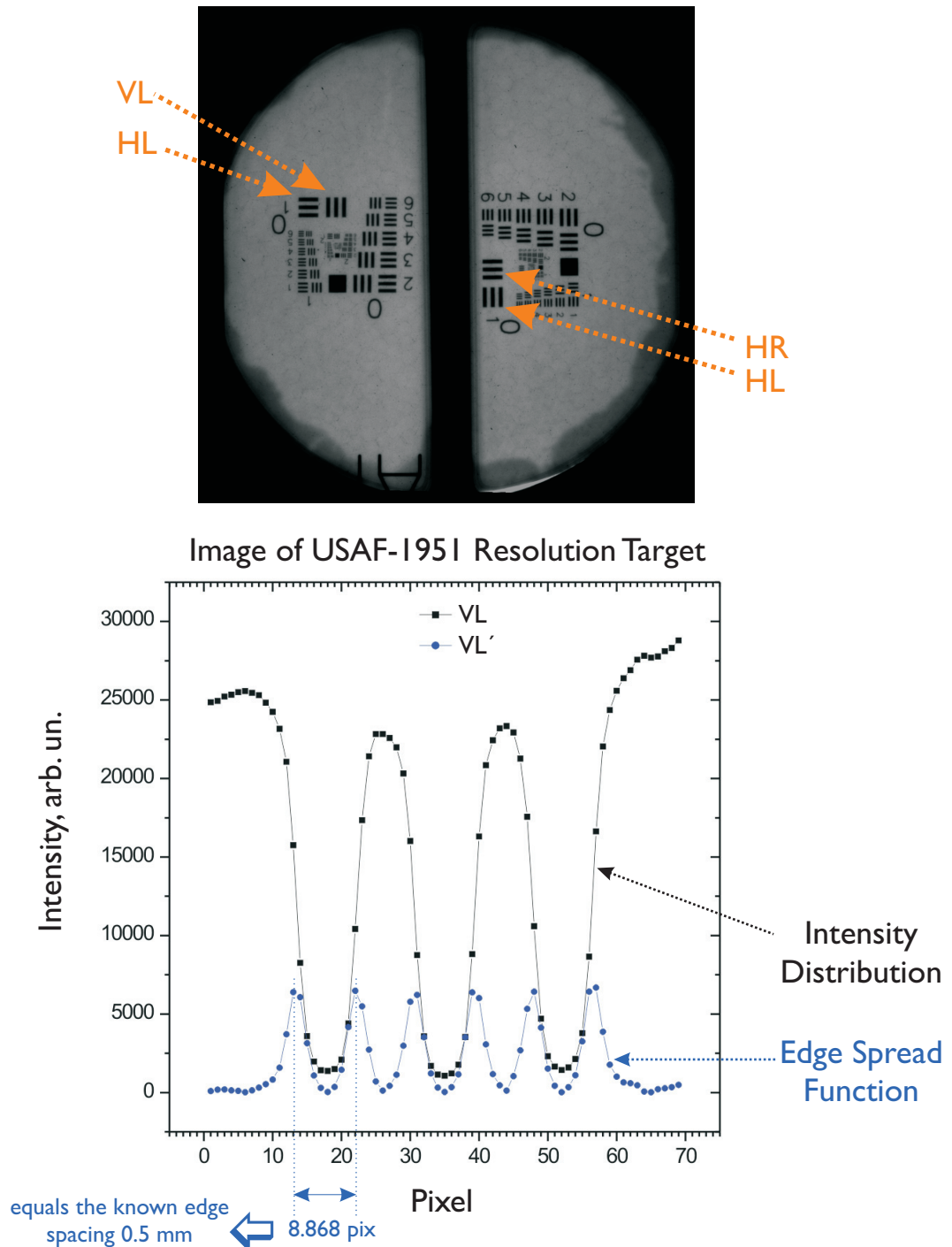


Figure 4-12. Calibration of the pixel size on the phosphor screen using Group 0, Element 1 of the USAF-1951 resolution target. The intensity distribution of the image is shown, the derivative of which gives the edge spread function. The peaks correspond to edges of the bar target, and hence, the peak spacing in pixels should correspond to the known edge spacing (0.5 mm).

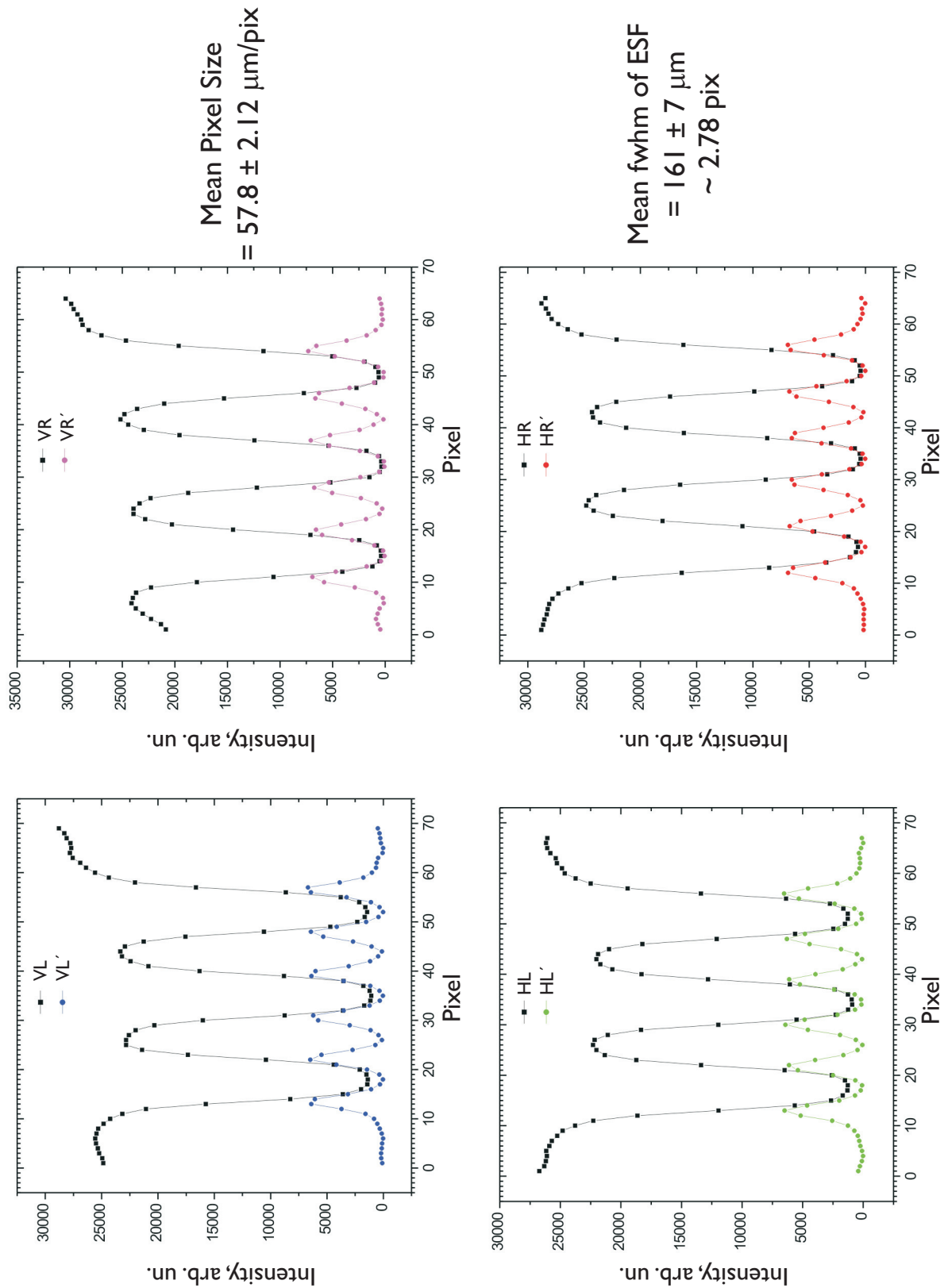


Figure 4-13. Determination of mean pixel size on the phosphor screen. Shown are all measurements over the 4 elements – VL, HL, VR and HR – described in Fig. 4-12.

USAF-1951 Resolution Target

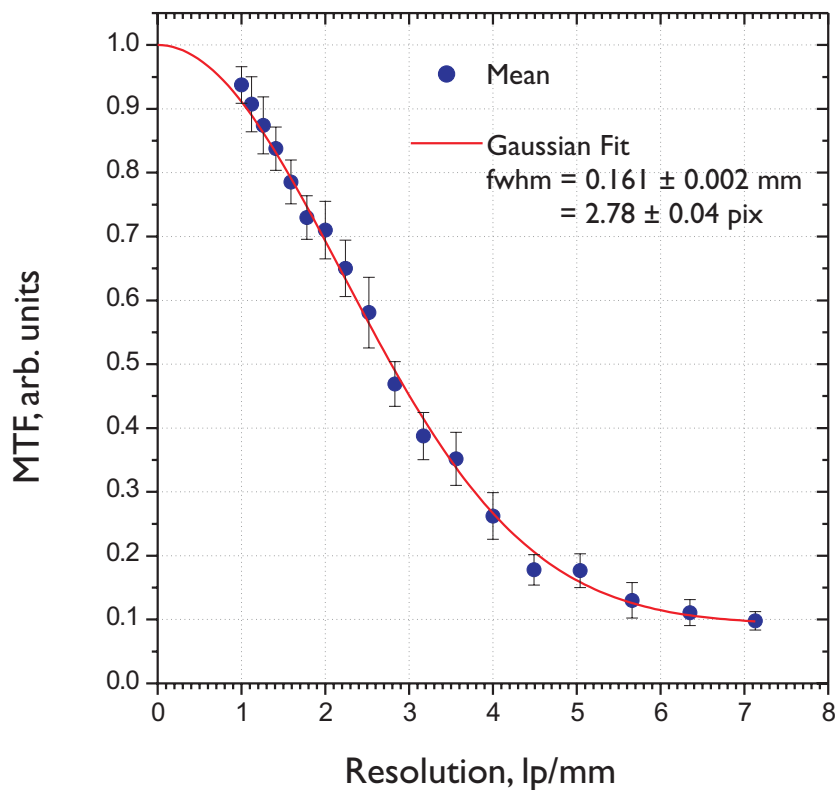
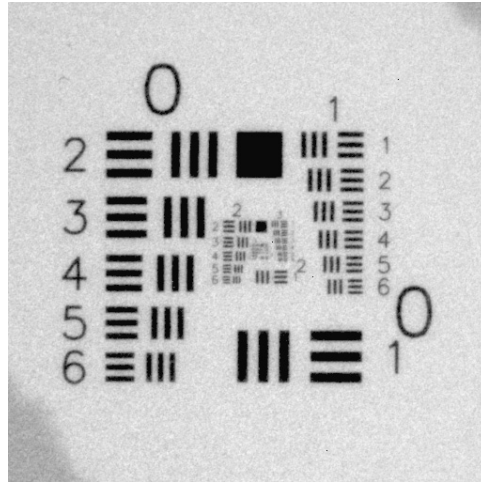


Figure 4-14. Modulation Transfer Function (MTF) for the ICCD camera. The plot indicates that the spatial resolution is 6.5 lp/mm. Shown on top is the USAF-1951 resolution target used for calibration of the imaging system. From the Gaussian fit to the MTF, the width of the point spread function is estimated to be ~ 2.78 pix.

Single Electron Calibration

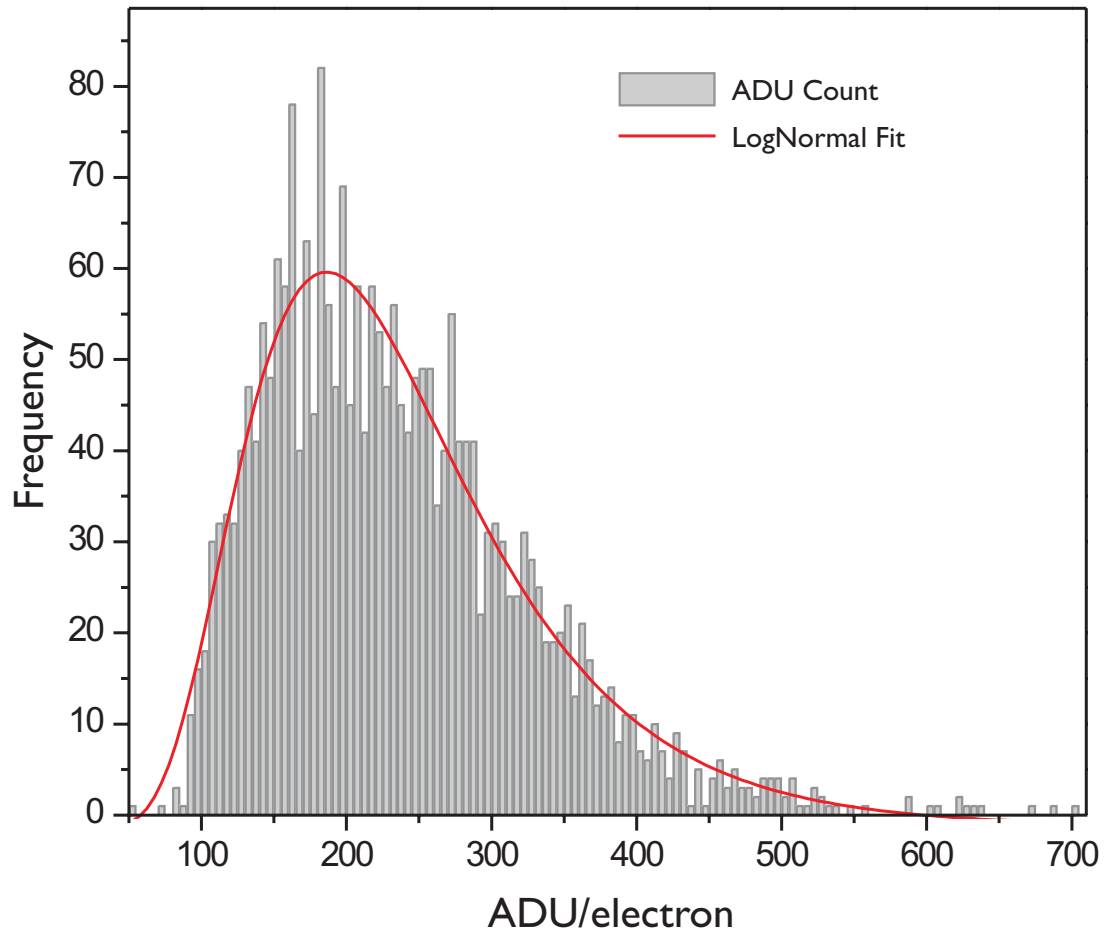


Image Intensifier Gain = 875 V
Phosphor = P-47
Mean ADU/electron = 186.3 ± 1.9

Figure 4-15. Calibration of single electron events on the detector with the P-47 phosphor screen at an image intensifier gain of 875 V.

Inverse Atomic Ratio Method

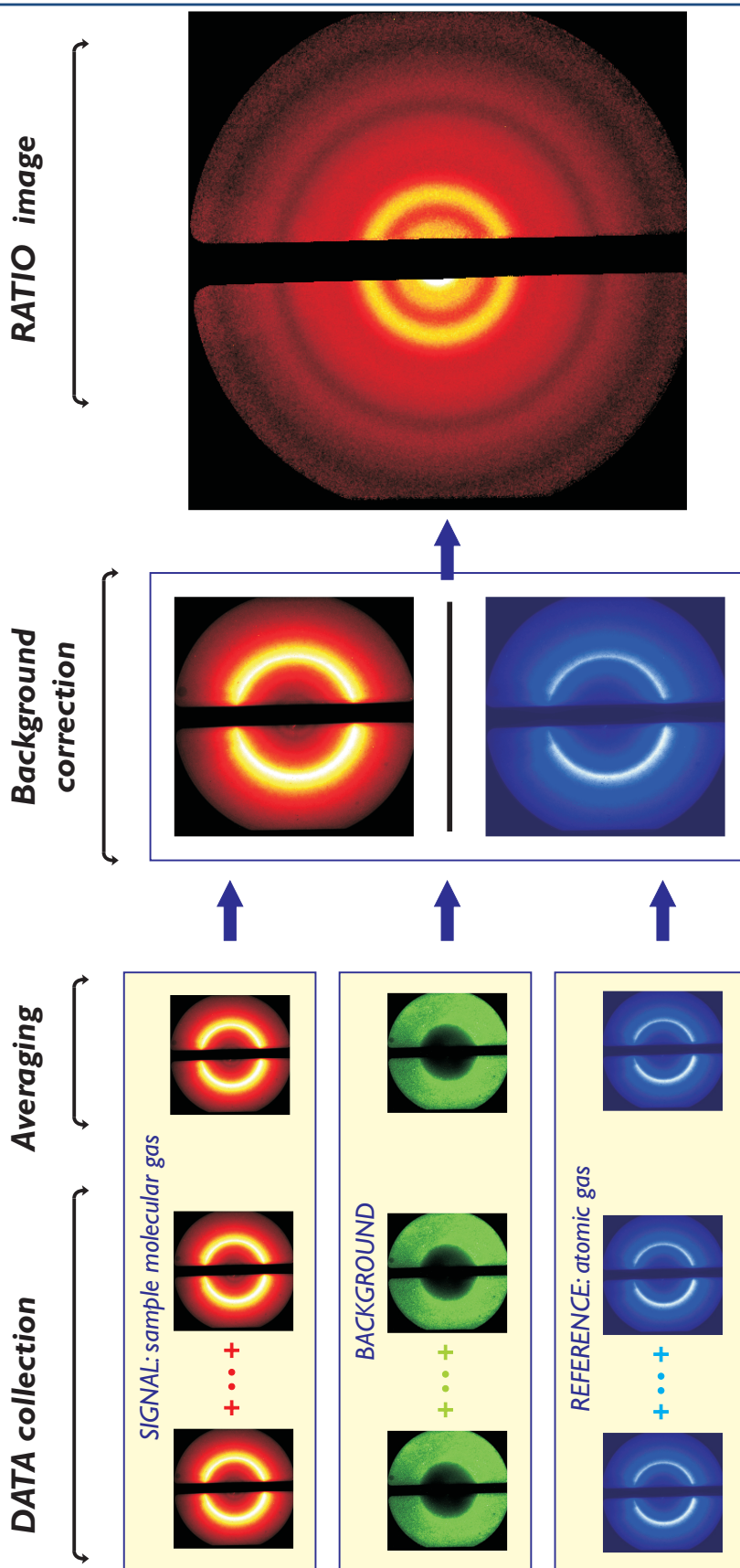


Figure 4-16. Schematic of inverse atomic ratio method that involves dividing the background-corrected signal image with that of a reference atomic gas (Xe) to account for the large incoherent atomic scattering, thereby recovering the coherent molecular scattering (manifested as rings in the 2D image).

Ground State Structural Analysis

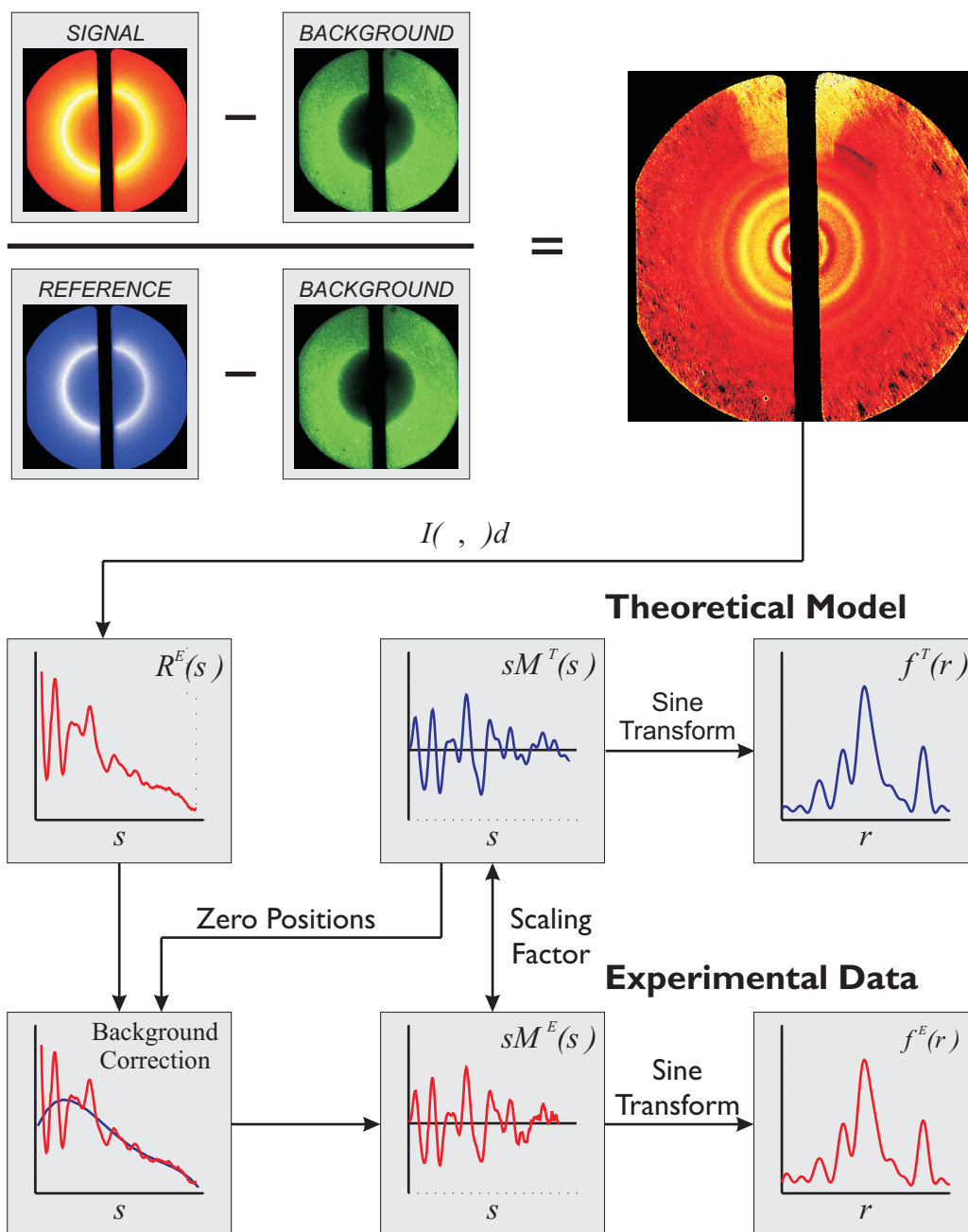


Figure 4-17. Schematic of the processing procedure for 2-D diffraction images and ground-state data analysis. Subtraction of the background image and division by the reference gas image yields a 2-D “ratio” image that clearly shows the rings of the molecular scattering signal. Following radial averaging of the ratio image, the unwanted background signal is subtracted from the 1-D curve to give the desired $sM(s)$ curve, which can be compared with theoretical curves generated with iteratively refined structural parameters describing a given molecular species; the corresponding $f(r)$ curves are obtained via sine transform.

Time-Resolved Structural Analysis

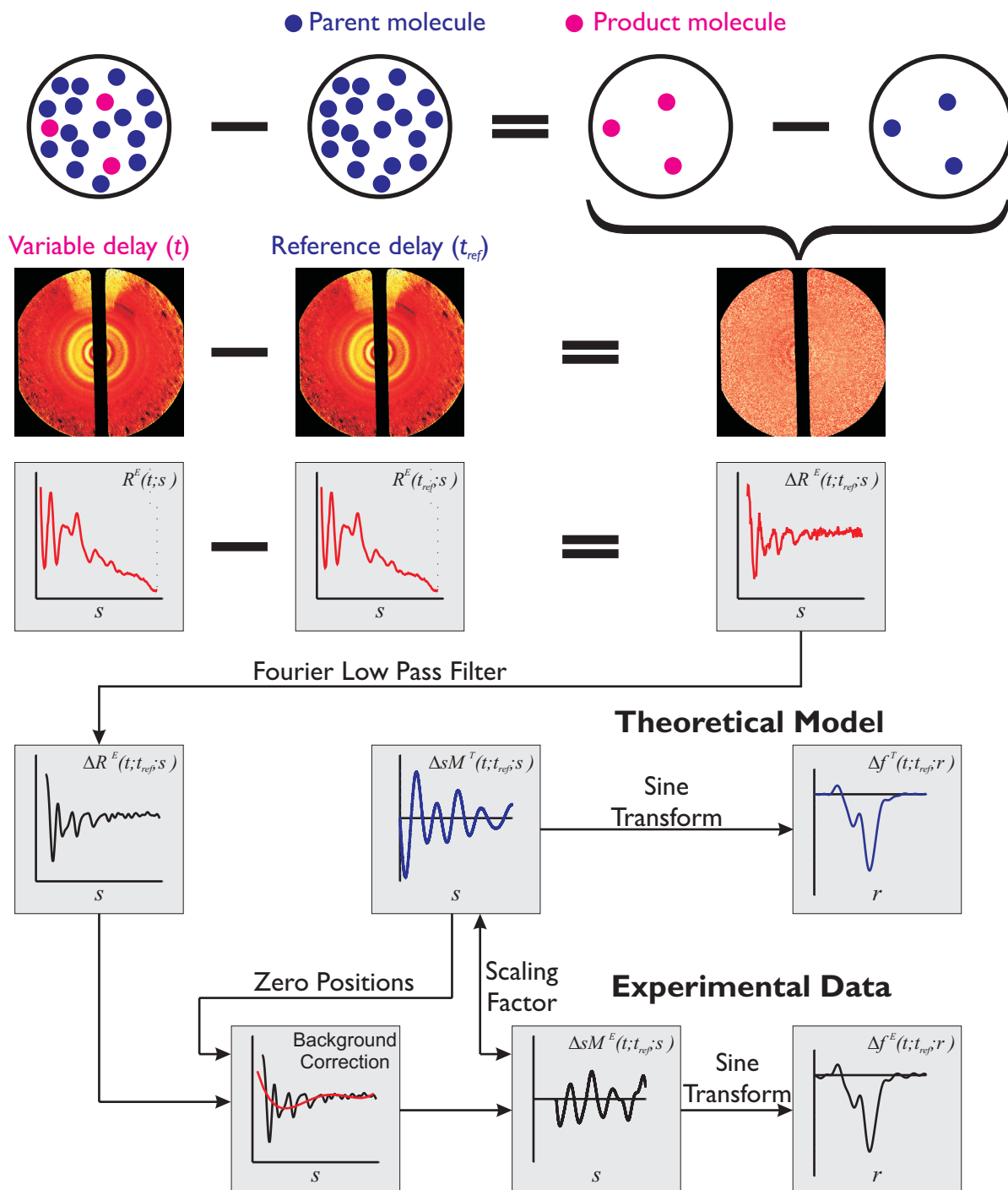
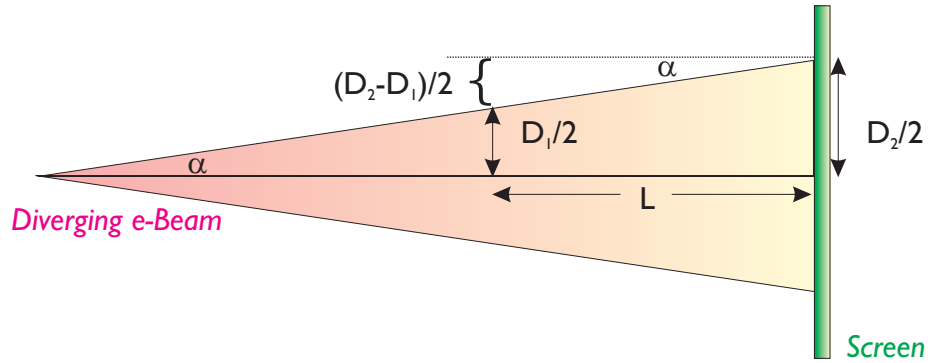


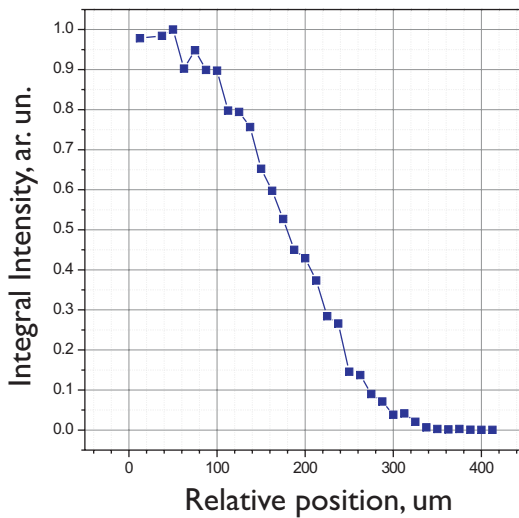
Figure 4-18. Schematic of the diffraction-difference analysis procedure for time-resolved experiments. The difference signal reflects only contributions from structural changes within the molecules. After Fourier filtering and background subtraction, information regarding the evolving structures can be obtained from the experimental $\Delta sM(s)$ curves.

e-Beam Divergence



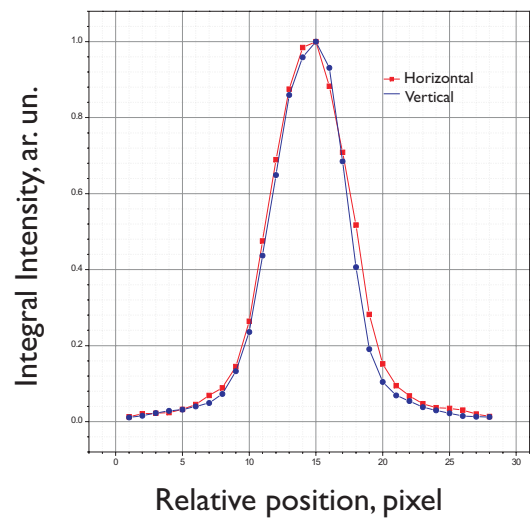
$$\text{Div} = \text{atan} \left(\frac{(D_2 - D_1)}{2L} \right)$$

Edge Spread Function of e-beam at distance L from the screen



$$D_1(\text{fwhm}) = 261.8 \pm 7.5 \text{ um}$$

Size of e-beam at the screen



Vertical Size = $6.26 \pm 0.11 \text{ pix}$
 $D_2(\text{fwhm}) = 361.9 \pm 15.5 \text{ um}$

$$\text{Div} = 0.35 \text{ mrad}$$

Figure 4-19. Divergence of the electron beam. The edge spread function is measured by introducing a secondary Al target into the path of the e-beam at a distance of $L = 143$ mm from the phosphor screen and with steps of 0.125 mm. The resultant integral intensity measured on the screen is plotted against the position of the Al edge.

5

REACTIVE INTERMEDIATE STRUCTURES: A CASE STUDY*

5.1 Introduction

The first application of our third-generation UED apparatus, UED-3¹ was a study of the structural dynamics in the elimination of iodine from 1,2-diodotetrafluoroethane ($C_2F_4I_2$) to form tetrafluoroethylene (C_2F_4) on the picosecond time scale, and the direct determination of the molecular structure of the short-lived C_2F_4I radical intermediate—we determined it to

* Adapted from Ihee, H.; Lobastov, V. A.; Gomez, U.; Goodson, B. M.; Srinivasan, R.; Ruan, C.-Y.; Zewail, A. H., *Science* **2001**, *291*, 458; Ihee, H.; Goodson, B. M.; Srinivasan, R.; Lobastov, V.; Zewail, A. H., *J. Phys. Chem. A* **2002**, *106*, 4087.

be classical, not bridged in nature. The relevant structures for this reaction are shown below in Scheme 5–1.

The elimination reaction of $C_2F_4I_2$ is a prototypical reaction in ultrafast spectroscopic studies of photoinitiated reactions.^{2,3} The consecutive (nonconcerted) nature of the C–I bond breakage was elucidated via picosecond photofragment spectroscopy.² Following UV excitation, a biexponential formation of atomic iodine was observed—with a prompt component (≤ 1 ps) and a much slower second component (~ 30 – 150 ps, depending on the total excitation energy)—indicating a two-step process with a weakly bound radical intermediate (C_2F_4I). The femtochemistry of $C_2F_4I_2$ was subsequently investigated using femtosecond kinetic-energy resolved time-of-flight (KETOF) mass spectrometry, permitting the state, velocity, and angular evolution of the relevant species to be resolved.³ Femtosecond UV excitation (at 277 nm) causes the rapid (≈ 200 fs) loss of the first iodine atom, the first C–I bond breakage, and the formation of the transient C_2F_4I radical intermediate—with the kinetic energy distributions of the fragments directly measured. The remaining internal energy, left to redistribute within the vibrational degrees of freedom of the C_2F_4I radicals, was enough to induce secondary C–I fragmentation in a majority of the hot intermediates—resulting in the loss of the second iodine atom and the formation of the tetrafluoroethylene product in ≈ 25 ps.

The chemistry of halogen elimination reactions is of general interest because products are usually formed under stereochemical control with respect to the final positions of the functional groups about the newly formed double bond.⁴⁻⁷ The origin of this well-known behavior has been hypothesized to lie in the geometry of the intermediate species of the reaction. For example, previous quantum chemical calculations⁸ have shown that CH_2BrCH_2 and CH_2ICH_2 radicals should form stable, symmetrically “bridged” structures, consistent with the Skell hypothesis for the origin of stereochemical control in such systems.^{9, 10} In a symmetrically bridged structure, the primary halide (i.e., I or Br) is shared equally between the two $-\text{CR}_2$ moieties, whereas in a “classical” structure the primary halide would reside predominantly on one $-\text{CR}_2$ moiety.¹⁰ A bridged structure would prevent rotation about the C–C bond, thereby maintaining the functional group positions in the final product. However, the substitution of hydrogens with highly electronegative fluorines can cause dramatic changes in molecular structure (and reactivity). For example, it is well known that the CF_3 radical is highly non-planar while CH_3 is planar, and the $\text{C}_2\text{F}_4\text{I}$ radical structure may be much different from that of $\text{C}_2\text{H}_4\text{I}$.

While the presence of CF_2XCF_2 radicals can be readily detected in photodissociation reactions of $\text{CF}_2\text{XCF}_2\text{X}$ molecules via spectroscopy, UED offers the means to track all of the nuclear coordinates over the course of a

chemical reaction, allowing the molecular structures of these radicals to be observed directly. Thus, the elimination reaction of $C_2F_4I_2$ is an ideal process to study with UED: (1) it affords the opportunity to observe the structural dynamics of a prototypical non-concerted reaction involving the loss of two highly-scattering heavy atoms (providing a strong diffraction difference signal), and (2) it permits the determination of the molecular structure of a transient radical intermediate that belongs to an important family of chemical reactions.

5.2 Experimental

Samples of $C_2F_4I_2$ (Lancaster, 98%) were used without further purification, but were degassed with several freeze–pump–thaw cycles and stabilized with copper filings. High-purity xenon (Spectra Gases, 99.999%) was used as an atomic reference gas (see discussion below), and the CF_3I gas (99%) used for determining the zero-of-time in the lensing experiments was purchased from Aldrich. In order to maintain satisfactory sample pressure at the needle (estimated to be a few torr), the sample bulb, gas manifold, and nozzle temperatures were respectively maintained at 60 °C, 100 °C, and 120 °C for the $C_2F_4I_2$ experiments. The background pressure of the scattering chamber was typically $\sim 2 \times 10^{-4}$ torr during the experiment.

5.3 Results and Discussion

A. Ground-State Structures of C₂F₄I₂. The experimental results concerning the ground-state structures of C₂F₄I₂ are shown in Figs. 5–1 and 5–2. In order to observe the ground-state structures, we time the electron pulse to arrive before the initiation pulse (i.e., at a negative time). The C₂F₄I₂ molecule is known to have two conformational minima with respect to torsional rotation about the C–C bond: an *anti* structure with a \angle ICCI torsion angle of 180° and C_{2h} symmetry, and a *gauche* structure with \angle ICCI \approx 70° and C₂ symmetry. In the study by Hedberg and co-workers,¹¹ the experimental structural parameters for C₂F₄I₂ were refined under the simplifying assumption that the *anti* and *gauche* conformers possess identical values for the structural parameters, except for the \angle ICCI dihedral angle. Correspondingly, identical *anti/gauche* parameter values were used in our analysis, although recent quantum chemical calculations have suggested that the C–C and C–F distances of the *anti* conformers may be slightly shorter, and the C–I distances slightly longer, than those of the *gauche* conformers.¹²

Both ground-state structures were observed in the electron diffraction data shown in Fig. 5–1; the ratio of these conformers was determined via least-squares refinement to be 76:24 \pm 2 *anti:gauche*. This ratio, which is governed by the sample temperature and the energy difference between the

conformers, was identical to the previous results obtained by Hedberg and co-workers at 120 °C.¹¹ The theoretical $sM^T(-95 \text{ ps}; s)$ curve, obtained from the refinement of the conformer ratio, is shown as the red curve in Fig. 5–2. Excellent agreement can be seen between $sM^E(-95 \text{ ps}; s)$ and $sM^T(-95 \text{ ps}; s)$, and in the corresponding experimental and theoretical $f(-95 \text{ ps}; r)$ curves shown in Fig. 5–2.

The various interatomic distances present in the anti and gauche $\text{C}_2\text{F}_4\text{I}_2$ structures are indicated at the bottom of the $f(r)$ curve in Fig. 5–2 and can be summarized as follows: the peak at $\sim 1.4 \text{ \AA}$ results from covalent C–F and C–C distances; the peak at $\sim 2.2 \text{ \AA}$ results from covalent C–I and non-bonded F··F and C··F distances; the broad peak at $\sim 3 \text{ \AA}$ is comprised of non-bonded F··I, C··I, and F··F distances; and the peaks at $\sim 3.8 \text{ \AA}$ and $\sim 5.1 \text{ \AA}$ respectively correspond to the non-bonded I··I distances for the gauche and anti conformers.

B. Structural Dynamics of the $\text{C}_2\text{F}_4\text{I}_2$ Reaction. UED images were acquired for the elimination reaction of $\text{C}_2\text{F}_4\text{I}_2$ over a range of time delays (t) from -95 ps to $+405 \text{ ps}$. The data at -95 ps served as a reference representing the signal contributed only by parent molecules. A set of diffraction-difference curves with $t_{\text{ref}} = -95 \text{ ps}$ was obtained from the images (see Fig. 5–3) using the procedures described in Chapter 4. Figure 5–4(a) shows the effects of the

Fourier filter on a raw diffraction-difference curve, $\Delta R^E(405 \text{ ps}; -95 \text{ ps}; s)$, while Fig. 5–5(a) shows the entire set of difference curves, $\Delta R^E(t; -95 \text{ ps}; s)$, and the corresponding residual background curves, $\Delta R_B^E(t; -95 \text{ ps}; s)$. No change is observed in the $t = -45 \text{ ps}$ data as the electron pulses probe the molecules prior to the initiation of the chemical reaction. At $t = 0 \text{ ps}$, a periodic pattern instantaneously appears (within our time resolution), resulting from structural changes in the molecules. The difference signal becomes more pronounced with increasing time.

The corresponding $\Delta sM^E(t; -95 \text{ ps}; s)$ curves, created in part by subtraction of the baseline curves obtained for each time delay, are shown in Fig. 5–5(b). The difference procedure removes most of the systematic background signal, resulting in a small, nearly linear background curve for the raw difference curves in Fig. 5–5(a). Finally, the corresponding time-dependent difference radial distribution curves, $\Delta f^E(t; -95 \text{ ps}; r)$, which directly indicate the structural changes occurring over the course of the reaction, are shown in Fig. 5–5(c). It is significant to note that the negative peak intensity at $\sim 5.1 \text{ \AA}$ in the $\Delta f(r)$ curves remains constant after 5 ps , whereas the peak intensities around $2\sim 3 \text{ \AA}$ continue to increase over a longer time scale.

As shown in the figure, the negative peak at $\sim 5.1 \text{ \AA}$ results from the

loss of the I·I internuclear separation of the anti conformer of the parent C₂F₄I₂ molecules, while those at 2~3 Å result primarily from the depletion of C-I, F·I, and C·I distances. These observations demonstrate the non-concerted nature of the structural changes in the reaction: the first step (C₂F₄I₂ → C₂F₄I + I) is essentially complete within our ~5 ps resolution—consistent with the ~200 fs time constant measured previously in this laboratory,³ whereas the second step (C₂F₄I → C₂F₄ + I) is considerably slower, taking place over tens of picoseconds.

Theoretical $\Delta sM^T(t; -95 \text{ ps}; s)$ and $\Delta f^T(t; -95 \text{ ps}; s)$ curves (red curves in Figs. 5-5(b) and 5-5(c)) were obtained by refining the relative fractions of the species present against the corresponding experimental $\Delta sM^E(t; -95 \text{ ps}; s)$ curve (blue) at each time delay. These refinements were performed as follows. The depletion of the C₂F₄I₂ parent molecules was fit using the structural parameters determined by Hedberg and co-workers, and with the anti:gauche conformer ratio held fixed at the 74:26 value determined above; the latter practice assumes that there is no disproportional selectivity in the depletion of anti *vs.* gauche C₂F₄I₂ conformers during the loss of the first iodine atom (i.e., that the C-I chromophores of the anti and gauche conformers have identical absorption cross sections and reactivity).

Starting structures for the C₂F₄I radical intermediate were constructed

using the structural parameters provided by recent quantum chemical calculations.⁸ While one goal of our studies was to experimentally determine the structure of this transient species, the calculations suggested that the structure of this species is non-bridged in nature, with anti and gauche conformers qualitatively similar to the parent structures. Nevertheless, we initially included a bridged C₂F₄I structure in our early fraction refinements; doing so, however, had a detrimental effect on the overall fits—and typically resulted in negative values for the bridged fraction. Therefore, our final fraction refinements of the $\Delta sM(t; -95 \text{ ps}; s)$ data included only the non-bridged, “classical” anti and gauche C₂F₄I structures.

The high internal energy of the C₂F₄I radical following laser excitation was included in our analysis. After each parent molecule absorbs a UV photon (107 kcal/mol) and fragments into C₂F₄I + I, 48 kcal/mol are available for the internal energy of the C₂F₄I radical and the translational motion of both fragments (for the I channel, whereas only 26 kcal/mol is left over after the formation of I*, spin excited iodine); 59 kcal/mol of the incident energy is required to break the first C–I bond (in addition to the 22 kcal/mol needed to match the spin-orbit energy of I*). According to previous experiments from this group,³ about 67% (for the I channel; 59% for I* channel) of the energy is partitioned into the translational degrees of freedom, whereas the remaining 33% [for the I channel (16 kcal/mol); 41% for the I* channel (11 kcal/mol)]

goes into the internal energy of the C_2F_4I radical. Accounting for the branching ratio of 30:70 for the I and I* channels³ yields 12.5 kcal/mol for the available internal energy acquired in the C_2F_4I radical. However, because some of the available thermal energy from the parent molecule at 393 K (~6.7 kcal/mol) remains in C_2F_4I , the total available internal energy is about 19 kcal/mol. If complete thermalization of the internal degrees of freedom is assumed, a vibrational temperature of ~800 K can be estimated for the C_2F_4I radical (based on the total remaining internal energy and quantum chemical predictions for the vibrational frequencies¹²). While the use of thermalized structures proved adequate for the present study, we note that in general, complete thermalization may not always be a good approximation—particularly for UED studies of complex molecules at high internal energies.¹³

Using theoretical values for the rotational barrier separating anti and gauche structures,¹³ microcanonical RRKM rates were calculated to predict the time constant for the conversion from the anti conformer to the gauche conformer to be ~13 ps, and that for the reverse isomerization to be ~3 ps. These time constants yield a steady-state anti:gauche conformer ratio of ~83:17. On the other hand, assuming complete thermalization of the internal degrees of freedom gives a similar conformer ratio of 81:19, estimated from the energy difference between the conformers (calculated to be ~3.3 kcal/mol¹²), and the internal temperature. In our refinements of the UED

data, the anti:gauche conformer ratio of the C_2F_4I radicals was therefore held fixed at 81:19. Note that the quantum chemical calculations predicted that the conformational energy difference between anti and gauche radicals is larger than the corresponding value for the parent conformers (~ 1.2 – 1.9 kcal/mol).¹² This larger energy difference apparently results from a relative stabilization of the anti radicals that has been rationalized in terms of hyperconjugation between the radical center and the $\sigma^*(C-I)$ molecular orbital.¹⁴

Finally, the structural parameters for the C_2F_4 product species were obtained from Ref. ¹⁵. The fraction refinements were thus simplified to a two-parameter fit: (1) the total fraction of $C_2F_4I_2$ parent molecules depleted, and (2) the total fraction of C_2F_4I radicals formed. The fraction of C_2F_4 product formed could then be determined from these values at each time point according to Eqn. 5–1:

$$\begin{aligned} \Delta sM(t; -95 \text{ ps}; s) = & -|\Delta p_{C_2F_4I_2}| \cdot sM(s)_{C_2F_4I_2} + |\Delta p_{C_2F_4I}| \cdot sM(s)_{C_2F_4I} \\ & + |\Delta p_{C_2F_4}| \cdot sM(s)_{C_2F_4} \end{aligned} \quad (5-1)$$

with

$$\Delta p_{C_2F_4} + \Delta p_{C_2F_4I} = -\Delta p_{C_2F_4I_2} \quad (5-2)$$

The time evolution of the distribution of structures is determined from

the $\Delta sM(t; -95 \text{ ps}; s)$ data. An initial depletion of the parental signal is observed to follow the response function of the UED apparatus, a result that is consistent with the ~ 200 fs time constant measured previously by femtosecond mass spectrometry.³ The amplitude of the diffraction-difference signals, when scaled to that of the ground state, shows that $\sim 8\%$ of the parent molecules participated in the reaction under the given experimental conditions. The relative fraction of $\text{C}_2\text{F}_4\text{I}$ rises briefly (within the response time of the apparatus) and then decays, while the fraction of C_2F_4 rises steadily. Fitting these time-dependent fractions results in an average time constant of 26 ± 7 ps for the depletion of $\text{C}_2\text{F}_4\text{I}$ transient structures (20 ± 5 ps) and formation of C_2F_4 molecules (31 ± 4 ps); the overall temporal resolution of the apparatus was explicitly included in the determination of these time constants. Given the available internal energy of the $\text{C}_2\text{F}_4\text{I}$ intermediate described above, this temporal behavior is entirely consistent with a barrier crossing process, as is the percentage of $\text{C}_2\text{F}_4\text{I}$ radicals undergoing further dissociation to form C_2F_4 ($55 \pm 5\%$).

C. Structural Change, Intermediate to Product: The $\text{C}_2\text{F}_4\text{I} \rightarrow \text{C}_2\text{F}_4 + \text{I}$ Process. As shown in the previous section, any reaction involving the parent molecules is complete within the first 5 ps. Thus, in order to highlight the structural changes of the reaction intermediate and product

only—with no contribution from any other species present—we generated a set of additional diffraction-difference curves with $t_{\text{ref}} = 5$ ps. Figure 5–6(a) shows raw difference curves [$\Delta R^E(t; 5 \text{ ps}; s)$] and the corresponding residual background curves [$\Delta R_B^E(t; 5 \text{ ps}; s)$]. The $\Delta sM^E(t; 5 \text{ ps}; s)$ curves, created in part by subtracting the baseline curves obtained for each time point, are shown in Fig. 5–6(b). As before, this difference procedure removes most of the background signal.

Figure 5–6(c) shows the corresponding difference radial distribution curves, $\Delta f^E(t; 5 \text{ ps}; r)$. The $\Delta f(t; 5 \text{ ps}; r)$ signals arise only from the transient $\text{C}_2\text{F}_4\text{I}$ and final product C_2F_4 species, with the depletion of the $\text{C}_2\text{F}_4\text{I}$ radical being evident at C–I, C·I, and F·I separations; note that the populations of other internuclear separations (e.g. C–F, C–C, and F·F) are essentially unchanged and make no contribution to the $\Delta sM^E(t; 5 \text{ ps}; s)$ or $\Delta f^E(t; 5 \text{ ps}; r)$ signals. The absence of an I·I component ($\sim 5.1 \text{ \AA}$) in the $\Delta f^E(t; 5 \text{ ps}; r)$ curves clearly shows that we are observing solely the population change of the transient $\text{C}_2\text{F}_4\text{I}$ structures forming C_2F_4 , and that the contribution from the unreacted $\text{C}_2\text{F}_4\text{I}_2$ population is negligible. Theoretical $\Delta sM^T(t; 5 \text{ ps}; s)$ and $\Delta f^T(t; 5 \text{ ps}; s)$ curves (red curves in Figs. 5–6(b) and 5–6(c)) were obtained by a single-parameter fit (the fraction of C_2F_4 species) of the experimental $\Delta sM^E(t; 5 \text{ ps}; s)$ curves according to Eqn. 5–3:

$$\Delta sM(t; 5 \text{ ps}; s) = -|\Delta p_{C_2F_4I}| \cdot sM(s)_{C_2F_4I} + |\Delta p_{C_2F_4}| \cdot sM(s)_{C_2F_4} \quad (5-3)$$

with

$$\Delta p_{C_2F_4} = -\Delta p_{C_2F_4I} \quad (5-4)$$

The time-dependent fraction of C_2F_4 formed after 5 ps, shown in Fig. 5-7, yields a time constant of 25 ± 7 ps, in total agreement with the above analysis of the $\Delta f(t; -95 \text{ ps}; r)$ curves.

D. Structure of the C_2F_4I Radical Intermediate. The molecular structure of the C_2F_4I radical intermediate was determined from the diffraction-difference curves $\Delta sM(t; 5 \text{ ps}; s)$; both bridged and classical C_2F_4I structures were considered in the fitting of the diffraction data. The symmetrically bridged structure has C_{2v} symmetry, whereas the *anti* and *gauche* conformers of the classical structure have C_s and C_1 symmetry, respectively. The $\Delta R^E(t; 5 \text{ ps}; s)$ difference curves from $t = +40$ ps to +405 ps were averaged (prior to Fourier filtering) to improve the precision of the fits. No significant changes in the structure of the radical are expected (or were observed) over this temporal range, as the internal energy of the radical should already be nearly equilibrated, and collisional cooling should not become important until well into the nanosecond regime under the present experimental conditions.

Prior to performing the time-averaged structural refinement for the $\text{C}_2\text{F}_4\text{I}$ radical, preliminary structural refinements were performed at each point in time in order to detect the presence of time-dependent structural changes within the $\text{C}_2\text{F}_4\text{I}$ species—manifested as far-from-equilibrium geometries¹³ in the early stages of the reaction. Most of the structural parameters showed little sign of temporal dependence, but the results for a few of the parameters were less conclusive. The C–I bond distance and $\angle\text{CCI}$ bond angle showed the greatest evidence for time-dependent changes at early time points (not shown), but further investigation is necessary before a definitive conclusion can be made; future UED studies with improved sensitivity, resolution, and analysis should be better able to determine the significance of far-from-equilibrium geometries in this reaction.

The signal, denoted $\Delta R^E(\infty; 5 \text{ ps}; s)$, was fit separately with starting structural parameters predicted from calculations for either the bridged species, or the 81:19 mixture of the classical (*anti* and *gauche*) species (the $\Delta R^E(\infty; 5 \text{ ps}; s)$ curve, along with the background curve obtained by fitting through the theoretical zero-crossing points, is shown in Fig. 5–4(c)). The results of this fitting procedure are contained in Fig. 5–8, where the experimental $\Delta sM^E(\infty; 5 \text{ ps}; s)$ and $\Delta f^E(\infty; 5 \text{ ps}; r)$ curves are shown along with the corresponding theoretical curves produced with the quantum chemical structures. As shown in Fig. 5–8, the theoretical curves for the mixture of

classical structures reproduce the experimental data extremely well, whereas the fit provided by the theoretical bridged structure is vastly inferior. Indeed, the $\Delta sM^E(\infty; 5 \text{ ps}; s)$ and $\Delta sM^T(\infty; 5 \text{ ps}; s)$ curves for the bridged structure in Fig. 5–8 clearly go out of phase, yielding manifestly different positions for the two prominent negative peaks in the corresponding $\Delta f^E(\infty; 5 \text{ ps}; r)$ and $\Delta f^T(\infty; 5 \text{ ps}; r)$ curves. Thus, we conclude that the structure of the $\text{C}_2\text{F}_4\text{I}$ radical intermediate is in fact classical in nature,¹ in general agreement with previous qualitative analysis from second-generation (UED-2) experiments.¹⁶

Significant improvements in sensitivity and resolution provided by the UED-3 apparatus permitted quantitative determination of the molecular structure of the $\text{C}_2\text{F}_4\text{I}$ radical from our experimental data, thereby allowing a direct comparison with quantum chemical calculations. A least-squares refinement of the $\Delta sM^E(\infty; 5 \text{ ps}; s)$ data was performed as follows. Reasonable assumptions were made to simplify the fit and reduce the number of adjustable parameters in the final structural refinement, as described below. Assuming a torsion angle of 180° , the *anti* conformer of the $\text{C}_2\text{F}_4\text{I}$ radical has 9 independent parameters—four covalent bond distances and five bond angles—when the structure is constrained to be geometrically consistent. The remaining (dependent) internuclear separations were obtained via trigonometric relations constructed in terms of the chosen independent parameters. The *gauche* conformer was treated similarly: it was described by

the same 9 independent parameters, but with values differing from those of the *anti* conformers by small constant amounts, as predicted by quantum chemical calculations.¹² For example, the calculations suggested that the C–I distance of the *gauche* conformer [$r(\text{C–I})_{gauche}$] would be less than that of the *anti* conformer by 0.015 Å; thus, $r(\text{C–I})_{gauche}$ was obtained by subtracting 0.015 Å from the refined value of $r(\text{C–I})_{anti}$. Again, following theoretical predictions, the primary dihedral angle of the *gauche* species was fixed at 56° as the dihedral angle was relatively insensitive in the fitting, partially due to the low amount of *gauche* structures present.

As before, the *anti:gauche* radical conformer ratio was held fixed at 81:19. The values for the mean amplitudes of vibration (l) and centrifugal distortion corrections (dr) for each atom–atom pair were calculated using the ASYM40 program developed by Hedberg and co-workers¹⁷ (assuming a thermal distribution of the internal energy within the C₂F₄I radical). These values were then entered into the structural refinement of the (geometrically consistent) internuclear distances (at the potential minima, r_e) and the bond angles using the relation $r_a \approx r_e + (3/2)al^2 + dr - l^2/r$, where r_a is the internuclear distance as measured by electron diffraction and a is the anharmonicity constant for the bond. The independent structural parameters obtained from the least-squares fit of the experimental data could then be compared to quantum chemical calculations.

The results of the least-squares structural refinement are shown in Fig. 5–9, and the values determined for the independent structural parameters are summarized in Table 5–1. The $r_e(\text{C–I})$ and $r_e(\text{C–C})$ distances of the $\text{C}_2\text{F}_4\text{I}$ radical are, respectively, longer and shorter than those of the parent molecule (for $\text{C}_2\text{F}_4\text{I}_2$, $r_e(\text{C–I}) \approx 2.136 \text{ \AA}$, $r_e(\text{C–C}) \approx 1.534 \text{ \AA}$),¹¹ while the $\text{C–F}'$ internuclear distance in the radical site ($-\text{CF}'_2$) is shorter than that of the $-\text{CF}_2\text{I}$ site. Moreover, the $\angle\text{CCF}'$ and $\angle\text{F}'\text{CF}'$ angles become larger than the corresponding angles of the parent (by $\sim 9^\circ$ and $\sim 12^\circ$, respectively¹¹), suggesting that the radical center ($-\text{CF}'_2$) of the $\text{C}_2\text{F}_4\text{I}$ intermediate relaxes following loss of the first I atom (naturally, a similar comparison may be drawn between these $\angle\text{CCF}'$ and $\angle\text{F}'\text{CF}'$ angles and the $\angle\text{CCF}$ and $\angle\text{FCF}$ angles on the other side of the radical). These results are consistent with the increased C–C bond order expected from the formation of the transient $\text{C}_2\text{F}_4\text{I}$ structure (Fig. 5–10). These trends were also well-reproduced by the quantum chemical calculations; indeed, the refined internuclear distances reported in Table 5–1 agree with the corresponding theoretical predictions to within 0.03 \AA .¹²

It is interesting to compare the molecular structure of the $\text{C}_2\text{F}_4\text{I}$ radical with that of the $\text{C}_2\text{H}_4\text{I}$ radical, and to consider the stereochemical implications for these intermediate species. However, while the geometry of the $\text{C}_2\text{F}_4\text{I}$ radical has now been studied with UED,^{1, 16} to date only quantum

chemical investigations of the C_2H_4I radical geometry have been performed (the high thermal instability of the $C_2H_4I_2$ parent molecule makes this substance notoriously difficult to work with in experimental studies). Quantum chemical structures of the C_2F_4I radical and the C_2H_4I radical, along with the corresponding energy contour maps, were calculated for both structures.^{8, 12} The energy contour maps, calculated using density functional theory (DFT) methods (B3PW91,^{18, 19} with the LAV3P basis set), were generated by optimizing the molecular geometry as a function of the position of the primary halogen atom (I); in both calculations, the position of the I atom was constrained to lie in the ICC plane bisecting the $\angle RCR$ angles (with $R=H$ or F). The dramatic difference between the C_2F_4I and C_2H_4I radical geometries in these calculations originated from the lower π electron density of the C_2F_4 moiety compared to that of the C_2H_4 moiety (due to electron withdrawal by the electronegative F atoms), which in turn affects the interaction between the p orbital of the primary halogen atom (I) and the π orbital of the $C-C$ bond in the bridged structure.

Recent theoretical investigations^{8,12} generalized this structural comparison to include a variety of CR_2XCR_2 -type radicals, where R represents either H or F , and X refers to the heavy halides (Cl , Br , and I). These calculations predicted that when $R=F$, then the most energetically stable radical structure is classical (with *anti* conformers always more stable

than *gauche* conformers); indeed, no minimum-energy structures with bridged geometries could be found for these species without at least one imaginary frequency (with the exception of CF_2ClCF_2 at the Hartree–Fock level). However, varying results were obtained with $\text{R}=\text{H}$: when $\text{X}=\text{I}$, then the most stable structure is predicted to be bridged; when $\text{X}=\text{Cl}$, the most stable structure is classical; and when $\text{X}=\text{Br}$, the result depends on the computational method used—B3PW91 DFT calculations using the LAV3P basis set predicted that the most stable structure would be bridged, but the same calculation using the LAV3P(d) basis set (which has an additional d orbital for the X atom) predicted a classical geometry for the global minimum (consistent with the results of a MRD-CI calculation performed elsewhere²⁰).

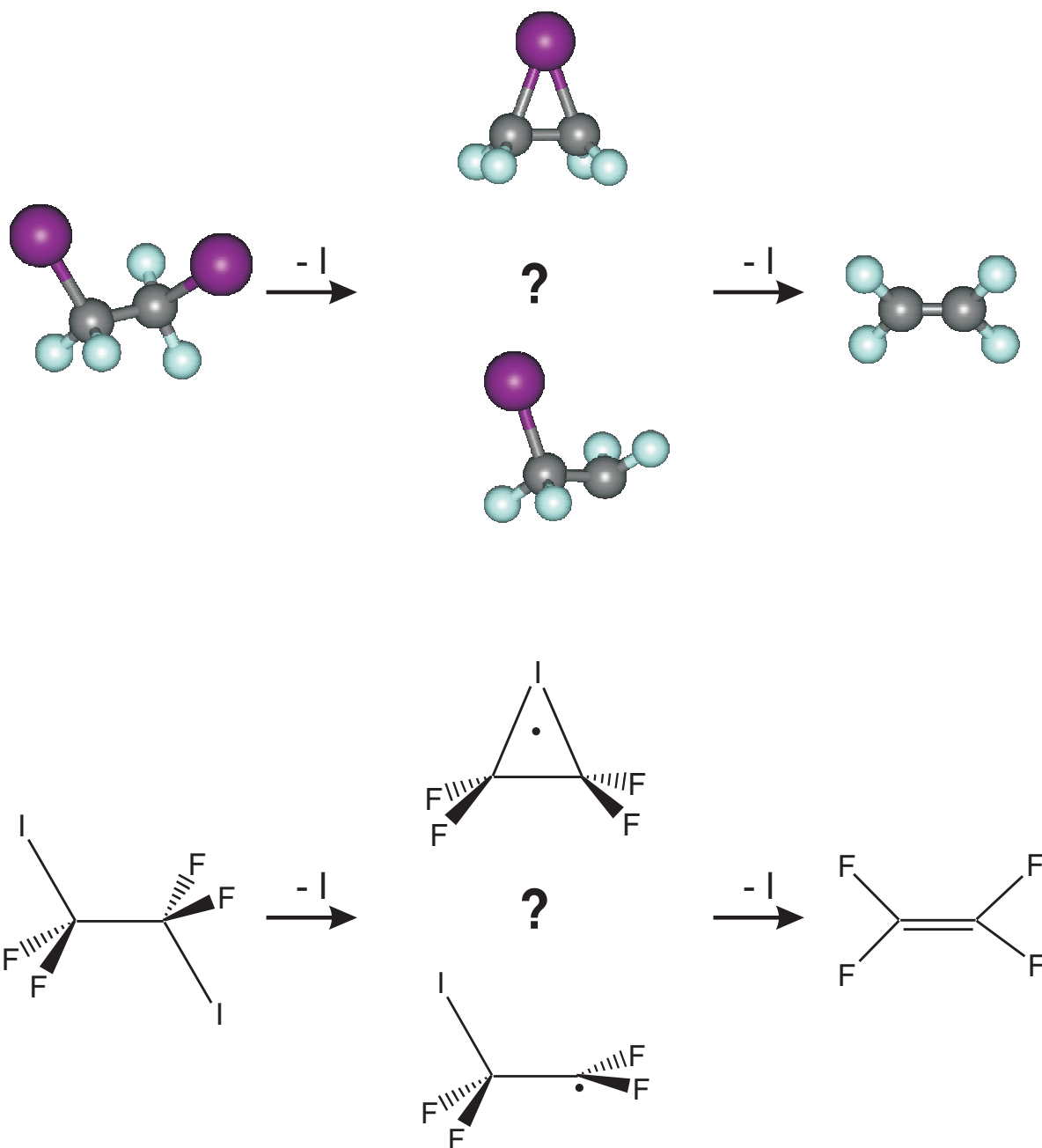
Much of the interest in the molecular structures of CR_2XCR_2 -type radicals lies in the relevance of structure and dynamics to the stereochemistry of reactions involving these transient species. For example, consider the generalized two-step elimination of 2X from $\text{C}_2\text{R}_4\text{X}_2$ giving C_2R_4 , shown schematically in Scheme 5–2. A number of $\text{C}_2\text{R}_4\text{X}$ intermediate structures could, in principle, be involved in the reaction, with different implications for the stereochemical control of the reaction with regard to the final positions of the $-\text{R}$ groups about the $\text{C}=\text{C}$ bond in the C_2R_4 product. The formation of a bridged $\text{C}_2\text{R}_4\text{X}$ structure prevents rotation about the $\text{C}-\text{C}$ bond, thereby ensuring stereochemical control in accordance with the Skell

hypothesis⁹ (a similar result would be obtained if the X atom were rapidly “shuttled” between the two $-\text{CR}_2$ moieties¹⁰). Alternatively, a classical structure could be formed, with either a “pyramidal” radical center (predicted for $\text{R}=\text{F}$ ¹²) or a nearly planar radical center (predicted for $\text{R}=\text{H}$ ¹²). Because rotation about the C–C bond is unhindered in classical structures, one might predict (contrapositively to the Skell hypothesis) that reactions involving $\text{C}_2\text{R}_4\text{X}$ radical intermediates that lack bridged geometries would *not* maintain stereochemical control (for nearly planar radical centers ($\text{R}=\text{H}$), the final positions of $-\text{R}_3$ and $-\text{R}_4$ could be scrambled through simple rotation about the C–C bond, whereas in species with $\text{R}=\text{F}$ the non-planar nature of the $-\text{CF}_2$ moiety might require some combination of rotation and inversion due to the high energy required to reach the “eclipsed” rotational transition state¹²).

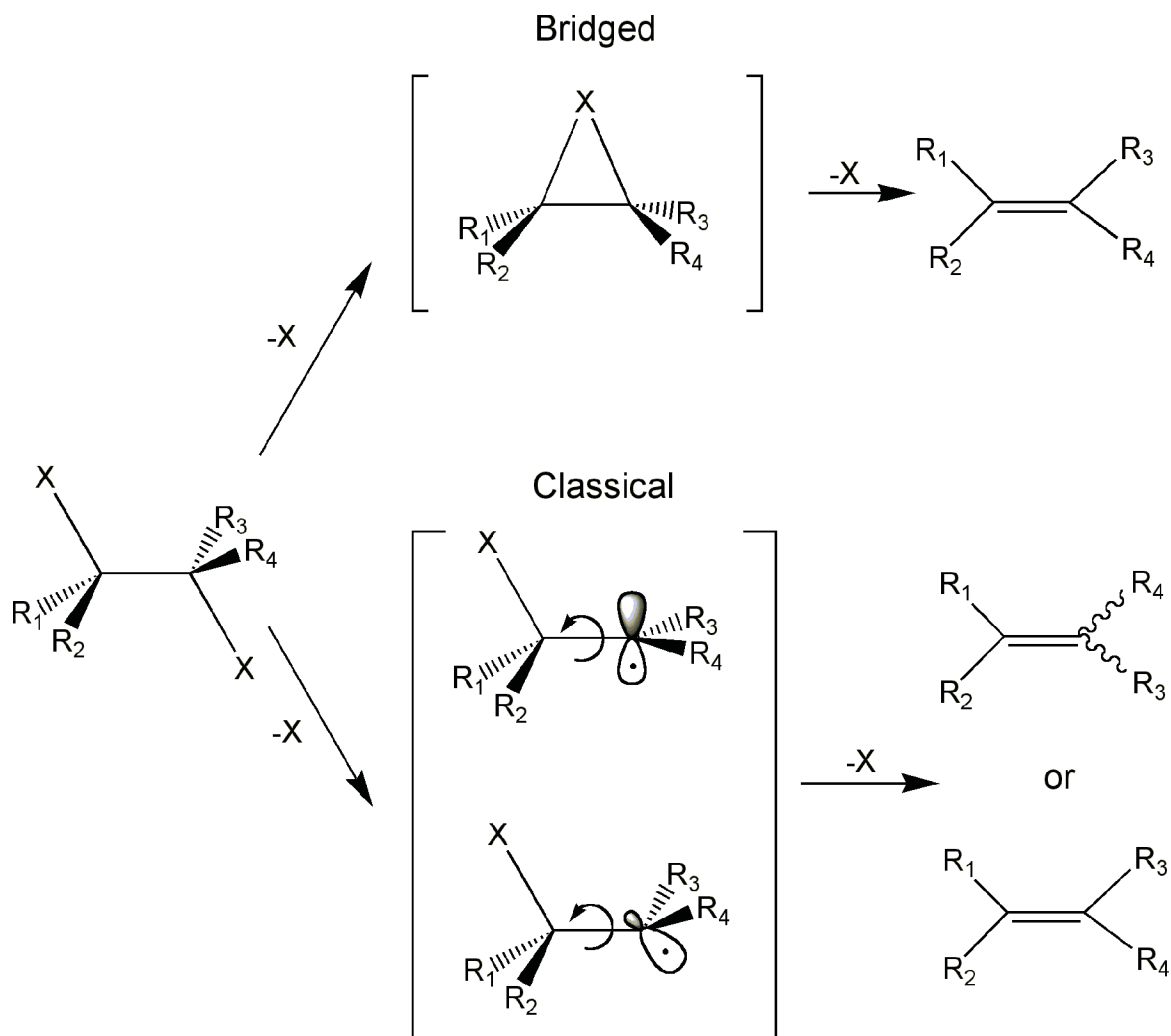
However, it should be considered that dynamical effects may also play a role in the retention of stereochemistry in such reactions; if the time for the second C–X bond breakage is shorter than that of rotation around the C–C bond, stereochemistry will be retained even in reactions involving classical $\text{C}_2\text{R}_4\text{X}$ structures. Future studies on other $\text{C}_2\text{R}_4\text{X}$ species may shine new light on the respective roles of structure and dynamics in determining the stereochemical nature of the products formed by various reactions.

5.4 Conclusions

In summary, significant improvements in instrumentation provided by our third generation apparatus now permit UED to study structural dynamics in chemical reactions with unprecedented temporal and spatial resolution. These experimental advances have been accompanied by improvements in data processing and use of the diffraction-difference analysis, which were described here in detail. These advances were borne out in the first application of the new apparatus—the study of the non-concerted elimination of iodine from $C_2F_4I_2$. The structural changes occurring over the course of the reaction were followed with temporal resolution of ~ 5 ps, with spatial resolution approaching 0.01 \AA , and with sensitivity to chemical change of $\sim 1\%$. The high sensitivity and spatiotemporal resolution permitted the molecular structure of the transient intermediate C_2F_4I to be determined and refined: the radical is classical, not bridged, in nature—in quantitative agreement with quantum chemical predictions to within 0.03 \AA . In the future, additional UED studies of other C_2R_4X intermediates and related species should provide considerable insight into the respective roles of structure and dynamics in stereochemical control.



Scheme 5-1. Non-concerted elimination reaction of $C_2F_4I_2$ with the hitherto unknown reaction intermediate.



Scheme 5-2. Schematic of dihalide elimination reactions involving C_2R_4X radical intermediates. Once the parent molecule $C_2R_4X_2$ loses the first X atom, the intermediate species C_2R_4X is formed. In the case of a bridged intermediate structure (top brackets), the retention of stereochemical selectivity is derived from the inhibition of rotation about the C-C bond (top product). However, in the case of the classical structure (bottom brackets), the situation is more complex. Rotation about the C-C bond is allowed; if the time scale for the elimination of the second -X atom is much faster than the rotation, one can expect stereochemical selectivity (bottom product), whereas stereochemical control would be lost if the situation were reversed (middle product). With regard to the geometry of the radical site in the classical structure, simple rotation about the C-C bond (prior to the loss of the second X atom) would suffice for the loss of stereochemical control for structures with planar radical centers (middle intermediate), whereas species with non-planar radical centers (bottom intermediate) may require a combination of rotation and inversion.

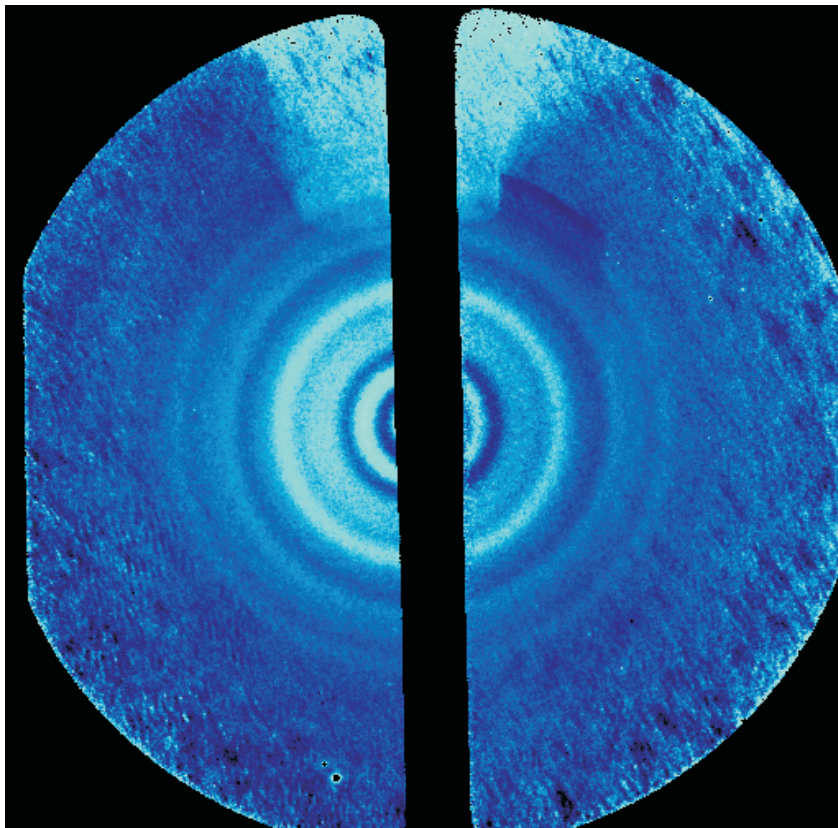


Figure 5-1. Ground-state molecular diffraction image of $C_2F_4I_2$.

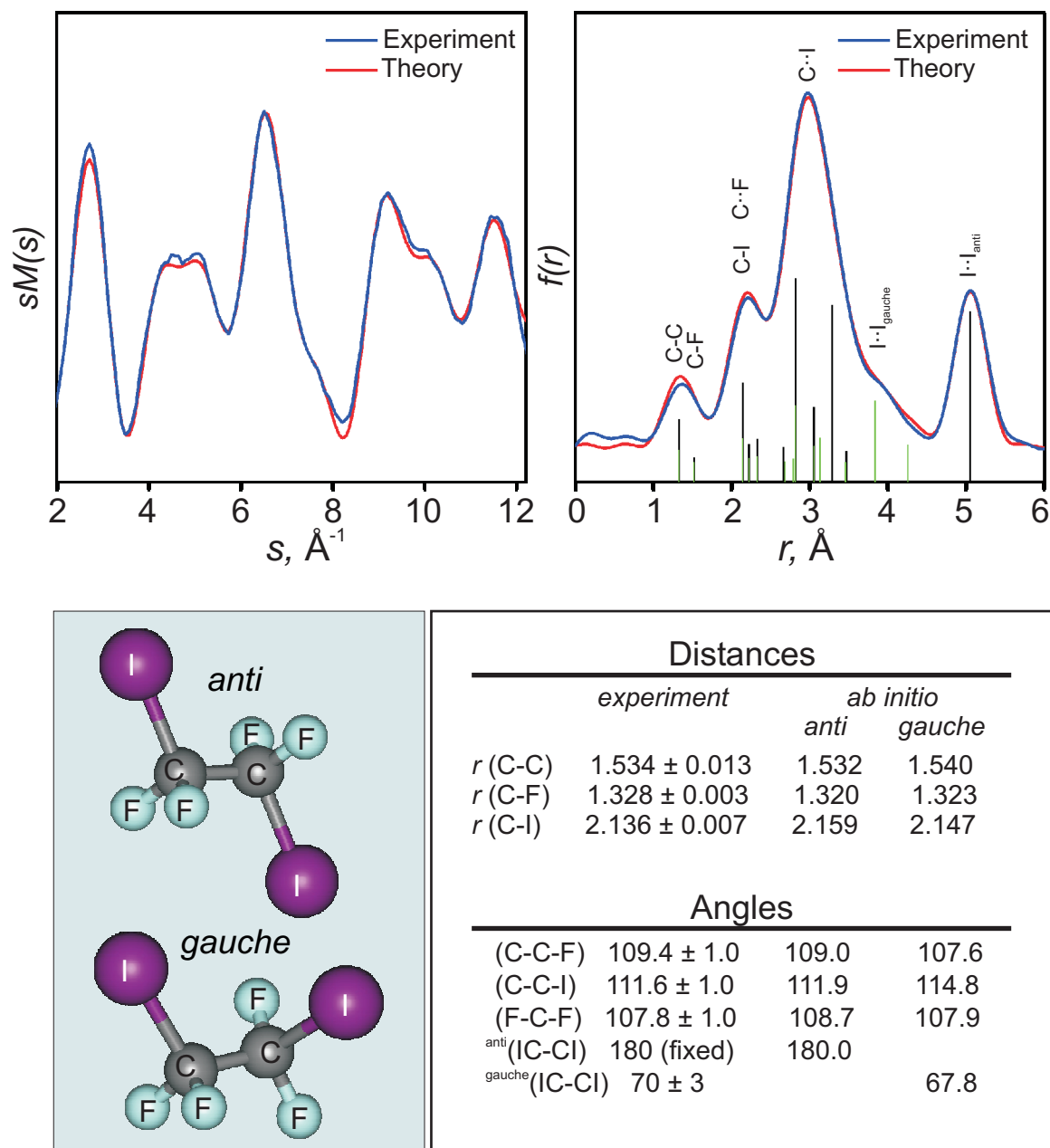
Molecular Structure of $C_2F_4I_2$ 

Figure 5-2. Refined ground-state structure of $C_2F_4I_2$. The comparison between the experimental and refined theoretical $sM(s)$ and $f(r)$ curves is shown, along with the determined bond distances and angles for the *anti* and *gauche* conformers. Distances are in ångströms, and angles are in degrees. The bond distances for the *anti* (black) and *gauche* (green) isomers are indicated by vertical lines at the bottom of the $f(r)$ panel.

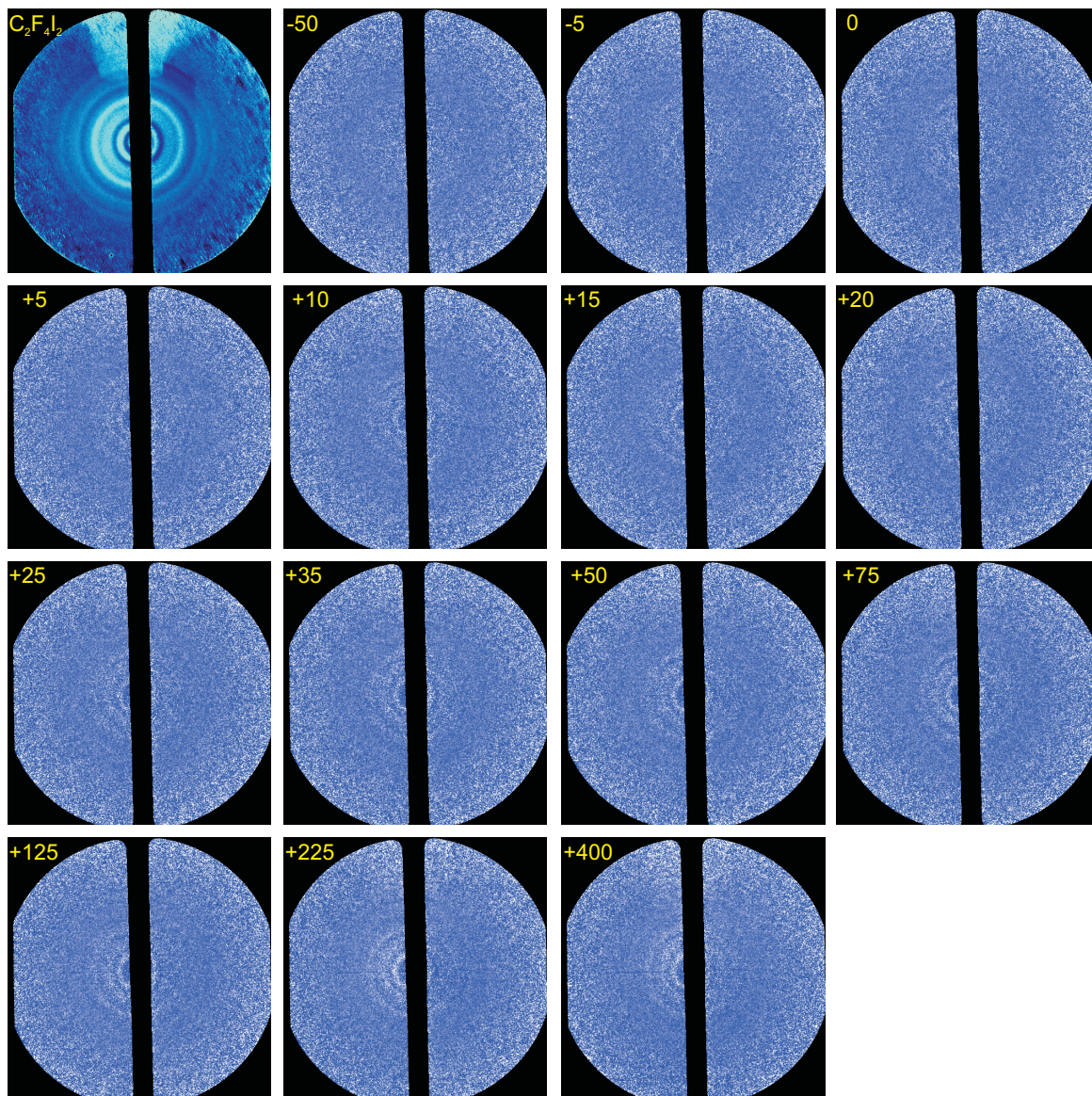


Figure 5-3. Time-resolved 2D diffraction-difference images of $C_2F_4I_2$ ($t_{\text{ref}} = -100$ ps). Each frame is identified by the relative time delay (in picoseconds) between the laser pump and electron probe pulses. The emergence of rings in the difference images with increasing time delay reflects the ensuing molecular structural dynamics. The first image is the ground-state image.

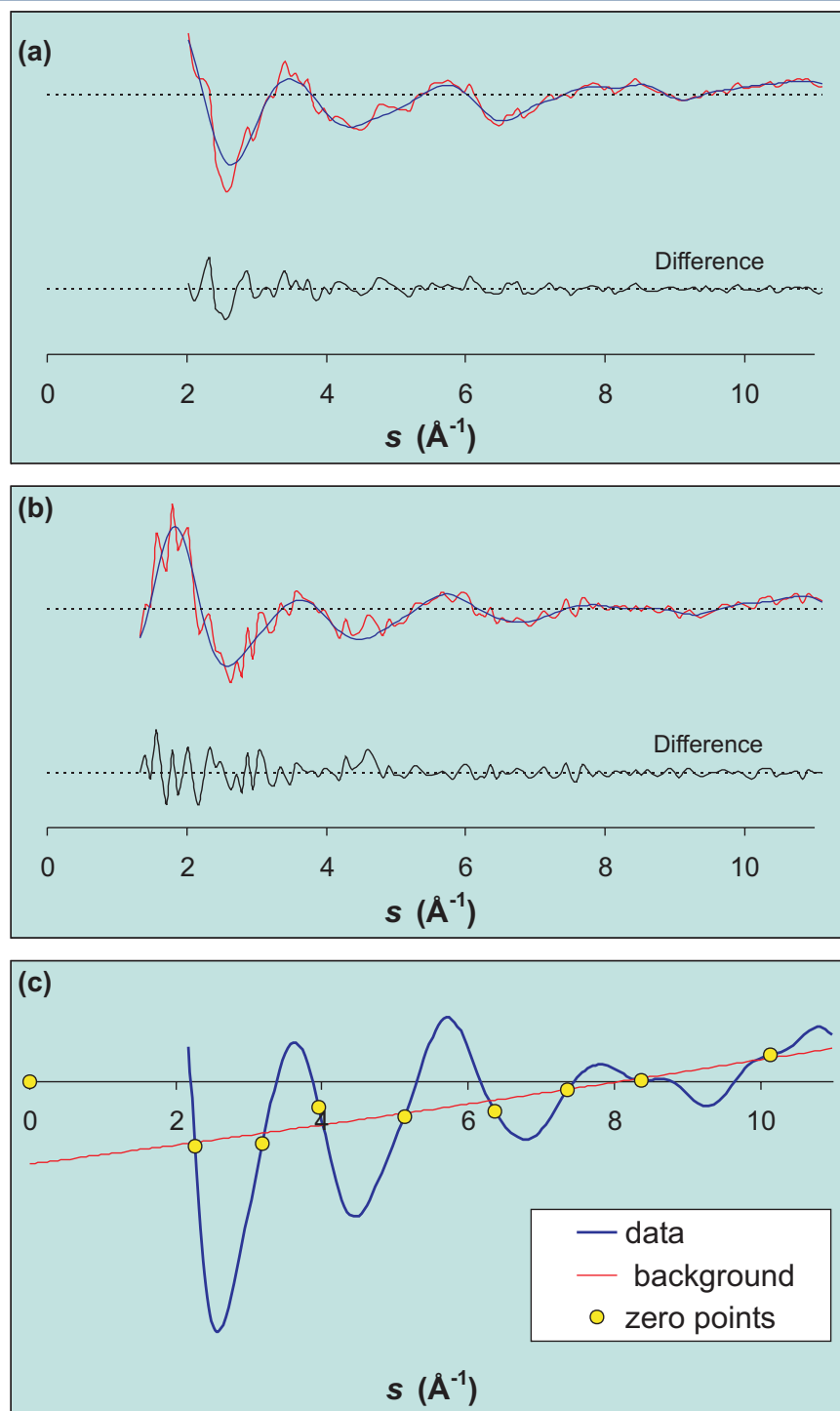


Figure 5-4. (a,b) The effect of Fourier filtering on 1-D raw diffraction-difference curves. The raw data is shown in red, and the Fourier filtered data (obtained with a 8.7-\AA low-pass filter) is shown in blue. The difference between the raw and filtered data shows the noise removed by the filter. (a) $R^E(405 \text{ ps}; -95 \text{ ps}; s)$. (b) $R^E(\infty \text{ ps}; 5 \text{ ps}; s)$. (c) Background fitting through the zero-crossing points of the experimental $R^E(\infty \text{ ps}; 5 \text{ ps}; s)$ data. The experimental $R^E(\infty \text{ ps}; 5 \text{ ps}; s)$ is shown in blue, and the background $R^E_B(\infty \text{ ps}; 5 \text{ ps}; s)$, obtained by fitting a low-order polynomial through the zero-crossing points (yellow circles), is shown in red.

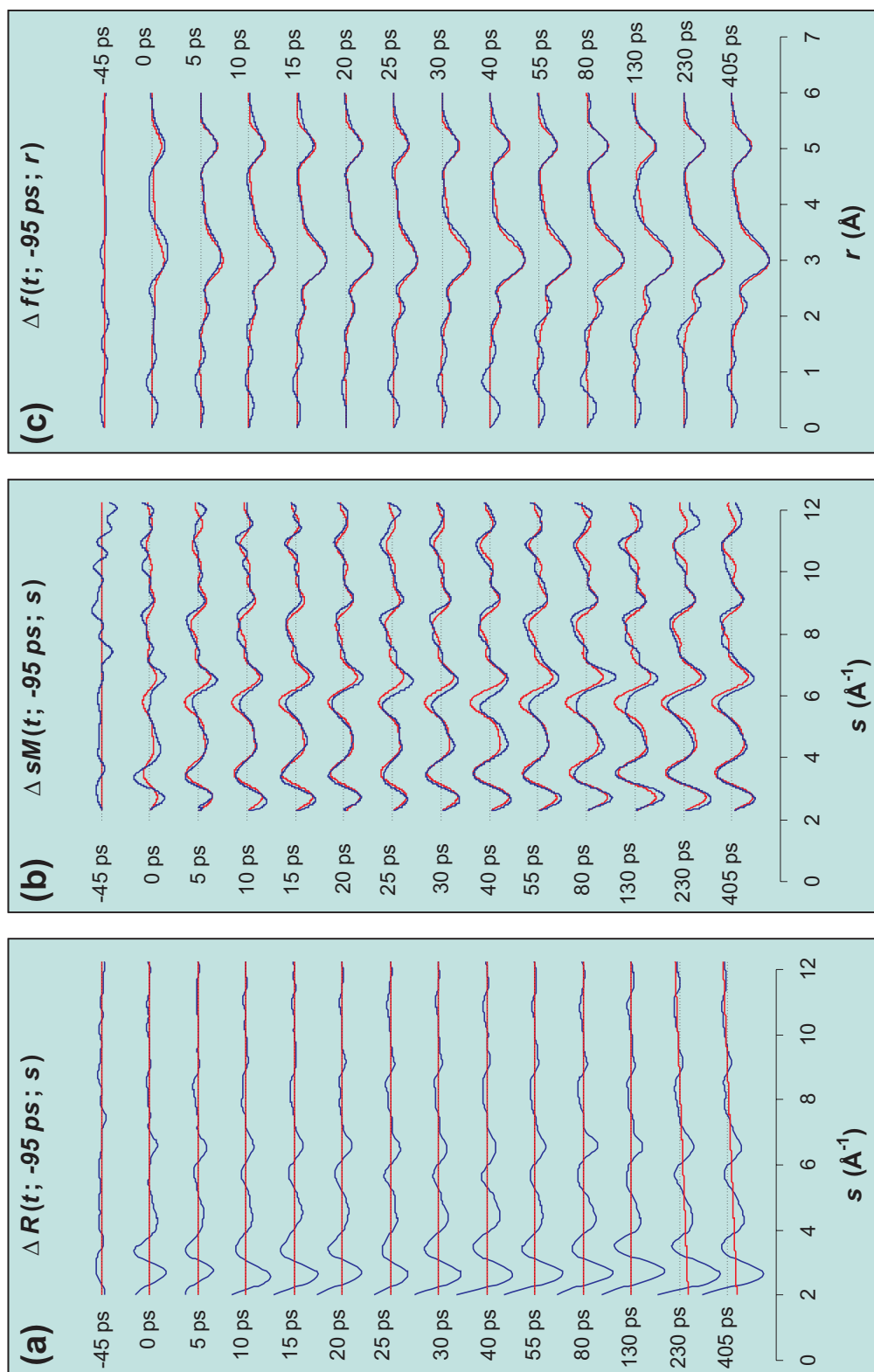


Figure 5-5. Time-resolved structural changes from the elimination of iodine from $\text{C}_2\text{F}_4\text{I}_2$. (a) Raw diffraction-difference signals, $R(t; -95 \text{ ps}; s)$, (blue curves), shown with the baseline curves (red). (b) Experimental (blue) and theoretical (red) $sM(t; -95 \text{ ps}; s)$ curves obtained at varying time delays. (c) Corresponding experimental (blue) and theoretical (red) $f(t; -95 \text{ ps}; r)$ curves. Major peaks are highlighted with arrows.

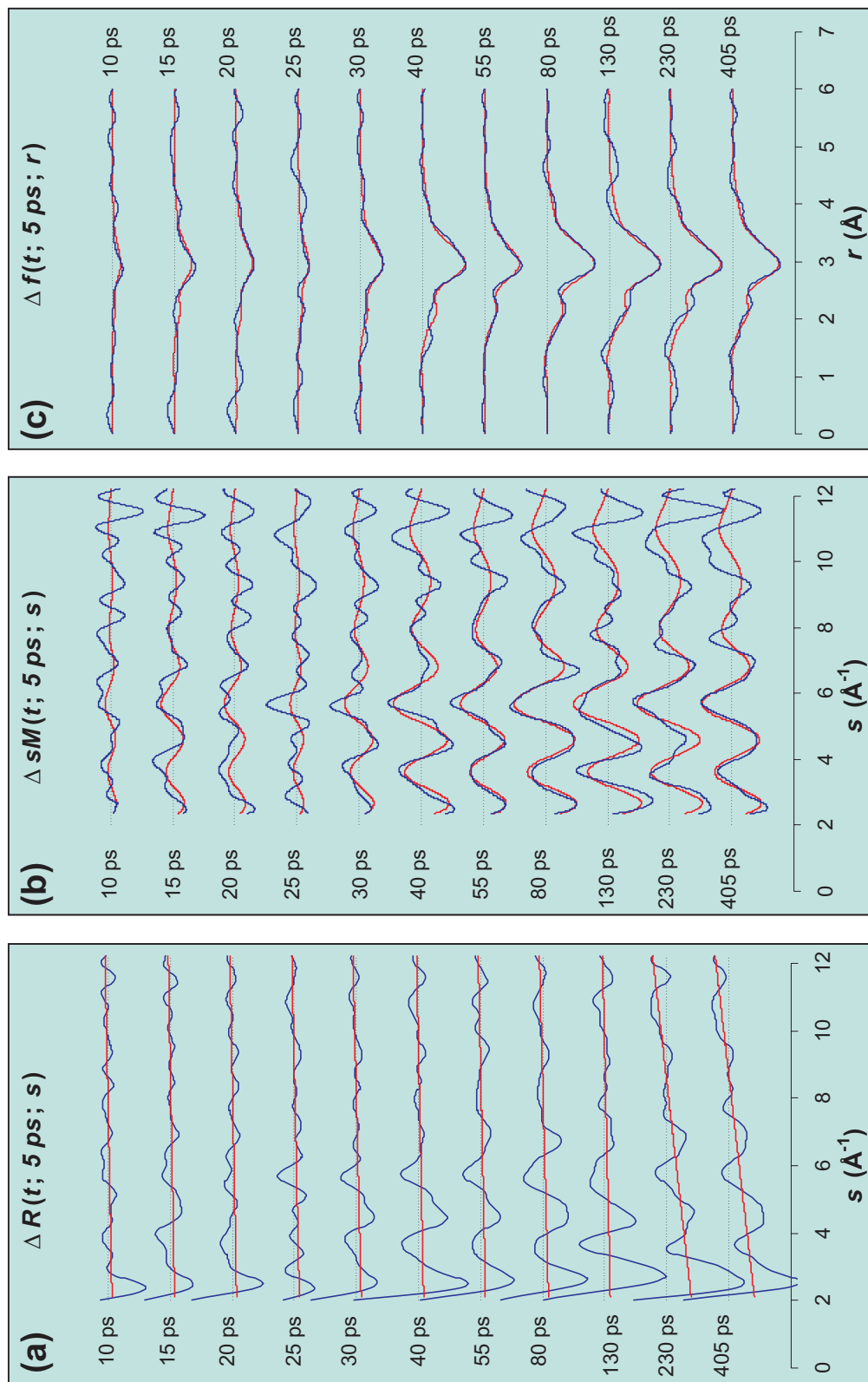


Figure 5-6. Time-resolved structural changes involving only the $\text{C}_2\text{F}_4\text{I} \rightarrow \text{C}_2\text{F}_4 + \text{I}$ contribution to the diffraction-difference signal. (a) Raw diffraction-difference signals, $R(t; 5 \text{ ps}; s)$, (blue curves), shown with the (nearly linear) baseline curves (red). (b) Experimental (blue) and theoretical (red) $sM(t; 5 \text{ ps}; s)$ curves obtained at varying time delays. (c) Corresponding experimental (blue) and theoretical (red) $f(t; 5 \text{ ps}; r)$ curves. Note the absence of a peak at $\sim 5.1 \text{ \AA}^{-1}$ corresponding to the depletion of $\text{I} \cdots \text{I}$ internuclear distances.

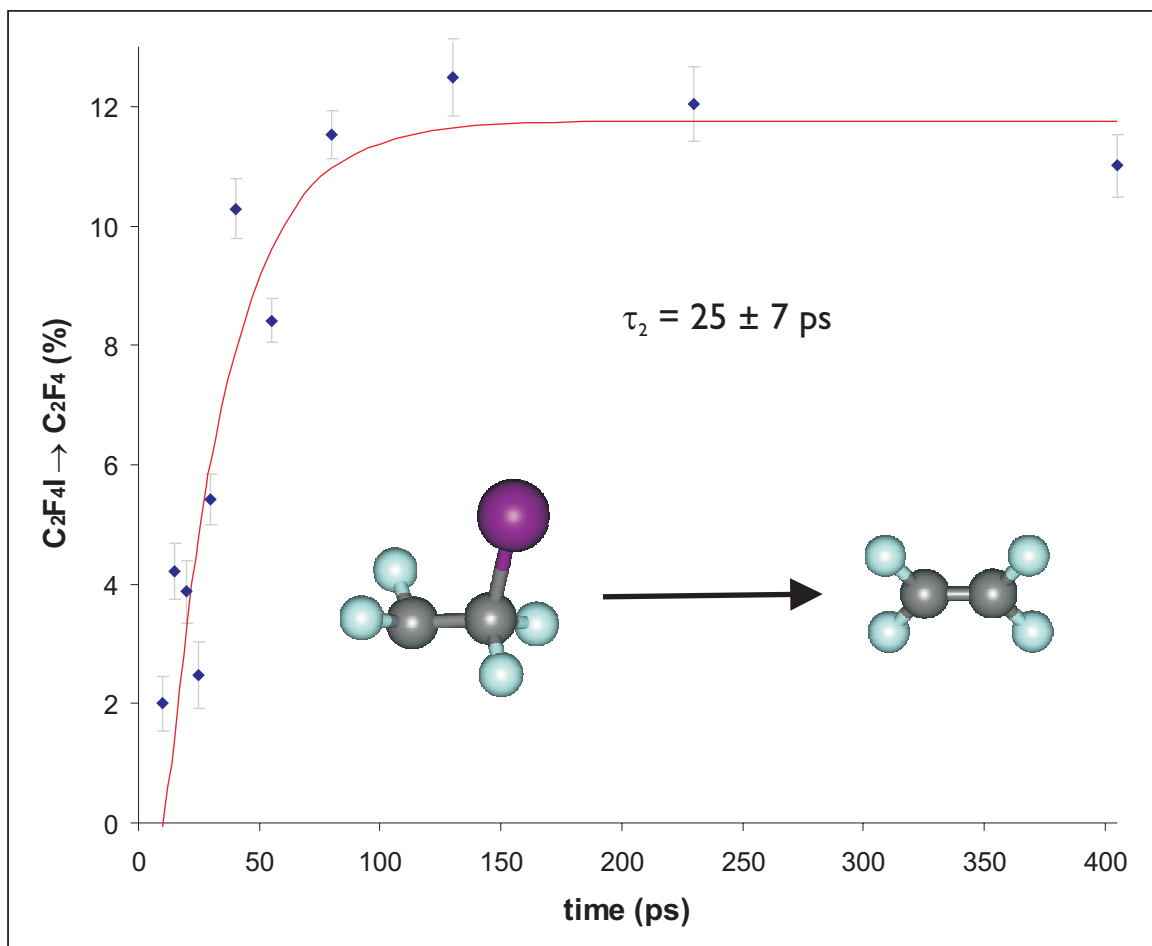


Figure 5-7. Time dependence of the formation of C_2F_4 molecules from the decay of C_2F_4I transient structures in the $sM(t; 5$ ps; s) data. The curve is an exponential fit of the C_2F_4 fraction (with the temporal pulse widths of the electron and laser pulses taken into account); the apparent time constant for the formation of C_2F_4 was of 25 ± 7 ps. Each error bar represents one standard deviation.

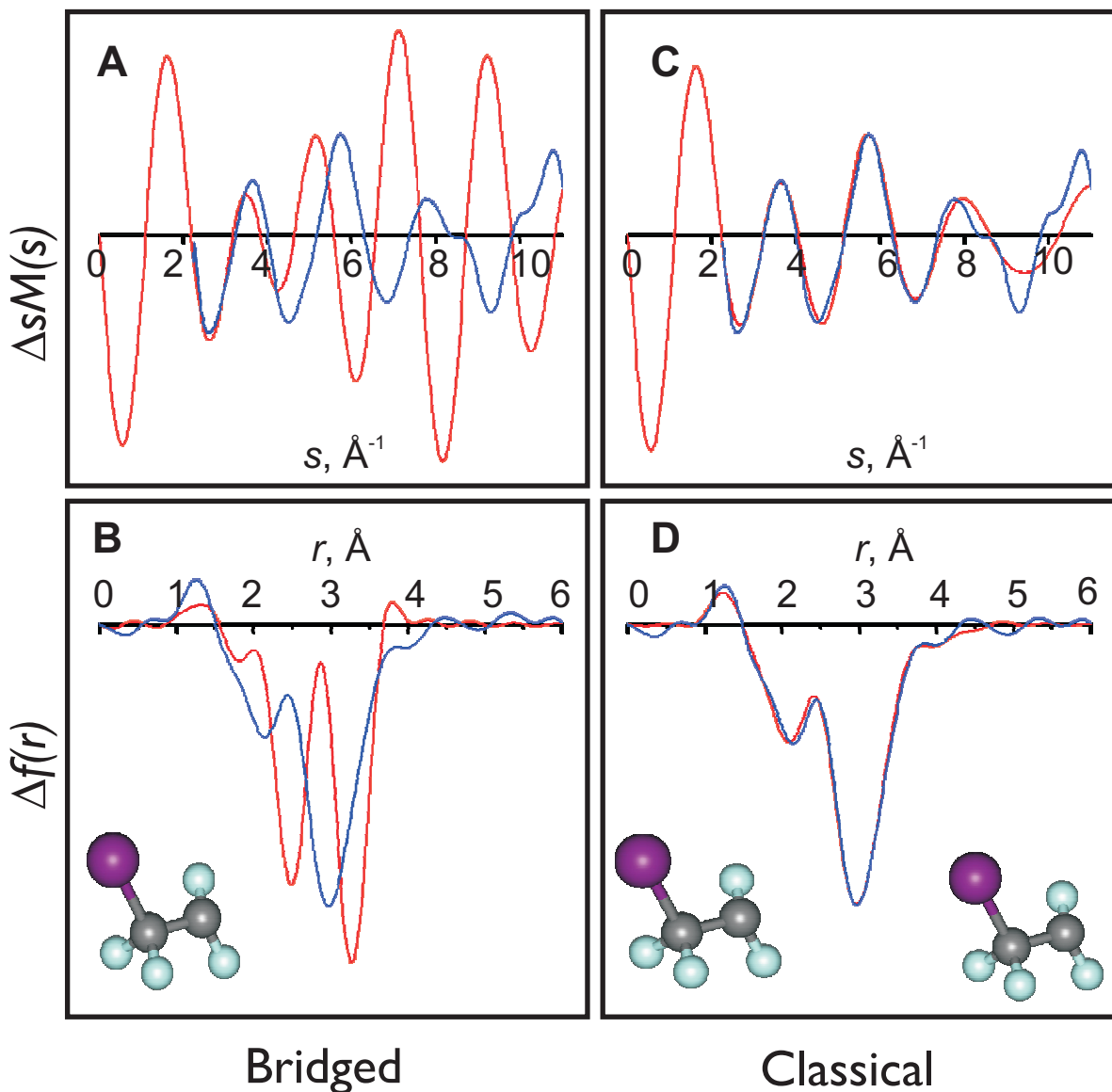
Structure of C_2F_4I Transient Intermediate

Figure 5-8. Structural determination of the transient C_2F_4I intermediate. **(A, B)** Comparison of experimental $sM(\infty; 5 \text{ ps}; s)$ and $f(\infty; 5 \text{ ps}; r)$ curves (blue) with corresponding theoretical curves (red) obtained via *ab initio* calculations of the bridged structure for C_2F_4I . **(C, D)** Comparison of experimental $sM(\infty; 5 \text{ ps}; s)$ and $f(\infty; 5 \text{ ps}; r)$ curves with theoretical curves obtained using the *ab initio* classical (*anti* and *gauche*) C_2F_4I structures.

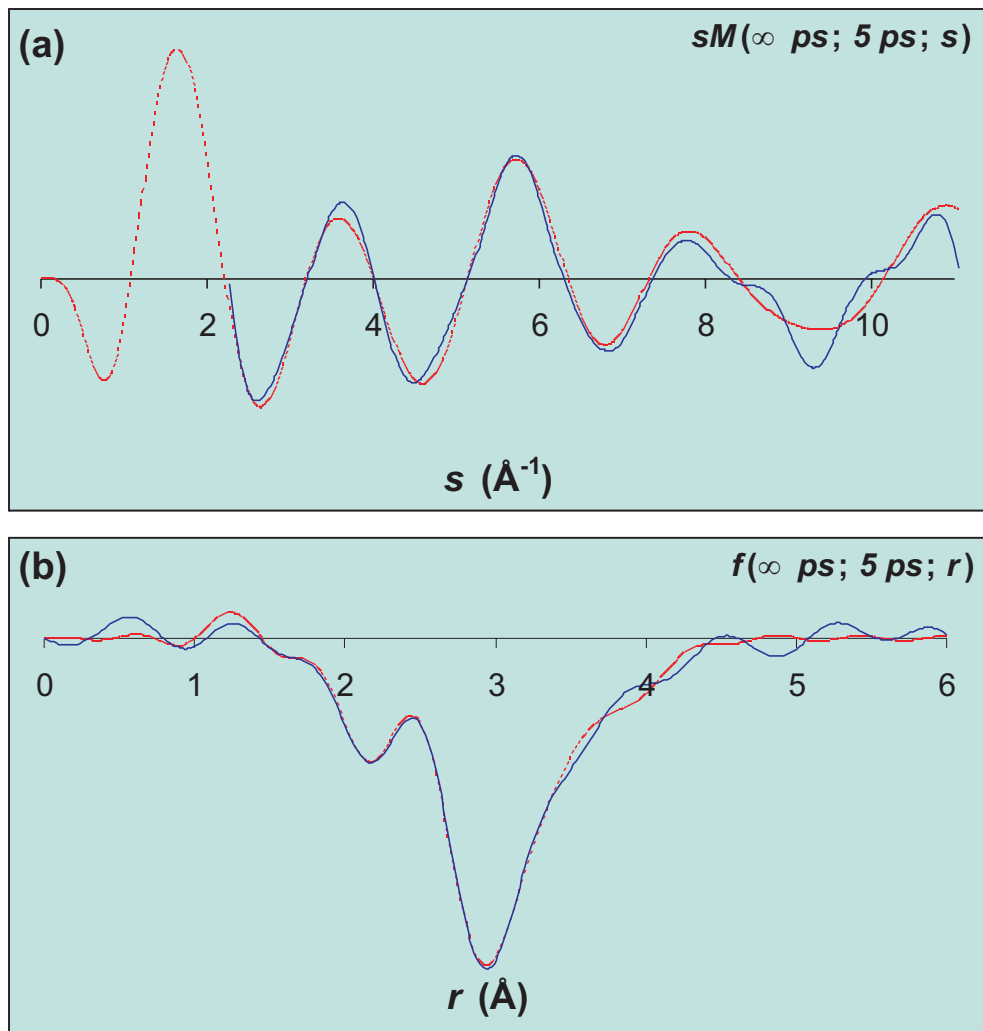


Figure 5-9. Refinement of the C_2F_4I radical structure. (a,b) Comparison of experimental $sM(5 \text{ ps}; s)$ (a) and $f(5 \text{ ps}; r)$ (b) curves (blue) with corresponding theoretical curves (red) obtained from the least-squares refinement of the C_2F_4I structure (see text).

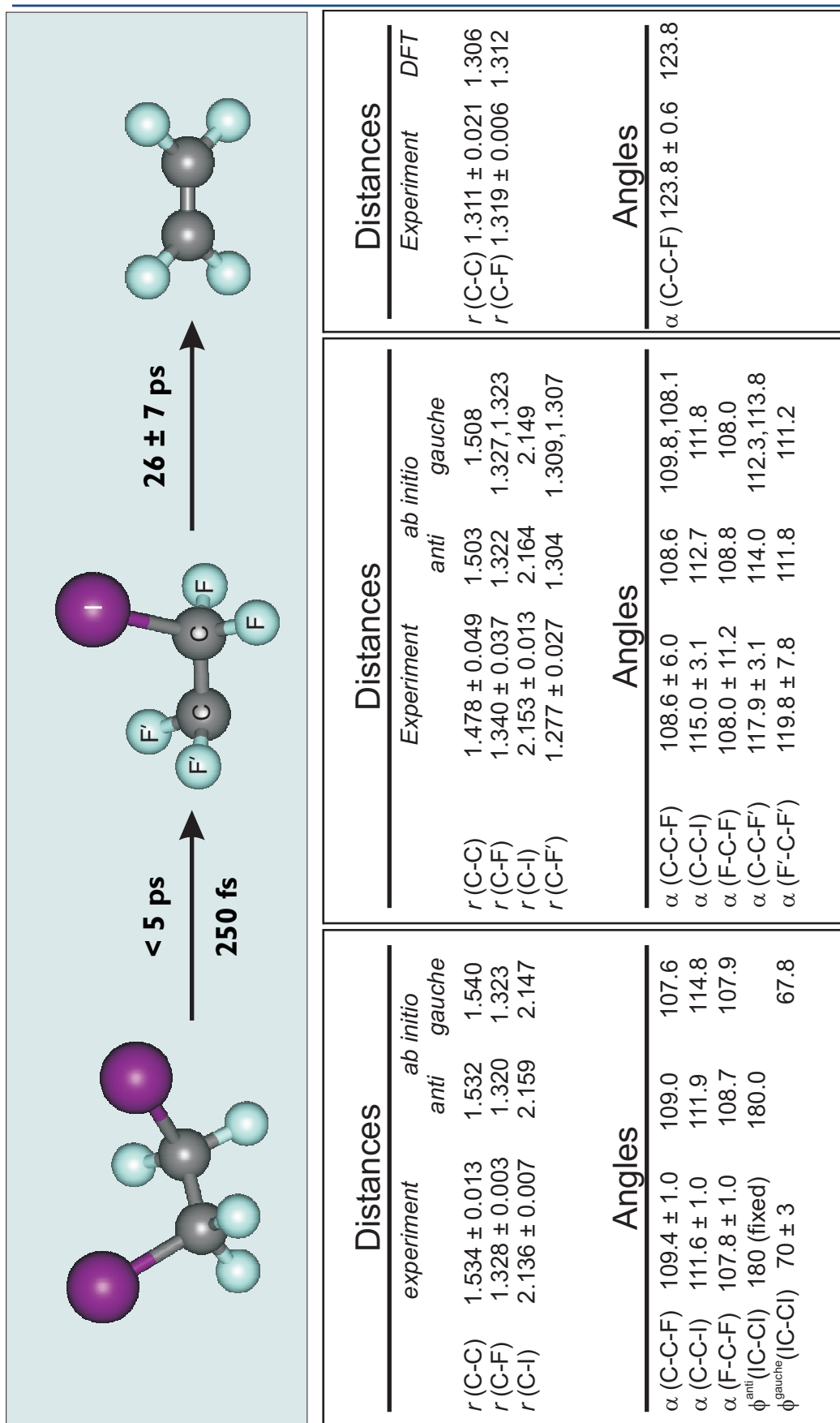
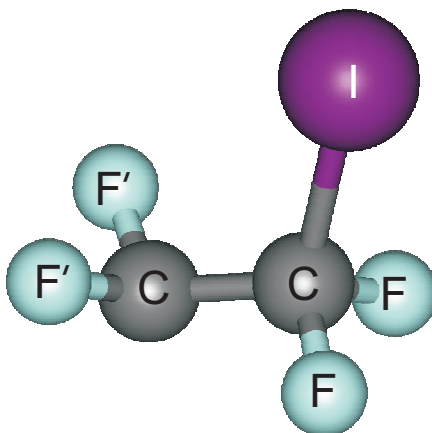


Figure 5-10. Complete structural determination of the $\text{C}_2\text{F}_4\text{I}_2$ elimination reaction. The bond distances and angles for all three species are shown, along with the DFT values for comparison. Distances are in ångströms, and angles are in degrees. Note that the C–C bond distance becomes progressively shorter from reactant through intermediate to product, thus reflecting the change in bond order from a single bond to a double bond. Also, note the change in bond angles of C_2F_4 which reflects relaxation of structure.



	Experiment	Predicted Values	
	<i>anti</i>	<i>anti</i>	<i>gauche</i>
$r(\text{C}=\text{C})$	1.478 ± 0.049	1.503	1.508
$r(\text{C}-\text{F})$	1.340 ± 0.037	1.322	1.327, 1.323
$r(\text{C}-\text{I})$	2.153 ± 0.013	2.164	2.149
$r(\text{C}-\text{F}')$	1.277 ± 0.027	1.304	1.309, 1.307
$\angle \text{CCI}$	115.0 ± 3.1	112.7	111.8
$\angle \text{CCF}$	108.6 ± 6.0	108.6	109.8, 108.1
$\angle \text{FCF}/2$	54.0 ± 5.6	54.4	54.0
$\angle \text{CCF}'$	117.9 ± 3.1	114.0	112.3, 113.8
$\angle \text{F}'\text{CF}'/2$	59.9 ± 3.9	55.9	55.6

Table 5-1. Comparison of the experimental values of the independent structural parameters of the classical $\text{C}_2\text{F}_4\text{I}$ radical intermediate with those obtained via quantum chemical calculations. The bond distances are in ångströms and the bond angles are in degrees.

References

1. Ihee, H.; Lobastov, V. A.; Gomez, U.; Goodson, B. M.; Srinivasan, R.; Ruan, C.-Y.; Zewail, A. H., *Science* **2001**, *291*, 458.
2. Khundkar, L. R.; Zewail, A. H., *J. Chem. Phys.* **1990**, *92*, 231.
3. Zhong, D.; Ahmad, S.; Zewail, A. H., *J. Am. Chem. Soc.* **1997**, *119*, 5978.
4. Kochi, J. K., *Free Radicals*. John Wiley & Sons: New York, 1973.
5. Beckwith, A. L. J.; Ingold, K. U., Free-Radical Rearrangements. In *Rearrangements in Ground and Excited States*, de Mayo, P., Ed. Academic Press: New York, 1980.
6. Kerr, J. A., *Handbook of Bimolecular and Termolecular Gas Reactions*. CRC Press: Boca Raton, 1981.
7. Fossey, J.; Lefort, D.; Sorba, J., *Free Radicals in Organic Chemistry*. John Wiley & Sons: New York, 1995.
8. Ihee, H.; Zewail, A. H.; Goddard III, W. A., *J. Phys. Chem. A* **1999**, *103*, 6638.
9. Skell, P. S.; Tuleen, D. L.; Radio, P. D., *J. Am. Chem. Soc.* **1963**, *85*, 2849.
10. Skell, P. S.; Traynham, J. G., *Acc. Chem. Res.* **1984**, *17*, 160.
11. Thomassen, H.; Samdal, S.; Hedberg, K., *J. Am. Chem. Soc.* **1992**, *114*, 2810.
12. Ihee, H.; Kua, J.; Goddard III, W. A.; Zewail, A. H., *J. Phys. Chem. A* **2001**, *105*, 3623.

-
13. Ruan, C. Y.; Lobastov, V. A.; Srinivasan, R.; Goodson, B. M.; Ihee, H.; Zewail, A. H., *Proc. Natl. Acad. Sci. USA* **2001**, *98*, 7117.
 14. Bernardi, F.; Bottoni, A.; Fossey, J.; Sorba, J., *J. Mol. Struct.* **1985**, *119*, 231.
 15. Carlos, J. L.; Karl, R. R. J.; Bauer, S. H., *J. Chem. Soc. Farad. Trans. II* **1973**, *70*, 177.
 16. Cao, J. M.; Ihee, H.; Zewail, A. H., *Proc. Natl. Acad. Sci. USA* **1999**, *96*, 338.
 17. Hedberg, L.; Mills, I. M., *J. Mol. Spectrosc.* **1993**, *160*, 117.
 18. Becke, A. D., *Phys. Rev. A* **1988**, *38*, 3098.
 19. Perdew, J. P.; Chevary, J. A.; Vosko, S. H.; Jackson, K. A.; Pederson, M. R.; Singh, D. J.; Fiolhais, C., *Phys. Rev. B* **1992**, *46*, 6671.
 20. Engels, B.; Peyerimhoff, S. D., *J. Mol. Struct.* **1986**, *138*, 59.

6

DARK STRUCTURES IN NONRADIATIVE PROCESSES

6.1 Introduction

Static and time-resolved spectroscopic investigations carried out with ever-increasing sophistication over the past six decades have largely shaped our current understanding of the complex interplay between radiative and nonradiative molecular processes across the chemical, physical, and biological sciences. The very nature of the light probe, however, obfuscates the detection of ‘dark’ *states* which have been frequently implicated but have never been *directly* observed. Utilizing ultrashort electron pulses as probes renders UED sensitive to *all structures*, and therein lies its unique potential to unravel the structural dynamics of photophysical and photochemical outcomes. This chapter showcases our UED studies of prototypical

heteroaromatic molecules (pyridine and its methylated analogues) with close-lying states in the excited state manifold.

Radiationless processes abound in a wide variety of chemical, physical, and biological systems yielding a rich diversity of phenomena. For example, the nature and dynamics of the excited electronic states created in nucleic acids by UV light influences the complex chain of events that culminates in DNA photodamage with profound biological consequences, including photocarcinogenesis. After light absorption, a molecule can undergo a number of different radiationless transitions, including photochemical processes such as fragmentation, isomerization and ionization, and photophysical processes such as internal conversion between electronic states of like multiplicity and spin-orbit-coupling-dependent intersystem crossing between dissimilar spin states. For more than eight decades, our understanding of such radiationless processes has been shaped by light-based tools used to interrogate them. The absence of light emission in such nonradiative phenomena has meant that information about the states involved has only been *indirectly* inferred from their influence on the more readily observed radiative and photochemical pathways (for example, through observations of the invariance of fluorescence spectra and fluorescence yields upon exciting successive upper singlet states, and on measurements of relative yields of phosphorescence to fluorescence). Moreover, such nonadiabatic phenomena occur at or near the breakdown of

the Born-Oppenheimer approximation, which has long been the cornerstone for the visualization of chemical processes. This breakdown is particularly common in complex polyatomic molecules, where there are a large number of energetically close-lying electronic states and many nuclear degrees of freedom. A particularly striking and important example of the result of the vibronic coupling between nuclei and electrons is a conical intersection between electronic states, which provide pathways for interstate crossing on ultrafast timescales.

Over the past nearly two decades, femtosecond time-resolved methods have been applied to chemical reactions ranging in complexity from bond-breaking in diatomic molecules to dynamics in supramolecular and biological molecules and have led to breakthroughs in our understanding of fundamental chemical processes. The information obtained from these experiments, however, is very much dependent on the nature of the state 'selected' by a given probe scheme. Spectroscopic methods involving transient absorption, nonlinear wave mixing, laser-induced fluorescence, and resonant multiphoton ionization usually require the probe laser to be resonant with an electronic transition in the species being monitored. Hence, as a chemical reaction evolves toward products, these probe methods are restricted to observation of the dynamics within a small region of the reaction coordinate. Moreover, in many studies of nonadiabatic processes in polyatomic molecules,

the initially prepared ‘bright’ state is often coupled to a lower-lying ‘dark’ state. The ‘darkness’ of this resulting state greatly obscures the observation of its dynamics, and, in many cases, renders it ‘unobservable’ leading to potentially erroneous conclusions about the presence or absence of energy flow pathways.

UED, on the other hand, uses electrons as probes and is sensitive to *all* inter-atomic distances in the molecule. By removing the reliance on a resonance condition, the physics of the UED probe is fundamentally different, enabling it to follow dynamics along the entire reaction coordinate. Consequently the probe pulse need not be tunable and, more interestingly, the excited state evolution can be followed to regions far from the equilibrium configuration. Moreover, by monitoring *structure* space instead of *state* space, UED offers dramatic and unique advantages for following nonradiative processes since diffraction is always ‘allowed’ and optically dark states are as readily observed as bright ones—there are no ‘dark’ states for diffraction.

An intriguing phenomenon in the gas-phase photophysics of collision-free S_1 benzene is the observation of a dramatic decrease in the quantum yield of fluorescence for vibrational energies exceeding about 3000 cm^{-1} .¹ Correspondingly, the absorption line width of the S_0 - S_1 system of gaseous benzene measured as a function of excitation excess energy reveals a sudden onset of line broadening at about this energy. These observations have led to

the suggestion that, for excess vibrational energies above this threshold value, a new nonradiative relaxation process, referred to as channel three decay, comes into play. An important new observation emerging from recent experiments with jet-cooled molecules² is that the onset of the channel-three decay becomes even more abrupt when thermal inhomogeneous congestion is removed by supersonic expansion. An even more intriguing fact is that the nonradiative rate (k_{nr}), as measured in fluorescence lifetime experiments, is a function of the symmetry of the vibronic band excited, i.e., some types of vibrations have an enhanced k_{nr} lower in the S_1 manifold than others. This is thought to be due to the fact that some vibrations (most probably the out-of-plane vibrations) can promote nonradiative decay more effectively than others. The channel three phenomenon was discovered over three decades ago,³ but to date no generally accepted explanation has been given. Several mechanisms have been invoked to explain the channel three process:

- (1) direct radiationless transition from the lowest excited state to S_0 enhanced by intramolecular vibration (IVR)
- (2) formation of an intermediate electronic state with a bound or unbound potential-energy surface, and
- (3) photochemical reaction.

The mechanism invoking direct internal conversion (IC) is based on the presence of out-of-plane modes whose frequency is much lower in the

lowest excited state than in the ground state. This large frequency change renders these vibrations exceptionally good accepting modes for radiationless transition between these states. In this mechanism, IVR leads to the production of excited molecules with a high degree of excitation of out-of-plane bending modes, and hence, the onset of channel three is believed to be related to the onset of IVR. The photochemical mechanism invokes the crossing of an isomeric state with the lowest excited state, whereby photochemical conversion of the S_1 molecule to an isomeric form leads to sudden opening of a new nonradiative decay channel. The third mechanism involves formation of an intermediate state, which could be an electronic state of an isomeric form or an electronic state of the parent molecule itself.

Azabenzenes are important parent molecular systems for numerous compounds such as biologically active nicotinic acid and the nucleotides cytosine, uracil, and thymine, and therefore, have been the subject of extensive experimental and theoretical studies. Azabenzenes are isoelectronic with benzene. The nitrogen atoms introduce perturbations to the benzene energy levels and give rise to new transitions due to excitation of their lone-pair electrons. Their lower electronic excitation spectra in the near and vacuum ultraviolet regions are due to both $n\pi^*$ and $\pi\pi^*$ valence transitions, and the lowest-lying transitions are of $n\pi^*$ origin; these form the

basis for differences in the photophysical behavior of azabenzenes and benzene.

Pyridine, the simplest aza-aromatic molecule obtained by replacing one methine (CH) group with a nitrogen atom, has been extensively studied with regard to the photophysics and photochemistry of its low-lying excited states. Although it is often thought of as a paradigm molecule, its properties are actually somewhat unusual. Pyridine had been believed⁴ to be a totally nonfluorescent molecule until 1977 when Yamazaki and Baba discovered weak fluorescence in the gas phase.⁵ A subsequent study⁶ revealed that the fluorescence quantum yield is only $\Phi_F = 5.9 \times 10^{-5}$ at the S_1 (n, π^*) 0^0 level—two to three orders of magnitude smaller than the diazabenzenes, pyrazine (1.3×10^{-3}) and pyrimidine (1.5×10^{-2}) at their respective S_1 origins. Such a low fluorescence quantum yield implies highly efficient nonradiative processes even at the S_1 origin. Furthermore, at $\sim 1600 \text{ cm}^{-1}$ above the S_1 origin, pyridine undergoes an order-of-magnitude drop in the quantum yield of intersystem crossing and a 50% drop in the fluorescence quantum yield—the channel three process.

For many years, the nature of the ultrafast internal conversion in pyridine relative to those of other azabenzenes had been thought to be a solved problem. Pyridine photophysics had been interpreted in terms of the proximity effect,⁷⁻¹² which states that rapid internal conversion results from

having a low-lying $\pi\pi^*$ electronic state very near the $n\pi^*$ state. Vibronic mixing between these two states leads to a large frequency change in the vibronically active out-of-plane modes in the $n\pi^*$ state, which increases the Franck-Condon factors and enables these modes to serve as accepting modes in the internal conversion process. The pyridine $\pi\pi^*$ state lies only 3500 cm^{-1} above the $n\pi^*$ state, compared to a S_1 – S_2 gap ranging from 7000 to 9250 cm^{-1} in the diazo molecules pyrazine, pyrimidine, and pyridazine.¹³ This small energy gap was postulated to result in extensive vibronic mixing between the S_2 ($\pi\pi^*$) and S_1 ($n\pi^*$) states, as mediated by vibrations of A_2 symmetry. The resulting shift in the potential surface causes a large frequency change in the A_2 vibrations between the ground and electronic states, providing good Franck–Condon factors for internal conversion.

Recent experiments,² however, have cast serious doubt upon the assertion that efficient internal conversion in pyridine results from the proximity effect. Model calculations predict that if the proximity effect is responsible for the rapid internal conversion in pyridine, then optical excitation of out-of-plane bending modes of A_2 symmetry should effect a dramatic increase in the internal conversion rate, relative to other vibrational modes, since modes of A_2 symmetry are most efficient in vibronically coupling the S_1 and S_2 states. Recently, Villa *et al.*² studied the photophysics of a variety of pyridine vibronic levels in a supersonic jet. They observed that

vibrational modes of A_2 symmetry are not particularly effective in promoting internal conversion, as would be expected if the proximity effect played an important role in the internal conversion process. They therefore cast doubt upon the previously generally accepted belief that efficient internal conversion in pyridine results from the proximity effect. Villa *et al.* proposed instead that rapid internal conversion may be caused by valence distortion, in which a change in the equilibrium position of the molecule upon electronic excitation results in favorable Franck–Condon factors for transitions having large changes in quantum number in the out-of-plane bending modes. This enables these modes to serve as accepting modes and enhances the internal conversion rate. However, even Villa *et al.* acknowledge that this explanation is also problematical, as a large geometry change would result in extensive vibrational activity in the displaced modes, which is not seen. There have been proposals from time to time that an excited-state photoreaction quenches the fluorescent singlet states of pyridine, but photoproducts have never been detected in the high yields necessary to explain the ultralow fluorescence quantum yields. These results suggest that we are still far away from achieving proper understanding of the photophysics of this beguiling simple molecule.

The proximity effect also enabled predictions to be made concerning the effect of substituents on the internal conversion rate.¹² Electron donating

moieties are known to lower the energy of $\pi\pi^*$ states and raise the energy of $n\pi^*$ states. Thus, for chromophores whose lowest electronic transition is $n\pi^*$, adding an electron donating substituent will tend to shrink the gap between the $n\pi^*$ and $\pi\pi^*$ states. This increases the magnitude of the vibronic coupling, which in turn causes a larger change in the vibrational frequency of the vibronically active mode. The net result is an enhancement of the internal conversion rate upon substitution of an electron donating moiety. Ring substituents alter the energies of $n\pi^*$ and/or $\pi\pi^*$ excited states of these systems, and our particular interest has been to explore the effect of these changes on the rates of nonradiative decay and the quantum yields. However, as the experiments of Baba and co-workers reveal^{6, 13-15}, the nonradiative decay rate actually decreases in 2-methylpyridine and completely disappears in 2,6-dimethylpyridine, in contradiction to the proximity effect.

In an effort to understand this puzzling behavior of the excited state photophysics with increasing substitution and to explore the structural manifestations of the channel three process, we performed detailed ultrafast electron diffraction (UED) studies of the structural dynamics of three azabenzenes—pyridine, 2-methylpyridine (2-picoline, α -picoline), and 2,6-dimethylpyridine (2,6-lutidine). UED, developed in our laboratory over the past 12 years and through four generations of machines, utilizes properly

timed sequences of ultrafast electron pulses to image complex molecular structures in the four dimensions of space and time with resolutions of 0.01 Å and 1 ps, respectively.^{16, 17} The new limits of UED provide the means for the determination of transient molecular structures, including reactive intermediates and non-equilibrium structures of complex energy landscapes. By freezing structures on the ultrafast timescale, we are able to develop concepts that correlate *structure* with *dynamics*. Examples include structure-driven radiationless processes, dynamics-driven reaction stereochemistry, pseudorotary transition-state structures, and non-equilibrium structures exhibiting negative temperature, bifurcation, or selective energy localization in bonds. Furthermore, the recent development of a new machine devoted to structures in the condensed phase, has established ultrafast crystallography as a powerful method for mapping out temporally changing molecular structures in chemistry, and potentially, in biology.¹⁸⁻²¹

6.2 Ground-State Structures

A. Pyridine

Figure 6–1 shows the 2D ground-state diffraction image of pyridine. The peaks in the corresponding radial distribution $f(r)$ curve (Fig. 6–2) reflect the covalent C–C and C–N distances occurring at ~ 1.3 Å, the second-nearest

neighbor C··C and C··N distances at ~ 2.3 Å, and the third-nearest neighbor C··C and C··N distances at ~ 2.8 Å. The ground state structure has been well-characterized by gas-phase steady-state electron diffraction (GED),²²⁻²⁴, X-ray crystallography,²⁵ microwave spectroscopy,²⁶ infrared spectroscopy,²⁷⁻²⁹ overtone spectroscopy,³⁰ and various computational methods³⁰⁻³⁵. Figure 6–3 shows the least-squares refined structure of the pyridine ground state. The parameters are in excellent agreement with previous experimental structures as well as recent high-quality quantum chemical calculations. While the earliest GED investigations of pyridine by Schomaker and Pauling²² and Almenningen *et al.*²³ were not able to address this change in the CNC angle owing to the limited possibilities of their time, the more recent GED results of Pyckhout *et al.*²⁴ did reveal this effect. Their GED structure also indicated that the ortho, meta, and para C–H bonds in pyridine are nonequivalent and that the meta CH bond is shorter than the para CH bond, which in turn, is shorter than the ortho CH bond; this has been confirmed by recent CH stretching overtone spectra³⁰ in conjunction with various *ab initio* calculations. However, given the orders-of-magnitude lower electron beam current of pulsed UED vis-à-vis static GED¹⁷ and the relative insensitivity of electron diffraction to hydrogens, our ground state results do not capture this relative ordering of the C–H bond lengths.

B. 2-Picoline

Figure 6–4 shows the 2D ground-state diffraction image of picoline. The peaks in the corresponding radial distribution $f(r)$ curve (Fig. 6–4) reflect the covalent C–C and C–N distances occurring at ~ 1.3 Å, the second-nearest neighbor C··C and C··N distances at ~ 2.3 Å, and the third-nearest neighbor C···C and C···N distances at ~ 2.8 Å. While all the peaks have similar mean positions as pyridine, note that the addition of the methyl group introduces several long indirect C···C distances that result in a broadening of the peak at ~ 3.7 Å. While the ground state structure of picoline has been previously determined by X-crystallography at 120 K³⁶ and 153 K,³⁷ our study is the first determination of the isolated picoline molecular structure by electron diffraction. Figure 6–5 shows the best-fit structural parameters of the picoline ground state. Again, the aromatic ring distances are nearly unchanged from pyridine and picoline.

C. 2,6-Lutidine

Figure 6–6 shows the 2D ground-state diffraction image of lutidine and Fig. 6–7 shows the 1D radial distribution curves in comparison with the other azines. The peaks in the radial distribution $f(r)$ curve reflect the covalent C–C and C–N distances occurring at ~ 1.3 Å, the second-nearest neighbor C··C and C··N distances at ~ 2.3 Å, and the third-nearest neighbor C···C and C···N

distances at ~ 2.8 Å. While all the peaks have similar mean positions as pyridine and picoline, note that the addition of the second methyl group introduces longer indirect C \cdots C distances which results in further broadening of the peak at ~ 4.0 Å (see Fig. 6–7). No previous electron diffraction study has been performed on 2,6-lutidine, although the crystal structure at 120 K has been determined.³⁸ Using molecular orbital calculations at the SCF level, Porcinai and Foggi³⁹ report that the most stable rotamer of 2,6-lutidine has C_{2v} symmetry with one of the C–H bonds of both methyl groups lying in the plane of the ring and pointing in the opposite direction with respect to the nitrogen atom. Figure 6–8 presents the refined ground-state parameters of lutidine obtained by UED.

6.3 Transient Structures

A. Pyridine

To resolve the structural changes during the course of the reaction, we collected UED images for a range of time delays from -90 ps to $+185$ ps. The 2D diffraction-difference images (with the image at -90 ps chosen as the reference image) clearly exhibit the emergence of periodic ring patterns (Fig. 6–9), whose intensity becomes more pronounced over time. These rings in the diffraction-difference images directly reflect the changes in the molecular structure from the reference structure at -90 ps. The corresponding 1D

difference curves, $\Delta f(t; t_{\text{ref}}; r)$, shown in Fig. 6–10 exhibit peaks with both negative and positive amplitudes: *the negative peaks (shaded blue) represent the depletion of covalent (~ 1.3 Å region) and second-nearest neighbor (~ 2.5 Å region) distances, whereas positive peaks (shaded red) denote the formation of new internuclear pairs* (those, with distances of ~ 1.1 and 1.3 Å and those with distances greater than 3.5 Å).

Upon excitation, several possible reaction pathways are open to the pyridine molecule, including valence isomerization, fragmentation, and ring opening, as indicated in Scheme 6–1. Figure 6–11 depicts some structures proposed in the literature for the photochemistry of pyridine: gas phase (Dewar- and Hückel-type isomers⁴⁰ and $\text{C}_4\text{H}_4 + \text{HCN}$ fragmentation^{40, 41}); liquid phase (Dewar isomer,⁴² azaprefulvene isomer⁴³); matrices (Dewar isomer^{44–46} and $\text{C}_4\text{H}_4 + \text{HCN}$ fragmentation^{44, 46}), and quantum-chemical calculations (azaprefulvene isomer^{43, 47}). To discriminate between the various possible reaction channels, the UED data was fit to a series of structural models. Figure 6–12 shows the comparison between the experimental transient-isolated $f(r)$ curves averaged over four time slices (from +60 ps to +185 ps) and the corresponding theoretical curves for various trial structures (adjusted for excess internal energy). The poor agreement between theory and experiment for the vibrationally hot Kekulé, Dewar, Hückel, azaprefulvene, and $\text{C}_4\text{H}_4 + \text{HCN}$ fragmentation channels precludes these

structures from being involved in the dominant reaction channel on our time scale. When a mixture of Dewar, Hückel, and vibrationally ‘cold’ (403 K) ring-opened diradical structures was fit to the experimental $f(r)$ curve, this multi-component fit indicated that ring opening was the major channel, with the isomerization to the Dewar structure being the minor one; the contribution of the Hückel isomer was vanishingly small.

A superior structural fit was obtained using just the ring-opened structure albeit with increased internal energy, manifested by mean amplitudes of vibration 70–100% higher than those of the cold structure at 403 K. These higher vibrational amplitudes—reflected as damping and peak broadening in the experimental $f(r)$ curves—could easily result from a non-thermal (non-Boltzmann) population in the molecule’s vibrational degrees of freedom, as has been elucidated by UED in pericyclic reactions.⁴⁸ In the presence of such hot ring-opened structures, the relative fractions of the Dewar and Hückel structures become negligible in a multi-component fit. These results establish that the primary product is a hot ring-opened diradical structure.

Figure 6–13 shows the ring-opened structure following least-squares refinement of vibrational amplitudes and internuclear distances, with the corresponding $sM(s)$ and $f(r)$ curves being shown in Fig. 6–14. The features of this refined structure are consistent with the diffraction-difference curves of

Fig. 6–10; for instance, C(1)–N distance of ~ 5.23 Å and C(1)–C(5) distance of ~ 4.33 Å correspond to the emergence of long internuclear separations, and hence, the loss of covalent and next-nearest neighbor distances. As shown in Fig. 6–13, the best-fit covalent-bond distances and all but one of the angles are consistent with quantum-chemical calculations performed in this laboratory. The primary exception is one of the skeletal torsional angles, which, with a best-fit value of $\sim 123^\circ$ (instead of 180°), distorts the planarity of the predicted ring-opened structure and places the N-atom $\sim 60^\circ$ above the plane defined by the C-skeleton. Because UED measures the structure obtained for all molecules, this result must reflect the multiple torsional conformations, in concordance with a flexible structure. Also, as can be seen from the final refined structures of the ground state and the transient intermediate in Figs. 6–3 and 6–13, the skeletal carbon–carbon bond distances change from being aromatic in the ground state (~ 1.4 Å) to become aliphatic in the diradical (C–C ~ 1.46 Å and C=C ~ 1.35 Å).

We obtained the structural evolution of the transient-isolated $f(r)$ curves, as shown in Fig. 6–15. Except for their relative intensities, the shapes of the transient-isolated curves were nearly indistinguishable over time—indicating that the transient structure remains nearly unchanged on the time scale of the experiment; its population alone changes. A least-squares fit of the transient population gave a time constant of 17 ± 1 ps (Fig. 6–16). These

results, in conjunction with the difference curves in Fig. 6–10, indicate that, upon excitation, the ultrafast ring opening of pyridine disrupts its aromaticity, and the ensuing open structure increases in population with a time constant of ~ 17 ps.

B. 2-Picoline

Upon excitation, several possible reaction pathways are open to the picoline molecule, including valence isomerization, fragmentation, and ring opening. To discriminate between the various possible reaction channels, the UED data was fit to a series of structural models, some of which are shown in Fig. 6–17. A superior structural fit was obtained using the ring-opened structure establishing that the primary product is a hot ring-opened diradical structure.

Figure 6–18 shows the ring-opened structure following least-squares refinement of vibrational amplitudes and internuclear distances, along with the corresponding $sM(s)$ and $f(r)$ curves. The best-fit covalent-bond distances and all but one of the angles are consistent with quantum-chemical calculations performed in this laboratory. We obtained the structural evolution of the product, as shown in Fig. 6–19. A least-squares fit of the transient population gave a time constant of 28.7 ± 7 ps.

C. 2,6-Lutidine

The 1D difference curves, $\Delta f(t; t_{\text{ref}}; r)$, shown in Fig. 6–20 exhibit peaks with both negative and positive amplitudes. Upon excitation, several possible reaction pathways are open to the lutidine molecule, including valence isomerization, fragmentation, and ring opening. To discriminate between the various possible reaction channels, the UED data was fit to a series of structural models some of which are shown in Fig. 6–21.

Figure 6–22 shows the comparison between the experimental transient-isolated $f(r)$ curves and the corresponding theoretical curves for various trial structures (adjusted for excess internal energy). The good agreement between theory and experiment for the vibrationally hot ground state structures establishes internal conversion to the ground state as the dominant channel. As can be seen from Fig. 6–22, the ring opening channel gives a much poorer fit. A least-squares fit of the transient population gave a time constant of 16.1 ± 2.3 ps, as shown in Figs. 6–23 and 6–24.

6.4 Photochemistry

A. Pyridine

The photochemical behaviour of pyridine has been the subject of numerous studies that reveal a rich array of reactions and invoke different intermediates as a function of the excitation wavelength and the phase.

Moreover, many different (and often contradictory) mechanisms have been proposed for the observed behavior. 254 nm irradiation of pyridine in the liquid phase was found to proceed via photoisomerization to a Dewar pyridine (2-azabicyclo[2.2.0]hexa-2,5-diene), which rearomatized completely to pyridine within 15 min at room temperature.⁴² On the other hand, at the same wavelength, Caplain *et al.*⁴⁹ suggested the presence of an azaprismane intermediate to explain their observed substitution products of pyridine.

In low-temperature rare-gas matrices, Chapman *et al.*⁴⁴ reported the formation of hydrogen cyanide and cyclobutadiene upon photolysis of pyridine at lower energies (> 290 nm) and speculated about Dewar pyridine as a possible intermediate, although no evidence was presented to support this. In contrast, the analysis of infrared product bands by Johnstone *et al.*⁴⁵ revealed no fragmentation products, but rather a photoproduct that was somewhat arbitrarily assigned to Dewar pyridine in analogy with liquid pyridine,⁴² although the possibility of other isomers was not ruled out. A recent matrix-isolation infrared spectroscopic experiment^{46,50} reported that the fragmentation products (HCN and C₄H₄) are produced by two channels: (i) direct photodissociation of pyridine (major channel), and (ii) secondary dissociation of Dewar pyridine (minor channel).

Early studies of pyridine photolysis in static gas led to the conclusion that pyridine vapor is unreactive⁵¹ when excited to the S₁ (n, π*)⁵² or the S₂

(π , π^*)^{52, 53} states. At shorter wavelengths, Mathias and Heicklen⁵⁴ reported that acetylene is the main product albeit with low quantum yields; however, they acknowledge that their results were limited by an inability to detect certain product fragments (i.e., HCN) due to reactions occurring on the chromatographic column. Lee and co-workers^{41, 55} combined molecular beams with photofragment translational spectroscopy to determine the primary products formed in unimolecular photodissociation of pyridine. At 193 nm,⁴¹ pyridine photodissociates to give HCN + C₄H₄ (59%), CH₃ + C₄H₂N (21%), C₃H₃ + C₂H₂N (11%), and H + C₅H₄N (9%) while at 248 nm,⁵⁵ the relative contributions are 80%, 1%, 0%, and 5%, respectively. However, more recent deuterium scrambling studies⁵⁶ have shown that pyridine undergoes photoisomerization to give transposition products via an azaprefulvene (and not Dewar) intermediate upon S₀ → S₂ (π , π^*) excitation at 254 nm in the vapor phase.

Over the past few years, we have investigated pyridine photochemistry on the ultrafast time scale using femtosecond time-resolved mass spectrometry in the gas phase⁴⁰ and femtosecond transient absorption spectroscopy in the liquid phase.⁴³ In the gas phase, upon 277 nm excitation, we observed a fast decay component of 400 fs (which reflects the initial displacement of the wavepacket and IVR in the reactive channel) and two slower time constants of 3.5 ps and 15 ps, which were assigned to

isomerizations to Dewar and Huckel pyridines, respectively, based purely upon the energetics. However, upon two-photon excitation at 307 nm, the dynamics is drastically different, resulting in the formation of ring opened pyridine in ~ 80 fs which then decays in ~ 130 fs to form the final products, HCN + C₄H₄. The liquid phase experiments show the two distinct timescales, with the fast decay (~ 2.2 ps) resulting from the reactive deactivation of the S₂ (π, π^*) state via isomerization to azaprefulvene, and the slow decay (~ 9 – 23 ps, depending on the solvent) resulting from the nonreactive deactivation of the S₁ (n, π^*) state, mostly by intersystem crossing to the triplet. Using *ab initio* methods we found a conical intersection between the PES of S₂ (π, π^*) and S₀ states responsible for the ultrafast deactivation of the pyridine molecule; the S₂ (π, π^*) excited state correlates to the ground state of azaprefulvenic pyridine.

In order to elucidate the exact nature of the ring opening process, we consider two possible reaction pathways on the excited state surface following excitation into the higher vibrational levels of S₁: (i) loss of the α -H atom to form the o-pyridyl radical, followed by ring cleavage to give the open radical, and (ii) direct C–N bond scission to give the ring opened diradical. While each of these processes can also occur in the vibrationally hot molecule on the electronic ground state following S₁ \rightarrow S₀ internal conversion, we do not observe the hot parent structure despite the proven sensitivity of our UED

apparatus to hot molecules,⁴⁸ thus precluding the participation of the hot ground state in the reaction pathway.

The observation that ring opening occurs in 2-methylpyridine and does not occur in 2,6-dimethylpyridine (see below) might lead one to believe that the presence of α -H atoms plays a critical role in the ring opening process—thereby giving more credence to the H loss initiated channel. Thermal decomposition of pyridine in shock tube pyrolysis experiments has been interpreted by Mackie *et al.*⁵⁷ as a chain reaction initiated by C–H bond scission. Although C–H bond scission in pyridine can lead to three unique pyridyl radicals, Mackie’s well-accepted mechanism of pyridine pyrolysis favors the o-pyridyl radical because of its ability to produce an open-chain cyano radical directly, which is expected to be overwhelmingly more stable than any other open-chain radicals produced by the ring fissure of pyridyl radicals. Subsequent theoretical calculations⁵⁸⁻⁶¹ have confirmed C–H bond scission in pyridine preferentially produces the o-pyridyl radical because the C–H bond ortho to the nitrogen is weaker by ~ 5 kcal/mol than the other two C–H bonds. The reduced strength of the C–H bond next to the nitrogen atom (~ 105 kcal/mol) relative to the parent benzene molecule (~ 112 kcal/mol)⁶² has been attributed to the stabilization effected by the interaction of the nitrogen lone pair with the adjacent C atom radical site. Calculations^{61, 63, 64} also indicate that ring-opening via C–N bond cleavage in o-pyridyl radical is more

favorable than C–C bond cleavage, as the former has a significantly lower activation barrier, and the resulting open-chain cyano radical C_4H_3CN is more stable than other linear C_5NH_4 radicals. However, the transient ring opened structure as revealed by UED does not arise from a C–H loss mechanism for the following reasons:

(1) The energy required to produce the o-pyridyl radical from pyridine is ~ 105 kcal/mol and the barrier for the o-pyridyl ring scission to produce the open chain radical is ~ 40 kcal/mol,⁶¹ implying a total energy requirement of ~ 145 kcal/mol. However, at 403 K with a photon energy of 107 kcal/mol, there is not enough energy to cleave the ring in our experiment via this pathway.

(2) Photodissociation of pyridine and benzene reveals notable differences between the two molecules in their photochemical pathways. In the photodissociation of benzene, 96% of the dissociation events result in the loss of one or two hydrogen atoms.⁶⁵ Pyridine, in contrast, loses a hydrogen in only 9% of events; the remaining percentage consists of events that result in the destruction of the ring structure.^{41, 55} This absence of the H loss channel in the unimolecular dissociation of pyridine precludes the formation of pyridyl radicals.

The ring opened diradical structure, therefore, results from direct C–N bond scission on the excited state surface. The near absence of pyridyl

radicals (H atom loss) in the 193-nm photolysis of pyridine vis-à-vis the dominance of the benzyl radical (H atom loss) in benzene photodissociation convincingly demonstrates that the presence of the nitrogen in the aromatic ring opens up other reactive pathways with lower activation energy. A direct measure of the weakening of the C–N bond in pyridine *vs.* the C–C in benzene is represented by the predicted bond orders of these bonds. In benzene, all of the C–C bonds are equivalent with 66.7% double bond character, whereas in pyridine, the C–N bond order is smaller³², resulting in C–N bond cleavage being more facile in pyridine than the analogous C–C bond rupture in benzene. C–N bond breakage in pyridine requires ~70 kcal/mol; in contrast, C–C bond breakage requires ~85 kcal/mol.⁴⁰ The relative ease of the C–N bond breakage in pyridine leads to the dominance of the HCN + C₄H₄ products (59%) at 193 nm, which can arise from further reaction of the open chain diradical. Similar stepwise elimination of HCN through a diradical intermediate has been invoked to explain the unimolecular photodissociation of pyrazine.^{55, 66} Thus, both experimental observations—the near-absence of the pyridyl channel and the dominance of the HCN channel—can be explained by the ring opened diradical intermediate. Previous DFT calculations⁴⁰ estimate that the ring opening of pyridine requires ~40 kcal/mol to overcome the resonance energy and ~70 kcal/mol to break one C–N bond. Since the estimated resonance energies for

pyridine vary from ~ 18 kcal/mol^{32, 67} to ~ 26 kcal/mol,^{32, 68} the ring-opening energy (~ 110 kcal/mol) calculated by Zhong *et al.*⁴⁰ is most likely overestimated. Moreover, based on the correlation of the channel-three onset to the barrier of the ring opening process (discussed below), we estimate the empirical ring-opening energy to be ca. 102–104 kcal/mol. Since the subsequent reaction to HCN + C₄H₄ requires an additional ~ 30 kcal/mol,⁴⁰ the molecule at 266 nm remains trapped as an open chain diradical on the time scale of our experiment (Fig. 6–16). This can also explain the apparent lack of reactivity of pyridine vapor at 254 nm reported by earlier investigators—at this energy (~ 113 kcal/mol), the diradical arising out of ring opening would be unable to react further to give the fragmentation products and would most likely undergo recyclization to reform the parent structure at longer times.

Based upon the above discussion, the following picture emerges for the unimolecular photodissociation of pyridine. Initial excitation with the 266 nm femtosecond light pulse prepares the pyridine molecule in the S₁(n, π^*) state with ~ 2700 cm⁻¹ (8 kcal/mol) excess vibrational energy. The molecule then predominantly undergoes direct C–N bond scission on the excited state surface to form the ring open diradical with a time constant of ~ 17 ps. There is also a minor channel which involves isomerization to Dewar pyridine. With this direct structural information of the transient intermediate elucidated by

UED, we can now revisit our earlier femtosecond mass spectrometric results.⁴⁰ The ~ 3.5 ps timescale can still be assigned to the Dewar isomer (which is a minor channel in the time-resolved mass spectra as well as in our UED data). However, the ~ 15 ps time scale (earlier ascribed by mass spectrometry to Hückel isomerization based on purely energetic considerations) is remarkably similar to the 17 ± 1 ps timescale of the UED ring opening process. Furthermore, the reported insensitivity of the timescales to deuteration (~ 15 ps for pyridine-*h*₅ vs. ~ 16 ps for pyridine-*d*₅) would be very surprising for the Hückel pathway given that valence isomerization involves the motions of two deuterium atoms. On the other hand, the direct ring opening process would not be sensitive to deuteration and could easily explain the lack of change in the timescales. Based on these considerations, therefore, we reassign the ~ 15 ps decay rate from the mass spectrometric experiment to the pyridine ring cleavage process.

B. 2-Picoline

In contrast to pyridine, there have been few photochemical studies of picoline reactivity. Caplain and Lablache-Combiere⁶⁹ reported that 2-picoline, when irradiated in the gas phase at 254 nm, undergoes photoisomerization to yield 4-picoline. This is in contrast to the report by Roebke⁷⁰ that the gas-phase photolysis of 2-picoline at 248 nm yields both 3- and 4-picoline in a

ratio 10:1, while photolysis at 266 nm yields 4-picoline alone with a quantum yield of 9×10^{-5} . To account for these photoisomerizations, both reports suggested a ring transposition mechanism involving azaprismane intermediates. Roebke also reports that irradiation of liquid picoline at 248 nm and 265 nm did not produce any products. Dewar 2-picoline with the C3–C6 bridging bond was observed in low-temperature argon matrices upon UV irradiation at 254 nm.^{50, 71}

That 2-picoline undergoes ring opening to produce the diradical with a time constant of 26.7 ± 6.7 ps is clear from the analysis discussed above. Because of the methyl group in α position to the nitrogen atom, C–N bond breakage in 2-methylpyridine can take place in two ways: between the nitrogen atom and the carbon atom of the methine group, or between the nitrogen atom and the carbon atom carrying the methyl group. The structural refinement of the transient intermediate shows that 2-methylpyridine ring opens preferentially on the side that does not contain the methyl group. It is interesting to note here that studies⁷² on the role of β hydrogen atoms of the methyl group in the hydrodenitrogenation of 2-methylpyridine show that the ring opening of 2-methylpiperidine occurred preferentially between the nitrogen atom and the methine group, rather than between the nitrogen atom and the carbon atom bearing the methyl group, owing to the methyl group

constituting a strong steric hindrance for the right adsorption conformation of the nitrogen atom and the β H atoms.

As in pyridine, 2-picoline can undergo ring opening in one of two ways: (i) loss of the β -H atom from the methyl group to form the 2-picoly radical, followed by ring cleavage to give the open radical,⁷³ which can further fragment into HCN + C₄H₄; and (ii) direct C–N bond scission to give the ring opened diradical. While each of these processes can also occur in the vibrationally hot molecule on the electronic ground state following S₁ → S₀ internal conversion, the poor fits of the hot parent structure render this pathway unacceptable. Again, as was the case in pyridine, the picoly radical channel is unfeasible due to energetic considerations as this channel requires ~140 kcal/mol to open the ring.⁷³ Hence, the picture that emerges is similar to pyridine in that direct C–N bond scission occurs on the excited state. The preferential scission of the bond between the nitrogen atom and the methine group can be understood in terms of the atomic charge distribution in the S₁ state as calculated by Kudoh *et al.*⁷¹ at the CIS/6-31++G** level. Their results reveal that while the charges on N₁, C₃, C₄, and C₆ are negative, those on C₂ and C₅ are positive—implying that the N₁–C₂ and C₄–C₅ bonds have double bond character while N₁–C₆ bond has single bond character, which is easier to cleave.

C. 2,6-Lutidine

Caplain and Lablache-Combier⁶⁹ reported that 2,6-lutidine, when irradiated in the gas phase at 254 nm, undergoes photoisomerization to yield 2,4-lutidine exclusively, which they postulate occurs via azaprismane intermediates that could arise from Dewar isomers. However, as pointed out by Pavlik *et al.*,⁷⁴ this mechanism imposes arbitrary selectivity upon the possible modes of formation of the initially formed Dewar pyridines as well as on the rearomatization of the subsequently formed azaprismanes. Recent experiments present contrasting results in that vapor-phase photolysis of 2,6-lutidine at 254 nm yields 2,3-lutidine (15%), 3,4-lutidine (4%), 2-picoline (1%), trimethylpyridine (14%), and polymer (66%) whose ¹H NMR analysis showed the presence of aliphatic hydrogen but no absorptions due to aromatic protons, suggesting that polymerization is accompanied by ring opening. Based on the major phototransposition products and various photochemical crossover experiments, they suggest that the isomerization of 2,6-lutidine occurs via 2,6-bonding to the azaprefulvene diradical, followed by nitrogen migration and rearomatization. These observations were later rationalized by a theoretical characterization of the photoisomerization channels on the singlet and triplet potential energy surfaces³¹ by suggesting that in addition to the azaprefulvene intermediate, the azabenzvalene intermediate could also account for the singlet phototransposition products.

Our UED data suggests that upon S_2 excitation at 266 nm, 2,6-lutidine undergoes internal conversion to the ground state producing vibrationally hot 2,6-lutidine along with its isomers with a time constant of 16.1 ± 2.3 ps. With the 3 ps time resolution of the UED technique, we have not observed either the azaprefulvene or azaenzvalene intermediates as discussed above. The lack of ring opening in 2,6-lutidine can be attributed to the fact that unlike pyridine and picoline, which are excited to high vibrational levels in S_1 , lutidine is excited to S_2 , and hence, can undergo very different reaction pathways. Moreover, as shown by the *ab initio* calculations of π Mulliken population data,³⁹ the presence of the two methyl groups in 2 and 6 positions stabilizes the pyridine ring as a consequence of an increased charged density: a nitrogen atom can better accommodate a higher π density.

6.5 Photophysics

The direct observation of the S_1 decay rate was performed by Yamazaki and co-workers for a number of S_1 levels of pyridine vapor in 1982, and its lifetime was 42 ps at the S_1 0^0 level. The lifetime of S_1 in solution is in the range of 9–23 ps, depending on the solvent.⁴³ Ultrafast electronic dephasing from the $S_1(n\pi^*)$ state was studied by time-resolved photoelectron imaging⁷⁵ in conjunction with (1+2') resonance-enhanced multiphoton

ionization (REMPI) via the S_1 state. The lifetime at the S_1 origin was determined to be 32 ± 5 ps from the decay of the total photoionization signal.

The above UED observations for pyridine are directly relevant to the ‘channel three’ non-radiative process. In our UED experiment on pyridine, the excess vibrational energy in $S_1(n, \pi^*)$ is $\sim 2,700$ cm^{-1} —well above the $\sim 1,600$ cm^{-1} threshold for ‘channel three’ behavior in pyridine. For picoline, the 266 nm photon prepares the molecule with ~ 2742 cm^{-1} excess energy in the $S_1(n, \pi^*)$ state—also above the picoline ‘channel three’ threshold. In lutidine, however, the pump pulse lands the molecule on the $S_2(\pi, \pi^*)$ with ~ 595 cm^{-1} excess energy in the second excited electronic state.

Historically, various explanations have been invoked to account for the channel three behavior; however, our UED data for pyridine and picoline does not support the following proposed scenarios: (i) direct $S_1 \rightarrow S_0$ internal conversion, which would land the molecule on the electronic ground-state with a concomitant increase in internal energy, making it vibrationally hot. We do not observe the hot parent structure despite the proven sensitivity of our UED apparatus to hot molecules; (ii) isomerization-mediated internal conversion (e.g., via the Dewar, Hückel, or azaprefulvene structures), which can also be ruled out based on the poor fits to these isomers (Fig. 6–12).

For aromatic pyridine and picoline, the nonradiative channel-three behavior is due to direct ring opening to form the diradical structure obtained

above. This is in stark contrast to the prevailing view that an ultrafast internal conversion pathway, mediated by the proximity of the first and second excited state surfaces, opens up at the channel three threshold leading to vibrationally-hot ground-state molecules. However, lutidine does not undergo ring opening, accounting for the lack of channel three behavior. This structural change explains the behavior in quantum yield observed in this series of molecules—in the channel three region pyridine and picoline show a change with vibrational energy (35,000–40,000 cm^{-1}) while lutidine does not, even though for all the initial (0,0) decay is similar and the yield is low in value due to the proximity of states. The ring opening pathway can also clarify other observations made in different phases, as will be detailed elsewhere.

The observed disparity in the transient intermediates for this homologous series of azabenzenes begs the question—why are profound differences in photophysical and photochemical behavior induced by subtle changes in the parent molecular structure? In pyridine, optical excitation at 266 nm involves the removal of a non-bonding electron on the nitrogen atom to the antibonding π^* orbital of the ring, thus lowering the strength of the C–N bond and resulting in its facile scission. If the time scale of this bond rupture is shorter than the lifetime of the state at that particular total energy, we expect this highly efficient nonradiative photochemical process to

actively deplete the radiative population, causing a decrease in emission quantum yield. The abruptness of the onset of the channel-three phenomenon is, therefore, a manifestation of the energy threshold for the ring-cleavage chemistry.

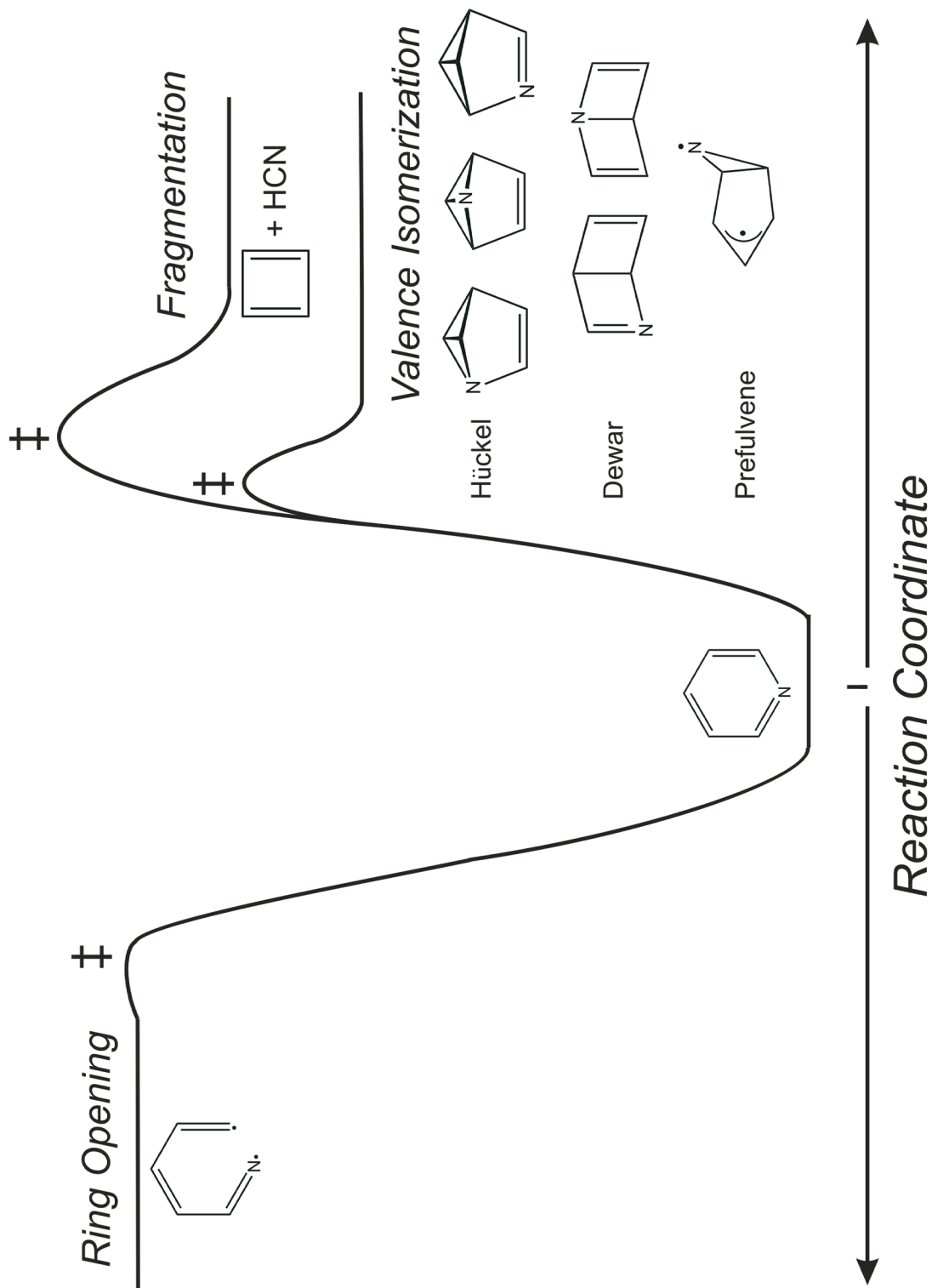
Upon methyl substitution, the electron-donating nature of these groups increases the electron density on the ring, leading to greater stability. Despite this increase in ring strength, structural refinement shows that 2-methylpyridine does indeed open the ring, preferentially on the side that does not contain the methyl group. This favored scission of the bond between the nitrogen atom and the methine group can be understood in terms of its weaker character relative to other skeletal bonds in the S_1 state. On the other hand, the presence of two methyl groups in 2- and 6- positions of lutidine further stabilizes the ring as a consequence of an increased charged density, and it is not surprising that the nonradiative process is photophysical internal conversion and not photochemical ring opening. The quantum yield measurement reflects this behavior of electronic structure changes (not density of vibrational states argument) as 3-picoline reverts to a pyridine-type behavior. It should be noted that addition of electron-donating methyl substituents tends to shrink the gap between the close-lying first ($n\pi^*$) and second ($\pi\pi^*$) excited states, and this effect is important for the overall decay even with no excess vibrational energy.

There is also a remarkable similarity in the measured and estimated decay rates of the singlet states with the time constants determined by UED. The S_1 decay rate of pyridine at the channel three threshold measured to be 20 ps is remarkably similar to the product growth rate of ~ 17 ps of the open diradical, further supporting the direct nature of the C–N bond scission on the excited hypersurface.

6.6 Conclusions

UED has probed the paradigm case of bond breaking and bond making in the prototypical nitrogen heterocycle, pyridine, and its methylated analogues. As detailed above, UED has been successful not only in identifying the dominant reaction channel among this plethora of possibilities, but also in elucidating the transient structure of the reaction intermediate. UED, for the first time, uncovered a previously unknown ring-opened diradical intermediate structure resulting from C–N bond scission in pyridine and picoline (Fig. 6–25)—this observed ring-opened structure casts new light on the decades-old puzzle of channel-three behavior occurring in many aromatic molecules. The ring-opened diradical structure was isolated from among a plethora of possibilities for reaction pathways. Through determination of the reactant and transient molecular structures, we are able to relate the structural changes in bond distances and angles to the timescale

of population changes involved in bond breaking and bond making. The direct correlation of the photochemical and photophysical timescales underscores the ability of ultrafast electron diffraction to elucidate ultrashort structural dynamics of isolated molecules subjected to complex radiative and nonradiative pathways.



Scheme 6-1. Pyridine reaction with multiple reaction pathways.

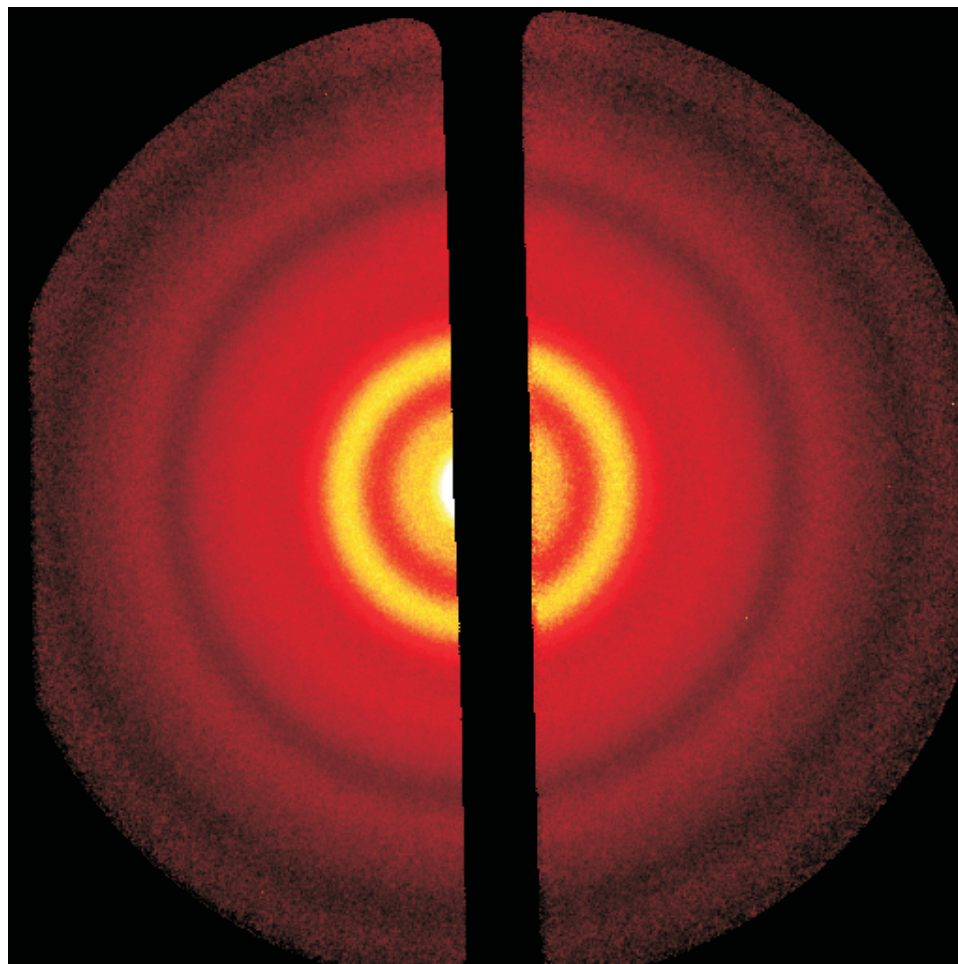


Figure 6-1. Ground-state molecular diffraction image of pyridine.

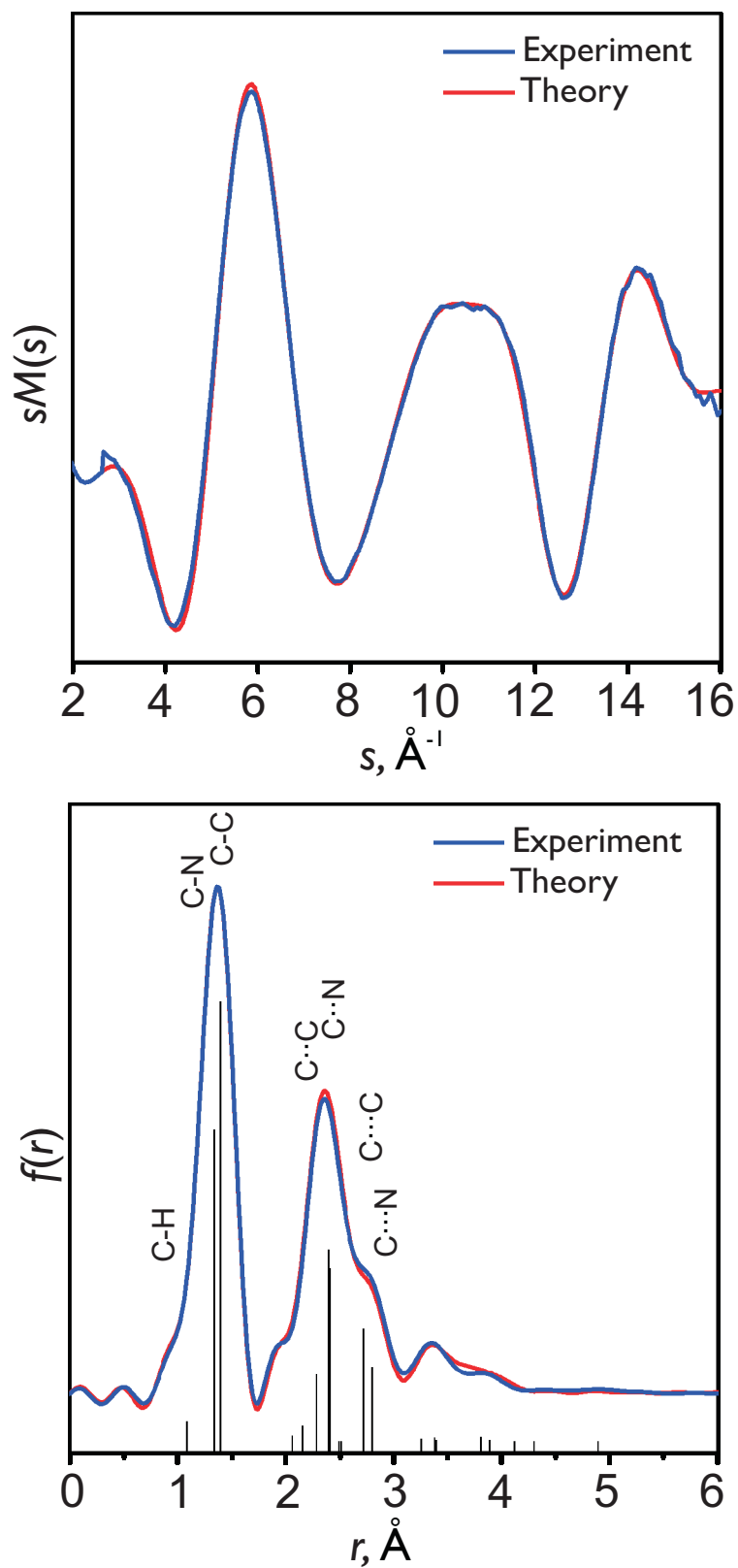
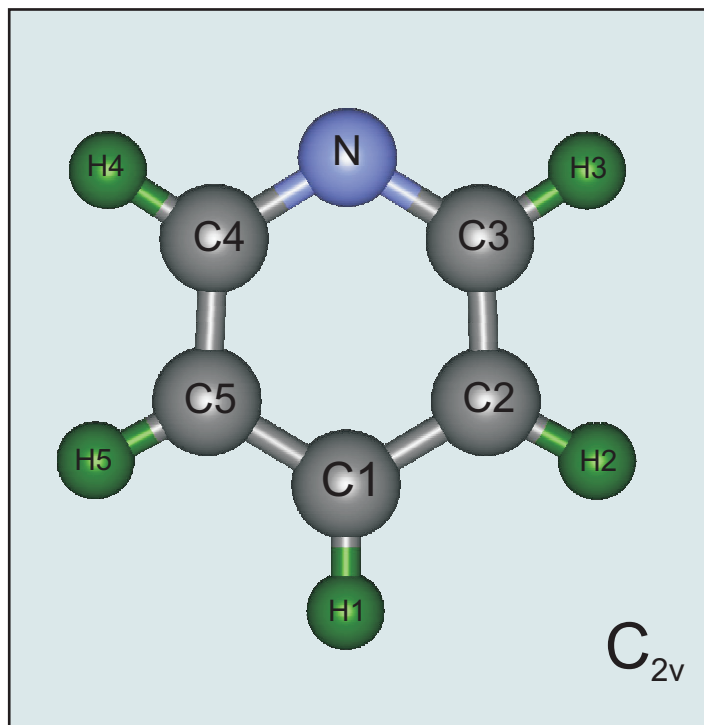


Figure 6-2. Refined ground-state structure of pyridine. Comparison between the experimental and refined theoretical $sM(s)$ and $f(r)$ curves is shown.



Distances		
	<i>experiment</i>	<i>DFT</i>
$r(\text{C1-C2})$	1.420 ± 0.002	1.391
$r(\text{C2-C3})$	1.414 ± 0.004	1.394
$r(\text{C3-N})$	1.308 ± 0.07	1.336
$r(\text{C1-H1})$	1.100 ± 0.005	1.084
$r(\text{C2-H2})$	1.112 ± 0.007	1.083
$r(\text{C3-H3})$	1.089 ± 0.005	1.086
$r(\text{C1-N})$	2.803 ± 0.009	2.80
Angles		
$\alpha(\text{H1-C1-C2})$	121.6 ± 0.58	120.7
$\alpha(\text{C1-C2-C3})$	118.6 ± 1.02	118.5

Figure 6-3. Refined ground-state structure of pyridine. Distances are in ångströms and angles are in degrees. The C3–N distance was not independently refined, but derived from other best-fit (refined) distances in the structure.

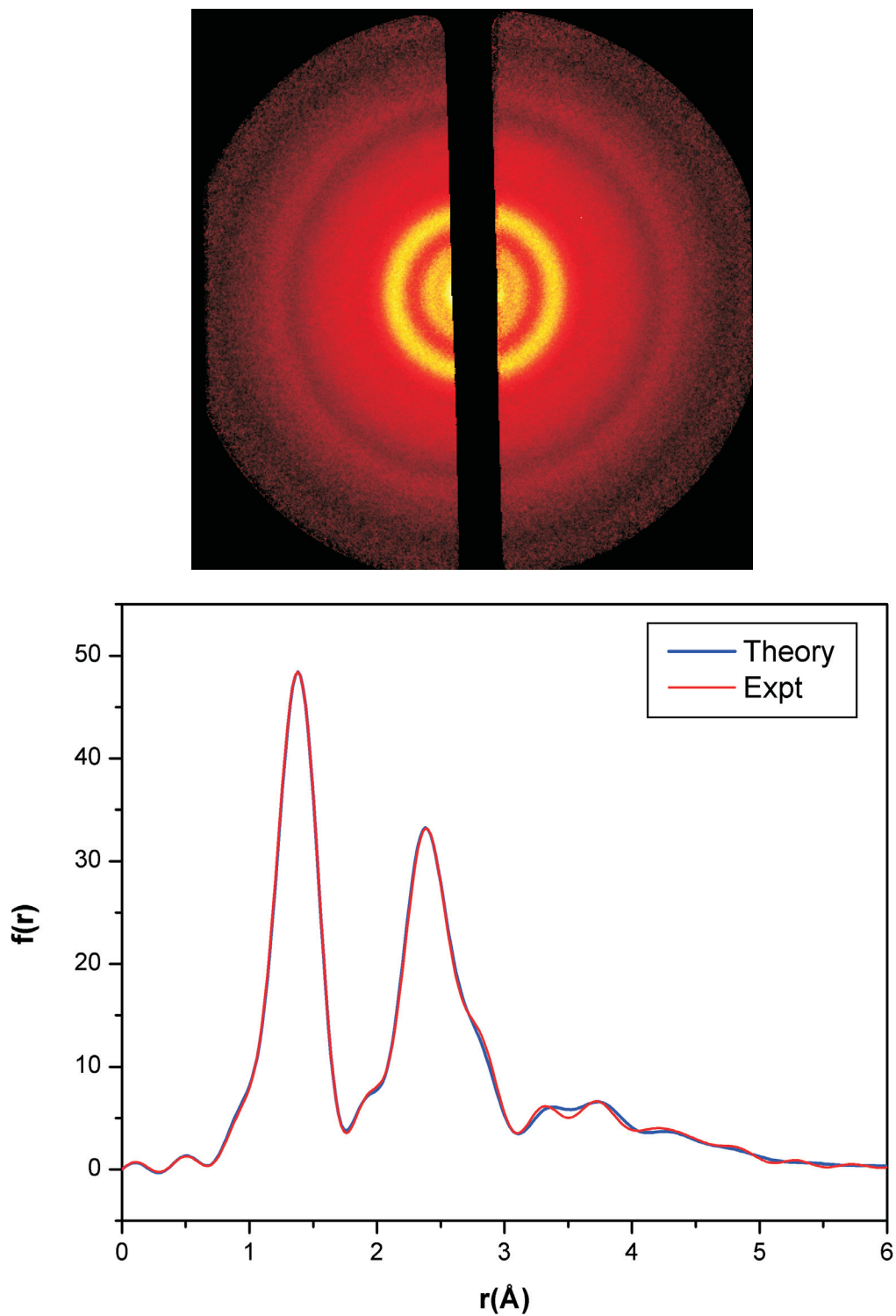
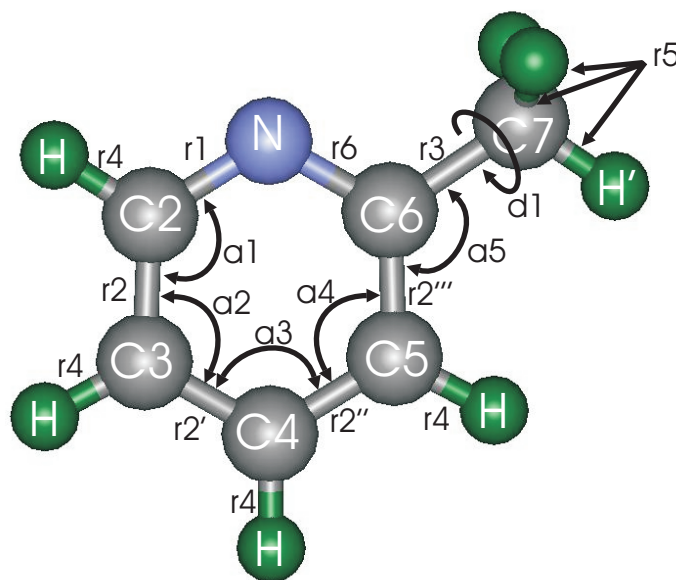


Figure 6-4. Picoline ground state. (Top) 2D diffraction pattern. (Bottom) Refined ground-state structure of picoline. Comparison between the experimental and refined theoretical $f(r)$ curves is shown.



Distances

r1(N-C2)	1.328 ± 0.027	(1.334)
r2(C2-C3)	1.410 ± 0.004	(1.393)
r3(C6-C7)	1.525 ± 0.008	(1.507)
r4(C2-H)	1.096 ± 0.012	(1.083-1.087)
r5(C7-H')	1.185 ± 0.026	(1.091-1.093)
r2'(C3-C4)	1.402	(1.391)
r2''(C4-C5)	1.402	(1.391)
r2'''(C5-C6)	1.404	(1.393)
r6(N-C6)	1.374	(1.341)

Angles

a1(N-C2-C3)	121.2 ± 3.1	(123.8)
a2(C2-C3-C4)	118.4 ± 2.0	(117.9)
a3(C3-C4-C5)	119.7 ± 1.9	(118.8)
a4(C4-C5-C6)	117.4 ± 2.0	(119.3)
a5(C5-C6-C7)	119.5 ± 1.3	(121.8)
d1(C5C6C7H')	-176.6 ± 107.6	(121.2)

Figure 6-5. Refined ground-state structure of picoline. Distances are in ångströms and angles are in degrees. DFT values for the structural parameters are given in parentheses. The distances marked in blue were not independently refined, but derived from other best-fit (refined) distances in the structure.

2,6-Lutidine

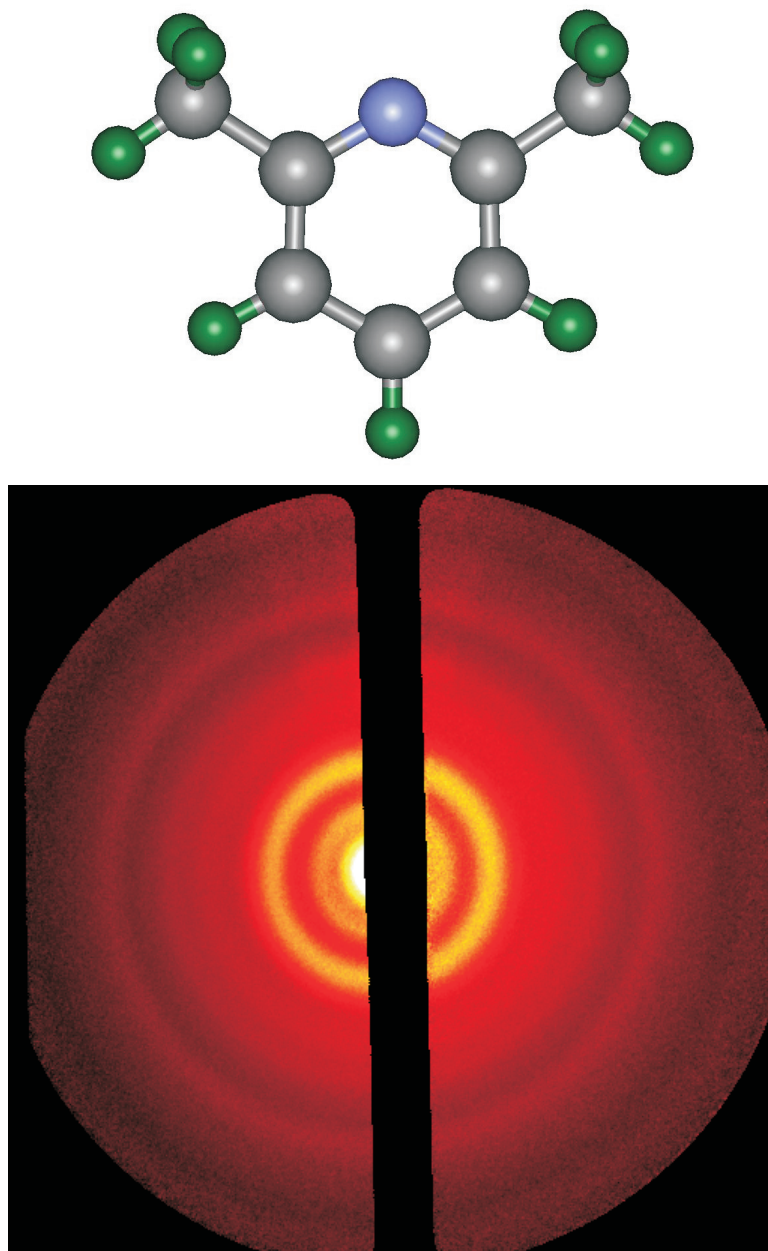


Figure 6-6. 2D ground state diffraction pattern of 2,6-lutidine.

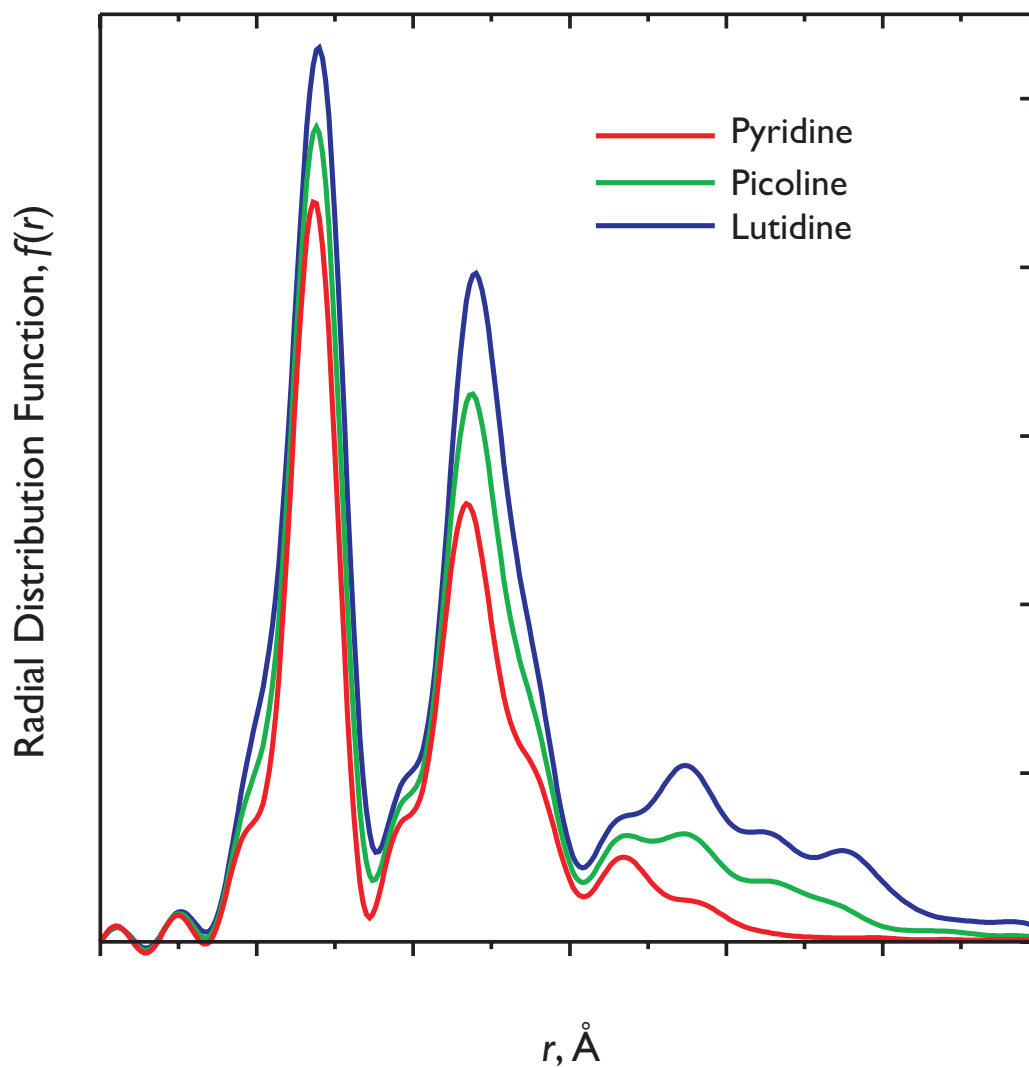
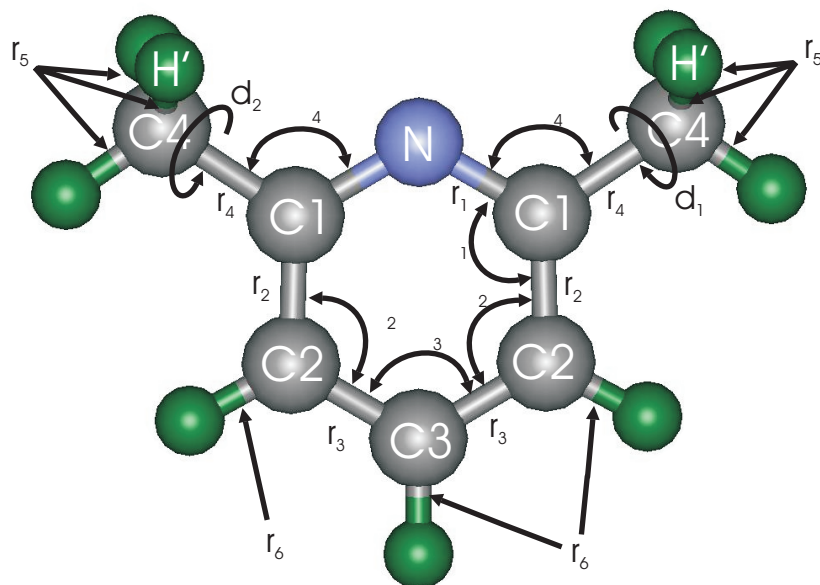


Figure 6-7. Comparison of ground-state structures of all three azines. The radial distribution curves clearly show that on going from pyridine to picoline to lutidine, the progressive addition of a methyl group leaves the direct covalent distances (first peak) nearly unchanged. However, the second nearest-neighbor distances (second peak) and longer indirect distances show significant increase in population with the addition of the methyl groups.



Distances

$r_1(\text{N-C1})$	1.328 ± 0.059	(1.339)
$r_2(\text{C1-C2})$	1.431 ± 0.008	(1.398)
$r_3(\text{C2-C3})$	1.386 ± 0.007	(1.390)
$r_4(\text{C1-C4})$	1.501 ± 0.005	(1.507)
$r_5(\text{H-C4})$	1.090 ± 0.009	(1.092-1.093)
$r_6(\text{H-C2,H-C3})$	1.101 ± 0.017	(1.084-1.085)

Angles

$\angle_1(\text{N-C1-C2})$	120.5 ± 1.1	(122.0)
$\angle_2(\text{C1-C2-C3})$	116.9 ± 0.5	(118.8)
$\angle_3(\text{C2-C3-C2})$	122.4 ± 1.0	(119.1)
$\angle_4(\text{N-C1-C4})$	118.4 ± 0.4	(116.2)
$d_1(\text{NC1C4H'})$	39.1 ± 4.0	(58.8)
$d_2(\text{NC1C4H'})$	1.1 ± 19.8	(58.8)

Figure 6-8. Refined ground-state structure of lutidine. Distances are in ångströms and angles are in degrees. DFT values for the structural parameters are given in parentheses.

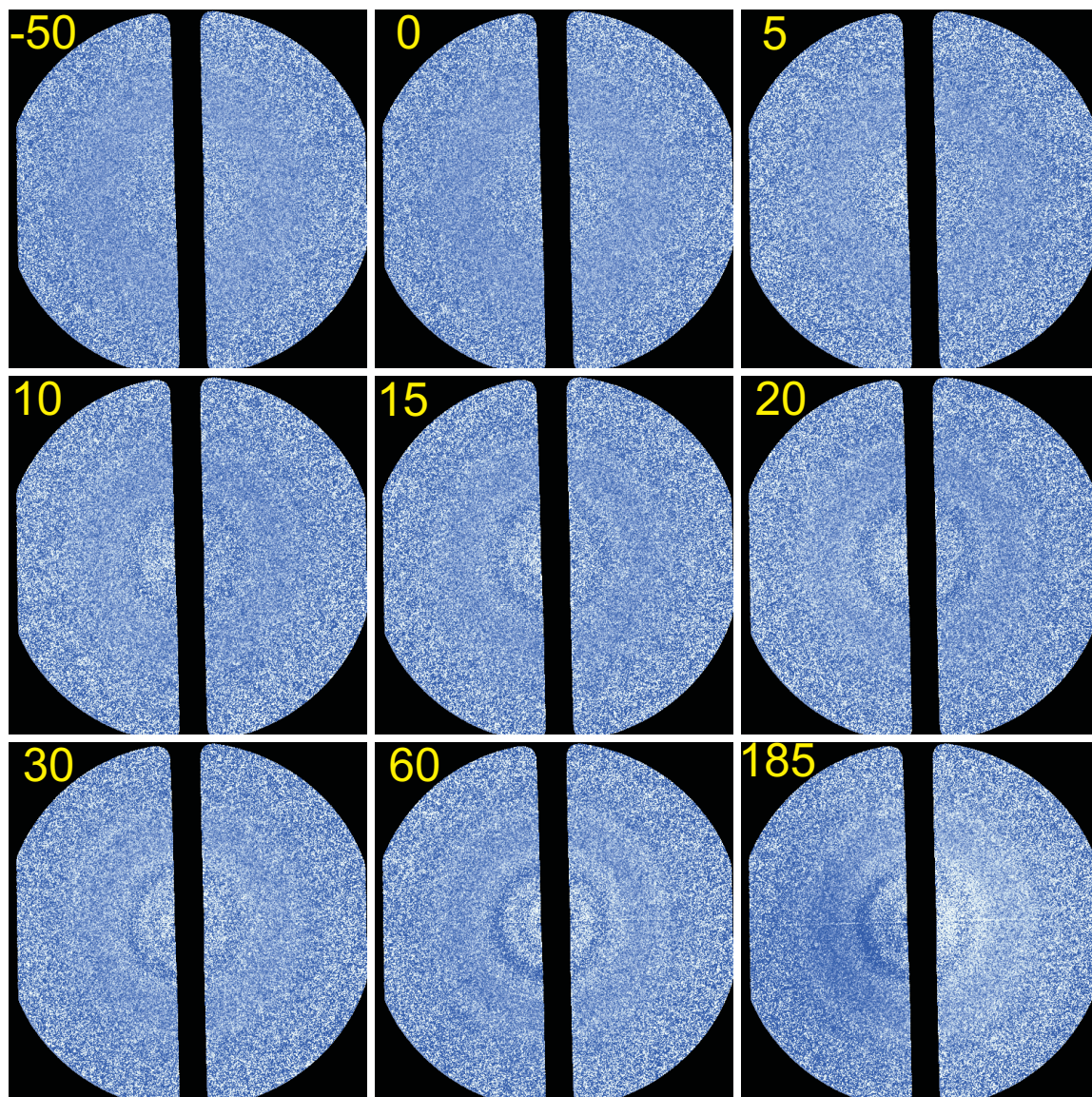


Figure 6-9. Time-resolved 2D diffraction-difference images of pyridine ($t_{\text{ref}} = -90$ ps). Each frame is identified by the relative time delay (in picoseconds) between the laser pump and electron probe pulses. The emergence of rings in the difference images with increasing time delay reflects the ensuing molecular structural dynamics.

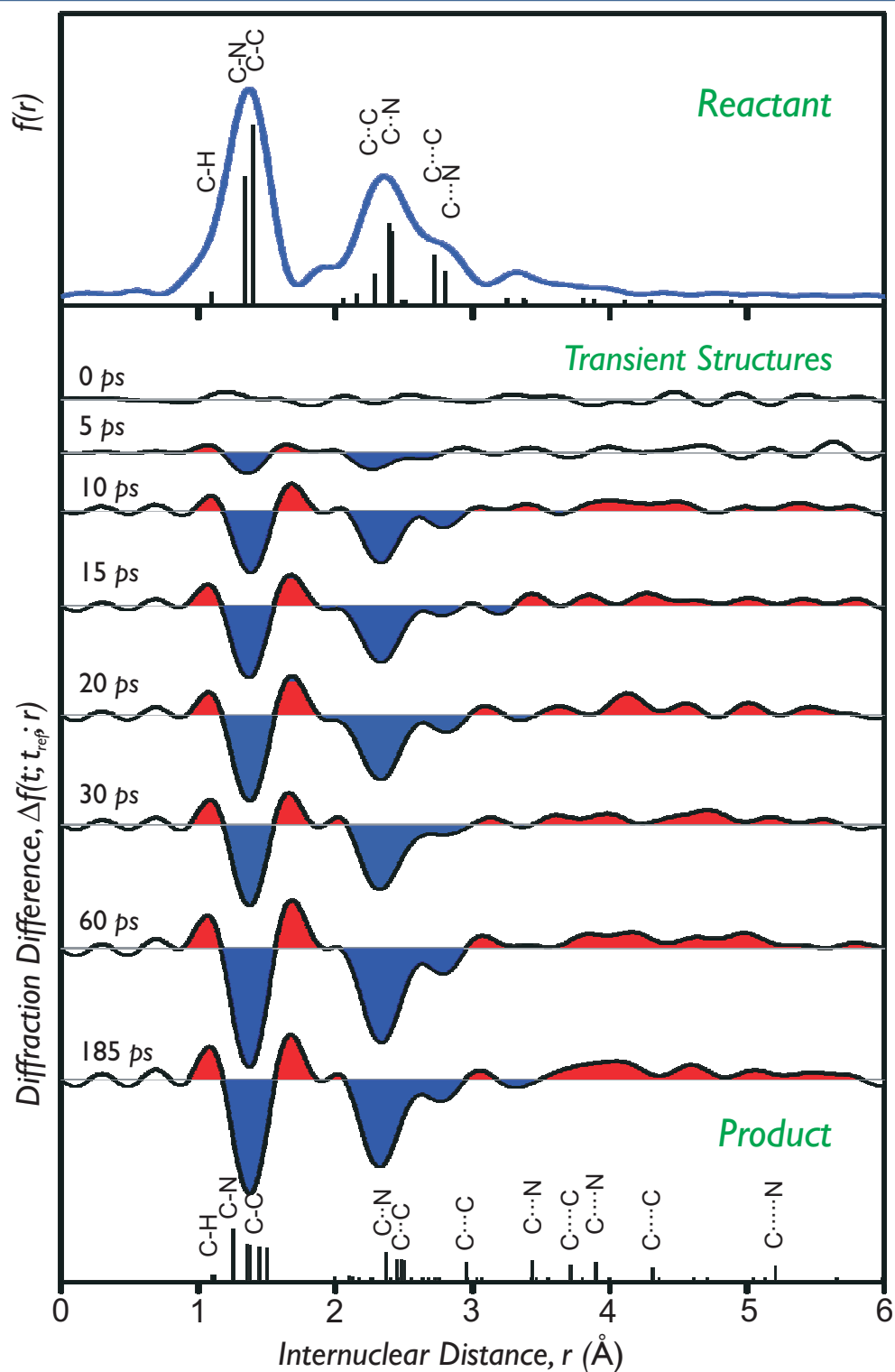


Figure 6-10. Radial distribution curves for pyridine. Parent (*top*) and $\Delta f(t, t_{\text{ref}}, r)$ curves (*bottom*). The vertical lines at the bottom indicate the relative contributions from various internuclear pairs, with the height of each line scaling with $(Z_i Z_j)/r_{ij}$ multiplied by the degeneracy. The *blue* highlighted regions represent net depletion of internuclear pairs (old bonds), whereas the *red* highlighted regions correspond to internuclear pairs with increasing population (new bonds).

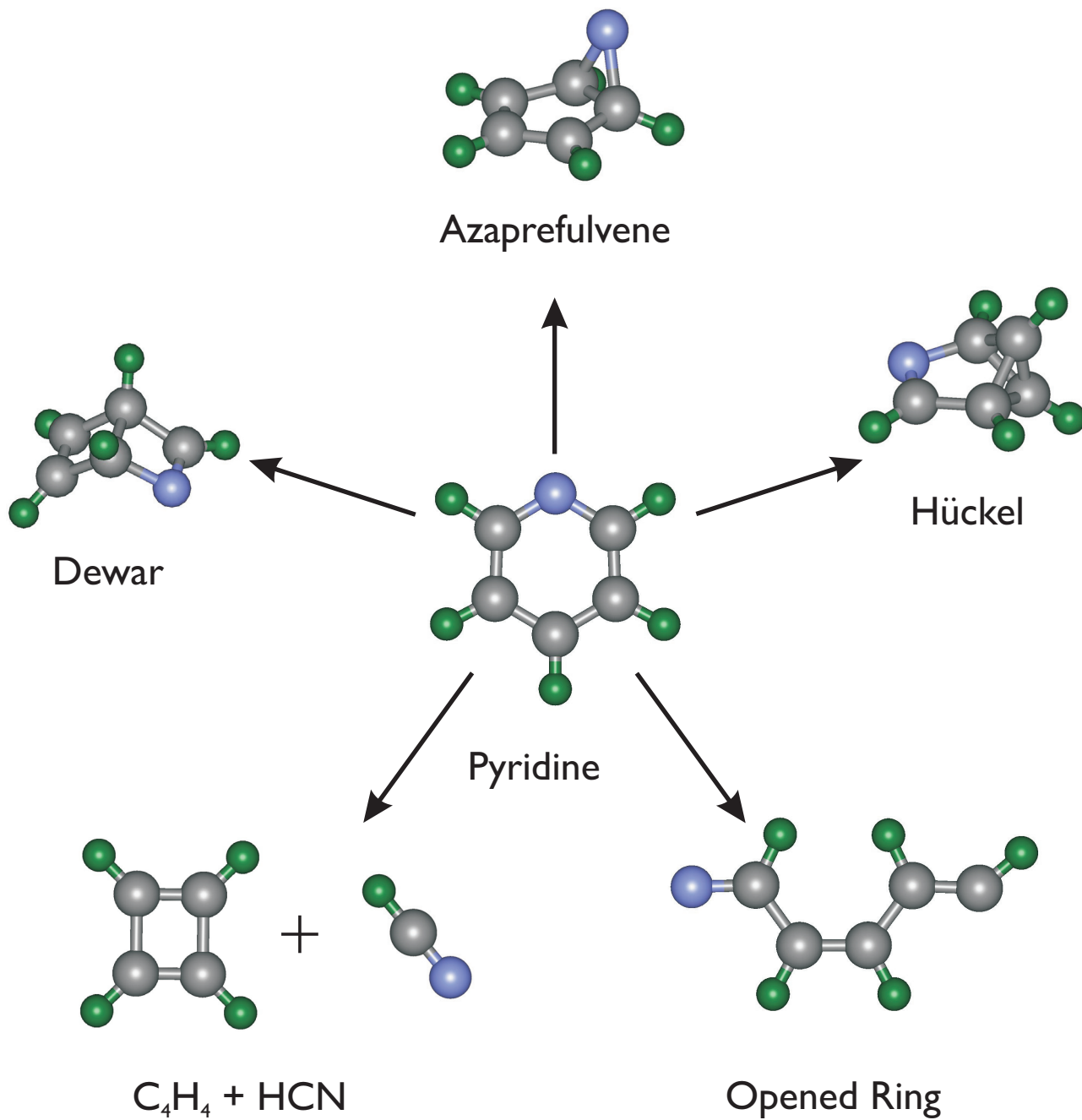


Figure 6-11. Possible structures from reaction of pyridine.

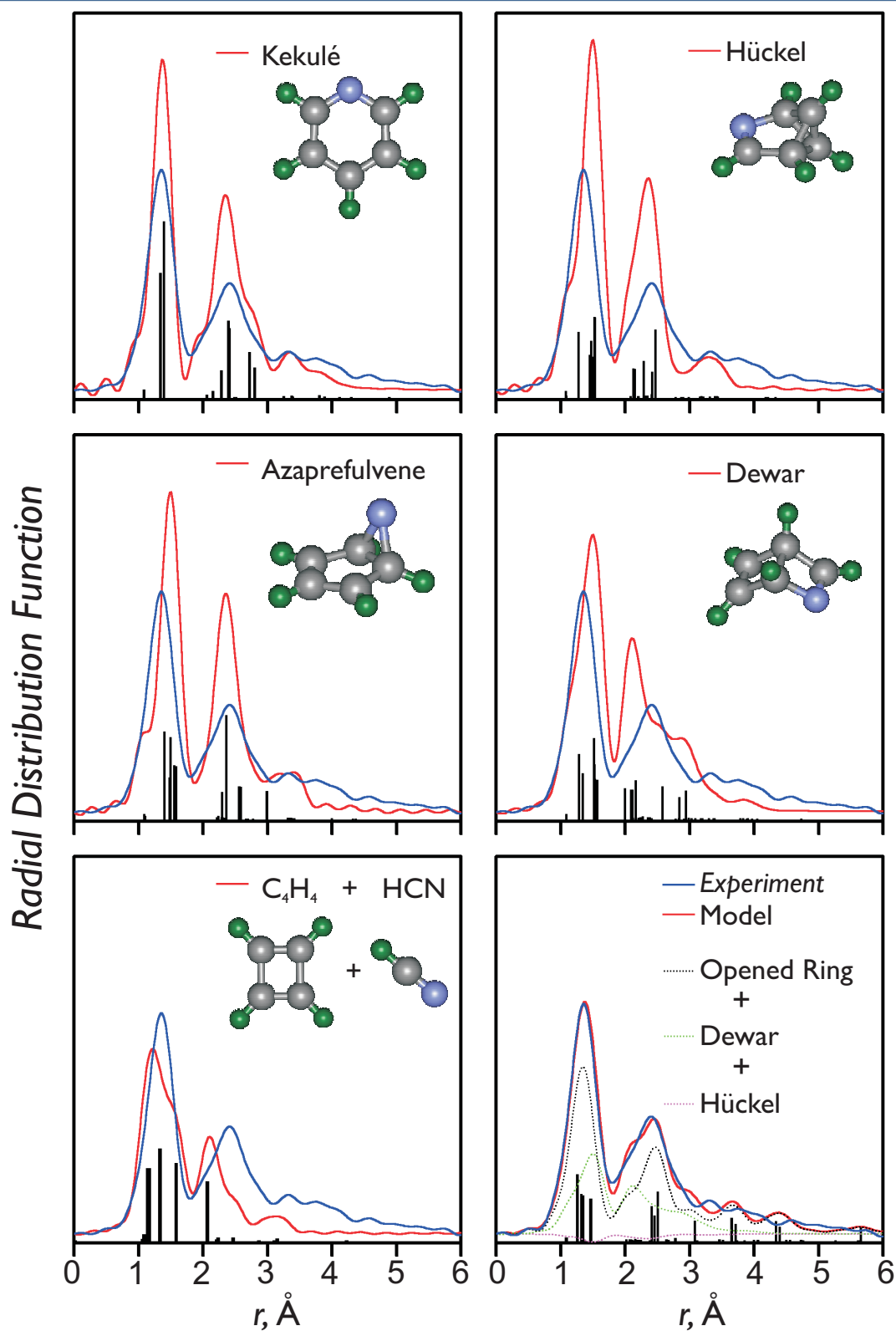
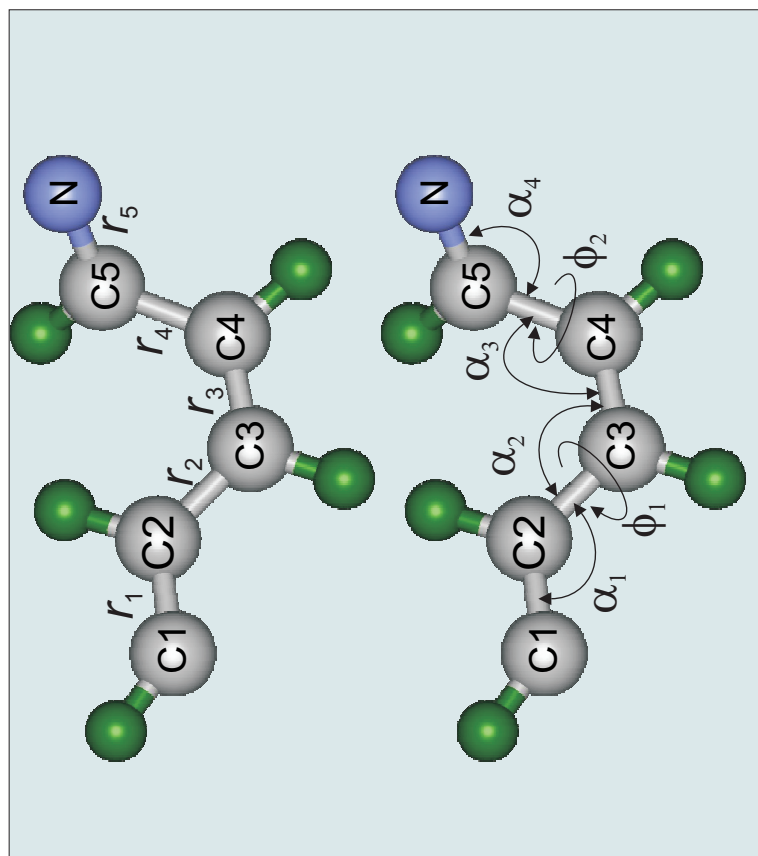


Figure 6-12. Comparisons of the experimental transient-isolated radial distribution $f(r)$ curve (blue) with normalized theoretical $f(r)$ curves (red), predicted for structures resulting from possible reaction channels. Discrepancies between theory and experiment are evident for all channels but one: that of the ring-opened structure with minor contributions from isomers.



Distances

	experiment	DFT
$r_1(\text{C1-C2})$	1.366 ± 0.011	1.318
$r_2(\text{C2-C3})$	1.433 ± 0.012	1.456
$r_3(\text{C3-C4})$	1.342 ± 0.033	1.348
$r_4(\text{C4-C5})$	1.487 ± 0.018	1.466
$r_5(\text{C5-N})$	1.244 ± 0.014	1.256

Angles

	experiment	DFT
$\alpha_1(\text{C1-C2-C3})$	127.7 ± 4.3	124.4
$\alpha_2(\text{C2-C3-C4})$	124.3 ± 3.3	127.0
$\alpha_3(\text{C3-C4-C5})$	123.4 ± 3.6	125.7
$\alpha_4(\text{C4-C5-N})$	121.1 ± 2.7	124.4
$\phi_1(\text{C1C2-C3C4})$	185 ± 36	180
$\phi_2(\text{NC5-C4C3})$	-123 ± 4	-180

Figure 6-13. Refined structural parameters for the pyridine ring-opened product compared to the corresponding values predicted by quantum chemical calculations. Distances are in ångströms, and angles are in degrees. Note that while the quantum calculations are for the *equilibrium* ring-opened structure, our refined structure accounts also for torsions that have a low-energy barrier; hence the discrepancy in ϕ_2 .

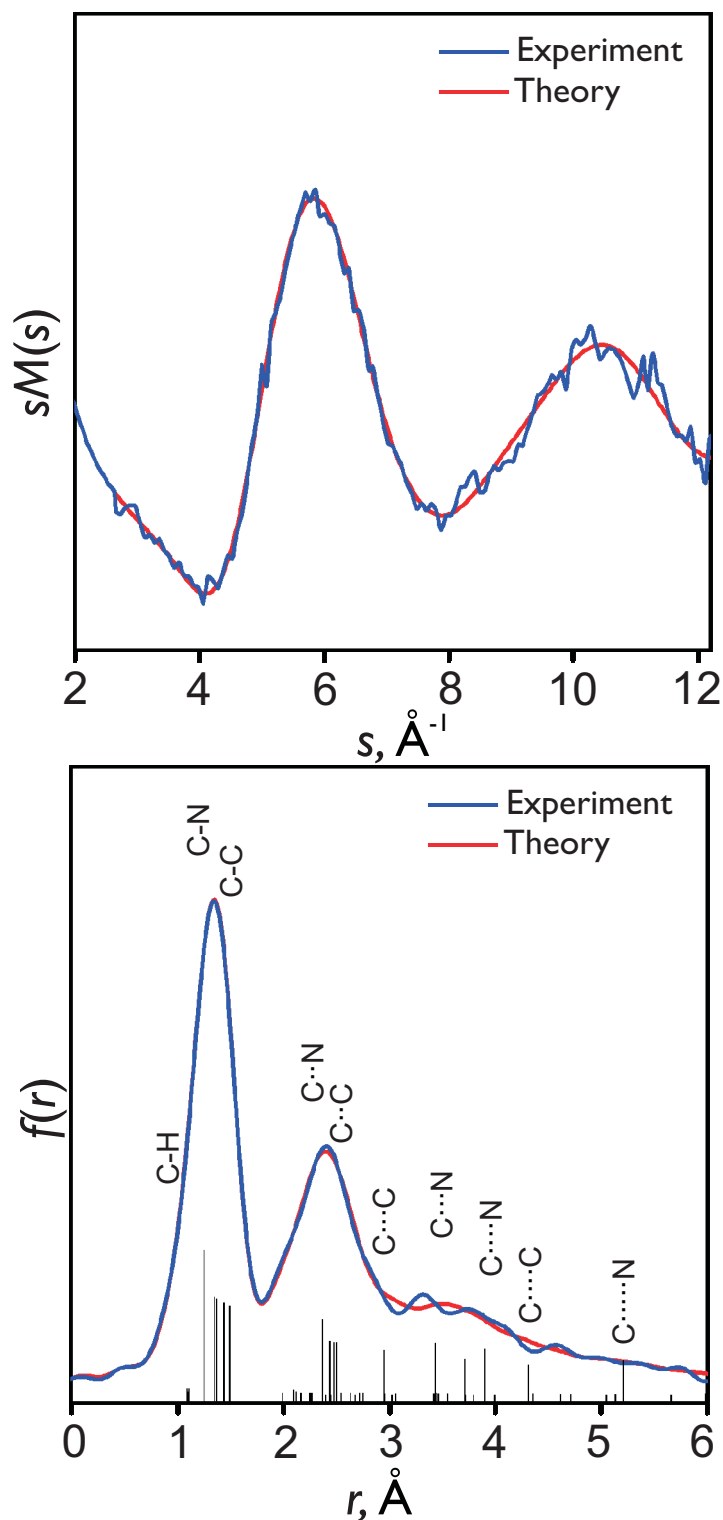


Figure 6-14. Refined ring-opened pyridine structure. Shown are the experimental diffraction (time-averaged) transient-only curves (blue) compared to theoretical curves corresponding to the ring-opened structure with mean l values 70-100% larger than those obtained at 403 K (red). The modified molecular scattering $sM(s)$ curves are shown on top, and the corresponding radial distribution $f(r)$ curves are shown below.

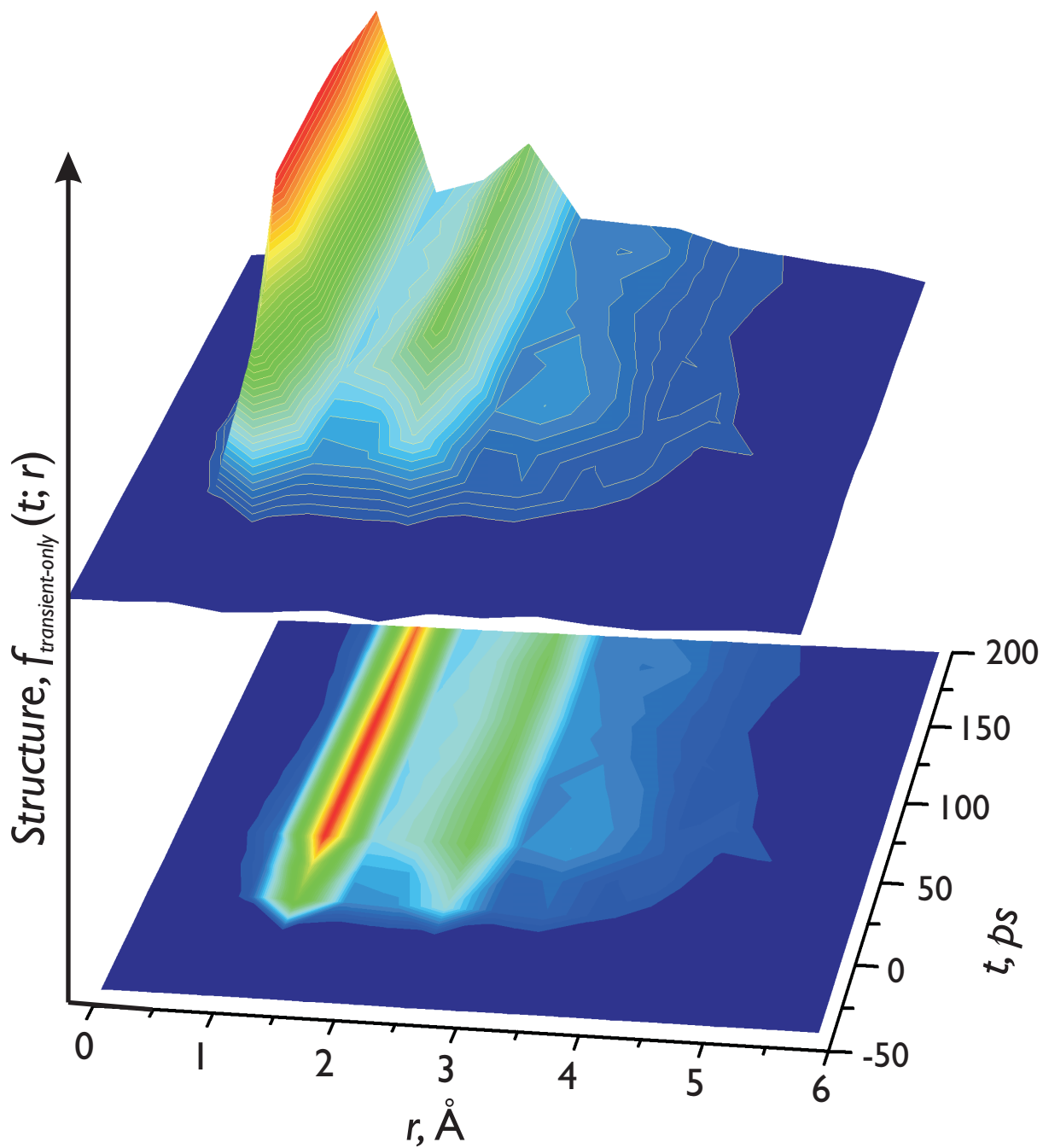


Figure 6-15. Pyridine structure and population change with time. The transient-isolated $f(r)$ curves show the formation of product structures following excitation. The 2D plot indicates the range of internuclear distances (0-6 \AA) and their change as a function of time; see text.

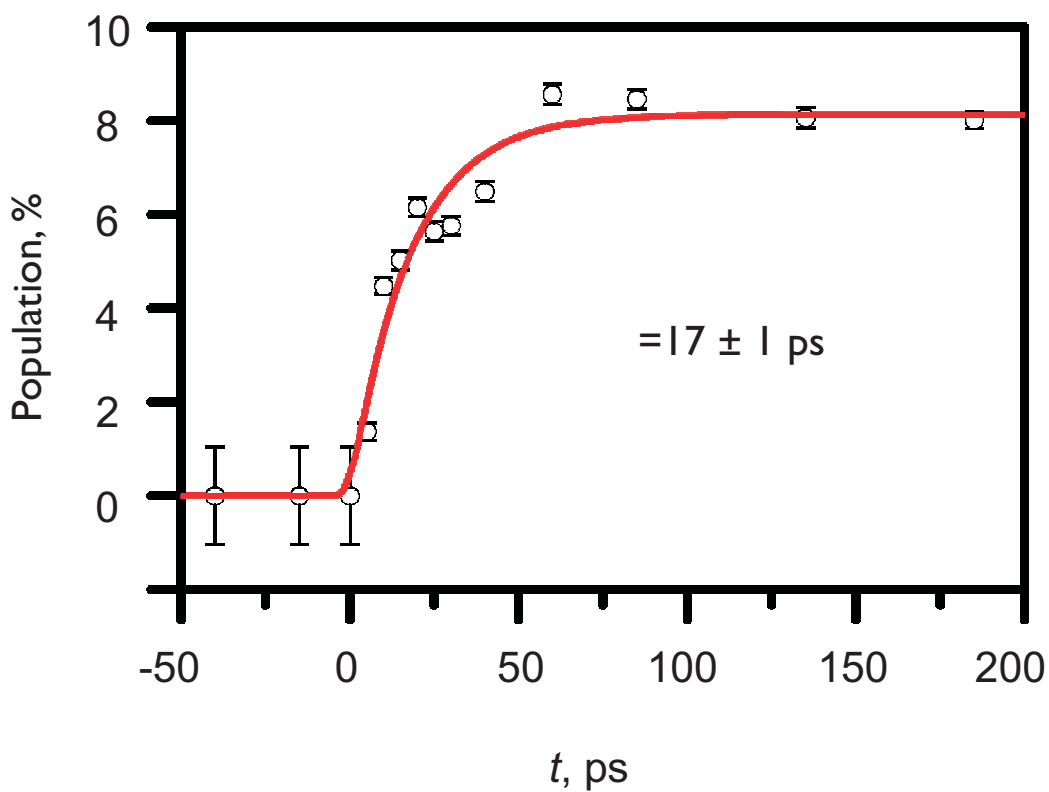


Figure 6-16. Temporal dependence of the product fraction, which fits a single-component rise (i.e., the formation of the pyridine ring-opened structure) and yields a time constant of 17 ± 1 ps.

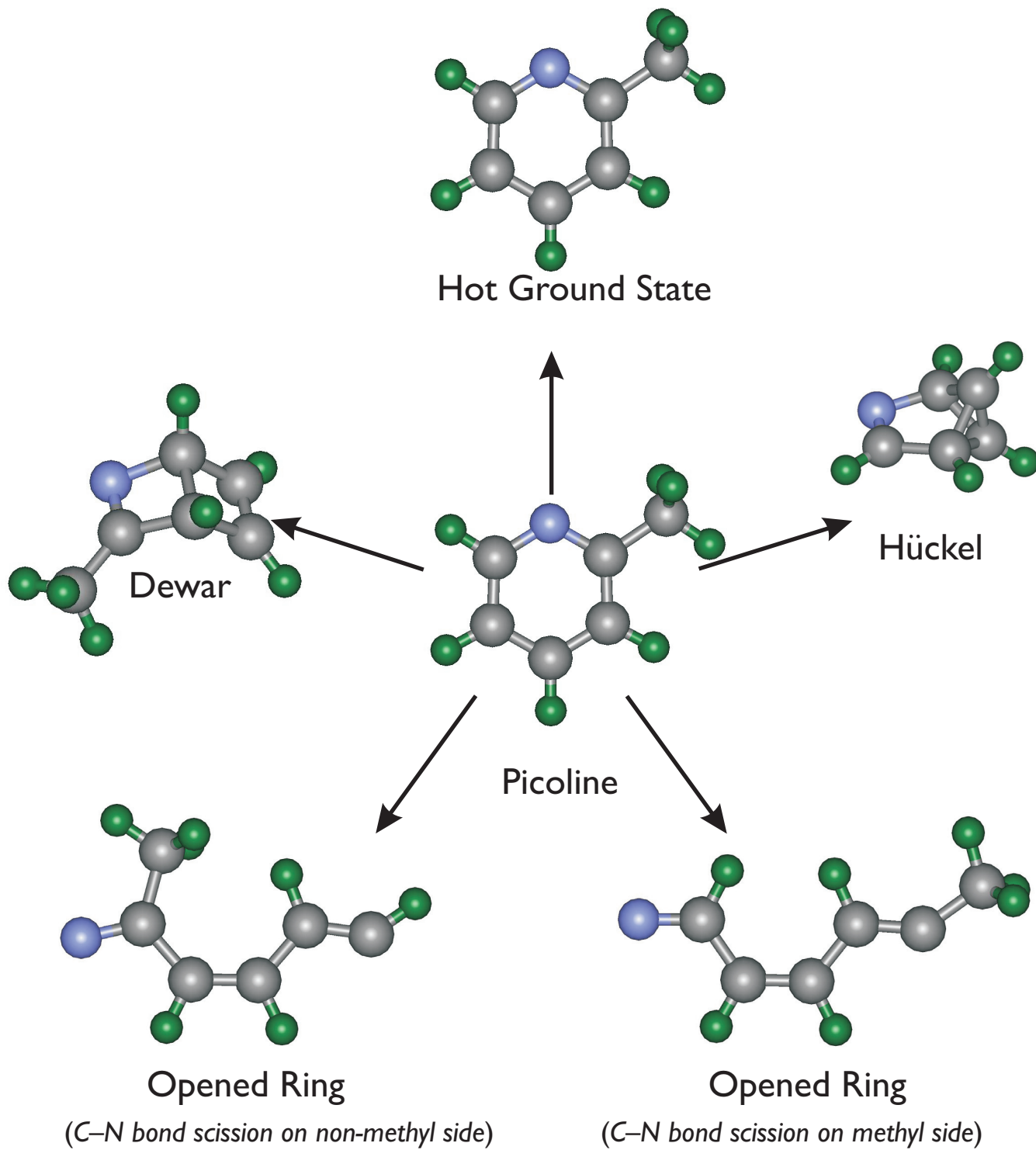


Figure 6-17. Possible structures from reaction of picoline.

Distances		
r1(N-Cl)	1.277 ± 0.022	(1.259)
r2(Cl-C2)	1.483 ± 0.009 *	(1.485)
r3(C2-C3)	1.346 ± 0.010 **	(1.345)
r4(C3-C4)	1.463 *	(1.454)
r5(C4-C5)	1.316 **	(1.313)
r6(Cl-C6)	1.527 *	(1.525)

Angles		
a1(N-Cl-C2)	116.6 ± 2.4 *	(124.4)
a2(Cl-C2-C3)	134.3 ± 2.0 **	(125.9)
a3(C2-C3-C4)	133.3 **	(124.3)
a4(C3-C4-C5)	128.6 ± 11.9	(126.4)
a5(C6-Cl-C2)	121.7 *	(116.5)
d1(N-Cl, C2-C3)	-21.7 ± 34.7	(0.0)
d2(C2-C3, C4-C5)	-127.3 ± 33.2	(180.0)

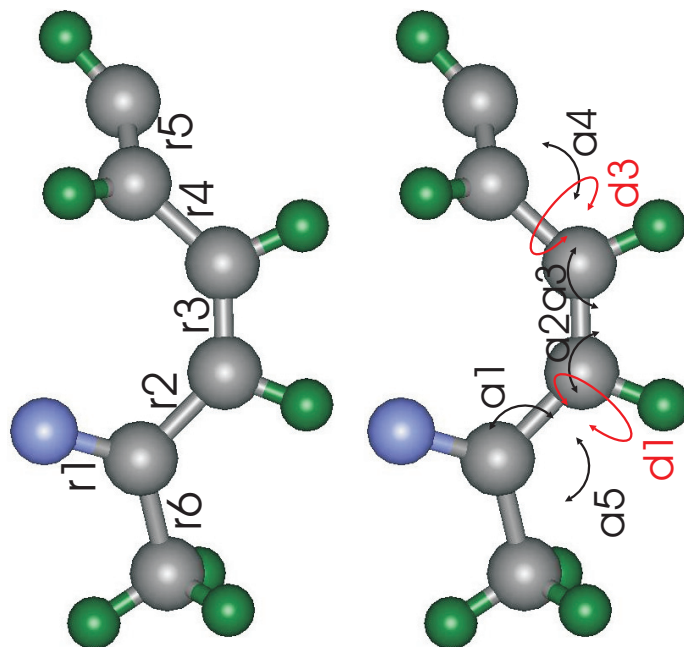


Figure 6-18. Refined structural parameters for the picoline ring-opened product compared to the corresponding values predicted by quantum chemical calculations (given in parentheses). Distances are in ångströms, and angles are in degrees. Note that while the quantum calculations are for the *equilibrium* ring-opened structure, our refined structure accounts also for torsions that have a low-energy barrier. The parameters marked with * and ** were not independently refined, but were derived from other best-fit distances.

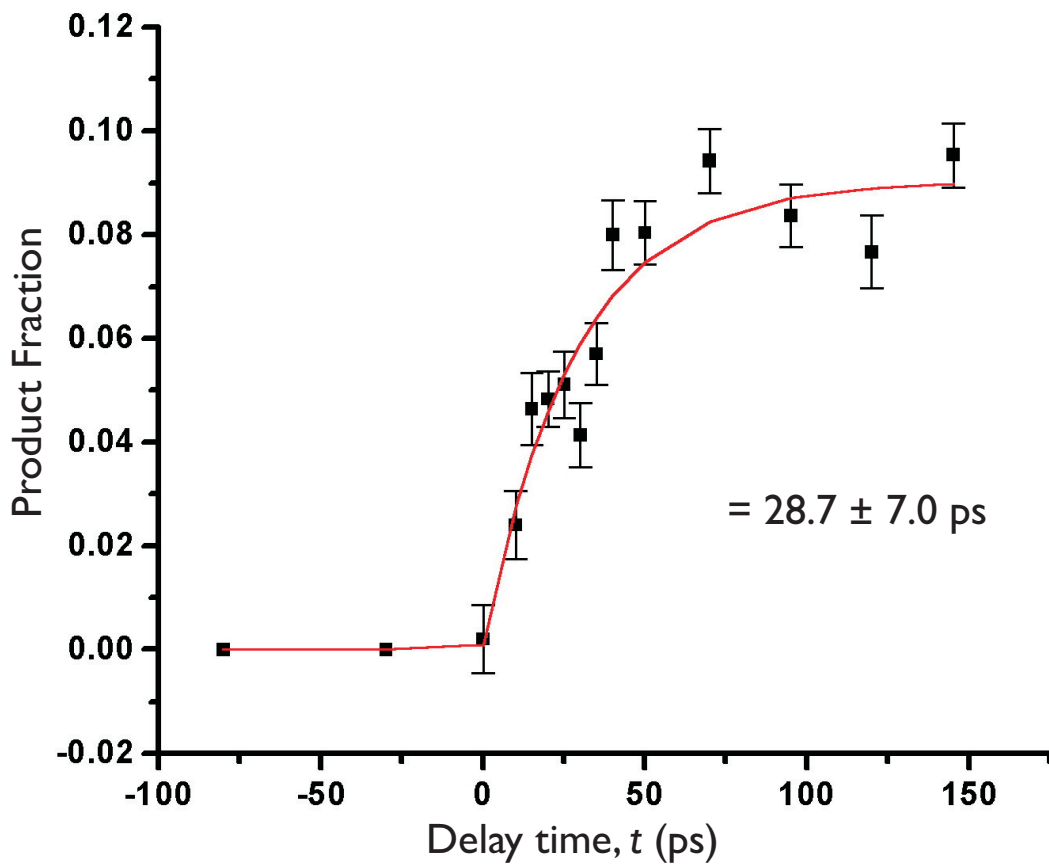


Figure 6-19. Temporal dependence of the product fraction, which fits a single-component rise (i.e., the formation of the picoline ring-opened structure) and yields a time constant of 28.7 ± 7.0 ps.

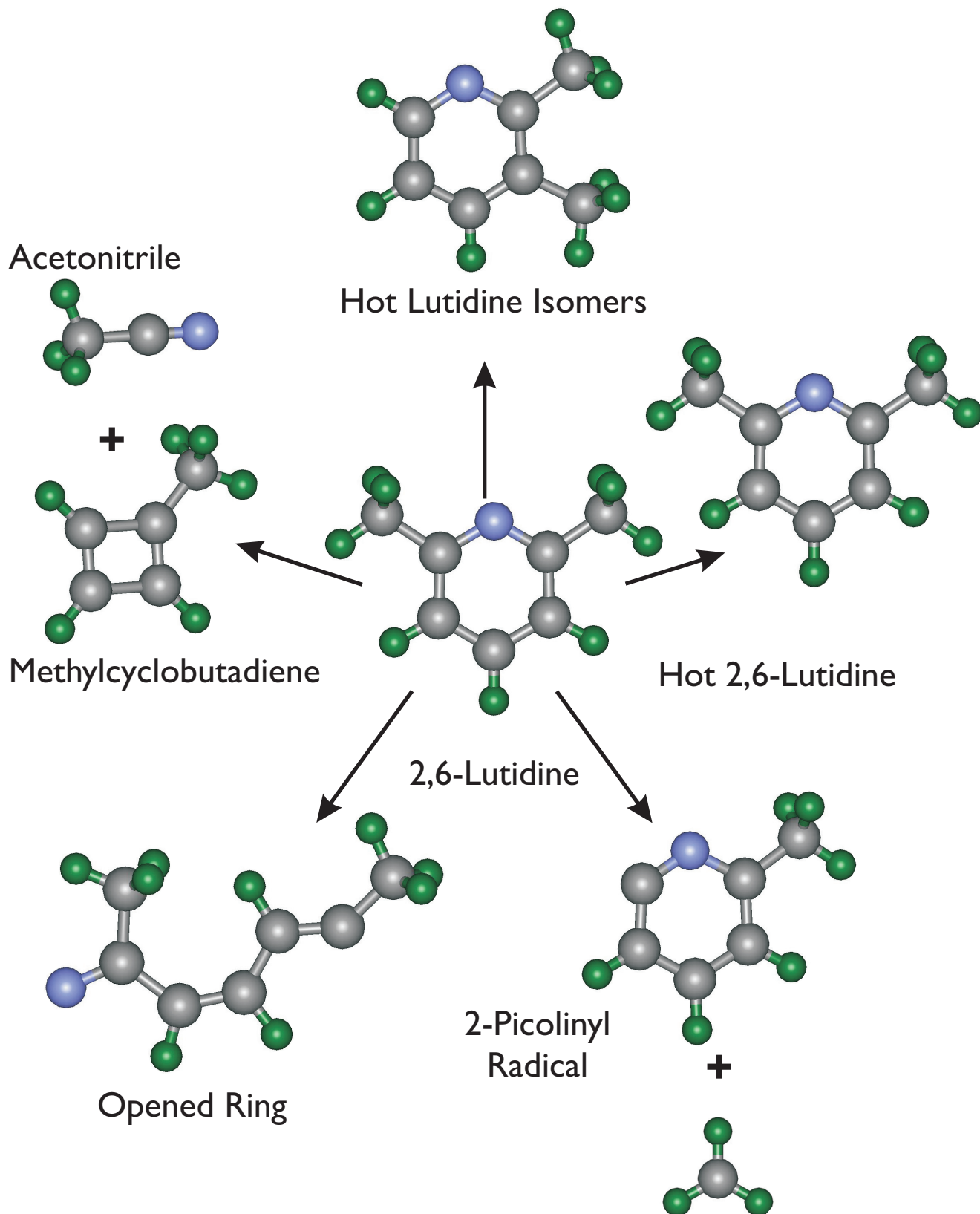


Figure 6-21. Possible structures from reaction of lutidine.

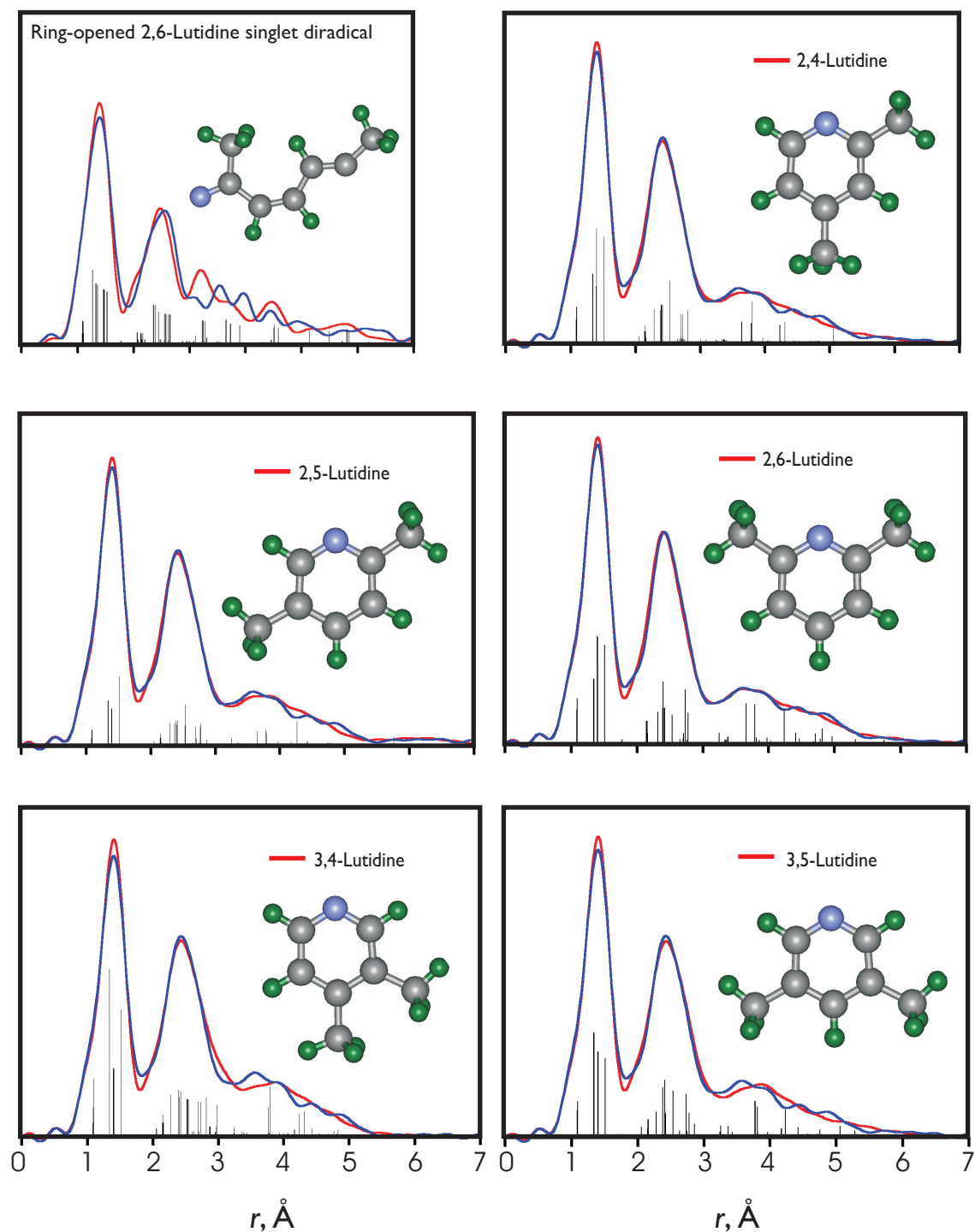


Figure 6-22. Comparisons of the experimental transient-isolated radial distribution $f(r)$ curve (blue) to normalized theoretical $f(r)$ curves (red), predicted for the structures resulting from various possible reaction channels. Unlike pyridine, the ring-opened diradical does not fit the data. However, the hot ground-state of lutidine isomers provides excellent fit to the data.

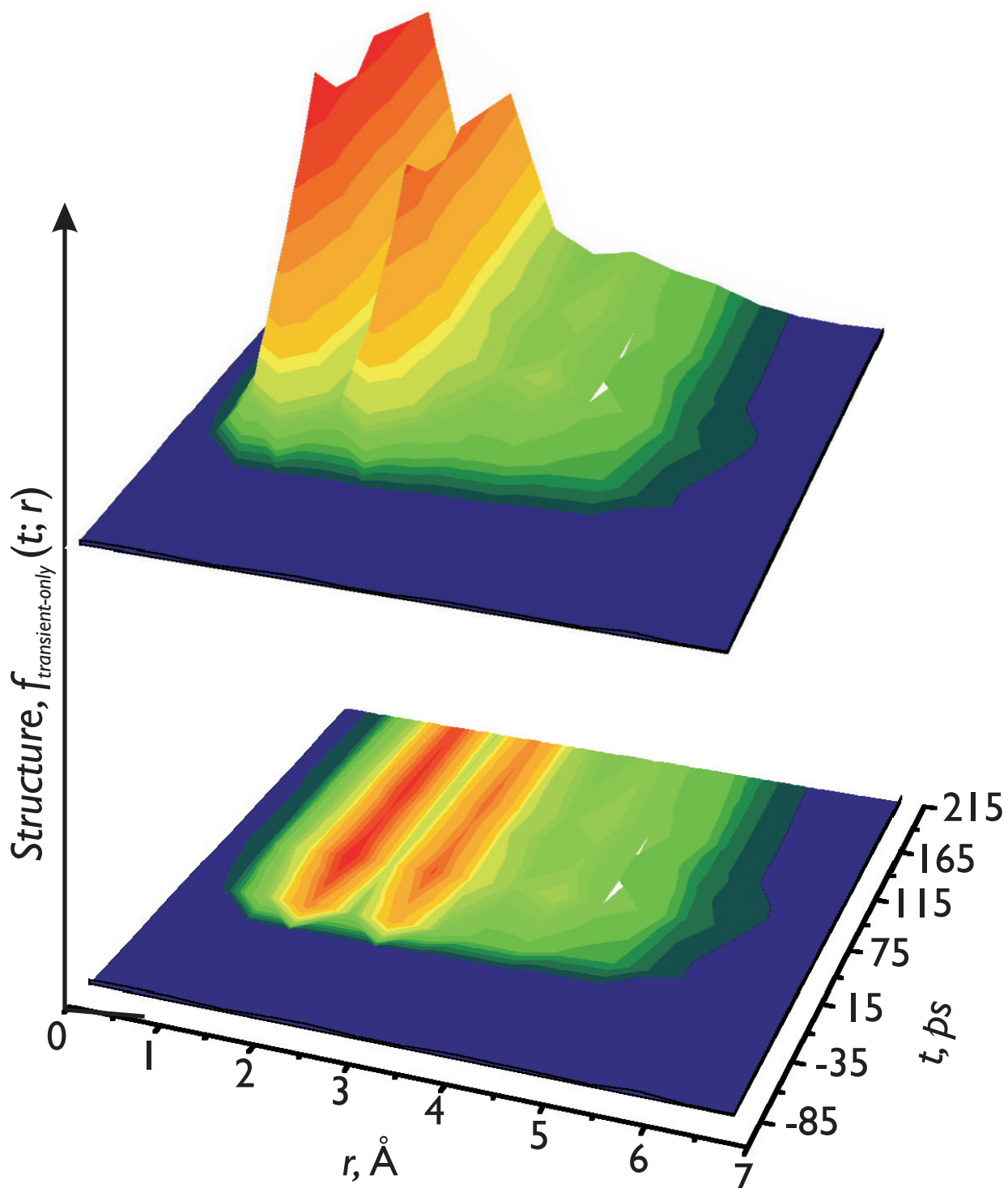


Figure 6-23. Lutidine structure and population change with time. The transient-isolated $f(r)$ curves show the formation of product structures following excitation. The 2D plot indicates the range of internuclear distances (0-7 Å) and their change as a function of time; see text.

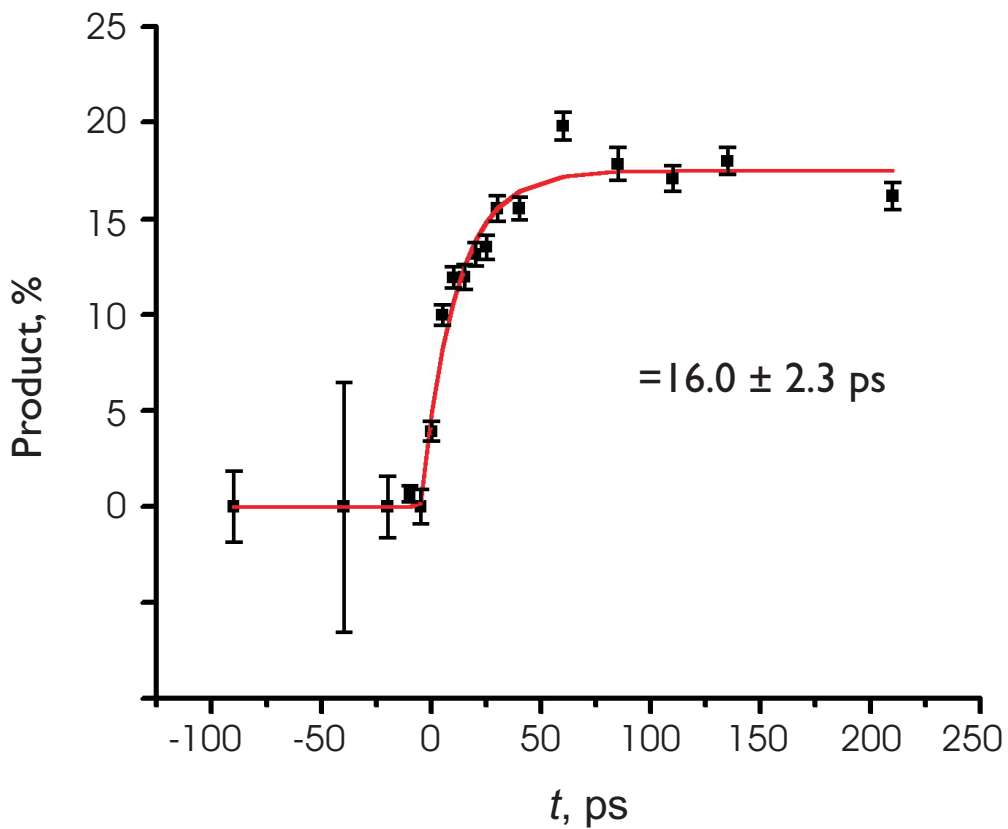


Figure 6-24. Temporal dependence of the product fraction, which fits a single-component rise (i.e., the formation of the lutidine hot ground-state structures) and yields a time constant of 16 ± 2.3 ps.

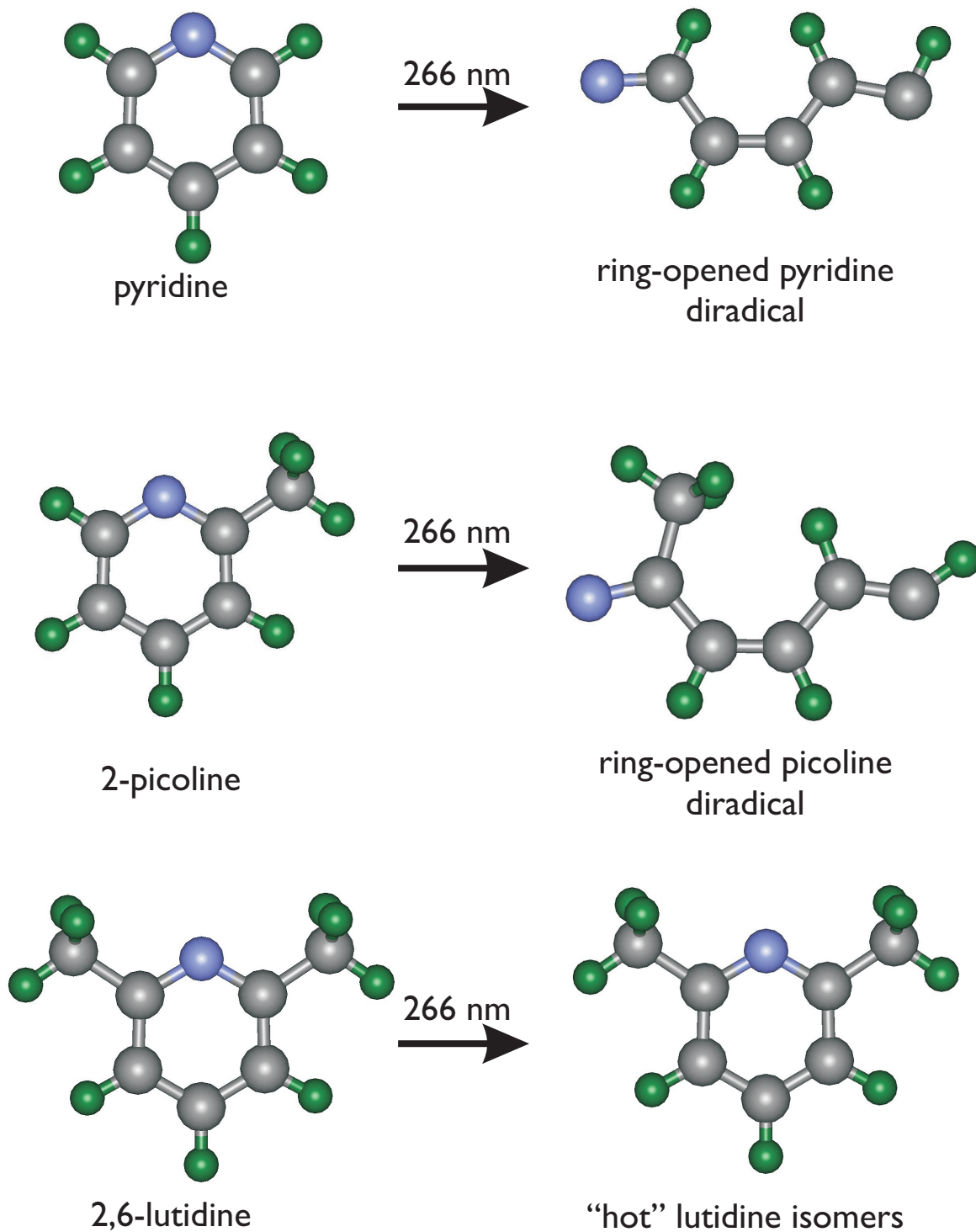


Figure 6-25. Photochemistry of azines elucidated by UED-3.

References

1. Otis, C. E.; Knee, J. L.; Johnson, P. M., *J. Phys. Chem.* **1983**, *87*, 2232.
2. Villa, E.; Amirav, A.; Lim, E. C., *J. Phys. Chem.* **1988**, *92*, 5393.
3. Callomon, J. H.; Parkin, J. E.; Lopezdel. R, *Chem. Phys. Lett.* **1972**, *13*, 125.
4. Knight, A. E. W.; Parmenter, C. S., *Chem. Phys.* **1976**, *15*, 85.
5. Yamazaki, I.; Baba, H., *J. Chem. Phys.* **1977**, *66*, 5826.
6. Yamazaki, I.; Sushida, K.; Baba, H., *J. Chem. Phys.* **1979**, *71*, 381.
7. Hochstrasser, R. M.; Marzzacco, C. A., In *Molecular Luminescence*, Lim, E. C., Ed., Benjamin: New York, 1969.
8. Wassam, W. A.; Lim, E. C., *J. Chem. Phys.* **1978**, *68*, 433.
9. Wassam, W. A.; Lim, E. C., *Chem. Phys. Lett.* **1977**, *52*, 295.
10. Wassam, W. A.; Lim, E. C., *J. Chem. Phys.* **1978**, *69*, 2175.
11. Wassam, W. A.; Lim, E. C., *J. Mol. Struct.* **1978**, *47*, 129.
12. Lim, E. C., *J. Phys. Chem.* **1986**, *90*, 6770.
13. Yamazaki, I.; Murao, T.; Yamanaka, T.; Yoshihara, K., *Faraday Discuss.* **1983**, 395.
14. Yamazaki, I.; Murao, T.; Yoshihara, K.; Fujita, M.; Sushida, K.; Baba, H., *Chem. Phys. Lett.* **1982**, *92*, 421.
15. Yamazaki, I.; Sushida, K.; Baba, H., *J. Lumines.* **1979**, *18-9*, 425.

16. Ihee, H.; Lobastov, V. A.; Gomez, U.; Goodson, B. M.; Srinivasan, R.; Ruan, C.-Y.; Zewail, A. H., *Science* **2001**, *291*, 458.
17. Srinivasan, R.; Lobastov, V. A.; Ruan, C. Y.; Zewail, A. H., *Helv. Chim. Acta* **2003**, *86*, 1763.
18. Vigliotti, F.; Chen, S. Y.; Ruan, C. Y.; Lobastov, V. A.; Zewail, A. H., *Angew. Chem.-Int. Edit.* **2004**, *43*, 2705.
19. Ruan, C. Y.; Lobastov, V. A.; Vigliotti, F.; Chen, S. Y.; Zewail, A. H., *Science* **2004**, *304*, 80.
20. Ruan, C. Y.; Vigliotti, F.; Lobastov, V. A.; Chen, S. Y.; Zewail, A. H., *Proc. Natl. Acad. Sci. USA* **2004**, *101*, 1123.
21. Thomas, J. M., *Angew. Chem.-Int. Edit.* **2004**, *43*, 2606.
22. Schomaker, V.; Pauling, L., *J. Am. Chem. Soc.* **1939**, *61*, 1769.
23. Almenningen, A.; Bastiansen, O.; Hansen, L., *Acta Chem. Scand.* **1955**, *9*, 1306.
24. Pyckhout, W.; Horemans, N.; Van Alsenoy, C.; Geise, H. J.; Rankin, D. W. H., *J. Mol. Struct.* **1987**, *156*, 315.
25. Mootz, D.; Wussow, H.-G., *J. Chem. Phys.* **1981**, *75*, 1517.
26. Mata, F.; Quintana, M. J.; Sørensen, G. O., *J. Mol. Struct.* **1977**, *42*, 1.
27. Wong, K. N.; Colson, S. D., *J. Mol. Spectrosc.* **1984**, *104*, 129.
28. Walters, V. A.; Snavely, D. L.; Colson, S. D.; Wiberg, K. B.; Wong, K. N., *J. Phys. Chem.* **1986**, *90*, 592.

-
29. Ureña, F. P.; Gómez, M. F.; González, J. J. L.; Torres, E. M., *Spectroc. Acta Pt. A-Molec. Biomolec. Spectr.* **2003**, *59*, 2815.
30. Kjaergaard, H. G.; Proos, R. J.; Turnbull, D. M.; Henry, B. R., *J. Phys. Chem.* **1996**, *100*, 19273.
31. Cai, Z.-L.; Reimers, J. R., *J. Phys. Chem. A* **2000**, *104*, 8389.
32. Fabian, J.; Lewars, E., *Can. J. Chem.-Rev. Can. Chim.* **2004**, *82*, 50.
33. Martin, J. M. L.; VanAlsenoy, C., *J. Phys. Chem.* **1996**, *100*, 6973.
34. Szafran, M.; Koput, J., *J. Mol. Struct.* **2001**, *565*, 439.
35. Becucci, M.; Lakin, N. M.; Pietraperzia, G.; Salvi, P. R.; Castellucci, E.; Kerstel, E. R. T., *J. Chem. Phys.* **1997**, *107*, 10399.
36. Bond, A. D.; Davies, J. E., *Acta Crystallogr. Sect. E.-Struct Rep. Online* **2001**, *57*, 01089.
37. Vorontsov, I. I.; Almásy, L.; Antipin, M. Y., *J. Mol. Struct.* **2002**, *610*, 271.
38. Bond, A. D.; Davies, J. E.; Kirby, A. J., *Acta Crystallogr. Sect. E.-Struct Rep. Online* **2001**, *57*, 01242.
39. Porcinai, S.; Foggi, P., *Nuovo Cimento Soc. Ital. Fis. D-Condens. Matter At. Mol. Chem. Phys. Fluids Plasmas Biophys.* **1997**, *19*, 889.
40. Zhong, D. P.; Diao, E. W. G.; Bernhardt, T. M.; De Feyter, S.; Roberts, J. D.; Zewail, A. H., *Chem. Phys. Lett.* **1998**, *298*, 129.
41. Prather, K. A.; Lee, Y. T., *Isr. J. Chem.* **1994**, *34*, 43.
42. Wilzbach, K. E.; Rausch, D. J., *J. Am. Chem. Soc.* **1970**, *92*, 2178.

-
43. Chachisvilis, M.; Zewail, A. H., *J. Phys. Chem. A* **1999**, *103*, 7408.
44. Chapman, O. L.; McIntosh, C. L.; Pacansky, J., *J. Am. Chem. Soc.* **1973**, *95*, 614.
45. Johnstone, D. E.; Sodeau, J. R., *J. Phys. Chem.* **1991**, *95*, 165.
46. Kudoh, S.; Takayanagi, M.; Nakata, M., *J. Photochem. Photobiol. A-Chem.* **1999**, *123*, 25.
47. Sobolewski, A. L.; Domcke, W., *Chem. Phys. Lett.* **1991**, *180*, 381.
48. Ruan, C. Y.; Lobastov, V. A.; Srinivasan, R.; Goodson, B. M.; Ihee, H.; Zewail, A. H., *Proc. Natl. Acad. Sci. USA* **2001**, *98*, 7117.
49. Caplain, S.; Catteau, J. P.; Lablache-Combier, A., *Journal of the Chemical Society D-Chemical Communications* **1970**, 1475.
50. Nakata, M., *Bull. Chem. Soc. Jpn.* **2002**, *75*, 1173.
51. Noyes, J. W. A.; Al-Ani, K. E., *Chem. Rev.* **1974**, *74*, 29.
52. Lemaire, J., *J. Phys. Chem.* **1967**, *71*, 612.
53. Linnell, R. H.; Noyes, W. A., *J. Am. Chem. Soc.* **1951**, *73*, 3986.
54. Mathias, E.; Heicklen, J., *Mol. Photochem.* **1972**, *4*, 483.
55. Chesko, J. D.; Lee, Y. T., In *Highly Excited Molecules*, 1997, 107.
56. Pavlik, J. W.; Laohasurayotin, S., *Tetrahedron Lett.* **2003**, *44*, 8109.
57. Mackie, J. C.; Colket III, M. B.; Nelson, P. F., *J. Phys. Chem.* **1990**, *94*, 4099.

-
58. Jones, J.; Bacskey, G. B.; Mackie, J. C.; Doughty, A., *J. Chem. Soc.-Faraday Trans.* **1995**, *91*, 1587.
59. Politzer, P.; Murray, J. S.; Concha, M. C., *J. Phys. Chem. A* **1998**, *102*, 6697.
60. Barckholtz, C.; Barckholtz, T. A.; Hadad, C. M., *J. Am. Chem. Soc.* **1999**, *121*, 491.
61. Liu, R.; Huang, T. T.-S.; Tittle, J.; Xia, D., *J. Phys. Chem. A* **2000**, *104*, 8368.
62. Davico, G. E.; Bierbaum, V. M.; DePuy, C. H.; Ellison, G. B.; Squires, R. R., *J. Am. Chem. Soc.* **1995**, *117*, 2590.
63. Hore, N. R.; Russell, D. K., *J. Chem. Soc.-Perkin Trans. 2* **1998**, 269.
64. Kiefer, J. H.; Zhang, Q.; Kern, R. D.; Yao, J.; Jursic, B., *J. Phys. Chem. A* **1997**, *101*, 7061.
65. Yokoyama, A.; Zhao, X.; Hintsä, E. J.; Continetti, R. E.; Lee, Y. T., *J. Chem. Phys.* **1990**, *92*, 4222.
66. Sevy, E. T.; Muyskens, M. A.; Rubin, S. M.; Flynn, G. W.; Muckerman, J. T., *J. Chem. Phys.* **2000**, *112*, 5829.
67. Salcedo, R., *Theochem-J. Mol. Struct.* **2004**, *674*, 125.
68. Baldrige, K. K.; Gordon, M. S., *J. Am. Chem. Soc.* **1988**, *110*, 4204.
69. Caplain, S.; Lablanch, A., *Journal of the Chemical Society D-Chemical Communications* **1970**, 1247.

-
70. Roebke, W., *J. Phys. Chem.* **1970**, *74*, 4198.
71. Kudoh, S.; Takayanagi, M.; Nakata, M., *Chem. Phys. Lett.* **1999**, *308*, 403.
72. Egorova, M.; Zhao, Y.; Kukula, P.; Prins, R., *J. Catal.* **2002**, *206*, 263.
73. Doughty, A.; Mackie, J. C., *J. Phys. Chem.* **1992**, *96*, 10339.
74. Pavlik, J. W.; Kebede, N.; Thompson, M.; Day, A. C.; Barltrop, J. A., *J. Am. Chem. Soc.* **1999**, *121*, 5666.
75. Tsubouchi, M.; Suzuki, T., *J. Phys. Chem. A* **2003**, *107*, 10897.

7

NON-EQUILIBRIUM STRUCTURES*

7.1 Introduction

Studies of molecular structures at or near their equilibrium configurations have long provided information on their geometry in terms of bond distances and angles. Far-from-equilibrium structures are relatively unknown—especially for complex systems—and generally, neither their dynamics nor their average geometries can be extrapolated from equilibrium values. For such non-equilibrium structures, vibrational amplitudes and

* Parts of this chapter have been adapted from Ruan, C.-Y.; Lobastov, V.A.; Srinivasan, R.; Goodson, B.M.; Ihee, H.; Zewail, A.H., *Proc. Natl. Acad. Sci. USA* **2001**, *98*, 7117.

bond distances play a central role in phenomena such as energy redistribution and chemical reactivity. UED provides a direct method for probing the nature of complex molecules far from equilibrium. Before considering specific examples of non-equilibrium structural determination, it would be instructive to discuss some key concepts underlying structures at equilibrium and those far-from-equilibrium.

7.2 Concepts of Equilibrium *vs.* Non-equilibrium Structures

In this discussion, we will classify molecular structures into the following four cases:

- (a) Equilibrium, Boltzmann distribution (Type I)—Cold Ground State;
- (b) Equilibrium, Boltzmann distribution (Type II)—Hot Ground State;
- (c) Non-equilibrium, non-Boltzmann distribution (Type I)—Inverted population, ‘negative temperature’; and
- (d) Non-equilibrium, non-Boltzmann distribution (Type II)—Bifurcation of internuclear distances

Differences between diffraction patterns of structures at equilibrium and those far-from-equilibrium can be understood by first considering the case of a single bond (Figs. 7–1 and 7–2). The diffraction of structures far from equilibrium manifests itself as

- i*) increased damping of the oscillating molecular scattering signal; and

ii) apparent shifts in internuclear distance(s).

As seen in Fig. 7-1, simple thermal heating of the molecule results in nearly the same average internuclear distance, but its vibrational amplitude increases with temperature. This elevated l value can be readily observed as enhanced damping of $sM(s)$; the relevant dependence is given by:

$$sM(s) \propto \exp\left(-\frac{1}{2}l^2 s^2\right) \cdot \frac{\sin(sr)}{r} \quad (7-1)$$

This damping is mirrored as broadened peaks in the $f(r)$ curve because of its Fourier (sine) transform relation to $sM(s)$. The damping reflects thermal averaging over the vibrational states in a Boltzmann distribution, given in the harmonic diatomic limit (l_h) as:¹

$$l_h^2 = \frac{h}{8\pi^2 \mu \nu} \coth\left(\frac{h\nu}{2kT}\right), \quad (7-2)$$

where μ is the reduced mass, ν is the vibrational frequency, k is the Boltzmann constant, and T is the vibrational temperature. In the limit of high energy, l_h scales as the square root of the vibrational temperature. In contrast to this thermal (Boltzmann) limit where the structures are near equilibrium, structures far-from-equilibrium would result if the system were

created with inverted (non-Boltzmann) distributions.

Figures 7–1 and 7–2 show our calculations for the case where wave packets are produced with Gaussian energy distributions at different mean energies, which, in turn, give rise to the corresponding probability densities in the long-time limit. Significantly inverted populations would lead to a clear bifurcation of the internuclear density, inducing splitting and shifting of peaks in the $f(r)$ curve. However, in the case where these non-Boltzmann populations occur at relatively low energies in the potential well, the density bifurcation becomes narrower, and the $f(r)$ curve may not display shifted peaks, but would exhibit increased damping—thus mimicking Boltzmann distributions albeit with exceptionally high l values. These concepts of enhanced damping and shifted bond distances, shown here for a molecule with a single bond far from equilibrium, are directly relevant to complex molecular structures where energy redistribution may or may not be complete, and where certain bonds determine the reaction coordinate.

In what follows, we discuss the UED determination of non-equilibrium structures of types I and II. UED Studies of transient structures for two cyclic hydrocarbons at high internal energies reveal markedly different structural behavior. For cyclohepta-1,3,5-triene (CHT), excitation results in the formation of hot ground-state structures (Scheme 7–1) with bond distances similar to those of the initial structure (non-equilibrium, Type I). In

contrast, cyclohexa-1,3-diene (CHD) undergoes a ring-opening reaction (Scheme 7–2) to form hexa-1,3,5-triene (HT) in its far-from-equilibrium state, as manifested by an inverted population in the torsional degrees of freedom and by highly elevated vibrational amplitudes (non-equilibrium, Type II).

7.3 Experimental Methodology

UED data were obtained with our third-generation apparatus. Samples of CHT (Fluka, 95%) and CHD (Aldrich, 97%) were degassed with several freeze–pump–thaw cycles, and high-purity xenon (Spectra Gases, 99.999%) was used as an atomic reference gas. The nozzle temperature for the diffraction experiments was maintained at 130 °C and 120 °C for CHT and CHD, respectively. To establish the point of reference for temporal studies, the zero-of-time was determined via photoionization-induced lensing of the undiffracted electron beam using CF₃I gas (Aldrich, 99%).

7.4 Data Processing and Analysis

A. Background Subtraction

A significant, slowly-varying background curve underlies the (structurally relevant) molecular interference pattern at each time point. These seemingly time-delay-dependent background curves probably originate from two major potential sources: (1) the shift of the residual background

seen in the ground-state diffraction pattern, possibly caused by the defocused photo-electrons (as well as the stray photo-induced spurious electron emission from the surface of the vacuum chamber); and/or (2) an artifact of the ion-lensing effect. For quick examinations of the data, the slowly varying background curves are removed by fitting the difference data set with 4th-order polynomials. Once the background curves are removed, the remaining high-frequency oscillation patterns for the 75–400 ps data set are almost identical (both in period and in amplitude). This procedure thus highlighted the robustness of the interference terms in the data, independent of the spurious background counts.

B. Generation of “Product-Isolated” Curves from Diffraction Difference Signals

The structure-rendering procedures used for the CHD data have been modified from our previously reported schemes in two aspects. First, the diffraction-difference scheme is extended to include *both* difference curve and “product-isolated” curve procedures. As described previously, the difference curve yields information regarding the proportions of the products obtained following photo-illumination. This procedure may also be used to determine the structure of a given photo-product in a theoretical model, which must include *both* the parent $sM(s)$ curve and that of the product. Both the

experimental difference data [which is produced, for example, by subtracting positive time data (contributed mostly by the parents, with the remaining ~1–15% coming from the photo-products) from the negative time data (100% parent)] and the corresponding curve generated from a theoretical model are comprised of 50% parent contributions and 50% product contributions. The diffraction-difference procedure has the advantages of removing systematic artifacts from the raw experimental data set, and of concentrating on the results of photo-reactions by highlighting only those contributions to the molecular scattering signal originating from internuclear distances that change over the course of the reaction. However, the success of this procedure depends on the success of the ground state structure fitting; moreover, the sensitivity with respect to the product structure is reduced by the contribution from the parent signal.

In light of these difficulties, we implemented a second structural fitting loop that permits the contribution from the product only to be extracted from the total diffraction difference curve. In the first step of this new procedure, the values of the parent/product proportions are obtained at each time point from the usual diffraction difference analysis; these values are then used to fit the temporal behavior of the reaction dynamics. The resulting “exponential” temporal curve is then used to obtain “true” values for the proportions of parent and product species at each point in the reaction. Next

(at each point in the reaction), the parent-only signal obtained at negative time points is scaled down according to the temporal curve and subsequently added to the difference curve at a given time point—effectively canceling out the parent contribution, and leaving only the products to contribute to the diffraction signal. Finally, the product signal is fit (see below). These two fitting loops are connected interactively for successive refining; the refinement is repeated iteratively until the fits converge. The advantages of the new product-isolated procedure are four-fold:

- (1) The experimental data is comprised of 100% products, giving greater sensitivity for studying the product structure(s) directly (particularly when the structural change is significant);
- (2) It provides a more intuitive framework for analysis and interpretation;
- (3) The data analysis is much less dependent on the parent structure fitting; and
- (4) It allows us to exploit the fact that the temporal behavior of the *entire reaction* is known with greater precision than that of the species distribution at any given time point.

C. Novel Aspects of the Product Structure Analysis Used for “Hot” HT Product

The second major deviation in data analysis from our previous methods is the inclusion of non-single-gaussian probability functions for certain bond distances and those for the primary torsional angles. The *former* attempts to take into account the possibility of inverted (non-Boltzmann) vibrational populations in a given portion of the vibrational manifold relevant to our investigation; the *latter* accounts for the distribution of HT conformers. Additionally, an alternative structure modeling/fitting scheme aimed at treating complicated molecular systems is proposed in this work; the methodology and its results should complement the current approach and will be mentioned later.

Before going further, it should be mentioned that these increasingly sophisticated procedures were implemented only after exhaustive attempts to fit the data with our previous, more conventional methods were determined to be unsatisfactory. In our earlier approaches with the CHD data, equations governing geometrically consistent models were carefully constructed for CHD, *cZc*, *cZt*, and *tZt*; these models were then introduced into the UED fitting program in the usual way (these models were independently determined to be quite self-consistent, with the greatest error in mathematical self-consistency of predicted distances to be ~ 0.05 Å for one

long-range non-bonded distance in cZc —nearly all other distances were within 0.005 Å for cZc and cZt , and *all* distances for CHD and tZt were within 0.001 Å. The relatively large error of ~ 0.05 Å was accepted because it was shown to be a result of the simplified geometrically-consistent model for cZc/cZt , and not a human error in algebraic formulation). An equilibrated vibrational temperature for the HT products was estimated to be ~ 2100 K, considering the left-over deposited energy and the vibrational frequencies of the 36 modes. Reasonable values for the mean amplitudes of vibration and the temperature corrections to the distances were obtained by meticulously constructing U-matrices for entry into ASYM40, along with appropriate Hessians from Gaussian for each species. Structural parameters for the various species were obtained from conventional electron diffraction, our own fit of the ground state, and from *ab initio* calculations. We could then perform our early fits, in which we could see qualitatively: (1) that the progress of the reaction was relatively slow (indeed, the time constant for the reaction was always in the ballpark of 30 ps, regardless of the model); (2) that the positive and negative contributions to $\Delta f(r)$ were consistent with ring-opening; and (3) that fitting the $\Delta f(r)$ curves to the different conformers gave relatively poor agreement (considering our signal-to-noise ratio) to the various possible static structures, but seemed to support cZc more than anything else.

The double-Gaussian probability distribution function for bond distances

In this approach, for each of the direct-bond distances in the CC skeleton, a double-Gaussian probability function is assigned; this may be compared with the single-Gaussian probability functions (characteristic normal Boltzmann thermal populations) normally used in static electron diffraction. The double Gaussians were allowed to vary in their mean positions and FWHMs, thereby giving the refinement freedom to qualitatively simulate an inverted vibrational population in which the density bifurcates towards the classical turning points of the local potential well. Naturally, if the mean positions of the two Gaussians merge together, then the normal single-Gaussian picture for a Boltzmann vibrational distribution is recovered.

The conformational evolution—analysis of the torsional angle distribution

The *first* novel analysis of the structure and torsional angle distribution (which ultimately reflects the HT conformer distribution) was performed as follows. The geometrically-consistent model of the generalized HT (specifically, *cZt*) structure was put into the refinement routine. For each of the two torsional motions under consideration [i.e., those involving rotation about the two C–C single bonds, namely through the torsion angles $\tau_1(\angle C1=C2-C3=C4)$ and $\tau_2(\angle C3=C4-C5=C6)$], a two-peak cyclic Gaussian

probability function was assigned, with mean positions centered (and fixed) at 48° (*cis*-) and 180° (*trans*-). Additionally, the distributions of these angles were fixed at 40° (FWHM); giving a distribution shown to give a better fit than that obtained by assuming delta functions for the dihedral angle distributions (but the value of 40° was not numerically optimized). The mean angle values, determined from *ab initio* calculations, and FWHM values, were held fixed at this stage in the processing in order to reduce the number of adjustable parameters. The weighing prefactors before the *cis*- and *trans*-normalized Gaussian functions were allowed to vary (but naturally were required to have a sum of 1). The two torsional motions were regarded as independent. With $2 \times 2 = 4$ weighing prefactors (only two of which are independent parameters), the relative portions of the *cZc*, *cZt*, and *tZt* conformers could then (in principle) be determined.

With the increased complexity of the total fit, each major step within the complete iterative refinement is broken into smaller steps according to the sensitivity of the fit to each given type of parameter; i.e., in terms of the fit sensitivity, product fraction > bond distances > torsional angles / conformational prefactors (standard three-atom bond angles, which do not differ more than a few degrees among the different HT conformers, were held fixed at the *ab initio* values). The low-frequency (DC) background-removing procedures (and convergence tests for avoiding divergence) are embedded

within the fitting iteration cycles for guidance towards the global minimum. For the sake of objectivity, the exact refinement sequences are directly coded into the software so that all time points are treated equivalently.

At this stage of structural refinement, there were 18 total independent fitting parameters. These included: 3 independent covalent C–C bond distributions (C1=C2, C2–C3, and C3=C4), each described by 2 independent Gaussians [with their own mean values (2 parameters), FWHMs (2 parameters), and relative amplitudes (1 parameter)], giving 15 independent parameters for the covalent distances; torsional prefactors for the conformational distribution (described by 2 independent parameters); and finally the fraction of the product (only 1 parameter for difference curve fitting) (15+2+1=18). Other structure parameters were taken from *ab initio* calculations, with the mean amplitudes of vibration estimated using the *ab initio* force constants extrapolated to 2100 K with ASYM40. Although the total number of fitting parameters is large, it was found that only the fraction of the product, the C–C distances, and the torsional prefactors are very important for determining the global outcome of the fit [the other parameters (e.g., the FWHMs and deviations from 50/50 proportionality of the two-Gaussian distributions) can be regarded as mere “by-standers” to the overall fit; however, of course the values of these “secondary” parameters would not be trustworthy if the global structure fitting did not yield good results].

During the structure/conformation refinement of the CHD data, it was found that iterative background-removing procedures and convergence-checking procedures were crucial for the ultimate success of this step-wise process.

D. The Generalized Monte Carlo Method: A Complementary Analysis

Although the significant features observed from the aforementioned modeling scheme should be robust, one could argue that certain *specific* structure features might originate from the specific assumptions and constraints we have applied in the model (e.g., the values and distribution of the torsional angles and the bifurcation of the C–C bond distance probability function). Thus, it could be argued that there might be yet *other* (improved, or at least equally good) minima in the χ^2 hypersurface in the configuration space that are also well justified by the quality of our experimental data—and would be located if the structure were described differently—but are not reachable under the current constraints of the model.

In order to alleviate this doubt, global scanning was performed using a Monte Carlo approach over the configuration space (defined by a geometrically consistent *Z*-matrix representation of the structure) to probe for the existence of local minima for in each time delay. The *Z*-matrix representation of molecular structures is widely used in many *ab initio* and semi-classical methods in optimizing molecular geometry and dynamics. The

flexibility of this construction allows us to treat least-squares refinements of UED in the molecular hyper-configurational space, and to survey the landscape of the χ^2 hypersurface. By examining all the possible minima, the *model-dependent* “correlations” among structure parameters (e.g., pairs of similar covalent bond distances) can be noted for further analysis; moreover, the universal structure features, which should be *model-independent*, can also be established; the Monte Carlo survey helps us to locate the true, global minimum and allows us to report global structure features with a high level of confidence.

This new modeling procedure has been applied to analyze our CHD data with two different initial conditions for the HT structure: 1) the *ab initio* structure of *tZt*; and 2) the *ab initio* structure for *cZc* (both refinements gave similar results). Unlike conventionally applied least-squares fitting routines, no non-thermal probability distribution functions are presumed in the initial models. Additionally, this approach has the “built-in” predisposition of treating all dynamical effects as being effectively averaged, providing a single, static framework for the molecule (e.g., there are no distributions assigned to the dihedral angles—instead, average values are directly determined for τ_1 and τ_2 for each minimum on the χ^2 hypersurface).

Even without the assumption of non-thermal probability distribution functions, the averaged structure revealed in this complementary analysis

shows clearly that one C–C single bond is extended to 1.7–1.8 Å, with the other C–C single bond varying between 1.35–1.45 Å; additionally, the average skeletal structure of the HT product clearly takes on the shape of some intermediate structure between that of the “static” *cZc* and *cZt* conformers. These results are robust and apply for nearly all the time frames. Those averaged (static) general characteristics are very consistent with the results obtained with the dynamically resolved non-thermal model.

7.5 Results and Discussion

A. Ground States of CHT and CHD

Figures 7–3 and 7–4 show typical ground-state diffraction images for CHT and CHD and the corresponding structures. Differences between the ring patterns of the two species are evident even in the 2D images, demonstrating the high sensitivity and resolution of our third-generation UED apparatus. Moreover, these three systems have no heavy atoms, and the diffraction, which is from only C- and H-atoms, is sensitive to the increased complexity of these two structures.

The major peaks in the $f(r)$ curves reflect relative populations of various C–C distances in these complex molecules. In CHT, for example, covalent C–C distances occur at ~ 1.4 Å, second-nearest neighbor at ~ 2.5 Å, and third-nearest neighbor at ~ 3.0 Å. The $f(r)$ curve for CHD (with one less C-

atom in the ring) clearly shows much lower density of third-nearest neighbor C···C distances compared to CHT, in good agreement with results obtained with conventional electron diffraction^{2, 3} and our own *ab initio* calculations. Figures 7–5 and 7–6 show the refined ground-state structures of CHT and CHD, along with the best-fit bond distances and angles, together with theoretical predictions.

B. Structural Dynamics of CHT

Upon excitation, CHT undergoes an ultrafast hydrogen shift,^{4,7} but with subsequent reformation of CHT at high internal energy. Except for their relative intensities, all the product-only $sM(t; s)$ curves were nearly indistinguishable. Figure 7–7 shows the experimental $sM(s)$ curve averaged from 75 to 400 ps, along with theoretical curves with the same internuclear distances as those of the initial structure,² but with varying l values. It is evident that the experimental curve is significantly more damped than the theoretical curve (for the initial structure) at 403 K, clearly establishing the “hotness” of product CHT. If the initially deposited energy (107 kcal/mol) were equipartitioned among the CHT modes⁸ with a Boltzmann distribution within their vibrational levels (*c.f.* Fig. 7–1), the molecule would have an internal temperature of ~2200 K (per mode). However, the poor fit of this thermalized model with our experimental data precludes Boltzmann

vibrational distributions.

Indeed, excellent agreement is obtained between experiment and theory with l values whose mean is nearly three times that at equilibrium, indicating a non-Boltzmann distribution in the vibrational levels (see Fig. 7–8). This dramatic increase in the vibrational amplitudes compared to those resulting from a Boltzmann assumption suggests that the hot (product) structure can be characterized by a negative temperature, wherein the upper vibrational levels have higher population than the lower levels. Note the similarity in frequency components between the theoretical $sM(s)$ curve for the equilibrium structure (at 403 K) and the experimental curve, indicating that internuclear distances (in the product) are nearly identical to those at equilibrium—in turn implying nearly complete energy redistribution.

Figure 7–9 shows the structural evolution of the CHT product, obtained by fitting the growing intensity of the $sM(t; s)$ curves with increasing time delay. Previous ultrafast spectroscopic studies⁵ have suggested that conical intersections are responsible for the ultrafast formation of product in tens to hundreds of femtoseconds. However, our structural dynamics studies indicate that the hot structure must be formed on a time scale of 16 ± 3 ps. This longer time scale implies that the product is formed via an avoided crossing or by longer-lived trajectories on the excited surface that involve intramolecular vibrational energy redistribution (IVR);

see below. This is not surprising as other studies on the femtosecond time scale⁹⁻¹¹ have shown the existence of a distribution of femtosecond and picosecond trajectories as molecules traverse a complex energy landscape. If all trajectories were on the femtosecond time scale and we were merely observing picosecond energy redistribution, our $sM(s)$ curves would have revealed structural changes as a function of time. On the other hand, if the structure were that of the excited state, the vibrational temperature would be much lower than that indicated above. It should be noted that UED probes the changes of *all* nuclear coordinates and therefore, the dynamics reported here are directly relevant to global structural changes in the molecule. In contrast, spectroscopic studies reported for the gas phase⁵ (femtoseconds) and condensed phase⁴ (26 ± 10 ps) monitor state populations. The roles of the solvent and intramolecular relaxation must be disentangled before direct comparisons can be made with our results of the isolated reaction dynamics.

C. Structural Dynamics of CHD

From a purely chemical standpoint, the photo-reaction of CHD is a prototypical reaction for the large field of polyene photochemistry, involving various types of chemicals (including dyes). Generally speaking, this reaction belongs to the family of *pericyclic rearrangements* (reactions believed to proceed with a transition state possessing a closed loop of interacting

orbitals); specifically, the photoreaction of CHD to form HT is known as *electrocyclic ring opening*. In general, the outcomes of pericyclic rearrangements can be predicted by the Woodward–Hoffmann rules, which were constructed using relatively simple molecular orbital symmetry arguments. For example, these rules predict that for a system with $4n$ π electrons (i.e., with two conjugated double bonds in the ring), photochemical ring opening will proceed with *conrotatory* specificity (that is, the ring opening will proceed such that the end groups at the ring opening position will *rotate* in the *same* direction), while systems with $4n+2$ π electrons will proceed via *disrotatory* motion of the end groups (for $n=0,1,2\dots$). The CHD reaction has also been used as a model system for studying the effects of substituents and solvent on the photo-reaction rate. For example, the effects of the presence of solvent on energy redistribution and transport—as well as the effects of friction of the solvent on bulk motion and morphological change of the solute over the course of a chemical reaction—have been studied. Additionally (and of direct relevance to this work), the ultrafast dynamics of this reaction have been studied experimentally and theoretically by a number of groups over the past 10 years, and there appears to be considerable disagreement regarding the interpretation of the various results regarding, for example, the rate of ring opening in the reaction.

The CHD/HT reaction has biological significance as well. Because this reaction is a model for polyene photochemistry in general, it is also relevant to a variety of polyene photo-isomerization reactions critical to various biological processes. Examples frequently cited in the literature include: the photo-isomerization of 11-*cis* retinal (a vitamin A derivative) to form all-*trans* retinal in rhodopsin (the fundamental process in dim-light vision of vertebrates); the photo-isomerization of all-*trans* retinal to form 13-*cis* retinal in bacteriorhodopsin (a fundamental process of photosynthesis in certain types of bacteria); and the *cis-trans* isomerization of urocanic acid in the epidermis by UVB light (a process that has been implicated in the suppression of immune response that ultimately leads to skin cancer). Moreover, the light-induced ring opening of CHD is directly relevant to the synthesis of vitamin D *in vivo*. Specifically, CHD models the chromophoric subunit of 7-dehydrocholesterol, which forms *cZc*-previtamin D upon UV irradiation in the primary step of vitamin D synthesis.

Although photochemical characteristics of CHD were studied long ago, various important investigations regarding its ultrafast dynamics have been carried out within the last decade. The initial UV excitation of CHD in its 1A_1 ground state creates a population in the 1B_2 state, which subsequently “decays” either by rapid motion out of the Frank–Condon region of the excited state potential energy surface, or by ultrafast internal conversion to an

optically forbidden 2A_1 state on a time scale of ~ 10 fs. Many spectroscopic tools encompassing resonance Raman scattering, UV absorption, resonance enhanced multiphoton ionization (REMPI), and dissociative intense field ionization have been incorporated to elucidate the photodynamics of the ring-opening reaction of CHD. The analysis of this reaction is, however, greatly complicated by the effects of vibrational excitation and the lack of information about the spectra of the possible conformers of HT, namely cZc and cZt (the spectrum for the lowest-energy conformer, tZt , is well-known).

One can easily see that *at least* four time scales are involved in this reaction:

- (1) the depopulation of the initially populated 1B_2 state into another excited state (most probably 2A_1);
- (2) the depopulation of the excited state into the vibrationally hot CHD ground state;
- (3) the depopulation of the excited state into the photoproduct of the ring-opening reaction (i.e., the step governed by the all-important ring opening rate); and
- (4) the isomerization of the initially formed photoproduct (most probably cZc) into other isomers (cZt and tZt).

In the condensed phase, the problem is complicated further due to possible

vibrational relaxation (thermalization) caused by the solvent molecules. The apparent difficulties associated with these complicated processes are evident in the fact that the suggested time scales for the processes scatter over an order of magnitude, depending on the detection methods and the various interpretations.

In reactive systems, where bonds are broken and formed, the partitioning of energy may result in its localization in certain bonds associated with the reaction coordinate. Indeed, we observed incomplete energy partitioning even up to 400 ps in hot 1,3,5-hexatriene (HT), formed by the ultrafast ring opening of CHD.¹²⁻¹⁵ Figure 7-10 shows the 2D diffraction-difference images and Fig. 7-11 shows the evolution of radial distribution curves for the ring-opening reaction of CHD. The product-only HT diffraction curves were significantly damped at all time points (manifested as peak broadening in the $f(t; r)$ curves), indicating the vibrationally hot nature of the product structure; however, unlike CHT, new peaks appear in $f(r)$. Shown below the experimental data in Fig. 7-11 are theoretical $f(r)$ curves for three hot conformers of HT (labeled cZc , cZt , and tZt with respect to the conformation of torsion angles about the C-C single bonds; see Fig. 7-15). Close inspection of the experimental $f(t; r)$ curves reveals greater similarity to the theoretical cZc curve than to that of the lower-energy tZt conformer. Furthermore, an anomalous peak at $\sim 1.7 \text{ \AA}$ can be seen as a shoulder in all

the experimental $f(t; r)$ curves; the presence of this peak—which is about 0.2 Å away from expected equilibrium C–C distances—was found to be reproducible in repeated diffraction experiments.

Least-squares refinement of the structural parameters yielded a HT molecular structure at each time slice; to locate the global minimum, Monte Carlo techniques were first applied for searching the configuration space, and finally the structure at each time represents the average over the local minima closest to the global minimum. These HT structures showed no *tZt* character, but consistently manifested a configuration intermediate between *cZc* and *cZt*—far removed from a thermally equilibrated conformer distribution of ~41% *tZt*, ~45% *cZt*, and ~14% *cZc* at 2100 K (estimated from *ab initio* calculations of the conformer energies). Moreover, the ~1.7 Å peak observed in the $f(t; r)$ curves was assigned to one C–C single bond in HT—a highly non-equilibrium value for a C–C internuclear separation. The remarkable departure from the predicted equilibrium conformation, together with the unusual C–C bond length, confirms the far-from-equilibrium nature of the HT structure.

The hot HT structure is formed with a time constant of 32 ± 2 ps (Fig. 7–12) and remains virtually unchanged over the course of the experiment (400 ps) as shown in Fig. 7–13. The refined ring-opened structure of HT is shown in Fig. 7–14, while time-averaged values for selected structural

parameters are summarized in Table 7–1, along with corresponding *ab initio* values for the three HT conformers. The persistence of this far-from-equilibrium structure even up to 400 ps indicates that unlike CHT, energy partitioning within HT is slow with respect to both the rate of product formation and the time scale of the UED experiment. The existence of a *cZc*-like conformation clearly indicates an inverted population on the potential energy surface (projected along the coordinate of torsional motion), with significant density at the classical turning points—this coherent nuclear motion is shown schematically in Fig. 7–15. Moreover, the ~ 1.7 Å distance assigned to a C–C bond would require ~ 15 kcal/mol of the available ~ 90 kcal/mol to be deposited in that C–C bond (assuming a simple Morse oscillator model)—providing further evidence for an inequitable partitioning of energy. Note that if energy partitioning were indeed complete, then each of the 36 modes in HT would have ~ 2.5 kcal/mol.

Coexistence of the two structural features—an inverted torsional conformation and a stretched C–C bond—over time strongly suggests a long-lived, low-frequency hybrid motion comprised of both torsion and asymmetric stretching of the carbon skeleton. Conceptually, one may picture that as the molecule oscillates between the turning points of the potential well (Fig. 7–15), the stretched C–C distance is shifted continuously from one C–C single bond to another and at the turning points, the torsional energy is partially

stored in the C–C bond stretch. That this far-from-equilibrium structure lasts for over 400 ps suggests a bottleneck in energy transfer from the inferred hybrid motion to other (higher frequency) modes, after the initial energy deposition. This energy localization could result from a mismatch in the frequencies of the coherent modes compared to all other modes (at these high internal energies). It is interesting to note here that torsional modes of this type have been isolated in dynamical calculations of polypeptides.¹⁶

Ultrafast spectroscopic studies of the CHD ring opening reaction have suggested contrasting time scales for the formation of the HT product—tens to hundreds of femtoseconds¹³⁻¹⁵ and 6 ± 1 ps¹²—with the presence of conical intersections invoked to rationalize the ultrafast time scales. The initial preparation of CHD is to the S_2 excited state; the S_2/S_1 conical intersection is along the readily accessible symmetric path (see below) and gives rise to femtosecond dynamics. Accordingly, the crossing/avoided crossing to the ground state (S_0) determines the longer (picosecond) time-scale of the dynamics. It is interesting to note that while we found virtually no contribution from hot CHD in the HT product diffraction patterns (despite our sensitivity to hot “parent” structures in CHT), static condensed-phase experiments have reported a 60/40 branching ratio for the CHD reformation/ring-opening pathways.¹⁷ This near-absence of hot parent structures, along with the long time observed by UED for ring opening,

signifies the crucial role played by the solvent (in contrast to the isolated molecule) in redirecting the fate of the reaction. For instance, the increased steric hindrance to ring opening in the solvent may favor the reformation of CHD over ring opening. Moreover, the solvent can induce slight perturbations in the relative positions of the potential energy surfaces, which can dramatically alter the time scales¹⁰ for reaction in the condensed phase.

The above diffraction experiments for CHT and CHD also reflect the nature of the nascent structures born at the point of descent to the ground state surface (the “transition state”). Both reactions have been the subject of recent *ab initio* calculations.^{6, 18} These calculations have suggested the existence of two regions on the excited-state energy surface, determined by the C–C stretch motion and the ring bending motion (a precursor to torsions). Also, the molecular structure at the conical intersection is highly distorted. If the conical intersection is reached directly in the initial motion, then femtosecond dynamics result, otherwise IVR is needed to redirect the trajectories. For example, at the point of descent from the excited state, CHT must adopt a near-planar geometry (as opposed to the minimum-energy boat-shaped geometry at equilibrium) for the [1,7]-sigmatropic hydrogen shift reaction to occur. Thus, efficient energy redistribution is essential in this transformation to the final geometry via a planar “transition state”. On the other hand, ring opening in CHD lands the structure in a highly asymmetric

geometry on the ground state and except for the subsequent hybrid (torsional and bond stretching) motion, the nature of the system is similar to that of the final product. In other words, the non-equilibrium features of the HT structure may reflect memory of an asymmetric geometry at the instant of ring-opening—suggesting that ring opening of CHD follows a symmetry-breaking pathway that violates the C_2 symmetry of the parent structure¹⁹. However, while *ab initio* calculations¹⁸ were performed for the minimum energy path, we are concerned here with nuclear dynamics of far-from-equilibrium structures. Thus, our diffraction results illustrate the crucial role played by structural changes in directing the subsequent dynamics in nuclear subspace (on the ground potential surface) of the reaction.

7.6 Review of Previous Studies in Light of Our UED Results

A. The Resonance Raman Studies of Mathies and co-workers^{20, 21}

Resonance Raman intensity analysis²⁰ has demonstrated that the initial excited-state evolution of CHD is along the conrotary reaction coordinate (as expected according to the Woodward–Hoffmann rules), and that depopulation of this state occurs in ~10 fs (determined from a linewidth analysis).

In 1993, Mathies and co-workers²¹ reported time-resolved UV resonance Raman studies of CHD→HT in the condensed phase. In their

results, the appearance time of the Stokes scattering from ground-state *cZc*-type HT is 6 ± 1 ps and the photoproduct anti-Stokes ethylenic intensity appears with a time constant of 8 ± 2 ps and decays in 9 ± 2 ps (this observation reflects the production and dissipation of “hot” HT-type product). Analysis of the photoproduct spectral evolution in the Stokes and anti-Stokes data as well as the observation of Raman lines characteristic of the *cZc* conformer in the anti-Stokes data demonstrates that *cZc* first appears on the ground-state surface, and then subsequently undergoes conformational relaxation to produce *cZt* with a time constant of about 7 ps. The photoproduct anti-Stokes ethylenic and single-bond stretch intensities further demonstrate that the initial photoproduct temperature at 4 ps is 1500 ± 500 K [a very reasonable observation when compared to the value we calculated for the expected “fully thermalized” temperature (~ 2100 K; they estimated ~ 1950 K for the initial product temperature) neglecting any dissipation of heat to the solvent] and that the cooling time is ~ 15 ps. It was also shown that the time scale for any final conversion of *cZt* to *tZt* takes longer than 200 ps.

We believe that these time scales and their interpretation do *not* contradict our UED results and interpretations. While the appearance time (6 ps) for the HT species is significantly shorter than what we measured (~ 30 ps), we believe that their faster rate can be at least *qualitatively* rationalized

by including the additional de-activation channel available in the condensed phase (i.e., the channeling of energy from CHD* into the bath via contact with the solvent, which efficiently quenches the reaction). If CHD* is quenched by the solvent with a time constant of about 7 ps, it would reduce the appearance time of HT from 30 ps to the 6 ps observed by Mathies *et al.*²¹ Alternatively, the solvent may alter the available phase-space in the excited state in some way, thus yielding a faster decay. However, since they were blind to the direct depletion of CHD*, it is difficult to say anything more definitive than that. Moreover, we note that the relaxing of HT product conformers takes considerable time, and requires the presence of the solvent; therefore, it is not surprising that we still see a highly non-thermal conformer distribution (with *cZc* dominating).

The Mathies results (inevitably) rely on *ab initio*-derived resonance-Raman spectra for the *cZc* and *cZt* conformers. For example, they state: “The presence of scattering at 829 cm⁻¹ [well into the ps regime] strongly argues for the presence of the all-*cis* conformer on the ground state surface.” This particular argument is based on the fact that neither the *ab initio cZt* or *tZt* spectra have frequencies anywhere near this region, whereas *cZc* is predicted via *ab initio* methods to have one at 849 cm⁻¹. Still, one might question the relevance of *ab initio* predictions of resonant Raman spectra (specifically, the *absence* of certain lines) for species at zero temperature involved in the

CHD→HT reaction, when it is known there is an *enormous* amount of energy bouncing around in HT. Indeed, it is this *potential* weakness that is invoked by Sension and co-workers to question the Mathies' interpretation²¹ that supports long-time (many ps) ring-opening.

B. The Initial Work of Sension and co-workers

Sension and co-workers²² used a complimentary technique of fs transient absorption spectroscopy to further investigate the rate of appearance of the *cZc* conformer from photoexcited CHD. One-color transient absorption signals of CHD in cyclohexane and methanol pumped at 262, 268, and 273 nm revealed a rising component of several ps. In their analysis, these authors made the following assumptions: 1) The *cZt* and *tZt* conformers, as well as the *cZc* conformer, are formed. 2) The quantum yield for the CHD→HT isomerization reaction was fixed at 0.4. 3) The oscillator strengths of the *cZc* and *cZt* conformers *were restricted* to be in the range of 0.25–0.5 and 0.5–1.0, respectively. 4) The oscillator strengths of the vibrationally hot *cZc* and *cZt* species *were restricted* to be *smaller* than those of the thermally equilibrated isomers. 5) The time constant of conformational relaxation from *cZc* to *cZt* *was constrained to 7 ps* as determined in the ps resonance Raman experiments of Mathies and co-workers described above.

Under the framework of their assumptions, the authors basically

concluded that the ring-opening reaction is finished essentially completely within 1 ps of excitation and suggested that the 6 ps appearance of resonance Raman scattering (of Mathies and co-workers) from the initial *cZc* photoproduct is somehow limited by vibrational relaxation in the ground state manifold. Sension and co-workers concluded that the assignment of a 6 ps time constant for the appearance of the *cZc* photoproduct (i.e., ring opening) was physically unreasonable, as it would require that the absorption cross section for the initially formed, vibrationally hot *cZc* be *two to three times higher* than the absorption cross section of the thermally equilibrated *cZt* photoproduct at all three probe wavelengths (at least within the other constraints of their model).

Neglected is the possibility that only *cZc* is formed in their solution without significant conversion into *cZt* or *tZt*. We also note that these authors were selective in using results from the Mathies work—they disregard the 6 ps ring opening assignment, yet actually use the 7 ps time constant assigned to *cZc*→*cZt* conformational relaxation in their model. Moreover, the transient absorption spectra for *cZc* and *cZt* are unknown. They admit that while calculations proved quantitatively unreliable, the calculations did successfully reproduce the trend of $\text{CHD} < cZc < cZt < tZt$. Their conclusions, however, are based on the application of somewhat complex models (with parameters that are not well-known, especially over the various conditions of

the experiment) to simple transient curves.

C. The Work of Fuss, Kompa, and co-workers

More recently Fuss and co-workers used the same technique of fs transient absorption¹³ to study the ring-opening dynamics of CHD and the subsequent processes such as isomerization and cooling in the condensed phase. The interpretations and time scales for the ring-opening and isomerization were drastically different from those of the Raman studies of Mathies and co-workers and were mostly consistent with the FTS studies of Sension and co-workers (which is not surprising, since the technique was the essentially the same). The interpretation starts from the analysis of the transient absorption at 404 nm of CHD dissolved in ethanol after excitation at 267 nm. Since CHD as well as HT absorb only at wavelengths shorter than 290 nm, this transient absorption at 404 nm was attributed to the excitation from the S_1 to higher electronic states S_n , requiring less energy than the excitation from the ground state to the S_1 state. The transient absorption signal clearly showed that the species giving the transient signal disappears within 300 fs. From this observation, they concluded that the ring-opening completes within 300 fs (i.e., $\text{CHD}^* \rightarrow \text{HT}$).

However, the observed behavior *might not be representative*, i.e., the conclusion is right (e.g., in this case, they are indeed seeing ring opening in

300 fs), but it is a picture only of what a small percentage of reacting molecules are doing, with the rest of the molecules being dark for some reason. Correspondingly, the second possibility is that the behavior is indeed representative of the entire ensemble, but the conclusion is wrong (e.g., in this case, the time constant *does not* represent ring opening, but merely results from the wave packet passing through a *narrow observation window* that happens to have a high absorption cross section at 404 nm compared with other species. Thus, the species giving a high absorption at 404 nm may not represent the *whole landscape* of the excited states (1B_2 and 2A_1) of CHD, and the ring has not opened yet, even after the wave packet passes through the 404 nm window).

The rest of the interpretation was merely based on this conclusion that CHD ring-opening occurs within 300 fs, and therefore, would be easily falsified if the initial conclusion were wrong. In their model, the concentrations of the conformers reach thermal equilibrium in a few picoseconds; during the first 10–20 ps, the concentrations follow the cooling of the molecule by the solvent, staying near thermal equilibrium (i.e., rapidly tending toward *tZt* in great majority); and a small quantity of *cZt*-hexatriene is trapped in its potential well on a time scale of 100 ps at the final temperature (300 K) (Note that *this* result is also very different from those of Mathies and co-workers). Their confidence about the short time scale for the

ring-opening process seems to have originated from their previous studies.²³ Also, see their later work in the gas phase¹⁵ where a short time scale was claimed. The earlier result of Sension and co-workers may have contributed to their biased assumption. Still, the authors spend a considerable amount of time deconstructing the results and interpretations of Mathies and co-workers, and make some strong arguments. While seemingly neglecting a few of Mathies' more qualitative yet convincing arguments (e.g., the presence/absence of particular resonances that could only be reasonably assigned to particular conformers), they directly challenge Mathies' quantitative interpretations. For example, they believe that if differences in transition dipole moments of the HT conformers were included by Mathies' group in their analysis, they would have concluded that their 6 ps rise was actually due to conformer isomerization, not ring opening. Additionally, Fuss and co-workers believe that one resonance assigned to *cZt* should have been assigned to *tZt*, leading Mathies to conclude that *tZt* was not appreciably formed over the course of their experiment, when in fact it was.

In their most recent study¹⁵ in the gas phase, the same researchers used dissociative intense-laser field ionization in an attempt to substantiate the ultrafast nature of the dynamics of CHD ring opening. All the transient mass signals showed very short time constants. On the basis of the rather different fragmentation pattern of CHD and HT when ionized by an intense-

laser field, the H^+ mass transient was attributed to the formation of HT. However, neglected is the possibility that the extremely strong laser fields may perturb the potential energy surfaces of the whole process of ring-opening and isomerization, instantly accelerating the ring-opening process and creating the product, thereby giving an artificially fast appearance time for the product.

However, we note that the potential problem with the intense-field ionization may be absent with the resonance-enhanced multiphoton ionization (REMPI) experiments performed by this group. Actually, the same authors²⁴ utilized time-resolved REMPI and obtained a 600 fs rise time, which was attributed to product formation by ring opening. However, later on they reassigned the 600 fs to the conformer isomerization in the hot product.

In other work by Sension and co-workers,²⁵ they expanded their transient absorption study in this system in solution. Their results and interpretations are almost identical to those of Fuss and co-workers.

7.7 Implications of UED Studies on Understanding IVR

The photo-initiated, non-dissociative radiationless decay processes in CHD embody a prototypical IVR problem. Indeed, there are two universal characteristics associated with this process that make this photo-reaction a particularly interesting case: (1) A vast amount of the electronic energy is

transferred to the vibrational energy of the molecule in a relative short period of time. (2) There is a direct coupling to the low-frequency skeletal torsion modes at higher vibrational levels. Because the reaction pathway connecting the ground and excited electronic levels is rather steep (with regard to the energy potential surfaces), and often begins with a well-characterized geometry, the initial condition of IVR (e.g., the geometry of the molecule and the locality of non-thermalized population distributions) is probably similar for all the molecules in the ensemble, albeit there is probably not a universal onset time for the decay of the molecules.

For CHD in particular, the ring opening is directly coupled to large-amplitude torsional motions along a potential well where the conformational barrier is rather low compared to the initial available vibrational energy. Here two questions come to mind: (1) In a collisionless environment, how is the energy which is initially deposited in the torsional modes (with their relatively high densities of state) coupled to other, higher-frequency modes of bond stretches and more rigid (higher-energy) torsional motions? (2) What is the time scale of this coupling, and how does it vary depending on the molecular environment and the nature of the excited-state preparation? In the gas phase, a very similar process is the collision-induced level-crossing non-adiabatic decay in bi-molecular reactions involving electronically excited species. Even more common in condensed phases is solvent-mediated non-

radiative decay, one of the primary energy channels in photolysis. Indeed, as indicated above, reaction dynamics may be greatly affected by the presence of solvent. Understanding the IVR process in the gas phase can also cast light on the effects of solvation in condensed phases. Additionally, while IVR is usually studied in the *energy domain* by following the frequency signatures associated with specific ro-vibrational motion of molecules, UED provides a different perspective in studying IVR by monitoring the structural evolution directly.

First, our result of a highly unexpected 1.7–1.8 Å C–C peak in the radial distribution curves suggests a rather long IVR time for the molecular motions coupled with this internuclear separation. This observation begs the question: what are the reaction coordinates involved in the manifestation of this extremely long bond distance? Perhaps a clue to the answer of this question lies in the conclusion that the averaged product structure is highly non-thermal, resembling an asymmetric *cZc*, or a more folded *cZt*, *even up to 400 ps after the reaction began*; thus, the non-thermal torsional motions around the C–C single bonds survive for at least 400 ps. As shown schematically at the top of Fig. 7–15, an inverted population in the torsional rotor mode has a higher probability to be seen in the geometries found near the classical turning points—i.e., the “folded” conformations found in both

halves of cZc (and one half of cZt)—in qualitative agreement with our observations.

As described elsewhere in this chapter, two attempts were made to theoretically explain the presence of the 1.75 Å peak. We reiterate that while the two fitting procedures used address the 1.75 Å peak in two rather different pictures, both models unmistakably assign the 1.75 Å peak to the C–C single bonds. In the first model, the origin of the averaged 1.75 Å peak is directly associated a non-Boltzmann population distribution of the local C–C stretching mode. A dual-Gaussian probability function was used to simulate a possible non-thermal bond-stretching. In such a scenario, the averaged 1.75 Å bond distance would originate from density at the *outer* classical turning point in the local Morse potential, whereas an averaged 1.4 Å distance would originate from density at the *inner* classical turning point. The energetics and eigenstate analysis showed that with 1.75 Å as the averaged outer turning position, the inner turning position should actually be around 1.2–1.3 Å, with a (demanding) mean vibrational energy of 25 kcal/mole *per bond*.

The second model, which employed a Monte Carlo search for the best-fitting Z -matrix representations of the averaged structure at each time point, instead indicated that one C–C bond was elongated to 1.75 Å while the other was somewhat shorter, at 1.35 Å (this is a subtle difference from the previous model, which considered *both* bonds to be in an *effective superposition* of long

and short). If one performs a calculation that adiabatically follows the *ab initio cZc* structure (with $\tau_1=\tau_2\sim 42^\circ$), stretching one of the C-C bonds to 1.75 Å takes about 10 kcal/mole. Also it is interesting to note that as the C-C bond was stretched, and the rest of the molecule was allowed to reorganize adiabatically from its initial *cZc* conformation, the molecule adopted a more open, asymmetric structure that is *not that different* from that obtained from the *Z*-matrix representation refinement of the effective averaged structure (e.g., with “G” referring to Gaussian, and “Z” referring to the *Z*-matrix data-refinement procedure, $\tau_1(\text{G})\sim 33^\circ$, $\tau_1(\text{Z})\sim 20^\circ$, $\tau_2(\text{G})\sim 59^\circ$, $\tau_2(\text{Z})\sim 63^\circ$) (Note that other structural features don’t compare as well—for example, Gaussian fails to make the second C-C bond shorter than the equilibrium value).

Thus, it could be argued that the second model—in which the long C-C distance really represents the time-averaged internuclear separation of one of the bonds, and which originates from coupling to the (manifestly non-thermal) torsional motion—provides a better, more self-consistent picture of the product structure and non-equilibrated behavior. Moreover, the preliminary analysis of the CHT data suggest that a *thermalized* model of hot CHT after internal conversion provides a good fit to the observed results (without requiring the existence a 1.75 Å C-C bond); this suggests that the non-thermal behavior manifested by the HT product results from the presence of the “floppy” torsional modes. This evidence provides further

support for the notion that the long CC single bond distance somehow originates from the non-thermal torsional mode vibrations.

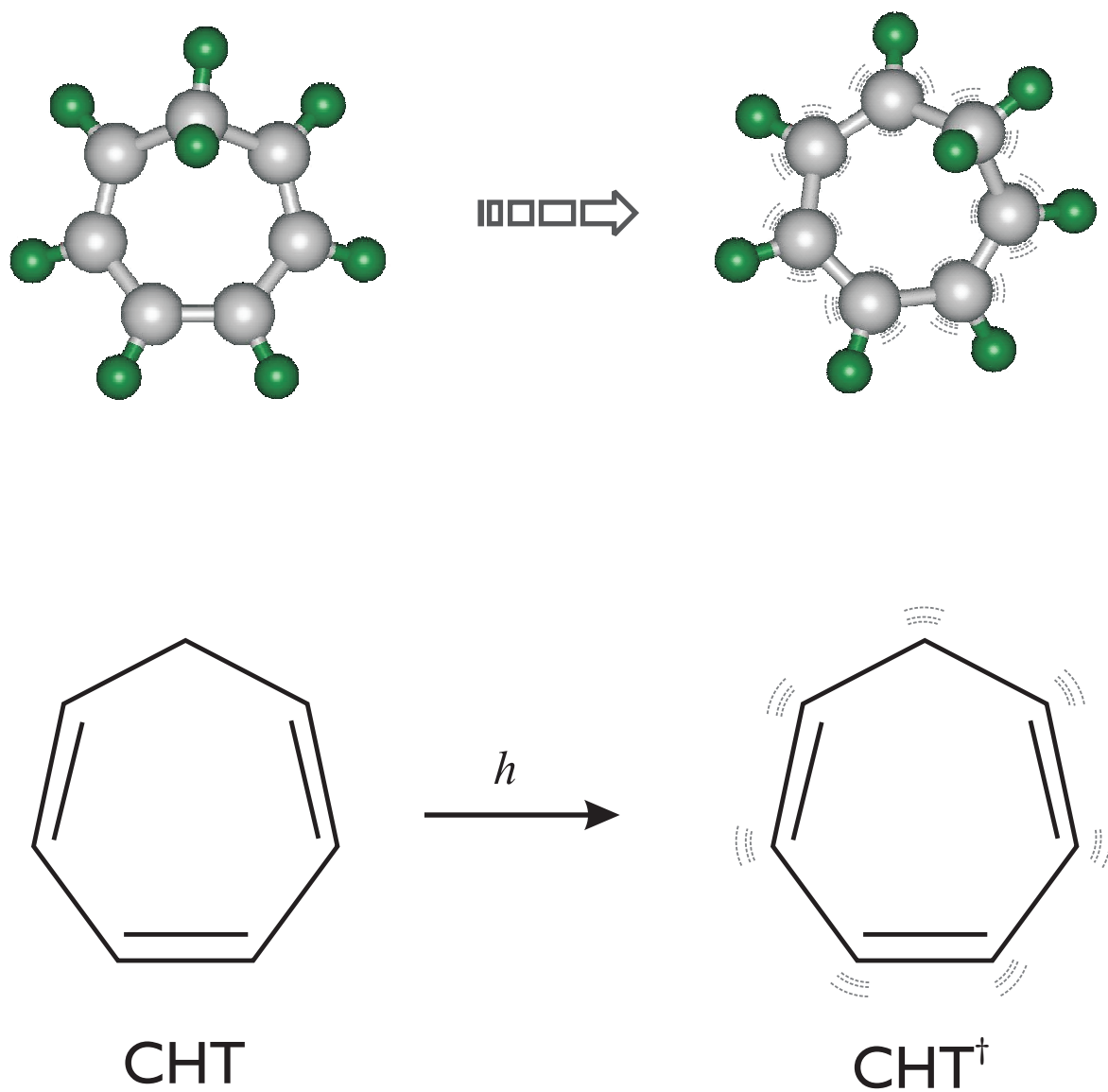
In a simple classical picture, one may visualize the two counter-propagating “rotors” of HT trying to pass by each other. At the classical turning points, the kinetic energy must be stored in the molecule, perhaps through stretching/compressing of the directly-coupled bond distances. In an *asymmetric* encounter, it is reasonable to stretch more on the faster moving arm as compared to the compression of the slow moving arm. This classical picture might be justified by the spatially localized initial preparation of a non-thermal ro-vibrational state resembling a wave-packet preparation on an excited vibrational manifold, and the close coupling of this motion to the reaction pathway following the ring-opening of CHD. (Note this classical “wavepacket” preparation refers to an *intramolecular* vibrational mode of a single molecule that just landed in the ground state surface. However, because the molecules leave the excited electronic surface randomly (characterized by a 33 ps life time), the preparation of the *ensemble* of molecules in the ground state surface is not a coherent one.) Additionally, it has been proposed that there is some long-lived “combination mode” comprised of the torsional motion and an asymmetric CC skeletal stretch, but we have not yet considered this possibility with any of our models.

Studies of vibrational motion with electron diffraction are complimentary to those performed with spectroscopic methods. The high-frequency local mode motions are associated with the mean amplitudes of vibration of the directly bonded distances. On the one hand, through the temperature effects seen via damping and frequency shifts in the molecular interference patterns caused by the increased mean amplitude motions, the local force fields can be extrapolated, complementing the spectroscopic information. On the other hand, the low-frequency large-amplitude motions can be studied through the changes of the indirect bond distances. The slow IVR processes associated with these motions, which usually are very hard to investigate directly by spectroscopic techniques, can now be studied by UED (as suggested in this work). The latter behavior is particularly relevant to larger, biologically-relevant systems. We should add that the analytical difficulties expected from such macromolecules are also addressed in our newly developed data-analysis procedures, in which the *Z*-matrix becomes the central pivoting element linking the molecular dynamical modeling of the UED data with the vastly available biomolecular structure databanks (not to mention freeing us from having to manually develop geometrically consistent equations for such macromolecules—no doubt a Herculean task). The separation of rigid-frame molecular motions from the floppy, often classical-

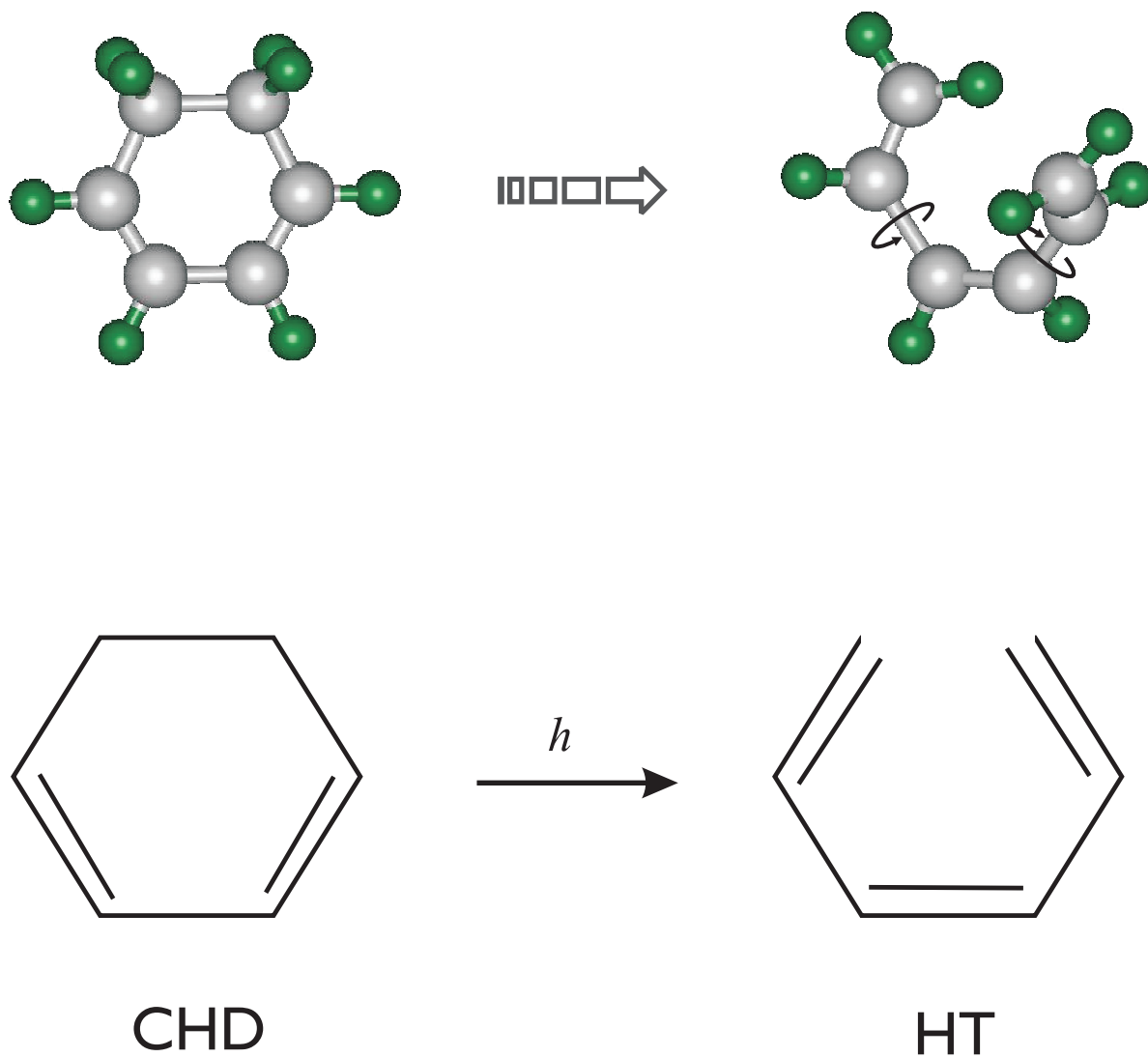
like, large-amplitude motions provides an additional advantage for using UED for studying complex molecular systems.

7.8 Conclusions

We have demonstrated the ability of ultrafast diffraction to observe the time evolution of molecular structures in non-equilibrium configurations. While non-thermal effects have been previously reported,²⁶⁻³¹ to our knowledge this is the first time that such far-from-equilibrium structures—in terms of both vibrational amplitudes and bond distances—have been directly observed in isolated complex molecules. The concept of negative temperature was invoked to describe the observed populations at high internal energies. The structural dynamics of the two hydrocarbons studied here underscore the importance of the following issues: (i) the critical influence of structural changes on energy redistribution and on persistence of certain bond motions; (ii) the nature of the nascent structure(s) born en route to the final product and the associated coherent dynamics; and (iii) the direct relevance of structural changes associated with bond breaking and making in understanding the disparities of measured time scales for state population dynamics in the condensed phase.



Scheme 7-1. Nonradiative decay of excited 1,3,5-cycloheptatriene (CHT) to 'vibrationally hot' ground state.



Scheme 7-2. Ring opening of 1,3-Cyclohexadiene (CHD) to form 1,3,5-Hexatriene (HT).

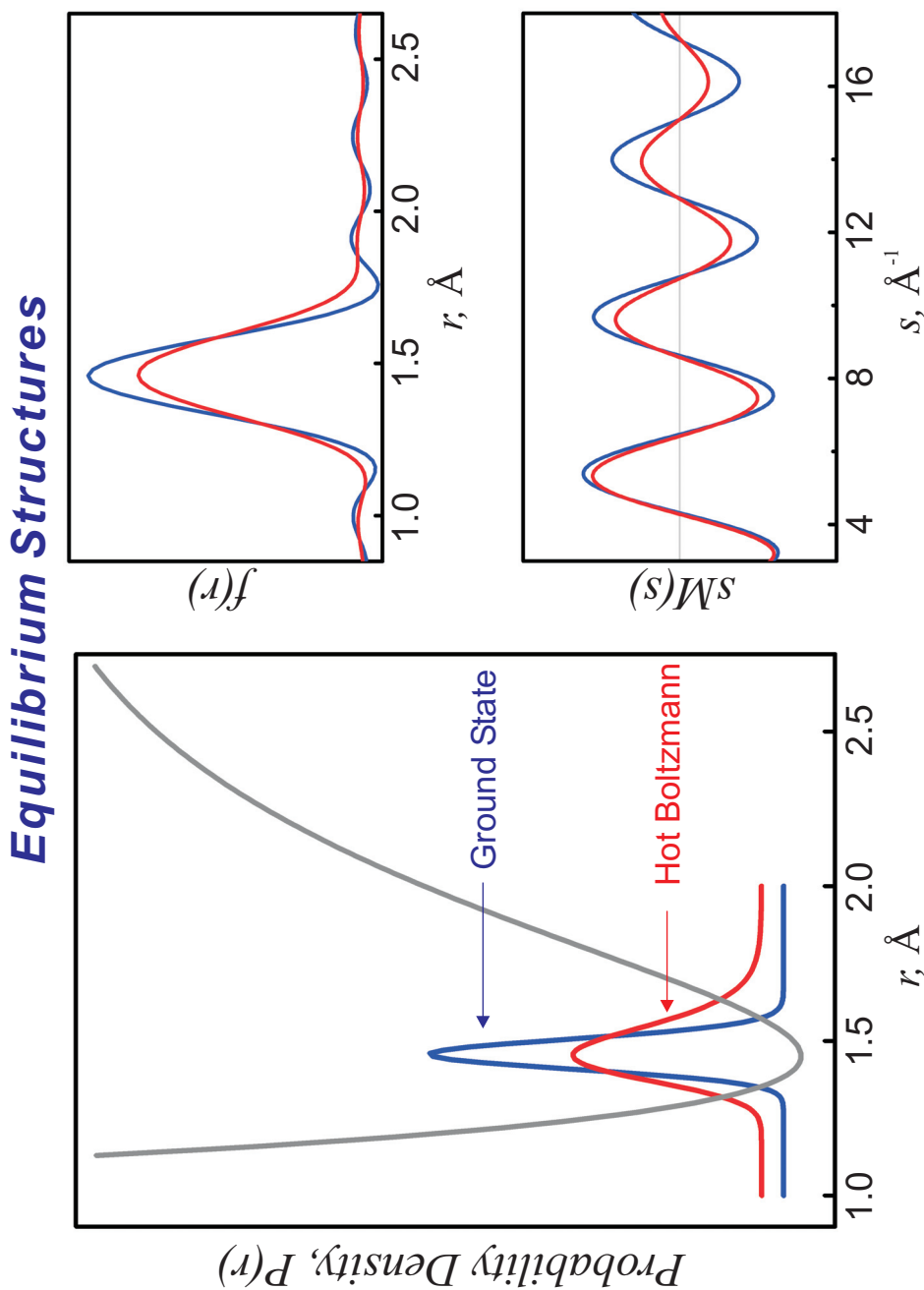


Figure 7-1. Calculated diffraction curves for a single bond in the *equilibrium* regime. Shown on the *left* are probability densities of the single bond distance, and on the *right* are the resulting $sM(s)$ and $f(r)$ curves. Thermal (Boltzmann) vibrational population at ground state is shown in blue and at a much higher temperature in red. Increased temperature results in broadening of the $f(r)$ curve and damping of the $sM(s)$ curve.

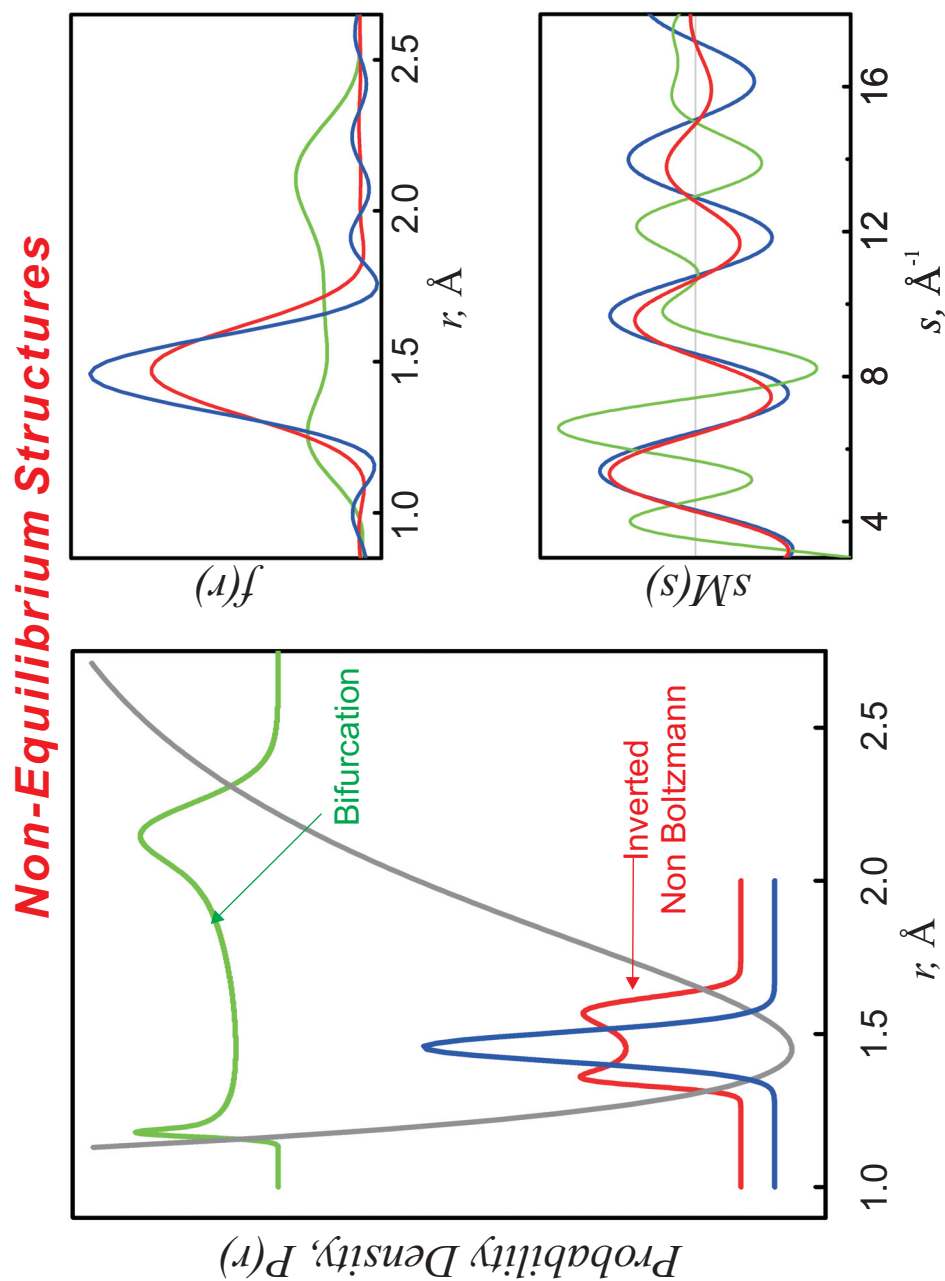


Figure 7-2. Calculated diffraction curves for a single bond in the *Non-equilibrium* regime. Shown on the *left* are probability densities of the single bond distance, and on the *right* are the resulting $sM(s)$ and $f(r)$ curves. Inverted (non-Boltzmann) vibrational populations are modeled with Gaussian distributions. Low-lying inverted populations (red) will cause broadening of the $f(r)$ curve and damping of the $sM(s)$ curve similar to the Boltzmann case above. Higher-lying populations (green) can lead to outright bifurcation of the internuclear density and significant changes in the frequency components of the $sM(s)$ scattering signal.

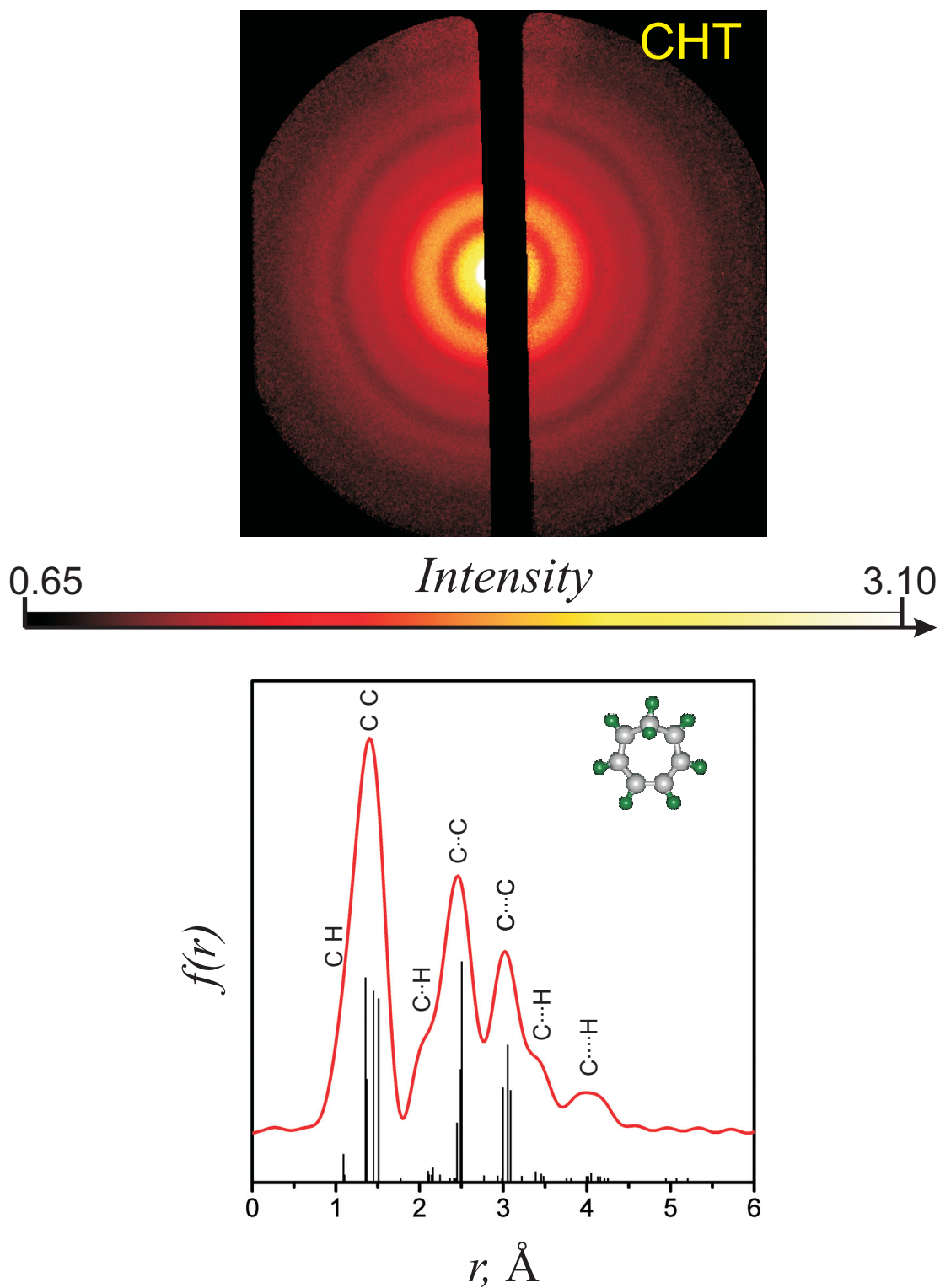


Figure 7-3. Observed ground-state diffraction image and corresponding $f(r)$ curve for CHT. The major bond distances (covalent C–C, second nearest-neighbor C··C, and third nearest-neighbor C··C) are shown above the corresponding $f(r)$ peaks.

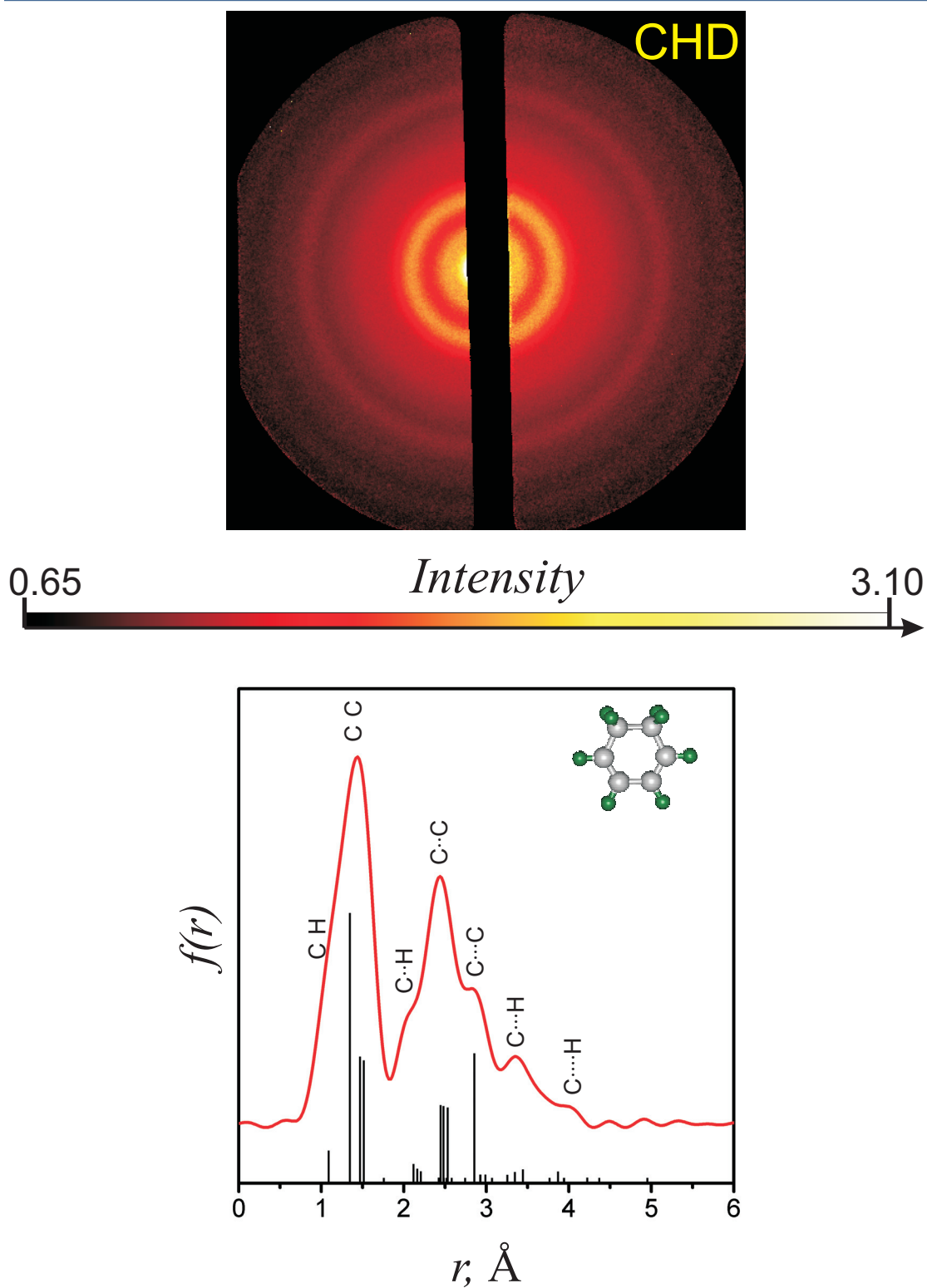
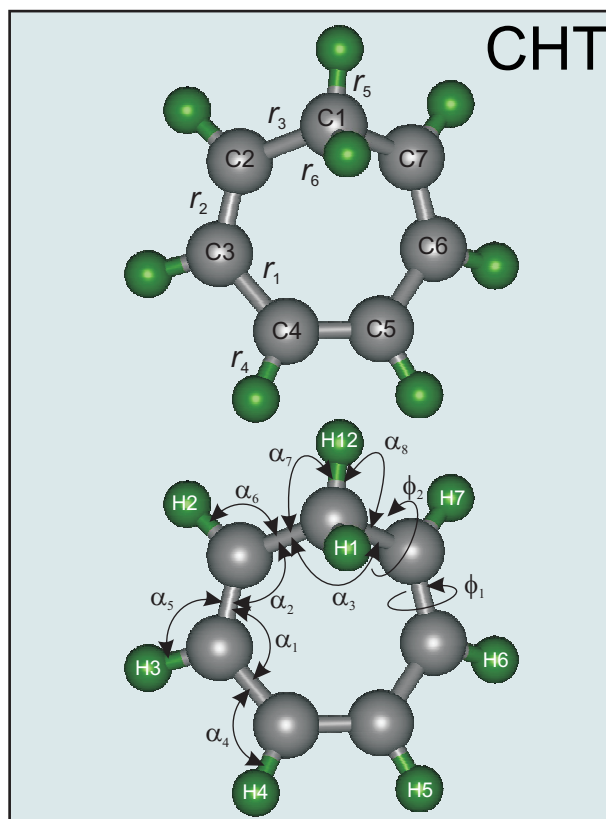


Figure 7-4. Observed ground-state diffraction image and corresponding $f(r)$ curve for CHD. The major bond distances (covalent C–C, second nearest-neighbor C·C, and third nearest-neighbor C··C) are shown above the corresponding $f(r)$ peaks.



Distances

$r_1(\text{C3-C4})$	= 1.429 ± 0.009	(1.47)
$r_2(\text{C2-C3})$	= 1.382 ± 0.008	(1.34)
$r_3(\text{C1-C2})$	= 1.523 ± 0.004	(1.52)
$r_4(\text{C4-H4})$	= 1.095 ± 0.012	(1.089)
$r_5(\text{C1-H12})$	= 1.104 ± 0.113	(1.093)
$r_6(\text{C1-H1})$	= 1.117 ± 0.080	(1.098)

Angles

$\alpha_1(\text{C2-C3-C4})$	= 122.5 ± 3.0	(125.6)
$\alpha_2(\text{C1-C2-C3})$	= 119.6 ± 2.3	(122.0)
$\alpha_3(\text{C2-C1-C7})$	= 117.0 ± 1.7	(108.2)
$\alpha_4(\text{C3-C4-H4})$	= 122.6 ± 2.7	(116.4)
$\alpha_5(\text{C2-C3-H3})$	= 116.6 ± 5.9	(117.8)
$\alpha_6(\text{C1-C2-H2})$	= 113.1 ± 8.8	(118.5)
$\alpha_7(\text{C2-C1-H12})$	= 101.8 ± 9.4	(110.3)
$\alpha_8(\text{C7-C1-H12})$	= 111.3 ± 8.3	(98.4)

Figure 7-5. Refined ground-state structure of CHT. The refined bond distances and angles are shown, along with the DFT values indicated in parentheses. Distances are in ångströms, and angles are in degrees.

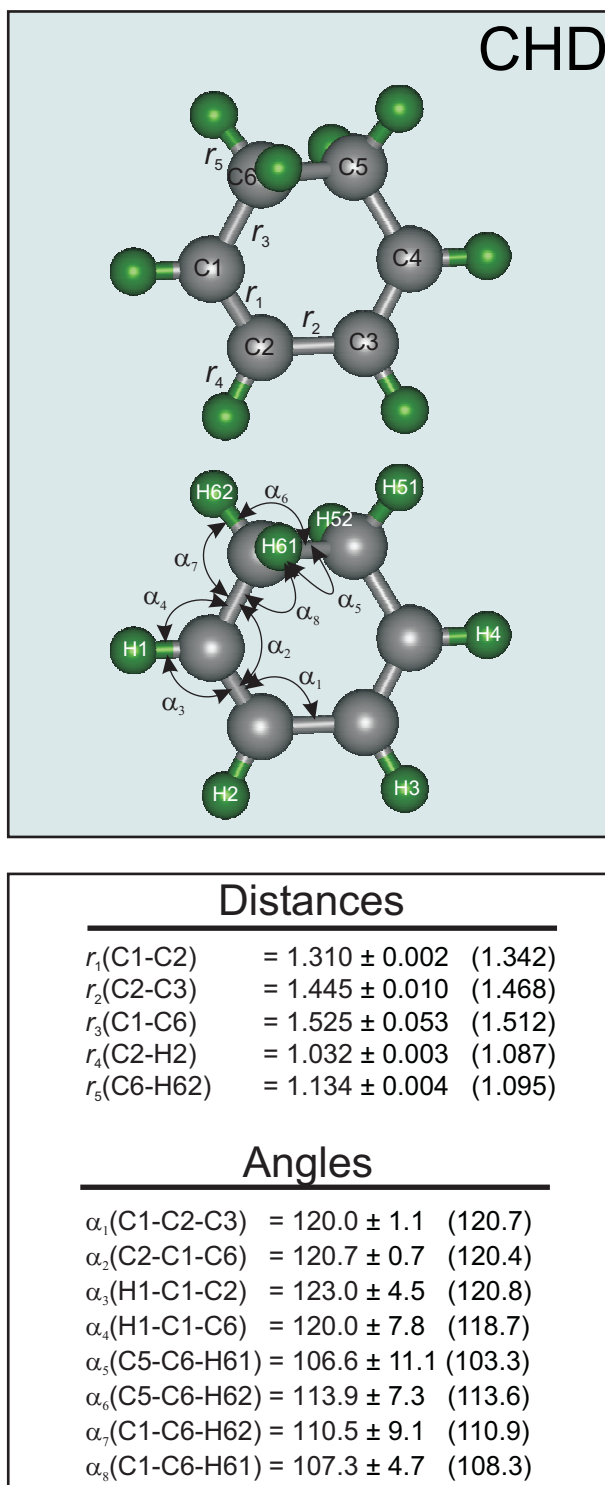


Figure 7-6. Refined ground-state structure of CHD. The refined bond distances and angles are shown, along with the DFT values indicated in parentheses. Distances are in ångströms, and angles are in degrees.

Non-Equilibrium CHT Structure

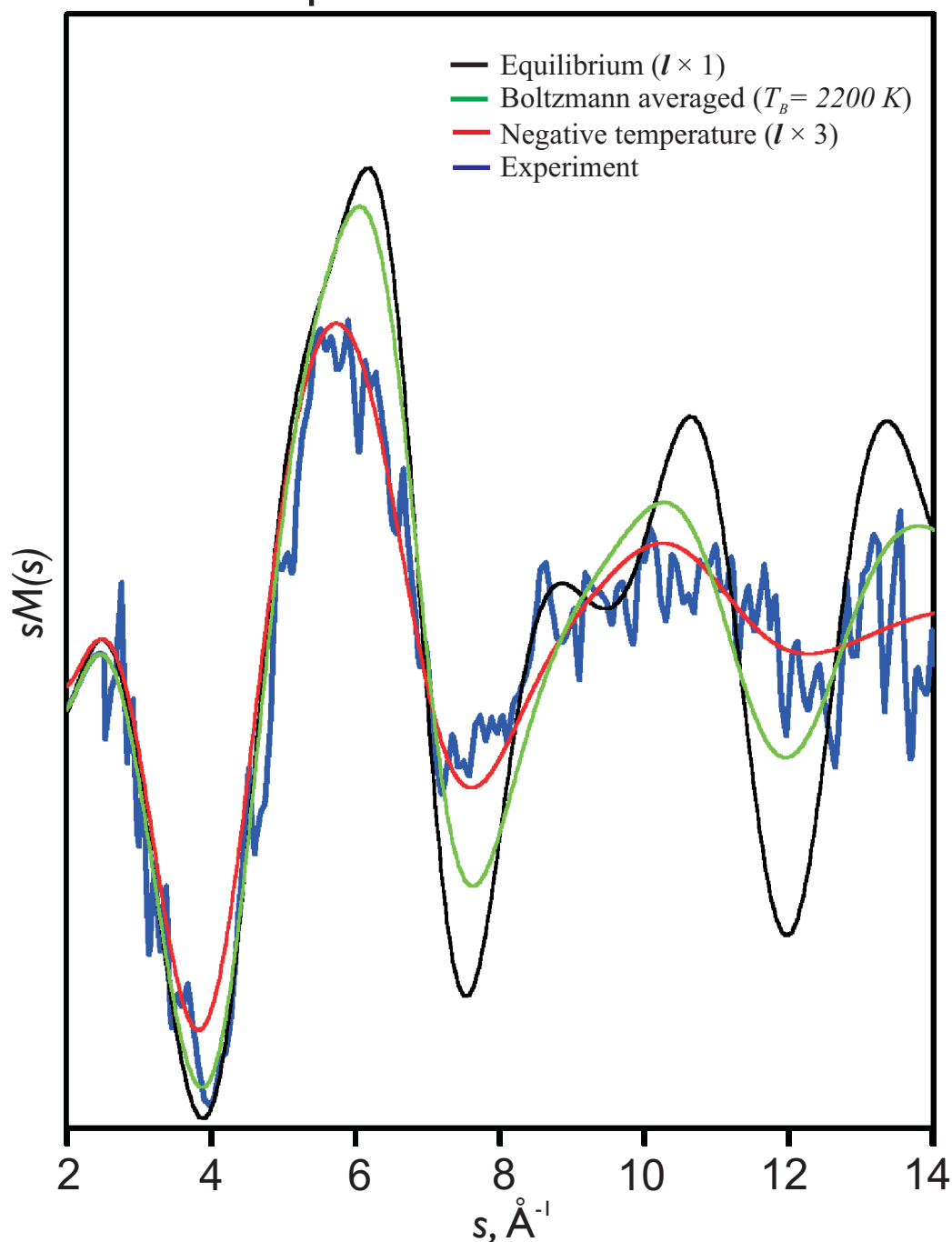


Figure 7-7. Non-equilibrium ‘negative temperature’ in CHT as reflected in the transient-only $sM(s)$ curves. The (blue) experimental curve averaged from 75 to 400 ps is shown, along with corresponding theoretical curves for the equilibrium structure at 403 K (black), the Boltzmann averaged structure at ca. 2,200 K (green), and a non-Boltzmann structure with a mean l value nearly three times that at 403 K (red). For details of structural analysis, see text.

Non-Equilibrium CHT Structure

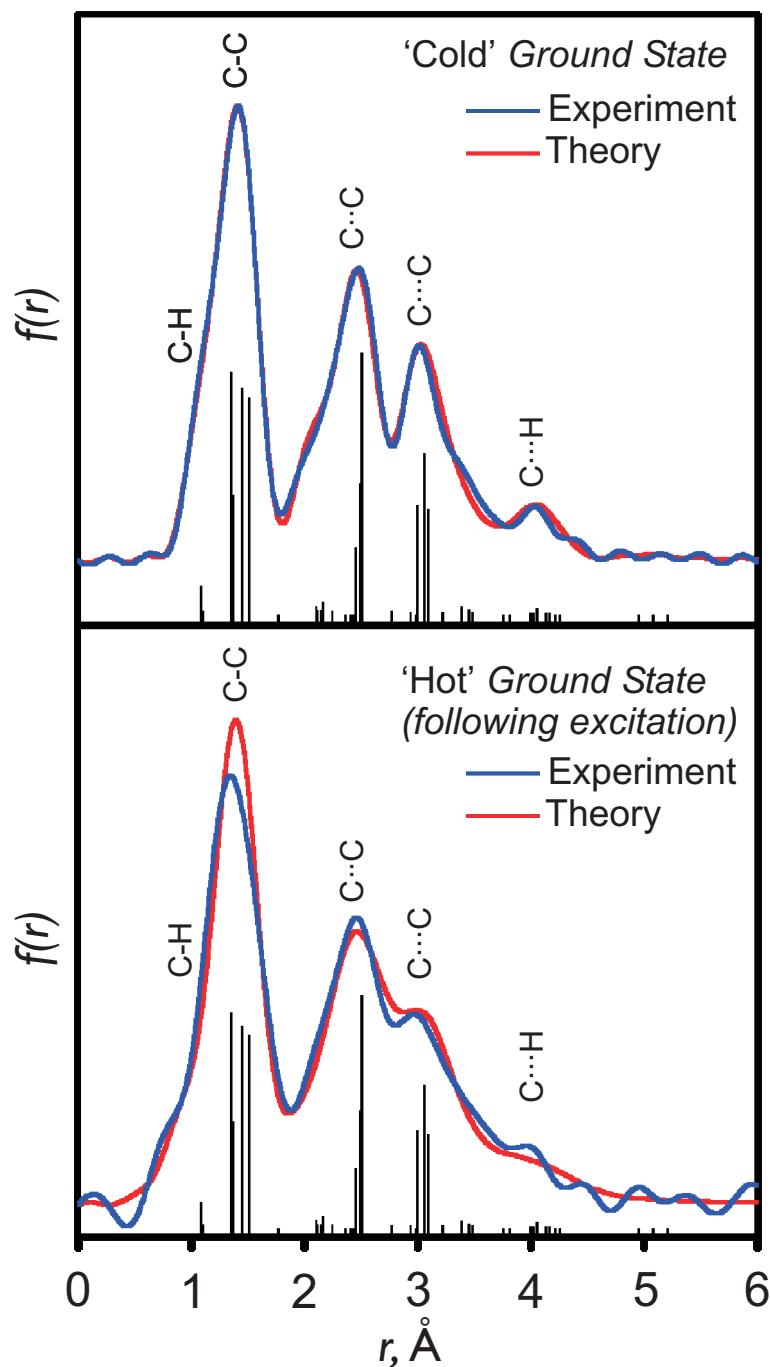


Figure 7-8. Non-equilibrium 'negative temperature' in CHT. Shown is the influence of high vibrational temperature on the ground-state and transient-only $f(r)$ curves. The $f(r)$ curves for the initial structure at 403 K (Top) and the hot CHT structure at a negative temperature (Bottom). Note the significant broadening of the $f(r)$ peaks in the hot structure compared to the cold ground-state; only l was adjusted.

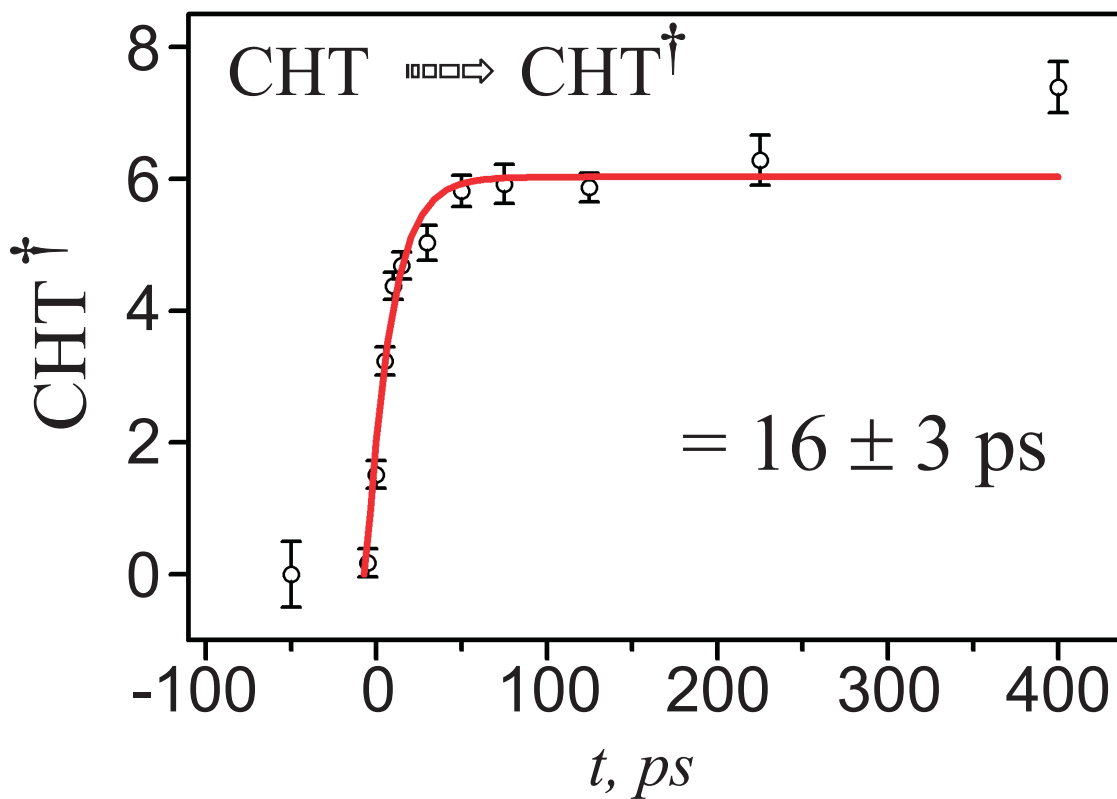


Figure 7-9. Evolution of transient non-equilibrium structure population in CHT.

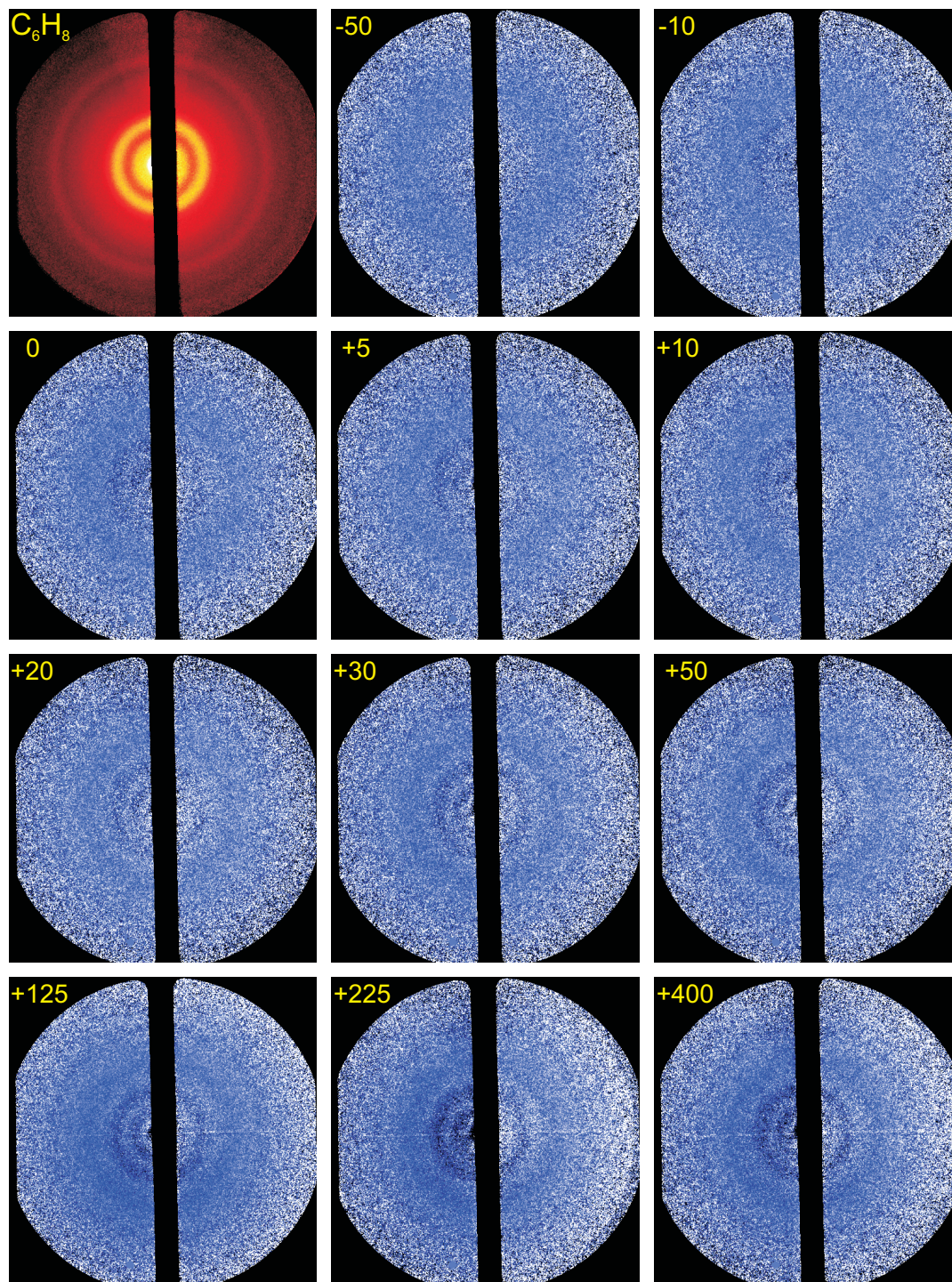


Figure 7-10. Time-resolved 2D diffraction-difference images of cyclohexadiene ($t_{\text{ref}} = -100$ ps). Each frame is identified by the relative time delay (in picoseconds) between the laser pump and electron probe pulses. The emergence of rings in the difference images with increasing time delay reflects the ensuing molecular structural dynamics. The first (*red*) image is the ground-state image.

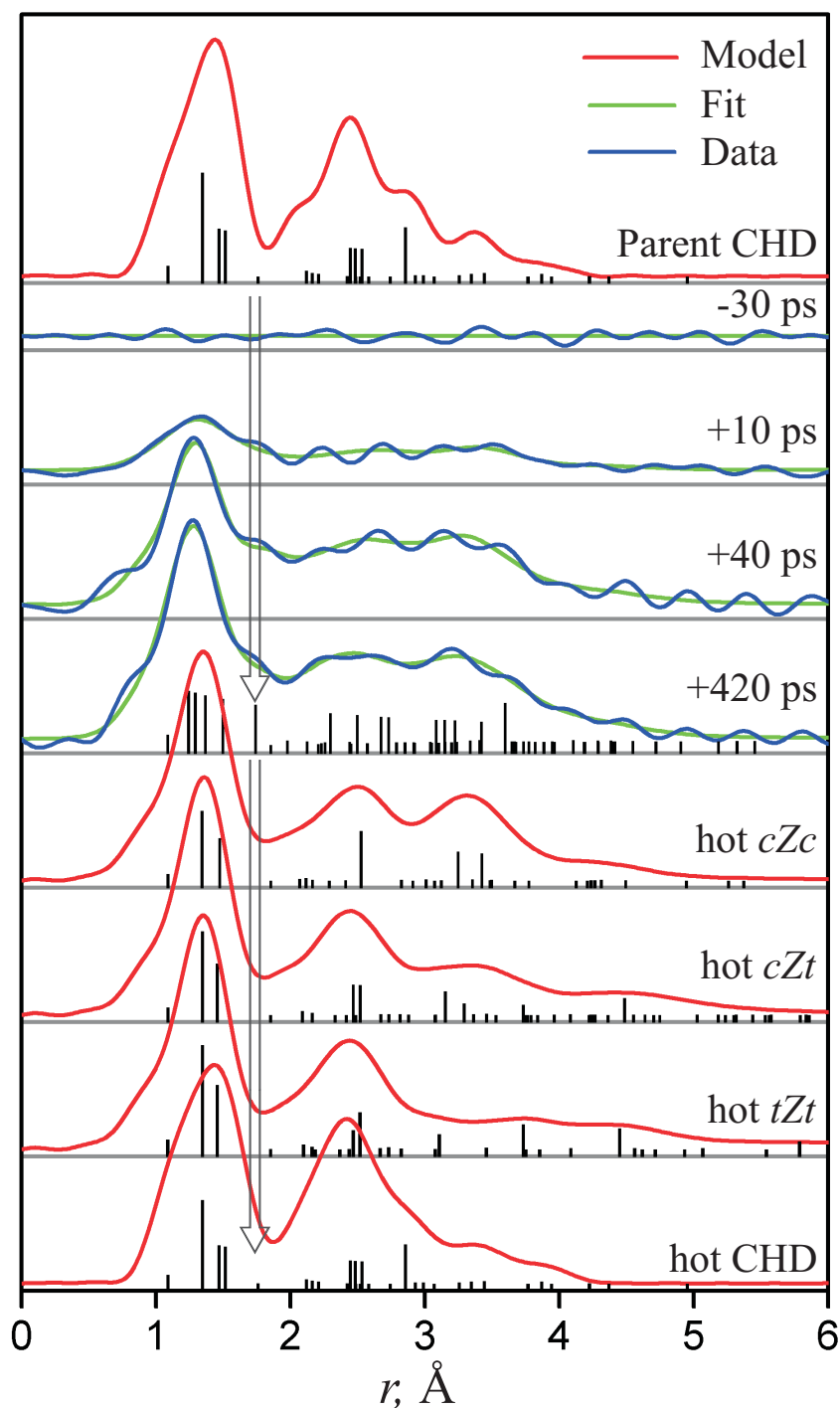


Figure 7-11. Time-resolved formation of hot HT structures after CHD ring opening. *Top:* DFT $f(r)$ curve (red) for the CHD parent structure at 403 K. *Middle:* comparison of selected experimental transient-only $f(t; r)$ curves (blue) with corresponding structural fits (green). *Bottom:* DFT $f(r)$ curves (red) for the three HT conformers (extrapolated to 2,100 K) and for hot CHD (extrapolated to 2,400 K) shown for comparison. The vertical arrows indicate the peak at ~ 1.7 Å, which is present in all experimental curves, but which is absent in the *ab initio* $f(r)$ curves of the three HT conformers.

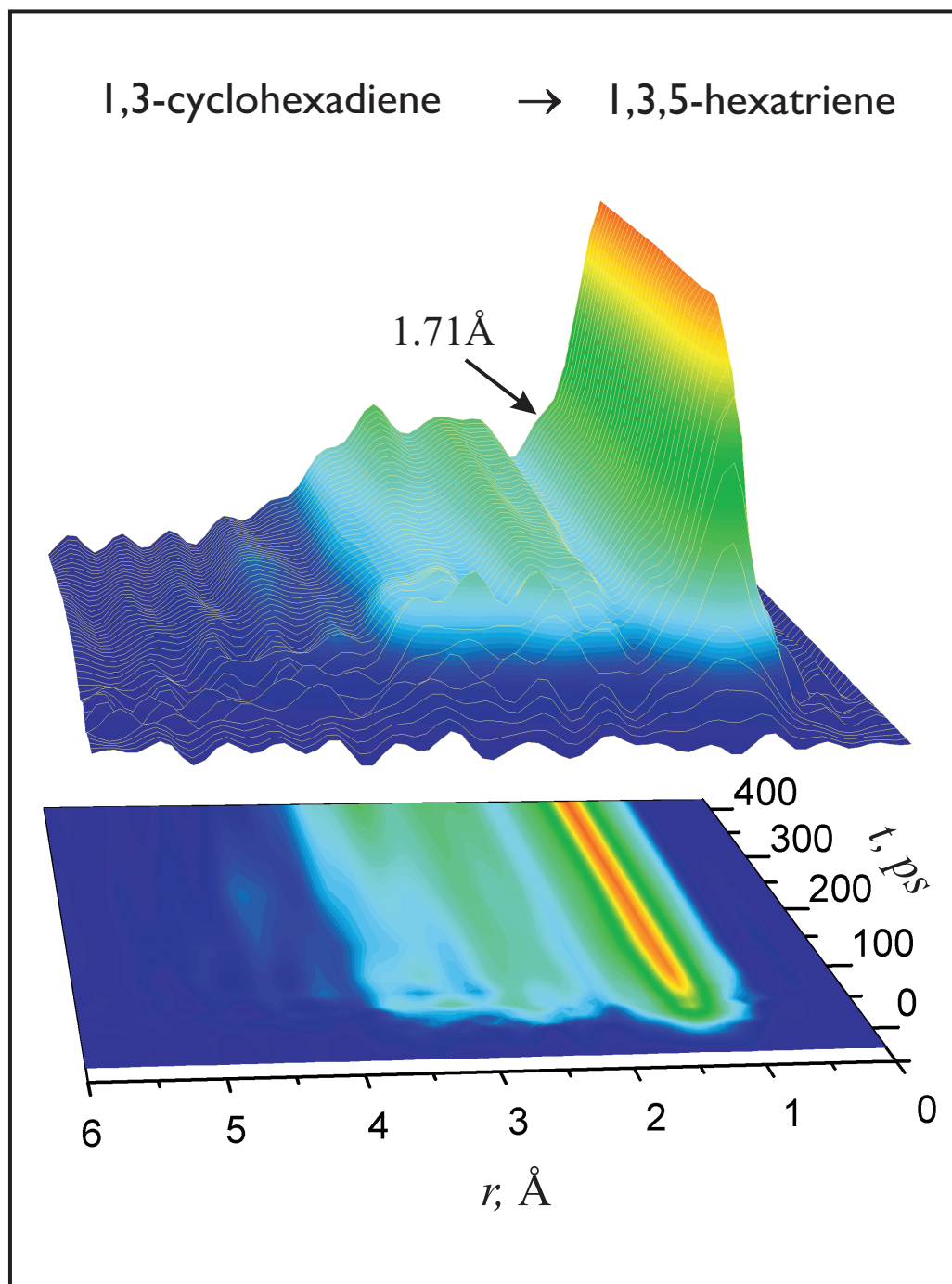
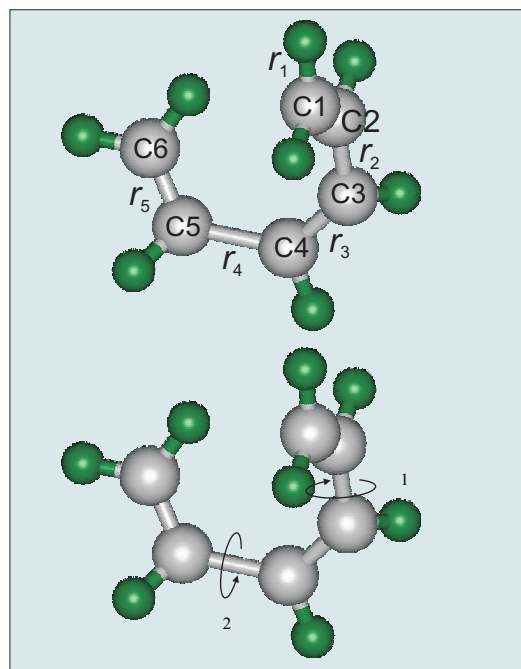
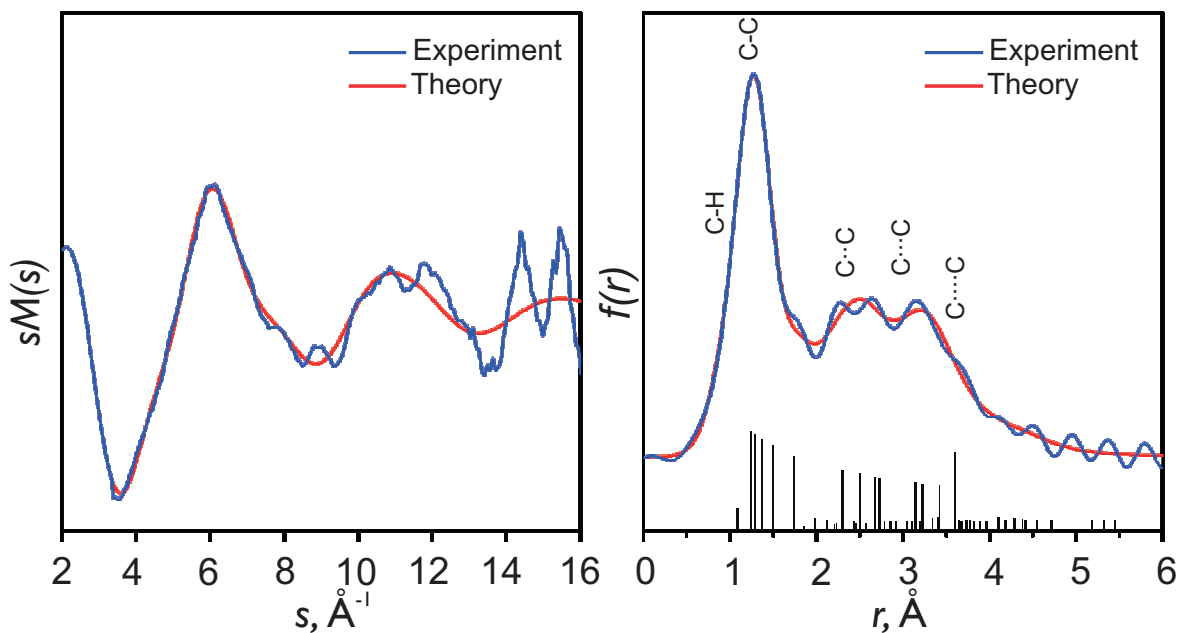


Figure 7-12. Time-resolved formation of hot HT structures after the ring opening of CHD. The Fourier-filtered $f(t; r)$ curves show product evolution over 400 ps; note the shoulder at $\sim 1.7 \text{ \AA}$.

Refined Ring-Opened Structure of HT



Distances

	<i>experiment</i>
$r_1(\text{C1}=\text{C2})$	1.29 ± 0.06
$r_2(\text{C2}-\text{C3})$	1.40 ± 0.10
$r_3(\text{C3}=\text{C4})$	1.41 ± 0.08
$r_4(\text{C4}-\text{C5})$	1.71 ± 0.05
$r_5(\text{C5}=\text{C6})$	1.32 ± 0.04

Angles

$\angle_1(\text{C1C2}-\text{C3C4})$	84 ± 41
$\angle_2(\text{C3C4}-\text{C5C6})$	15 ± 22

Figure 7-13. Structure refinement of ring-opened HT structure. Shown on *top* are the experimental $sM(s)$ and $f(r)$ curves, along with the best-fit theoretical curves. At the bottom is shown the refined HT structure, with its corresponding structural parameters. Distances are in ångströms, and angles are in degrees. The structural parameters were obtained by averaging over the Monte Carlo search results over all time points. The standard deviations represent the spread of the minimum basin in configuration space. Note the elongated (~ 1.7 Å) C4–C5 bond distance.

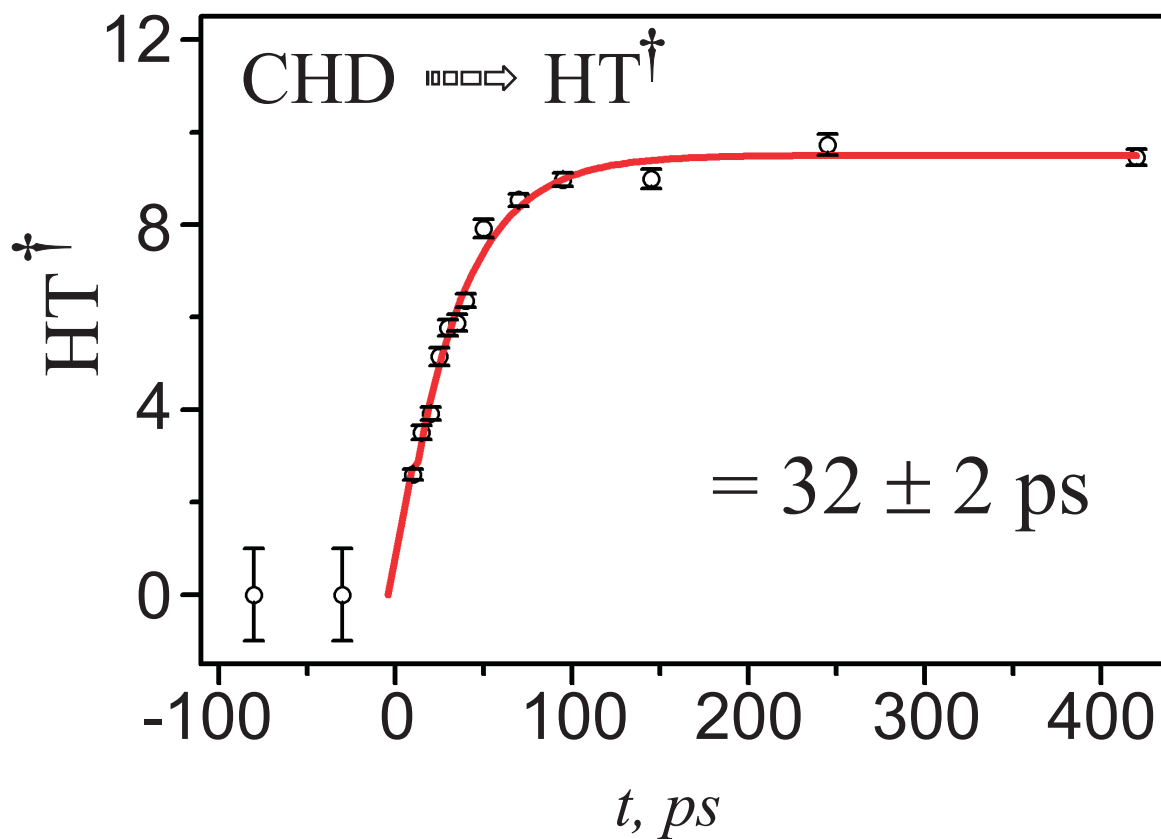


Figure 7-14. Evolution of transient *far-from-equilibrium* structure population in CHD. The time constant for the structural change in CHD is twice that in CHT.

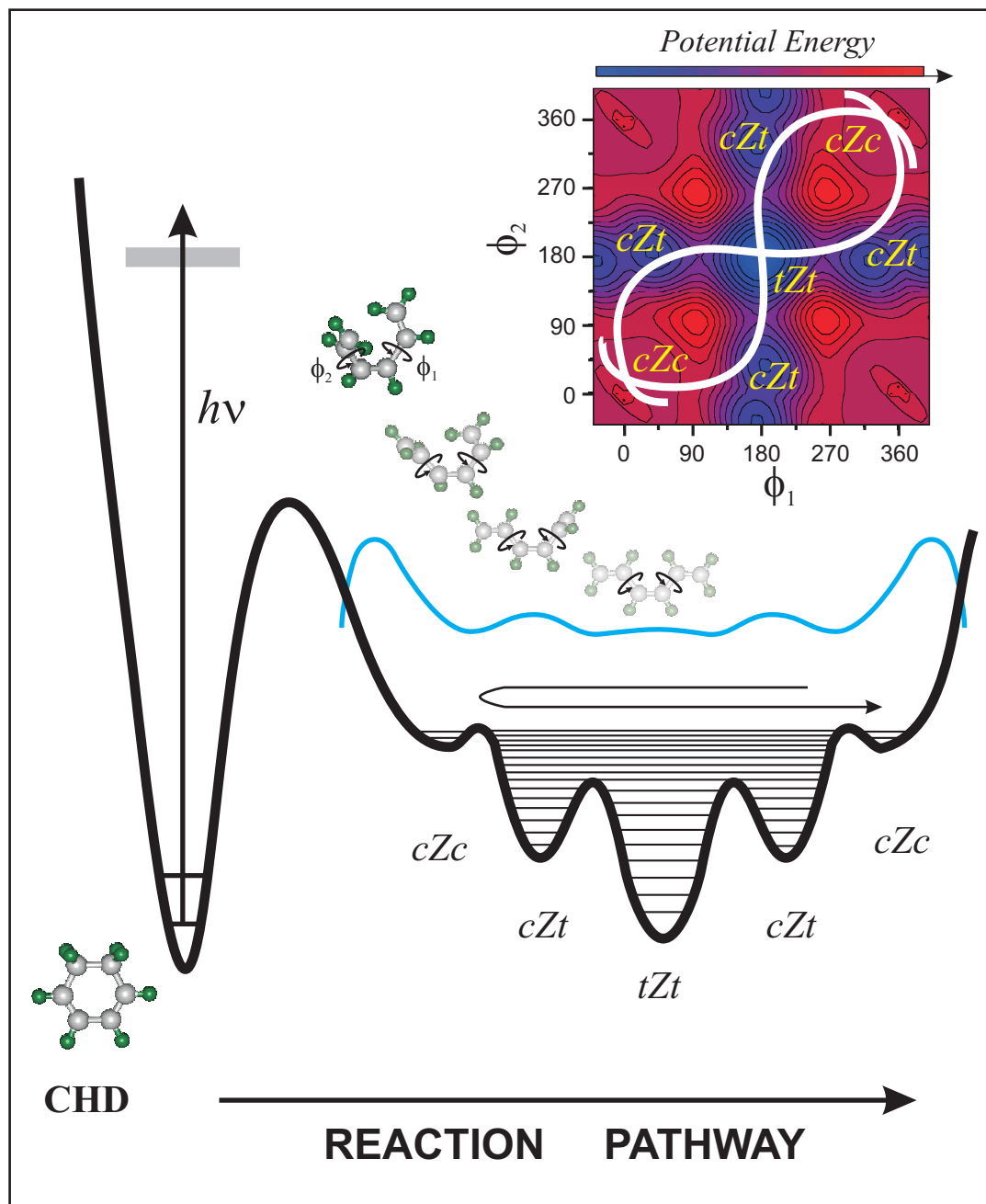


Figure 7-15. Potential energy landscape relevant to the formation of HT. A probability density curve (blue) on the schematic HT ground-state surface depicts the high-energy nature of the product structure. The higher density near the classical turning points reflects significant population in *cZc*-type conformations; the refined molecular structure shown at one of these points represents the average far-from-equilibrium structure over 400 ps. The “faded” structures denote the lower-energy *cZc*, *cZt*, and *tZt* conformations. Inset shows the corresponding *ab initio* 2D potential energy surface governing HT torsion angles (ϕ_1 and ϕ_2) about the C–C single bonds. The white curves illustrate possible trajectories leading to a time-averaged structure with considerable *cZc/cZt* character, but virtually no contribution from *tZt*.

Table 7-1. Selected refined structural parameters for the far-from-equilibrium HT structure

Structural Parameter	Mean [†]	s_{mean} [‡]	s_{fit} [§]	cZc [¶]	cZt [¶]	tZt [¶]
$r(\text{C1}=\text{C2})$	1.29 Å	0.06 Å	0.04 Å	1.338 Å	1.342 Å	1.342 Å
$(\text{C2}-\text{C3})$	1.40 Å	0.10 Å	0.02 Å	1.471 Å	1.453 Å	1.452 Å
$r(\text{C3}=\text{C4})$	1.41 Å	0.08 Å	0.04 Å	1.350 Å	1.353 Å	1.355 Å
$r(\text{C4}-\text{C5})$	1.71 Å	0.05 Å	0.02 Å	1.471 Å	1.465 Å	1.452 Å
$r(\text{C5}=\text{C6})$	1.32 Å	0.04 Å	0.03 Å	1.338 Å	1.341 Å	1.342 Å
$\phi_1(\text{C1C2}-\text{C3C4})$	84°	41°	11°	35.5°	-174.7°	180°
$\phi_2(\text{C3C4}-\text{C5C6})$	15°	22°	11°	35.5°	37.7°	180°

[†]Structural parameters obtained from averaging over all time points.

[‡]Standard deviation (spread) of the mean value.

[§]Standard deviation (error) of the least-squares fit.

[¶]Structural parameters for the HT conformers, calculated using *ab initio* methods (B3LYP/6-311G** basis set), shown for comparison.

References

1. Hargittai, I.; Hargittai, M., *Stereochemical Applications Of Gas-Phase Electron Diffraction*. VCH: New York, 1988.
2. Traetteberg, M., *J. Am. Chem. Soc.* **1964**, *86*, 4265.
3. Oberhammer, H.; Bauer, S. H., *J. Am. Chem. Soc.* **1969**, *91*, 10.
4. Reid, P. J.; Shreve, A. P.; Mathies, R. A., *J. Phys. Chem.* **1993**, *97*, 12691.
5. Trushin, S. A.; Diemer, S.; Fuss, W.; Kompa, K. L.; Schmid, W. E., *Phys. Chem. Chem. Phys.* **1999**, *1*, 1431.
6. Steuhl, H.-M.; Bornemann, C.; Klessinger, M., *Chem. Eur. J* **1999**, *5*, 2404.
7. Hertwig, A.; Hippler, H.; Schmid, H.; Unterreiner, A.-N., *Phys. Chem. Chem. Phys.* **1999**, *1*, 5129.
8. Paulick, W.; Jung, C.; Kempka, U.; Sühnel, J.; Gustav, K., *J. Mol. Struct.* **1981**, *85*, 235.
9. Möller, K. B.; Zewail, A. H., *Chem. Phys. Lett.* **1998**, *295*, 1.
10. Diau, E. W.-G.; Feyter, S. D.; Zewail, A. H., *J. Chem. Phys.* **1999**, *110*, 9785.
11. Yan, M.; Rothberg, L. J.; Callender, R., *J. Phys. Chem. B* **2001**, *105*, 856.
12. Lawless, M. K.; Wickham, S. D.; Mathies, R. A., *Acc. Chem. Res.* **1995**, *28*, 493.
13. Lochbrunner, S.; Fuss, W.; Schmid, W. E.; Kompa, K. L., *J. Phys. Chem. A* **1998**, *102*, 9334.

14. Andersen, N. A.; Pullen, S. H.; Walker II, L. A.; Shiang, J. J.; Sension, R. J., *J. Phys. Chem. A* **1998**, *102*, 10588.
15. Fuss, W.; Schmid, W. E.; Trushin, S. A., *J. Chem. Phys.* **2000**, *112*, 8347.
16. Clary, D. C.; Meijer, A. J. H. M., *J. Chem. Phys.* **2002**, *106*, 9829.
17. Minnard, N. G.; Havings, E., *Recl. Trav. Chim.* **1973**, *92*, 1315.
18. Garavelli, M.; Bernardi, F.; Olivucci, M.; Vreven, T.; Klein, S.; Celani, P.; Robb, M. A., *Faraday Discuss.* **1998**, *110*, 51.
19. Garavelli, M.; Bernardi, F.; Olivucci, M.; Vreven, T.; Klein, S.; Celani, P.; Robb, M. A., *Faraday Discuss.* **1998**, *110*, 51.
20. Trulson, M. O.; Dollinger, G. D.; Mathies, R. A., *J. Am. Chem. Soc.* **1987**, *109*, 586.
21. Reid, P. J.; Doig, S. J.; Wickham, S. D.; Mathies, R. A., *J. Am. Chem. Soc.* **1993**, *115*, 4754.
22. Pullen, S.; Walker, L. A.; Donovan, B.; Sension, R. J., *Chem. Phys. Lett.* **1995**, *242*, 415.
23. Trushin, S. A.; Fub, W.; Schikarski, T.; Schmid, W. E.; Kompa, K. L., *J. Chem. Phys.* **1997**, *106*, 9386.
24. Fuß, W.; Schikarski, T.; Schmid, W. E.; Trushin, S.; Kompa, K. L., *Chem. Phys. Lett.* **1996**, *262*, 675.
25. Pullen, S. H.; Anderson, N. A.; Walker, L. A.; Sension, R. J., *J. Chem. Phys.* **1998**, *108*, 556.

-
26. Zewail, A. H., *Angew. Chem. Int. Ed.* **2000**, *39*, 2587.
 27. Ischenko, A. A.; Schäfer, L.; Luo, J. Y.; Ewbank, J. D., *J. Phys. Chem.* **1994**, *98*, 8673.
 28. Mizutani, Y.; Uesugi, Y.; Kitagawa, T., *J. Chem. Phys.* **1999**, *111*, 8950.
 29. Helliwell, J. R.; Renzepis, P. M., *Time-Resolved Diffraction*. Oxford University Press: New York, 1997.
 30. Rouse, A.; Rischel, C.; Fourmaux, S.; Uschmann, I.; Sebban, S.; Grillon, G.; Balcou, P.; Forster, E.; Geindre, J. P.; Audebert, P.; Gauthier, J. C.; Hulin, D., *Nature* **2001**, *410*, 65.
 31. Techert, S.; Schotte, F.; Wulff, M., *Phys. Rev. Lett.* **2001**, *86*, 2030.

8

CONFORMATIONAL DYNAMICS ON COMPLEX ENERGY LANDSCAPES*

8.1 Introduction

Complex transient structures are ubiquitous in chemical and biological reactions. Progress has been made in elucidating structures¹⁻³ (near) their equilibrium states, but to reach intermediate structures in the transition region between reactants and products the time resolution must be ≤ 1 ps.⁴ Pericyclic reactions—processes in which bonds are believed to be concertedly

* Adapted from Goodson, B.M.; Ruan, C.-Y.; Lobastov, V.A.; Srinivasan, R.; Zewail, A.H., *Chem. Phys. Lett.* **2003**, *374*, 417.

forged and broken in a cyclic transition state—have such complex structures, and they occur on the ultrafast time-scale. These reactions, which are central in chemistry, can be described by the orbital symmetry correlations of Woodward and Hoffmann,⁵ with the resulting products and stereochemistry often depending on whether the reaction is activated by heat or light. An archetypical example is that of Cope rearrangement of 1,3,5-cyclooctatriene (COT3).⁶ The synthesis of COT3 gives a mixture of COT3 and bicyclo[4.2.0]octa-2,4-diene (BCO), and it has been shown that above 100 °C, both species rapidly interconvert *thermally* by an electrocyclic ring opening/closure process,⁷ as shown in Scheme 8–1.

In contrast, the *photochemistry* of COT3 (and BCO), which has been studied in solution⁸⁻¹¹ and in matrices¹²⁻¹⁵ for both the neutral and cationic species, has shown that COT3 undergoes electrocyclic ring opening. The product is 1,3,5,7-octatetraene (OT),¹⁰⁻¹⁴ and the reaction is shown in Scheme 8–2.

The nascent OT species is transient and cyclizes to (re-)form COT3 thermally on a time-scale of seconds;¹⁰ upon absorption of additional UV light, it isomerizes.^{10,15} (Similarly, BCO upon UV absorption gives predominantly OT, which ultimately gives COT3.¹²) For these complex reactions, it is essential to elucidate the structures involved, equilibrium and far-from-equilibrium (transients).

COT3 represents a particularly challenging system to study via UED for a variety of reasons, including the number of different structures potentially involved, the lack of symmetry in most of these structures, the large number of atoms in each species, and the complex landscapes of transient products. With the temporal and spatial resolutions achieved in UED-3, we performed the first ground-state electron diffraction study of this system and resolve the two structures (COT3 and BCO) involved in the thermally mediated interconversion. For the light-mediated reactions, following femtosecond UV excitation and imaging with ps electron pulses, we determined the transient structure involved in the ring opening (OT structures). Unlike ground-state reactions, the nascent structures of the ring opening process are far-from-equilibrium, as shown below.

8.2 Methodology

Diffraction images were obtained with our third-generation UED apparatus. Briefly, ultraviolet femtosecond laser pulses ($\sim 200 \mu\text{J}$, $\sim 267 \text{ nm}$, $\sim 120 \text{ fs}$, 1 kHz repetition rate) were directed into the scattering chamber to initiate structural change, whereas the weaker beam ($\sim 5 \mu\text{J}$) was directed into a delay line and focused onto a back-illuminated silver photocathode to generate electron pulses via the photoelectric effect. The pulse width in these experiments was $\sim 4 \text{ ps}$ ($\sim 25\,000$ electrons). The pulses were accelerated into

the scattering chamber at 30 keV (de Broglie wavelength: 0.067 Å). Electron diffraction images were recorded with a low-noise image-intensified 2-D CCD camera assembly capable of single-electron detection. The camera length for these experiments (13.41 cm) was calibrated by comparing experimentally derived diffraction data obtained from high-purity CO₂ gas with literature values.¹⁶ The reaction zero-of-time, i.e., the overlap of the initiating femtosecond pulse and probing electron pulse, was determined by the ion-induced lensing technique.¹⁷ In a cross-beam geometry, the laser, electron, and molecular beam intersected in a region of ~400 μm wide. The molecular beam pressure was a few torr while the background pressure within the scattering chamber was $\sim 2 \times 10^{-4}$ Torr over the course of the experiment. Diffraction images were processed using computer-interface to the CCD camera.

8.3 Structure Refinement

The modified molecular scattering intensity of each pair of atoms (i, j) in an isotropic sample can be written as:

$$sM(s) \propto \sum_{i,j} \frac{\sin(sr_{ij})}{r_{ij}} \cdot \exp\left(-\frac{1}{2}l_{ij}^2 s^2\right) \quad (8-1)$$

where s is the momentum transfer parameter, r_{ij} is the internuclear separation between the two atoms, and l_{ij} is the corresponding mean

amplitude of vibration. The corresponding radial distribution curves were obtained via Fourier (sine) transform of $sM(s)$ curves:

$$f(r) = \int_0^{s_{\max}} sM(s) \sin(sr) \exp(-ks^2) ds \quad (8-2)$$

where the damping constant k accounts for the finite s range of the detector. The procedures used for obtaining mean amplitudes of vibration and corresponding corrections for internuclear distances at high temperature were described elsewhere.¹⁸ The structure parameters are constructed using the internal coordinates of a geometrically consistent structural model for the molecule in terms of Z -matrix formalism. All data analysis and structural refinement were performed using software developed in this laboratory. Reported error bars represent one standard deviation of the least-squares fit. The quality of a given least-squares fit was evaluated in terms of the resulting statistical R value.¹⁶

8.4 DFT Calculations

All calculations utilized in this work were performed using the GAUSSIAN 98¹⁹ commercial quantum chemistry package on a Windows-based PC. The B3LYP density functional theory (DFT) method (at the 6-311G** level) was employed to calculate the geometries, vibrational

frequencies, and energies of the relevant species. Closed-shell restricted wave functions were used for all calculations.

8.5 Monte Carlo Global Structural Optimization

In order to ensure all possible structures are considered in the refinements, Monte Carlo sampling procedures are applied to search all possible good fits to the data (in terms of χ^2) in a configuration space set up by the *Z*-matrix coordinates. The distance between any two given structures is defined as the square root of the sum of the squared displacements between all corresponding nuclear coordinates of the two structures. Based on the distance between randomly sampled structures to a starting structure, the hyper configuration space is first partitioned and then searched for local minima. When the samplings within the partitioned subspace are found to converge to a local χ^2 minimum, the radius of convergence is determined along each adjustable coordinate in the *Z*-matrix to give the size of local minimum basin. Finally, lowest local minima structures are statistically analyzed to reveal the ensemble distribution of a global minimum structure.

8.6 Results and Discussion

A. Structures of Cope Rearrangement

The UED image obtained from the ground-state structures is shown in

Fig. 8–1(a); the corresponding 1-D radial average is shown in Fig. 8–1(b). The isomerization of 136COT to 135COT and the facile thermal equilibration between BCO and 135COT are some of the many interconversions of the C_8H_{10} isomers that have been observed. The latter, which is in fact a reversible Cope rearrangement involving a 1,2-diallylcyclobutane, has been shown by Cope *et al.*⁶ to be rapid at 100 °C. Such rearrangements are known to proceed via a six-center transition state. The interconversion of the three C_8H_{10} isomers – 136COT, 135COT, and BCO – is shown in Scheme 8–3.

Greathead and Orchard⁷ have measured the gas-phase equilibrium and rate constants for the isomerization of 136COT to 135COT between 390 and 490 K. The equilibrium constant for the $136COT \rightleftharpoons 135COT$ reaction is given by the van't Hoff equation:

$$\ln K_1^0 = (0.24 \pm 0.04) + (13.78 \pm 0.15 \text{ kJ/mol}) / RT \quad (8-3)$$

Similarly, the gas-phase equilibrium and rate constants for the isomerization of BCO to 135COT have been measured between 330 and 475 K. The corresponding equilibrium constant for the $135COT \rightleftharpoons BCO$ reaction fits the van't Hoff equation:

$$\ln K_2^0 = (-1.20 \pm 0.02) - (0.40 \pm 0.07 \text{ kJ/mol}) / RT \quad (8-4)$$

At the temperature of our experiment (433 K), 1,3,6-COT3 is in dynamic equilibrium with COT3 and BCO. From the above van't Hoff

equations, the relative fractions of the three isomers at 160 °C are estimated to be ~1.3% 136COT, ~77.7% 135COT, and ~20.9% BCO. Due to the vanishingly small contribution (~1%) of the 136COT species, it was not considered further in our refinements.

Both COT3 and BCO ground-state structures were observed in our diffraction data. Our initial refinements examined the relative fraction of these structures in dynamic equilibrium, governed by the sample temperature and the energy difference between the molecules. A series of least-squares refinements were performed on the relative fractions of theoretical (DFT) COT3 and BCO structures, with systematic variation of the initial fractions. We obtained a global minimum with a 73.3:26.7 COT3:BCO ratio at 160 °C (with a statistical 1σ uncertainty of $\pm 2\%$), in good agreement with the value predicted by the results of previous chromatographic experiments (77.7:20.9).⁷ The resulting fit to the UED data using the unrefined DFT structures was excellent ($R=0.105$); the corresponding (black) residual curve is shown in Fig. 8–2.

To our knowledge, the structure of COT3 has not previously been studied in the gas phase; we, therefore, performed a partial refinement of its molecular structure with our electron diffraction data. To combat parameter-correlation problems, we reduced the number of adjustable parameters in our refinement by making the following simplifications:

1. The COT3 molecule was divided in half (along its pseudo- C_2 axis) and set each covalent CC distance on the “left” side of the molecule to be equal to the corresponding (refined) distance on the “right” side, plus a small difference predicted by our calculations (although all skeletal bond angles and torsional angles were still refined independently—see Table 7–1).
2. Each covalent C–H distance was assigned one of two (refined) values, depending on its hybridization.
3. DFT-predicted values were used for all bond angles and torsional angles involving hydrogen atoms. Our refinement of the COT3 molecular structure was thus comprised of a total of 17 adjustable parameters (6 covalent distances, 6 skeletal bond angles, and 5 skeletal torsional angles). Subsequent fraction refinement left the COT3:BCO ratio essentially unchanged (72.5:27.5).

The results of the structural fit to our UED data are shown in Fig. 8–3, and the refined structural parameters are presented in Table 8–1 and compared with values predicted by DFT. Agreement between theory and experiment was further improved by the refinement, shown clearly by the reduced residual $sM(s)$ curve (green) (see Fig. 8–2) and lower R value for the fit (0.068). The peaks in $f(r)$ show contributions from both ground state

structures, with covalent C–H and C–C distances at ~ 1.1 Å and ~ 1.4 Å, second nearest-neighbor C··H and C··C distances at ~ 2.2 Å and ~ 2.6 Å, and third and fourth nearest-neighbor C··H and C··C distances at ~ 2.7 Å to ~ 5 Å. The molecular structure obtained for COT3 from our UED data is shown alongside Table 7–1; the overall conformation of COT3 is “twist-boat” in nature (with C_1 symmetry), in agreement with previous solution-state NMR conformational studies,²⁰ as well as theoretical predictions reported here and in previous work.^{20, 21} Inspection of the corresponding structural parameters in Table 7–1 shows good agreement between the refined experimental values and those predicted by our DFT calculations. Some deviations from theory may be the result of parameter correlation (e.g., the apparent inversion of r_1 and r_3 , and of the two C–H distances); however, the observed differences are generally within the uncertainty of the refinement.

B. Ring Opening Reactions

To observe structures of the light-mediated reactions, we acquired UED images at three time delays (t) between the laser and electron pulses: -100 , -50 , and $+150$ ps, all with a resolution of 4 ps. Unlike previous UED-3 experiments, only a single positive time slice was obtained in order to limit the amount of expensive sample used during the course of the experiment. The diffraction signal at -100 ps, which results only from parent structures,

was used as our reference in generating the diffraction difference images shown in Fig. 8–4. No diffraction signal was observed in the $t = -50$ ps image, differenced from the -100 ps image, as the electron pulse for both times only images the reactant structures. However, diffraction rings could be clearly seen in the $+150$ ps image, which are derived exclusively from structural changes induced by the femtosecond initiating pulses. The experimental $\Delta sM(s)$ and $\Delta f(r)$ curves at $+150$ ps are shown in Figs. 8–5 and 8–6.

The diffraction curves at positive time, shown in Figs. 8–5 and 8–6, give the structures of the species along the primary reaction pathway. Energetically allowed reaction pathways, based on our DFT calculations, identify the ring opening to form OT as a definite pathway, but also identify another possible path for fragmentation (to form benzene and ethylene or 1,3-cyclohexadiene (CHD) and acetylene) or isomerization (to 1,3,6-COT3). Naturally we also consider all possible structures at the internal energy possible (up to 100 kcal/mol) of the parents (COT3 and BCO) and of transient OT (conformations of Fig. 8–7). The effect of the high internal energy is directly manifested in the structural parameters, as elevated vibrational amplitudes, inverted torsional distribution, and/or changes in averaged bond distances from those expected for the equilibrium structures.¹⁸ We found the best agreement, an R value of ~ 0.5 without refinements, when the reaction path is that of ring opening with the product being vibrationally hot. In

contrast, our fits with the hot ‘parent’ structures (1,3,5-COT3, 1,3,6-COT3, and BCO) were poor as judged by R values of ~ 0.9 , ~ 1.0 , and ~ 1.4 , respectively. The depletion ratio of parents was fixed at 76:24 (COT3:BCO), adjusted for the slightly higher absorption cross-section of COT3 at 267 nm.⁶

The ring-opening pathway is also evident upon the inspection of the data $\Delta f(r)$ curves shown in Fig. 8–6. At the same positive time delay we observe peaks with *negative* and *positive* amplitudes: the negative peaks (red regions) correspond to the net *loss* of internuclear density (i.e., the loss of covalent and second, third, and fourth nearest-neighbor distances in the parent structures), whereas the positive peaks (blue regions) correspond to a net *gain* in internuclear density (e.g., the formation of new bond pairs at distances greater than 4 Å). Such a pattern is entirely consistent with ring-opening processes that form more extended structures in the transient species, and this is evident more quantitatively by the agreement between experiments (distances and amplitudes) and theory.

C. The Observation of Non-equilibrium Configurations in OT

The parent (COT3 and BCO) and product (OT) structures are nearly isoenergetic; thus, the OT structures formed by ring opening are left with high excess internal energy from the absorbed UV photons (>100 kcal/mol). Our previous UED studies of light-mediated pericyclic reactions showed that

such energies can be directly manifested as changes in geometrical parameters and vibrational amplitudes from those expected with equilibrium structures.¹⁸ We therefore examined the UED signals for the signatures of such non-equilibrium product structures: namely, elevated vibrational amplitudes, non-equilibrium bond distances, and inverted torsional distributions.

The good fit of the UED data to the higher-energy *tcGct* structure provided the first indication of the non-equilibrium nature of OT; a thermally equilibrated conformer distribution (with an estimated Boltzmann temperature of ~1900 K) would be comprised mostly of lower-energy *tcAct* and *tcAcc* structures (~70%, based on thermochemical values obtained from our DFT calculations). Indeed, when we fit the UED signals with multiple conformers simultaneously, we found the best reproduction of our data using the canonical OT structures with a two-part mixture of highest-energy *ccGcc* structures (~55%) and lowest-energy *tcAct* structures (~55% / 45% *ccGcc* to *tcAct*; $R=0.260$). As before, theoretical mixtures with the *ccAcc* conformers gave lower-quality fits (or more often, led to insignificant or negative fractions of these conformers), indicating that the average OT structure in our experiment is poorly represented by the *ccAcc*-type torsional configurations. We also observed elevated vibrational amplitudes in all of our fits. To obtain the fitted results shown, the CC and CH vibrational

amplitudes had to be respectively increased by an average of ~ 3.1 and ~ 2.3 times the ambient temperature values (at 433 K), corresponding to a $\sim 40\%$ increase over what would be expected for a thermally equilibrated distribution of the excess internal energy over the vibrational degrees of freedom.

In our studies of the light-induced ring opening of CHD to form high-energy (ground state) HT, we observed a stretched CC single-bond distance—in addition to an inverted torsional configuration and elevated vibrational amplitudes—that persisted in the average product structure for at least 400 ps. In order to obtain an improved representation of the ensemble-average OT structure (and with our previous UED observations of far-from-equilibrium structures in mind) we performed a Monte-Carlo / least-squares refinement of the three CC single bonds and the corresponding dihedral angles using the experimental $\Delta sM(s)$ curve.

Because of the high sensitivity achieved here, the different conformations of transient OT structures (Fig. 8–7) were further examined in the UED analysis and reduced to the *gauche* structures. The higher energy *gauche* structure, so-called *tcGct*, was found to be the best of the *R* values. Being a dominant structure at high energies elucidates its non-equilibrium state of dynamics. If equilibrium structures are the only one present at the Boltzmann temperature of ~ 1900 K (determined by the internal energy), the

lower-energy *anti* structures (*tcAct* and *tcAcc*) would be the dominant one(s) (~70%), contrary to the findings. The CC and CH vibrational amplitudes for the refined *gauche* structure are increased by an average of ~3.1 and ~2.3 times the ambient temperature values (at 433 K), corresponding to a ~40% increase over what would be expected for a thermally equilibrated distribution of the excess internal energy over the vibrational degrees of freedom.

In order to determine the nature of the landscape of molecular conformations and to obtain a final representation of the ensemble-average OT structure, we performed a Monte Carlo/least-squares refinement of the three CC single bonds and the corresponding dihedral angles. Our search of the configuration space began at the all folded OT (*ccGcc*) structure, freeing the parameters to change $\pm 0.25 \text{ \AA}$ for the C–C bonds and $\pm 180^\circ$ for the dihedral angles. After 375,000 sampling steps, 22 local minima that gave nearly identical fits to the UED data were obtained (with $R = 0:33\text{--}0:36$ for the difference curves). Further least square refinements were applied to the local minimum structures, but their scopes of adjustments were limited within the radius of convergence associated with each minimum. The results of these fits are generally superb (with $R = 0:32\text{--}0:35$ for the difference curves, and $R = 0:17\text{--}0:19$ for the corresponding transient-only curves) as shown in Figs. 8–6 and 8–8.

The success in reaching this determination of the complex structures with multiple conformations was finally confirmed from the transient-only diffraction curves. Figs. 8–8(a,b) show the comparison of the experimental and theoretical $sM(s)$ and $f(r)$ of these transient-only curves, obtained using the structural parameters of the first minimum of the Monte Carlo/least-squares refinements. Fig. 8–8(c) shows the structures of five selected minima superimposed for comparison, as well as a table summarizing the values of the refined parameters. The structures of all minima clearly show considerable *gauche tcGct/ccGct* character and not the *anti* equilibrium OT structures (Fig. 8–7), indicating an inverted (non-Boltzmann) torsional distribution. This non-Boltzmann behavior is also revealed in the disparities of the torsional motions and in the corresponding CC single bond distances. We found that the two terminal torsions (ϕ_1, ϕ_3) in the side groups of OT have broad distributions ($\pm 40^\circ$); in contrast, the torsion at the central C–C bond (ϕ_2), which establishes the *gauche* character of OT, is rather confined ($\pm 6^\circ$). Correspondingly, the central C–C bond distance (r_2) was found to be slightly lengthened while all the rest of the C–C bonds remain at (near) equilibrium distances. These far-from-equilibrium structures reflect large amplitude torsional motions comprised of ϕ_1, ϕ_3 , and r_2 , which are involved in the ring opening of COT3. The motions persist for long times and are resolved in our experiments. Moreover, they are not in thermal equilibrium with the rest of

molecular motions as shown here and for even less complex structures. The results are surprising in that the persistence of torsional motions across large complex energy landscape and for long times indicate a bottleneck in energy redistribution between these very low frequency modes and the surrounding thermal bath modes.

It is interesting to compare the present results of ring opening in the COT3/BCO system with our previous UED studies of light-mediated pericyclic reactions in CHT and CHD. The observation of an inverted torsional configuration and highly elevated vibrational amplitudes indicate the non-equilibrium nature of the OT structures following ring opening and are similar to the highly elevated vibrational amplitudes we observed in CHT (following a [1,7]-sigmatropic hydrogen-shift), as well as the inverted torsional configuration we observed in HT (following electrocyclic ring opening of CHD). However, it is interesting to note that no stretched C–C distances are observed in OT (at least not one that lasts 150 ps), a clear difference from our previous UED observations of a significantly stretched C–C distance (to ~ 1.7 Å) in HT that lasted for at least 400 ps. In this previous report, we hypothesized that the resulting far-from-equilibrium structures observed by UED may reflect memory of the structural features of the excited molecule at the point of descent to the ground-state surface. While the electrocyclic ring-opening reactions of COT3 and CHD both resulted in the

observation of inverted torsional configurations in the hot product structures, the absence of non-equilibrium (stretched) covalent distances in OT may indicate that the reaction surface of COT3 may have more in common with that of CHT than with that of CHD. Such potential similarities are reminiscent of those observed for COT3 and CHT in the solution-phase resonance Raman experiments of Mathies and co-workers:¹¹ their results suggested that while the initial wave packet motion for CHD is indeed along the expected conrotatory ring-opening coordinate, the initial motion of COT3 (like CHT) was toward ring-planarization (and not ring opening). The connection between the structural features observed in these systems by UED and the landscapes of the corresponding energy surfaces awaits further experimental and theoretical investigation.

The photochemical changes uncovered by UED, in conjunction with previous studies in the literature, provide a detailed description of the initial dynamics that lead to the disrotatory ring opening of COT3. The nuclear evolution launched by the absorption of a photon is immediately directed towards bringing the eight members of the ring into the same plane. Since complete planarization is impossible without severe bond angle strain, this movement amounts to the distribution throughout the ring of the torsion originally present primarily in the saturated portion of the ring. The absence of movement along the CH₂-twisting coordinate reveals that this step of the

reaction does not occur until further along the reaction coordinate. Thus, the ring opening of COT3 is a sequential reaction: the planarization step precedes any significant evolution along the more intuitive reactive modes, including the actual opening of the ring (lengthening of the CH₂–CH₂ bond), and rehybridization (methylene C–H bond shortening) and movement of the CH₂ groups into the plane (CH₂–twisting). However, it is important to note that the preliminary planarization step does not preclude the reactive changes from occurring in a concerted fashion, as predicted by pericyclic reaction theory. The planarization step establishes the proper orientation required for the changes in bonding orbital overlap to occur.

Although the photochemical reaction of COT3 is more closely allied chemically to the ring-opening reaction of cyclohexadiene, its excited-state dynamics more closely parallel those of cycloheptatriene, which involve significant evolution along a low-frequency “boat-to-boat” mode and which exhibit no evolution along the reactive C–H stretching coordinate. Both triene’s rings are boat structures that exhibit large movements towards planarity when excited and delay motion along their respective “reactive modes” until after the planarization is well under way. While both cycloheptatriene and COT3 exhibit similar excited-state dynamics, their unique ground-state structures require different movements to achieve the orbital overlap that will facilitate the subsequent stages of the reactions.

Both of these trienes can be contrasted to the excited-state dynamics of cyclohexadiene, which is only slightly nonplanar. Cyclohexadiene exhibits nuclear evolution along the “reactive modes” indicative of a conrotatory ring-opening reaction immediately after excitation: the CH₂–CH₂ bond lengthens as the CH₂ groups twist towards the molecular plane in a conrotatory fashion. The similarities and differences between the initial excited-state dynamics of these three systems suggest that a planar or near-plane structure is required before a pericyclic reaction can proceed.

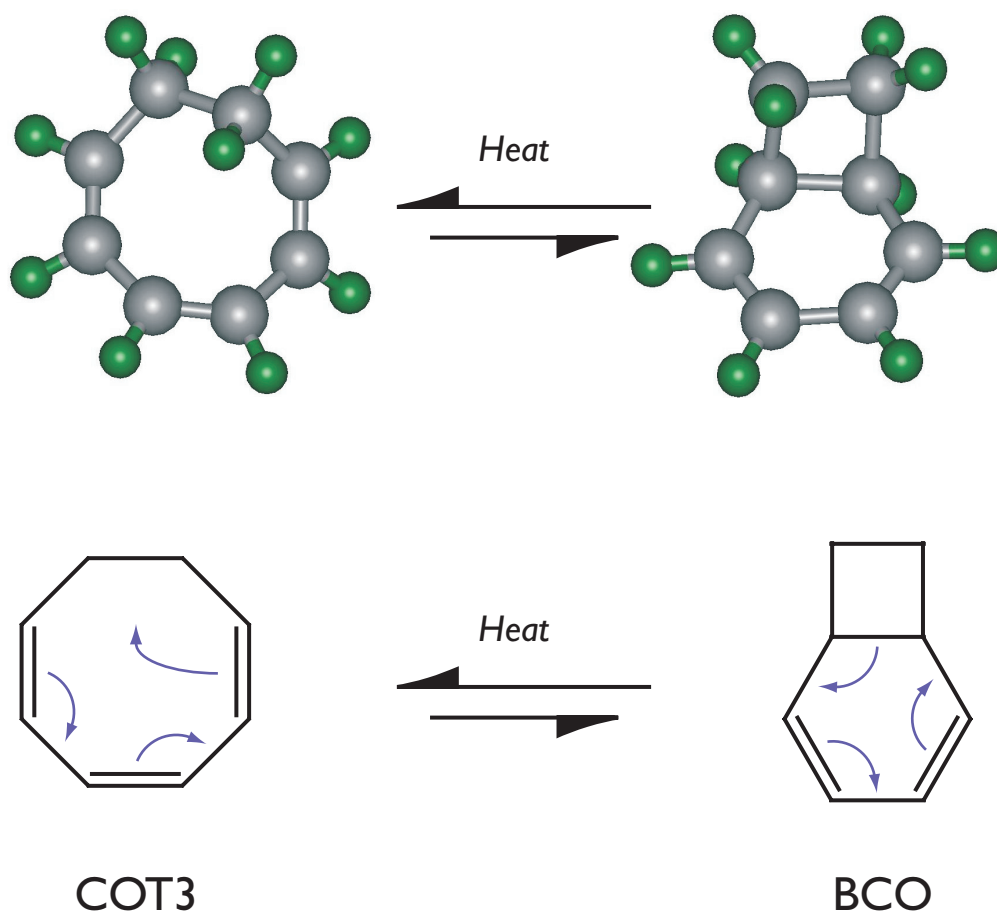
8.7 Conclusions

We have exploited the unmatched spatio-temporal resolution of ultrafast electron diffraction to probe the molecular structures resulting from thermal- and light-mediated electrocyclic reactions in COT3—one of the most challenging systems studied by UED to date. For the thermal processes, we were able to observe COT3 and BCO structures in dynamic equilibrium and performed a partial refinement of the COT3 molecular structure. For the light-mediated processes, we determined that OT—the primary product of the photochemical reaction pathway—has a non-equilibrium structure manifested by an inverted torsional configuration and highly elevated vibrational amplitudes (but no stretched C–C bond distances). This non-

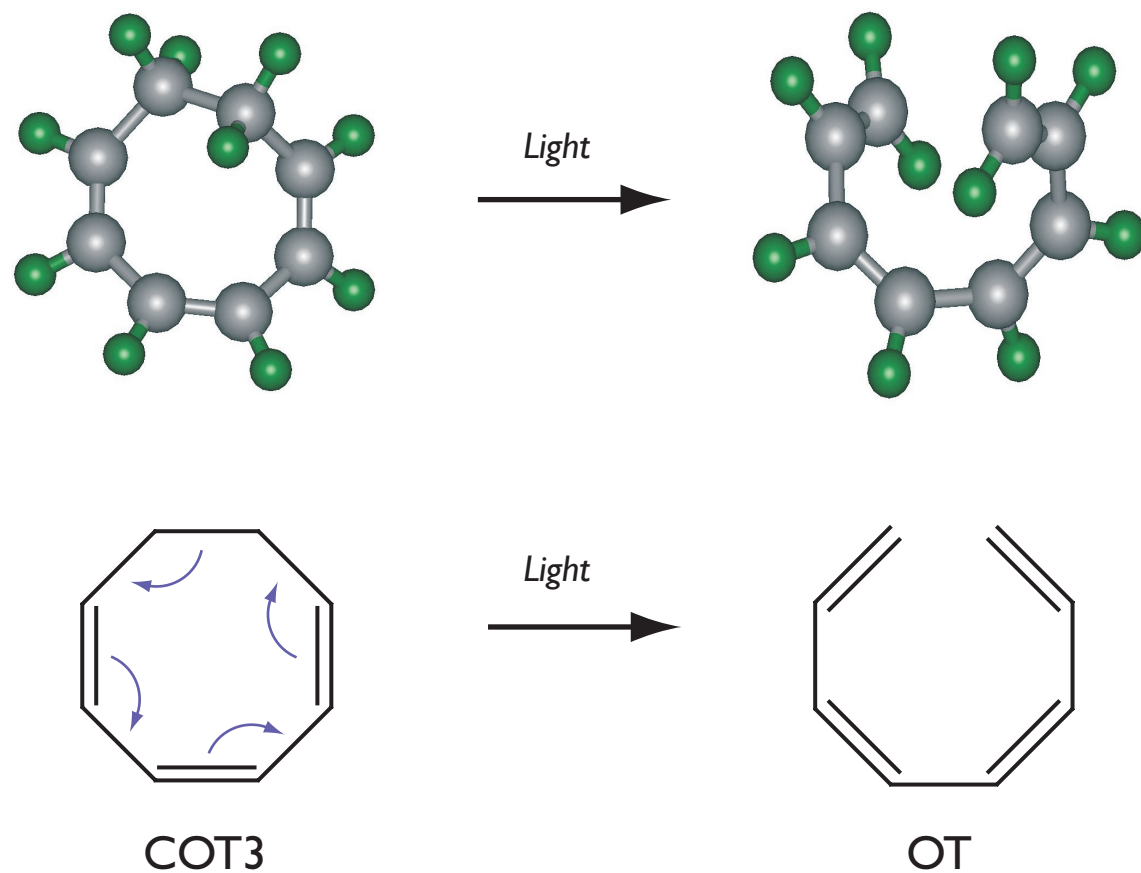
equilibrium structure is a direct result of the high excess internal energy deposited by the absorbed UV radiation.

These discoveries have ramifications in the studies of macromolecular dynamics since torsional modes of this type have been identified as important in the first steps of protein folding.²² Because the dynamics are comprised of elementary steps made by torsions, directing large amplitude motions in restricted nuclear subspace makes possible the effective movements of residues (proteins) and bases (DNA). Unlike the time scale of a single bond (femtoseconds), the longer times involved in these torsions (10–100s of picoseconds) and their localization and isolation may be a key for biological function of macromolecules.

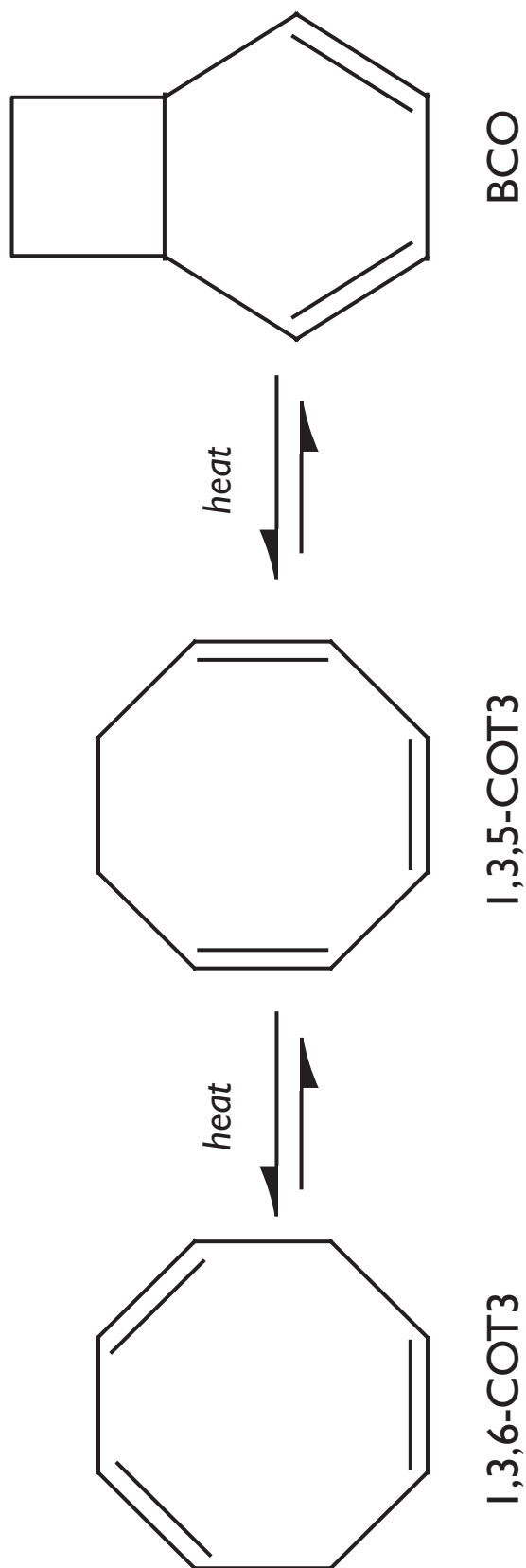
In the future, observing the *structural dynamics* of ring opening in COT3 and other conjugated polyenes may shed new light onto the structural ramifications of energy redistribution and the choice of reaction pathway, permitting not only a more complete comparison with the pericyclic reactions studied previously by UED, but also yielding new insight into a wide class of photophysical and photochemical processes found throughout chemistry and biology.



Scheme 8-1. Thermal Cope rearrangement of 1,3,5-cyclooctatriene (COT3) to bicyclo[4.2.0]octa-2,4-diene (BCO).



Scheme 8-2. Light-mediated electrocyclic ring opening of 1,3,5-cyclooctatriene (COT3) to 1,3,5,7-octatetraene (OT).



Scheme 8-3. Ground-state species in thermal equilibrium: 1,3,6-cyclooctatriene (1,3,6-COT3), 1,3,5-cyclooctatriene (1,3,5-COT3), and bicyclo[4.2.0]octa-2,4-diene (BCO). At the temperature of the experiment (160 °C), the respective equilibrium fractions are ~1%, ~78%, and ~21%.

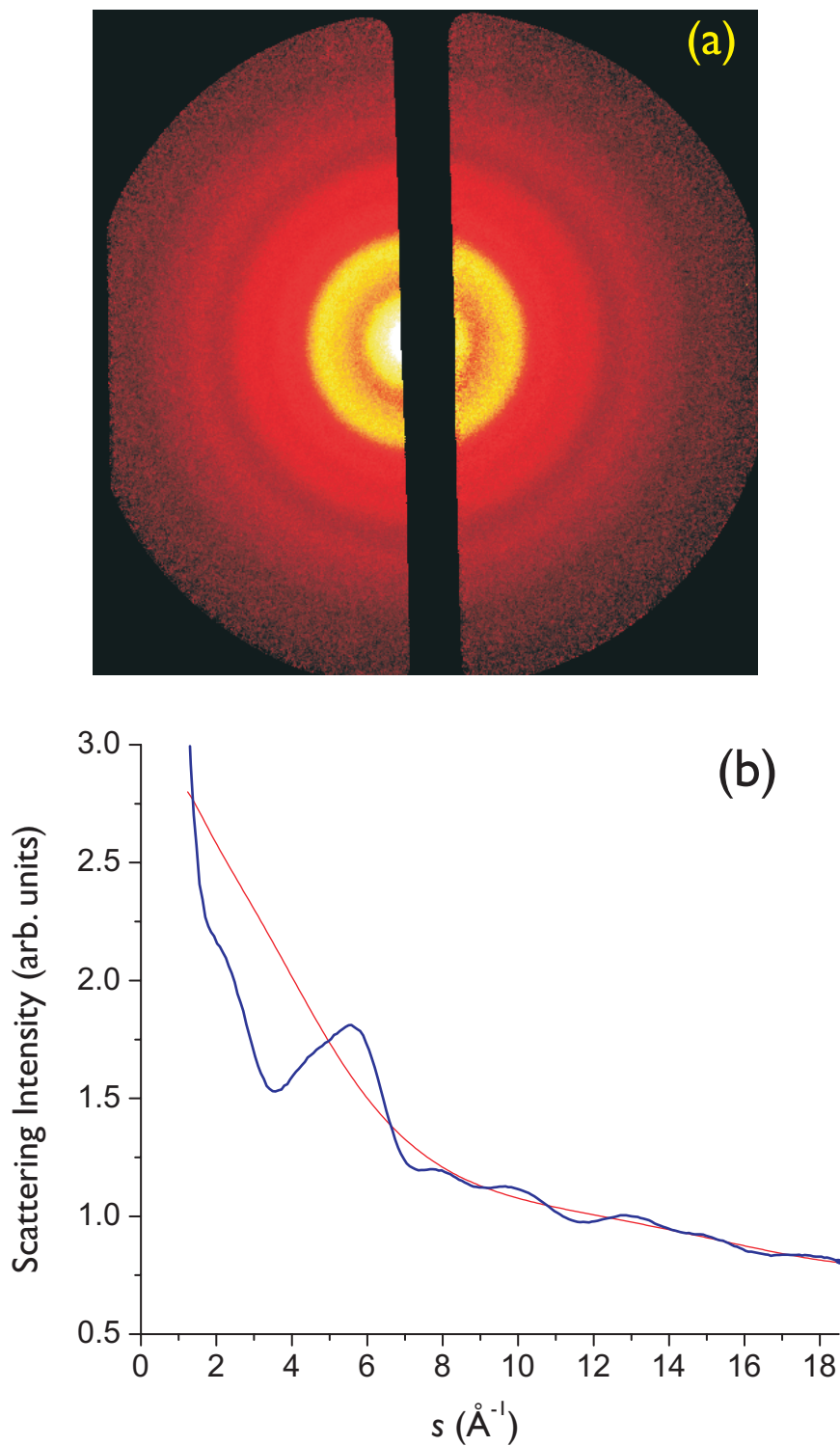


Figure 8-1. Diffraction of ground-state COT3 and BCO structures in thermal equilibrium. **(a)** 2-D UED image obtained following division by the atomic (Xe) reference signal. **(b)** Corresponding 1-D diffraction data (blue curve) obtained via radial summation of the 2-D data. The smooth baseline curve is shown in red.

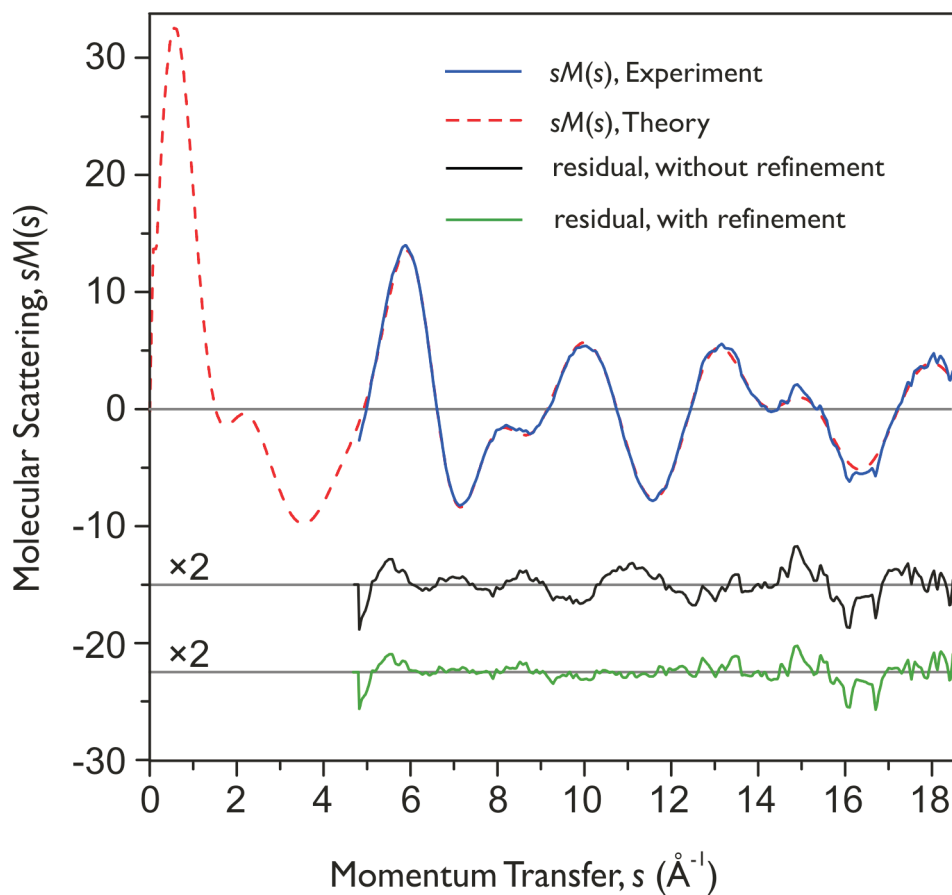


Figure 8-2. Ground-state molecular scattering curves. Comparison of theoretical (red) and experimental (blue) $sM(s)$ curves following refinement of the relative fractions of the COT3 and BCO structures, and partial refinement of the COT3 structural parameters; see text. The magnified ($\times 2$) residual curves were obtained from two different fits: the top residual (black) was obtained from a fraction-fit of the DFT ground-state structures without refinement, whereas the improved residual (green) was obtained from the partial refinement of the COT3 structural parameters combined with a fraction fit.

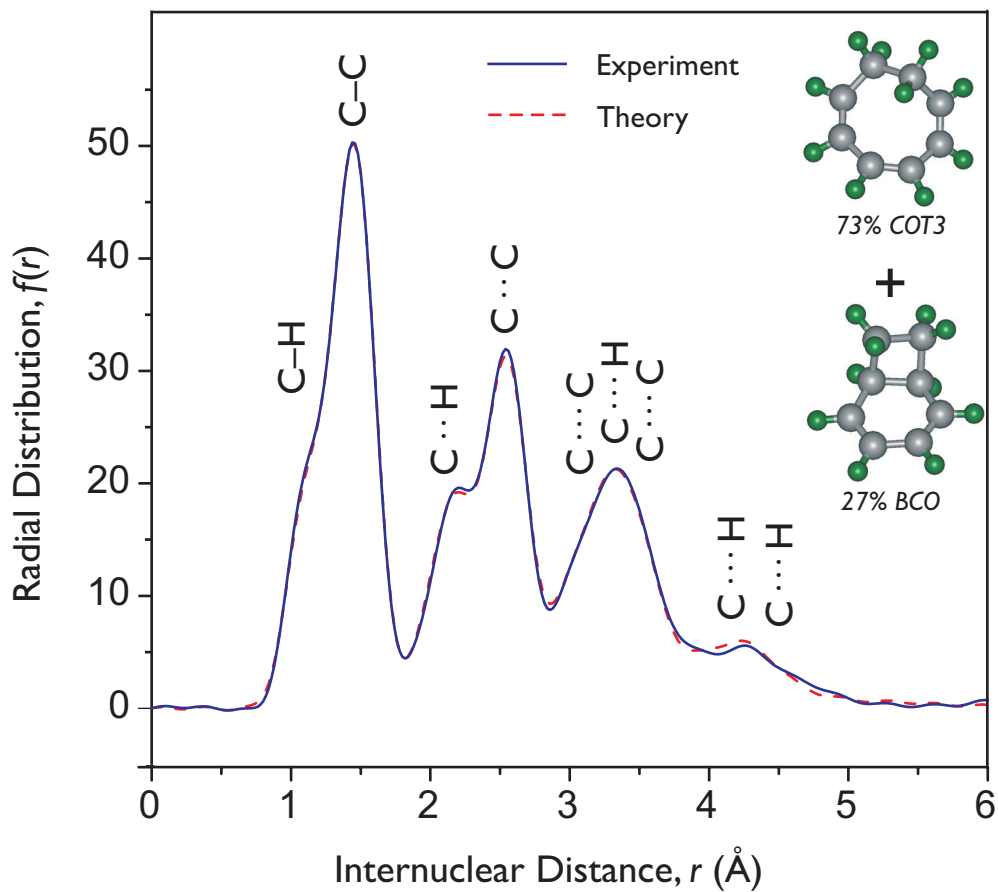


Figure 8-3. Ground-state radial distribution functions. Comparison of corresponding theoretical (red) and experimental (blue) $f(r)$ curves obtained following sine transformation of the $sM(s)$ curves in Fig. 7-2. The fraction fit results in ~73% COT3 and ~27% BCO; see text.

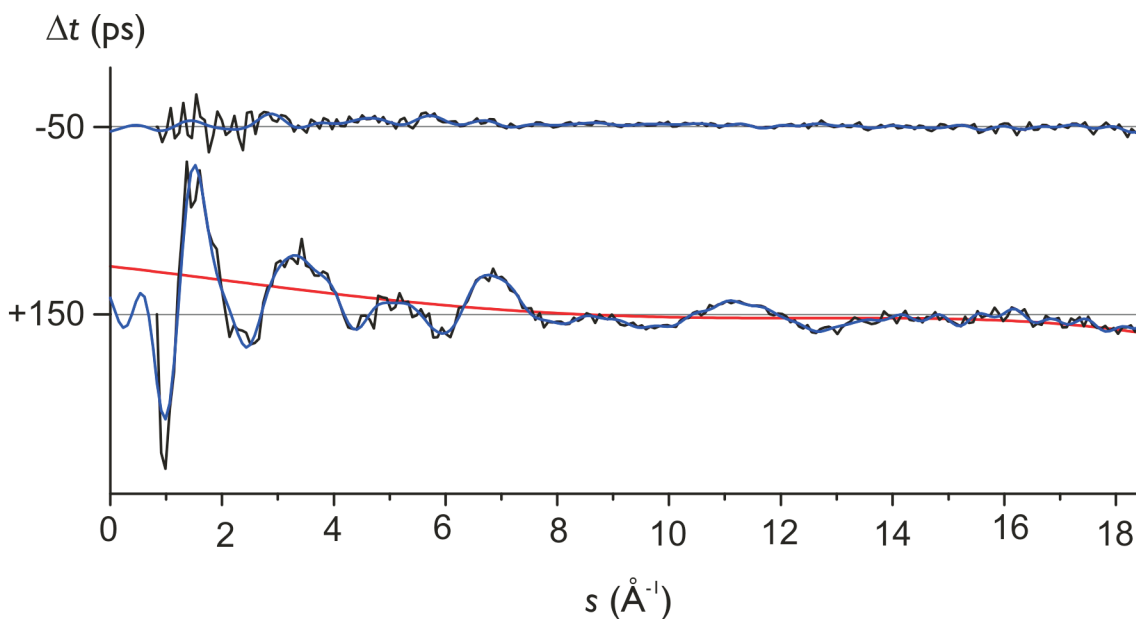
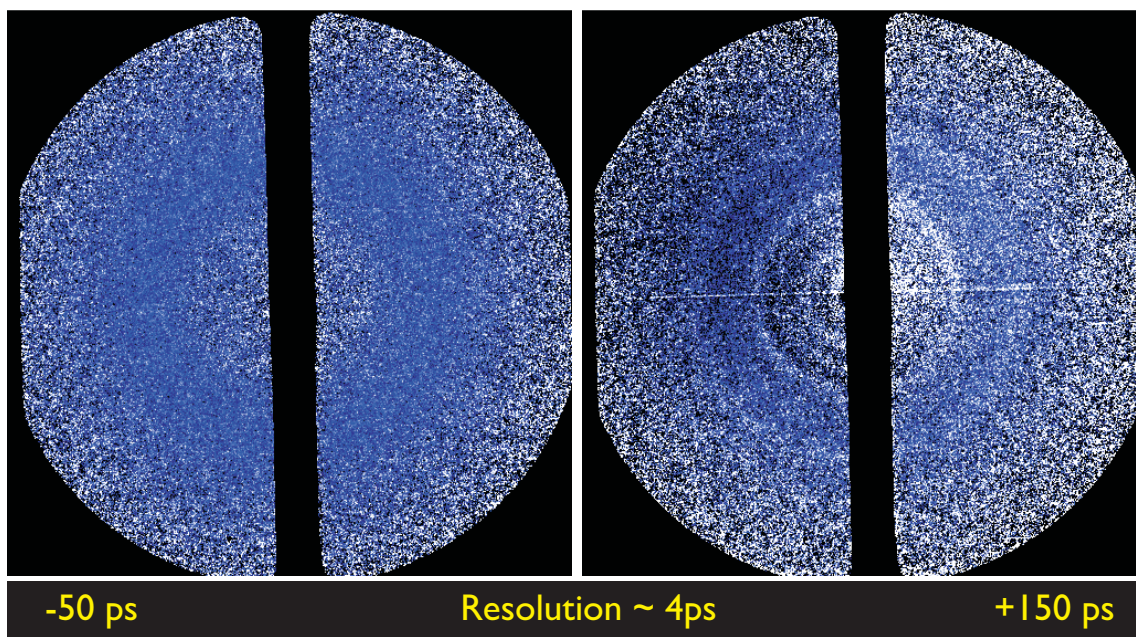


Figure 8-4. Diffraction-difference images of transient structures in light-mediated reaction of COT3. **(Top)** 2-D difference images obtained at 50 and +150 ps. **(Bottom)** Corresponding 1-D diffraction difference signals obtained via radial summation of the 2-D images. The raw diffraction data are shown in black, whereas the Fourier-filtered curves are shown in blue; the smooth base-line curve used for the fit of the +150 ps data is shown in red.

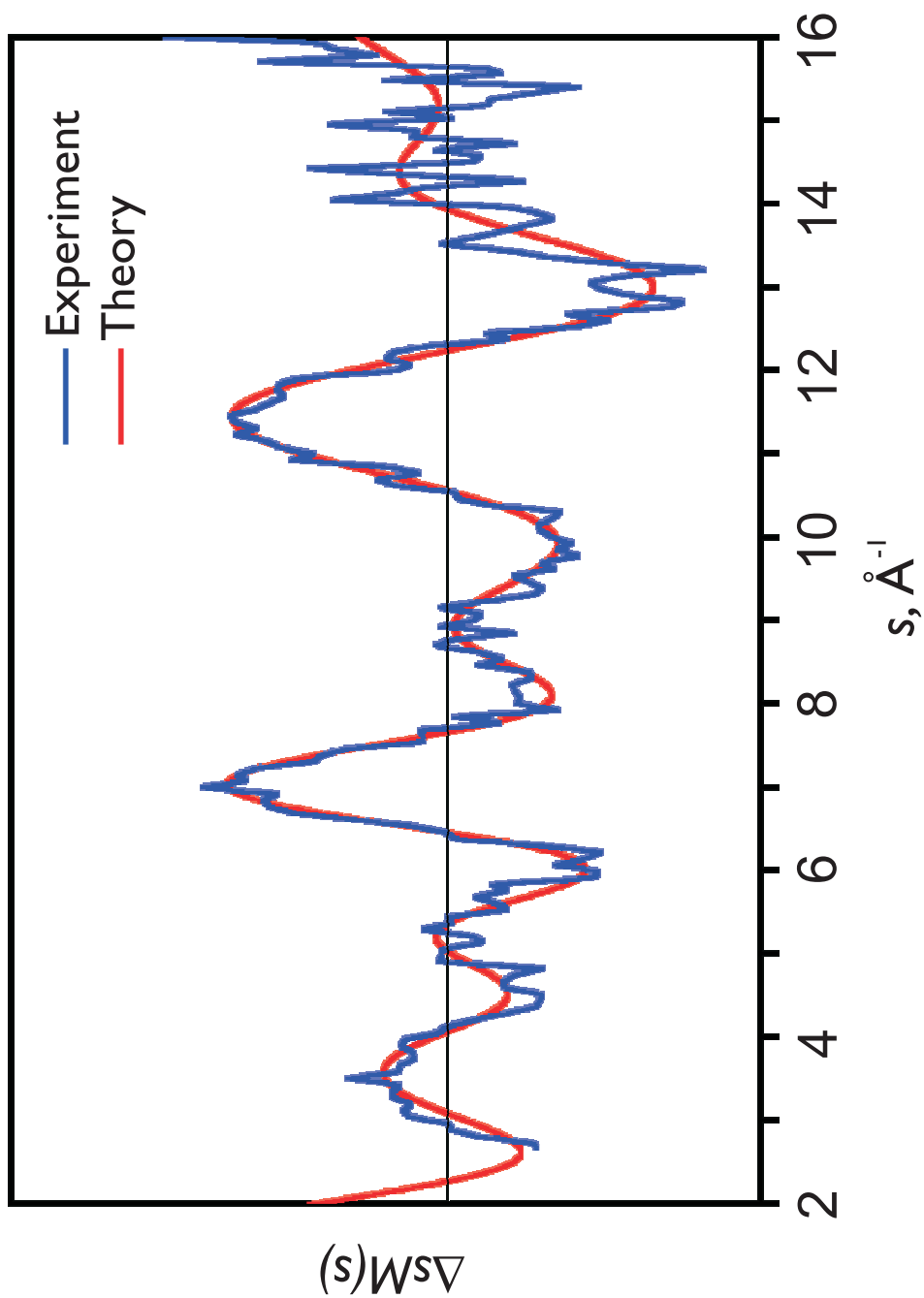


Figure 8-5. CO T3 difference curves. Comparison of experimental $\Delta sM(s)$ curve (blue) obtained at +150 ps with the corresponding theoretical curve (red) obtained using the structural parameters of the first minimum of the Monte Carlo/least-squares refinements of *gauche* OT.

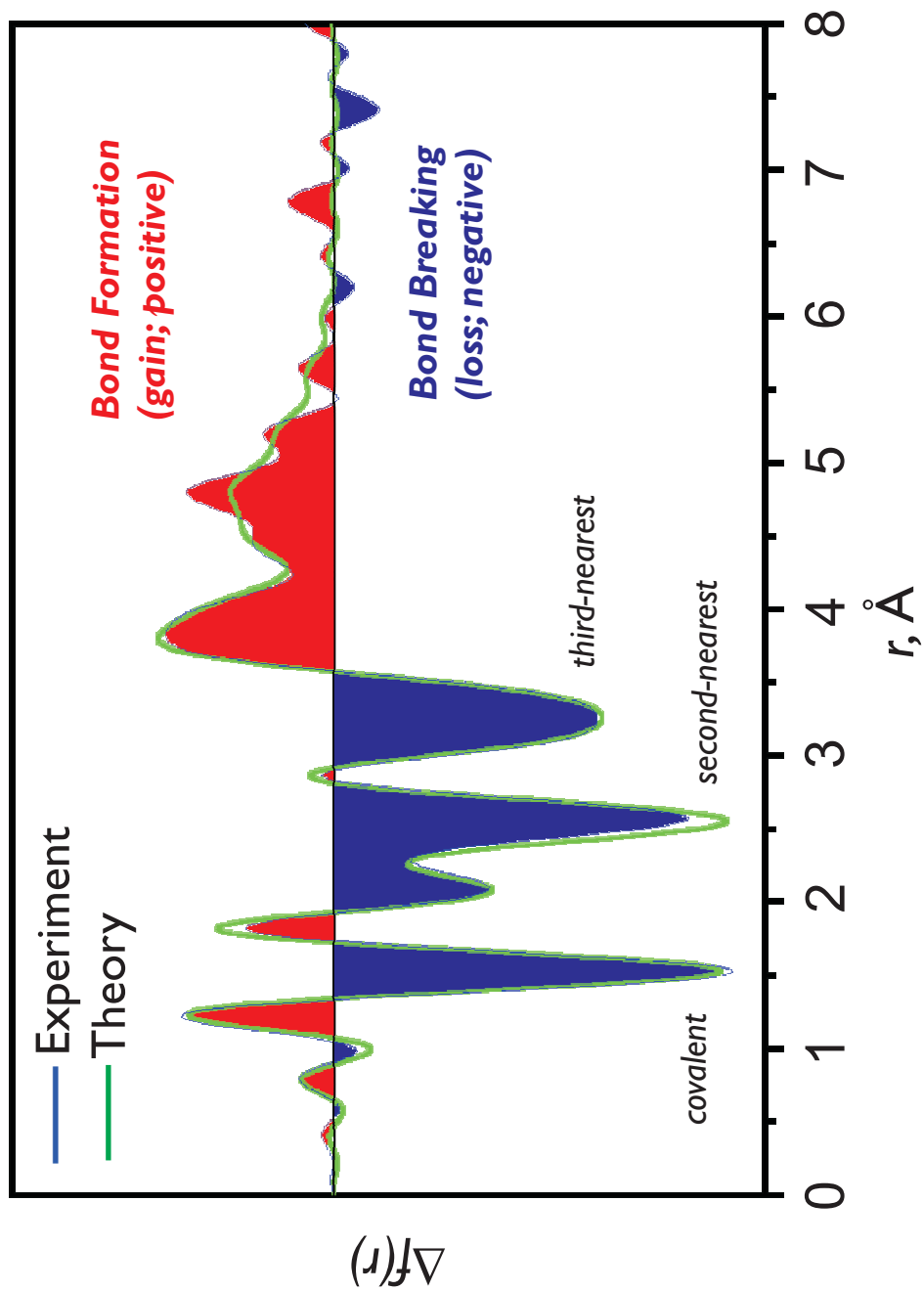


Figure 8-6. COT3 difference curves. Experimental $\Delta f(r)$ curve (blue); the blue highlighted regions represent net depletion-of internuclear pairs, whereas the red regions correspond to net gain-bond formation-of internuclear pairs. The green curve was obtained by sine transform of the theoretical $sM(s)$ curve in Fig. 8-5.

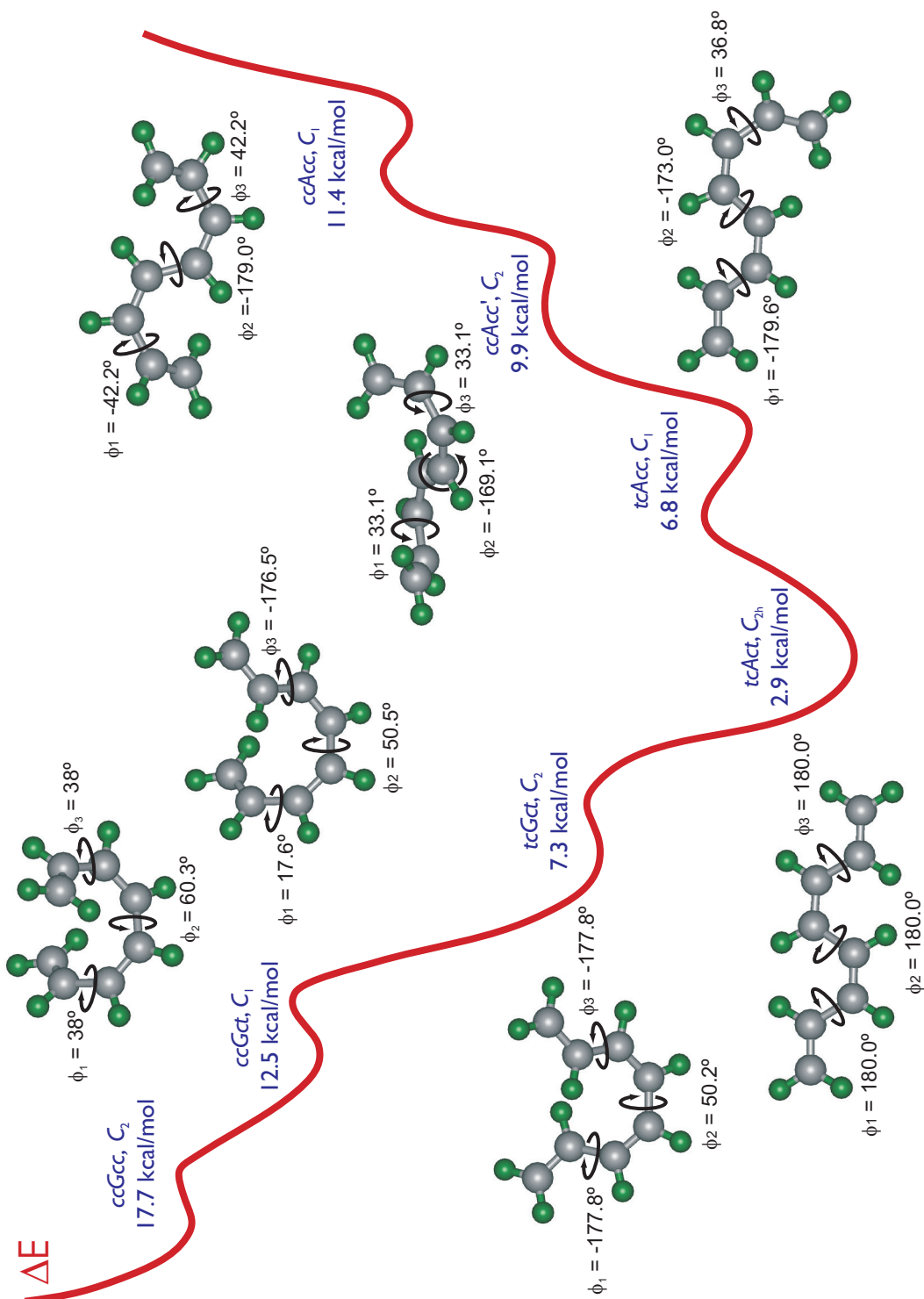


Figure 8-7. Equilibrium (*cis, cis*) OT conformer structures obtained via DFT (6-311G** level) including energies (relative to the COT3 ground state), symmetries, and values for single-bond torsional angles. The nomenclature convention used in the figure corresponds to the OT torsional degrees of freedom as follows: positions 1, 3, and 5 in a given name correspond to torsion around single bonds, whereas positions 2 and 4 correspond to torsion around double bonds (and hence are always 'c' for 'cis' in the conformers of *cis, cis*-OT). Positions 1 and 5 may be denoted 't' (for *trans*) or 'c' (or 'c'); however, the use of 'A' (*Anti*) and 'G' (*Gauche*) was deemed more appropriate for position 3.

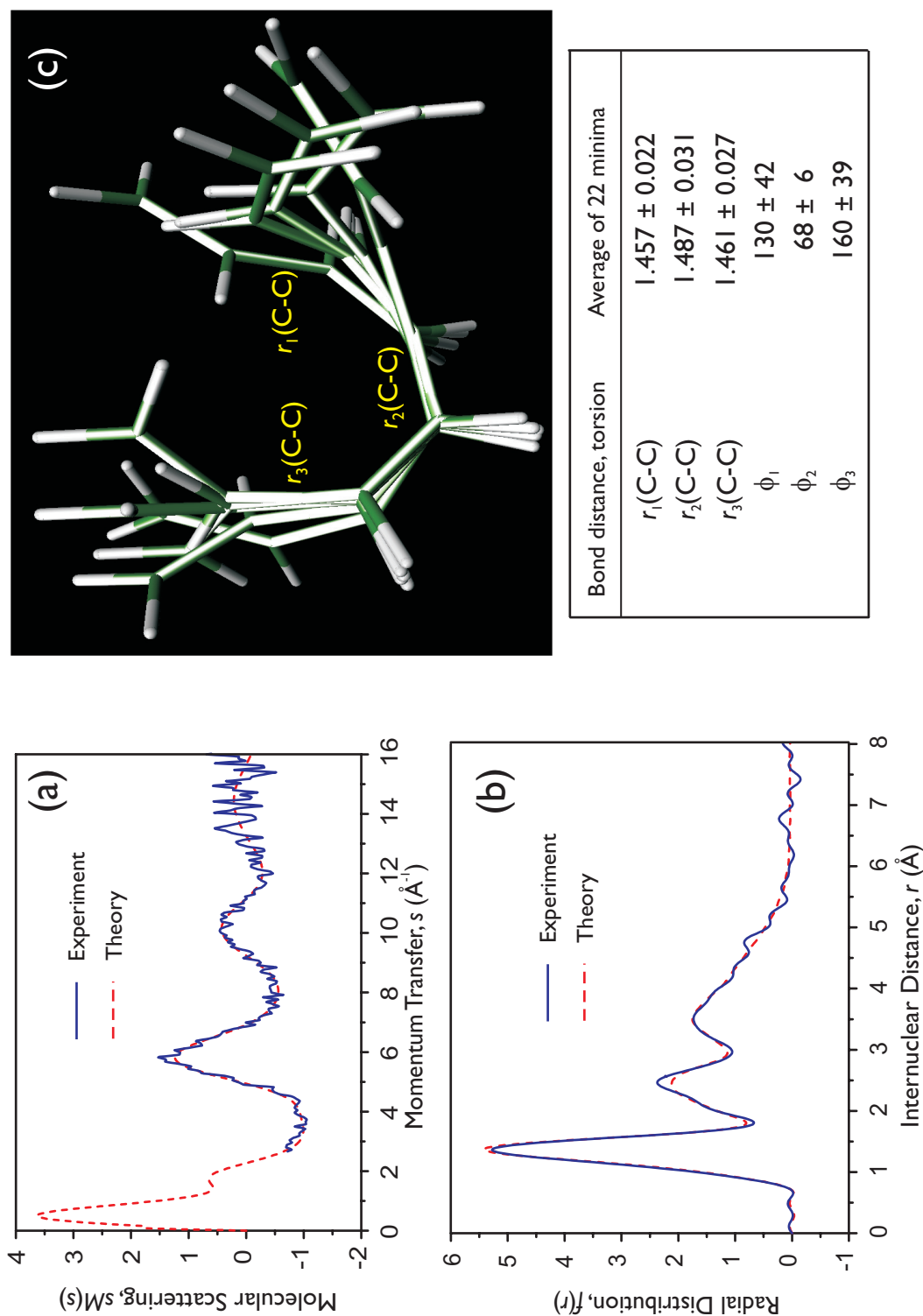
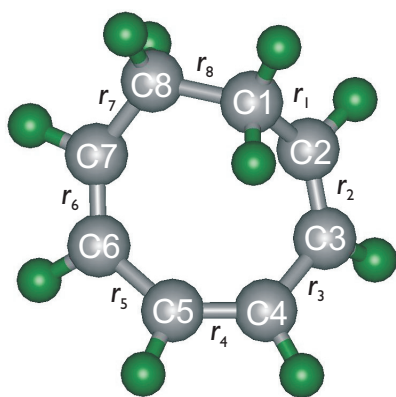


Figure 8-8. Transient-only structures obtained from UED curves. (a) Comparison of theoretical (red) and experimental (blue) transient-only $sM(s)$ curves for the diffraction signal at +150 ps; the theoretical curve was obtained using the structural parameters of the first minimum of the Monte Carlo/least-squares refinements. (b) Corresponding experimental and theoretical transient-only $f(r)$ curves. (c) Overlaid skeletal structures for the five selected minima obtained from the Monte Carlo/least-squares refinement.



Bond distance/Angle	Value	Theory
$r_1(\text{C1-C2})$	1.464 ± 0.040	1.502
$r_2(\text{C2=C3})$	1.321 ± 0.025	1.339
$r_3(\text{C3-C4})$	1.483 ± 0.077	1.458
$r_4(\text{C4=C5})$	1.367 ± 0.055	1.348
$r_5(\text{C5-C6})$	$r_5 = r_3 + 0.0087^a$	1.467
$r_6(\text{C6=C7})$	$r_6 = r_2 + 0.0048^a$	1.344
$r_7(\text{C7-C8})$	$r_7 = r_1 + 0.0005^a$	1.503
$r_8(\text{C8-C1})$	1.518^b	1.537
$r(\text{C-H})$ 'sp ³ '	1.072 ± 0.033	1.096
$r(\text{C-H})$ 'sp ² '	1.113 ± 0.018	1.088
$\alpha_1(1-2-3)$	129.2 ± 5.3	125.2
$\alpha_2(2-3-4)$	122.8 ± 2.1	125.6
$\alpha_3(3-4-5)$	128.2 ± 7.5	128.3
$\alpha_4(4-5-6)$	133.5 ± 9.8	131.7
$\alpha_5(5-6-7)$	132 ± 10	134.8
$\alpha_6(6-7-8)$	134.1 ± 6.8	132.6
$\alpha_7(7-8-1)$	117.6^b	116.5
$\alpha_8(8-1-2)$	119.1^b	113.5
$\phi_1(1-2-3-4)$	20 ± 22	2.3
$\phi_2(2-3-4-5)$	37 ± 39	39.8
$\phi_3(3-4-5-6)$	3 ± 41	6.9
$\phi_4(4-5-6-7)$	-36 ± 15	-39.3
$\phi_5(5-6-7-8)$	-17 ± 48	-4.9
$\phi_6(6-7-8-1)$	27^b	1.6
$\phi_7(7-8-1-2)$	48^b	70.5
$\phi_8(8-1-2-3)$	-94^b	-90.9

^aParameter not fit; obtained using the deviation values predicted by DFT at the 6-311 G** level

^bDependent parameter (not fit)

Table 8-1. Structural coordinates obtained for COT3 from the least-squares partial refinement of UED data, compared with values obtained from theoretical DFT calculations. Some uncertainties of the fit are somewhat larger than the instrumental limits (~ 0.01 Å for ground state structures) due to the correlation effects among fitting parameters in the twist-boat structure.

References

1. Thomas, J. M.; Catlow, C. R. A.; Sankar, G., *Chem. Commun.* **2002**, *24*, 2921.
2. Harris, K. D. M.; Tremayne, M.; Kariuki, B. M., *Angew. Chem. Int. Ed.* **2001**, *40*, 1626.
3. Saes, M.; Bressler, C.; Abela, R.; Grolimind, D.; Johnson, S. L.; Heimann, P. A.; Chergui, M., *Phys. Rev. Lett.* **2003**, *90*, 0474031.
4. Helliwell, J. R., *Phys. World* **2001**, *14*, 25.
5. Woodward, R. B.; Hoffmann, R., *The Conservation of Orbital Symmetry*. 3rd ed.; Verlag Chemie International: Weinheim, 1981.
6. Cope, A. C.; Haven, A. C.; Ramp, F. L.; Trumbull, E. R., *J. Am. Chem. Soc.* **1952**, *74*, 4867.
7. Greathead, J. M.; Orchard, S. W., *Int. J. Chem. Kinet.* **1983**, *15*, 1069.
8. Chapman, O. L.; Borden, G. W.; King, R. W.; Winkler, B., *J. Am. Chem. Soc.* **1964**, *86*, 2660.
9. Roth, W. R.; Peltzer, B., *Angew. Chem. Int. Ed. Engl.* **1964**, *3*, 440.
10. Goldfarb, T. D.; Lindqvist, L., *J. Am. Chem. Soc.* **1967**, *89*, 4588.
11. Reid, P. J.; Lawless, M. K.; Wickham, S. D.; Mathies, R. A., *J. Phys. Chem.* **1994**, *98*, 5597.
12. Datta, P.; Goldfarb, T. D.; Boikess, R. S., *J. Am. Chem. Soc.* **1969**, *91*, 5429.

13. Hossain, M.; Kohler, B. E.; West, P., *J. Phys. Chem.* **1982**, *86*, 4918.
14. Dunkin, I. R.; Andrews, L.; Lurito, J. T.; Kelsall, B. J., *J. Phys. Chem.* **1985**, *89*, 1701.
15. Bally, T.; Nitsche, S.; Roth, K., *J. Chem. Phys.* **1986**, *84*, 2577.
16. Hargittai, I.; Hargittai, M., *Stereochemical Applications Of Gas-Phase Electron Diffraction*; VCH: New York, 1988.
17. Srinivasan, R.; Lobastov, V. A.; Ruan, C. Y.; Zewail, A. H., *Helv. Chim. Acta* **2003**, *86*, 1763.
18. Ruan, C. Y.; Lobastov, V. A.; Srinivasan, R.; Goodson, B. M.; Ihee, H.; Zewail, A. H., *Proc. Natl. Acad. Sci. USA* **2001**, *98*, 7117.
19. Frisch, M. J. *et al. Gaussian 98*, Revision A.1; Gaussian Inc.: Pittsburgh, PA, 1998.
20. Anet, F. A. L.; Yavari, I., *Tetrahedron Lett.* **1975**, *48*, 4221.
21. Thomas IV, B. E.; Evanseck, J. D.; Houk, K. N., *Israel J. Chem.* **1993**, *33*, 287.
22. Clary, D. C.; Meijer, A. J. H. M., *J. Chem. Phys.* **2002**, *106*, 9829.

9

HYDROGEN-BONDING IN ACETYLACETONE*

9.1 Introduction

Hydrogen bonds are ubiquitous in chemistry and biology. While the strength of the “classical hydrogen bond” is around 3–5 kcal/mol, hydrogen bond strengths span more than two orders of magnitude (0.2–40 kcal/mol), with the nature of the hydrogen bond (HB) varying as a function of its electrostatic, dispersion, charge-transfer, and covalent contributions.¹ In the extreme limit, for symmetric hydrogen bonds X–H–X, the H-atom is equally

* Adapted from Srinivasan, R.; Feenstra, J. S.; Park, S. T.; Xu, S. J.; Zewail, A. H., *J. Am. Chem. Soc.* **2004**, *126*, 2266; Xu, S. J.; Park, S. T.; Feenstra, J. S.; Srinivasan, R.; Zewail, A. H., *J. Phys. Chem. A* **2004**, *108*, 6650.

shared; no distinction can then be made between the donor and acceptor, or the “covalent” X–H and “noncovalent” H···X bond.² Such unusually strong interactions can result either from charge-transfer assisted HBs in polarizable systems or from so-called resonance-assisted[†] HBs due to conjugation in neutral systems.³⁻⁵

Enolones, the enol tautomers of β -diketones, contain two neutral donor and acceptor oxygen atoms connected by a system of conjugated double bonds (Scheme 9–1); the consequent synergistic reinforcement of H-bonding and π -delocalization can lead to strong intramolecular resonance-assisted O–H···O HBs. Increasing delocalization may transform the HB from an asymmetric O–H···O interaction (double well) to a symmetric O–H–O bond (single well), with the O···O distance being a measure of the strength of the HB. In the limit of complete delocalization, the C–C and C=C bonds as well as the C–O and C=O bonds become equal to each other, the O···O distance becomes very short, and the H-atom lies midway between the two oxygens. Acetylacetonone (AcAc), a prototypical enolone, has been the subject of numerous

[†] Strictly speaking, resonance involves the superposition of two or more structures with different electronic distributions but *identical* nuclear positions. Here, besides single- and double-bond electronic conjugation, motion of the hydrogen atom is also involved.

experimental⁶⁻¹⁸ and theoretical efforts¹⁹⁻²⁵ to understand the nature of such strong HBs.

AcAc comprises two tautomeric forms in dynamic equilibrium, with the enol form dominating in the gas phase at room temperature due to stabilization by the internal HB (Scheme 9–2).^{13, 19} Previous gas-phase electron diffraction experiments present conflicting enol structures: Lowrey *et al.*⁶ and Andreassen and Bauer⁷ report a symmetric (C_{2v}) structure with a symmetric, linear HB, while Iijima *et al.*⁸ support an asymmetric (C_s) structure with an asymmetric, bent HB. Surprisingly, the two experiments reporting a symmetric structure give very different O···O distances, (2.381 Å⁶ *vs.* 2.514 Å⁷). Moreover, theoretical investigations remain unsettled on the relative energies of these structures,²¹ placing C_{2v} anywhere from slightly below¹⁹ to >20 kcal/mol above²³ the C_s structure.

In this chapter we elucidate the keto–enol tautomeric equilibrium, the structure of both keto and enol forms, and the nature of the intramolecular O–H···O HB in enolic AcAc using electron diffraction—thereby resolving this long-standing controversy in the literature. With its proven ability to study complex molecular systems in thermal equilibrium, our third-generation Ultrafast Electron Diffraction apparatus (UED-3) was employed to study the gas-phase diffraction of ground-state AcAc (2,4-pentanedione, 99+%, Aldrich) at 155°C.

9.2 Experimental

The molecular sample was introduced into the chamber through a nozzle maintained at 155 °C. Acetylacetone (2,4-pentanedione) was purchased from Aldrich (>99.0%) and degassed before use by three cycles of the freeze–pump–thaw procedure.

The starting geometries for structural analysis were obtained by quantum chemical (DFT) calculations at the B3LYP/6-311G(d,p) level. Structural refinement was conducted with Monte Carlo sampling and least-squares fitting incorporated into home-built analysis software. Theoretical models were quantitatively rated by their R values, a typical statistical measure used in electron diffraction.

9.3 Ground State

Figure 9–1 shows the ground-state diffraction image of the H-transfer reaction and Fig. 9–2 shows the modified molecular scattering intensity, $sM(s)$, and its sine Fourier transform, the radial distribution curve $f(r)$, whose peaks reflect the relative density of internuclear distances in the molecule.²⁶ The first peak at ~ 1.5 Å corresponds to direct bond distances in both the enol and keto forms, the peak at ~ 2.5 Å to second nearest-neighbor distances, and

the peaks at longer distances to the unique O···O and C···O distances in the enol and keto tautomers.

Structural determination of AcAc tautomers requires an accurate estimate of the relative populations of the enol and keto forms. Diffraction data were fit using a mixture of enol (C_s) and keto AcAc, with their starting geometries derived from density functional theory (DFT) calculations. Initial fitting of the populations of these DFT structures yielded an enol–keto ratio of $88:12 \pm 1$, which is in stark contrast to that expected at 155°C —thermodynamic equilibrium constants obtained by a variety of techniques (NMR, UV, IR)¹²⁻¹⁶ predict a ratio between 71:29 and 79:21 in the gas phase. To resolve this discrepancy, we revisited the starting geometry of the keto form, which is free to undergo internal rotation about its C–C single bonds.^{19, 20} The resultant array of keto rotamers was accounted for by floating the skeletal (and methyl) torsion angles of the DFT keto structure. The partially-refined keto structure is quite different from that reported in the literature—the oxygen atoms are much further apart ($\sim 3.520 \text{ \AA}$; dihedral $\angle\text{OCCO} = 104.7^\circ$) compared to that previously reported ($\sim 2.767 \text{ \AA}$; dihedral $\angle\text{OCCO} = 48.6^\circ$).⁶

Refitting the equilibrium population using this partially-refined keto structure gave $78:22 \pm 4$, in excellent agreement with the results of gas-phase NMR¹³ and IR absorption,¹⁶ thus highlighting the crucial importance of keto

internal rotation. It is pertinent to note here that simple calculations of equilibrium populations from DFT energies (using a fixed keto conformation) predict a ratio of $\sim 98:2$ at 155°C due to a serious underestimation of the entropic term (2.4 cal/mol/K); using the experimental¹³⁻¹⁵ value of 8.3 cal/mol/K , we in fact obtain a ratio of $\sim 80:20$. Furthermore, using a C_{2v} enolic model underestimates the ratio at $68:32 \pm 3$.

Structural refinement of the enol was then performed using the fit values for the equilibrium ratio and the keto geometry. Figure 9–2 shows the remarkable agreement between experiment and theory. The refined enolic structure is asymmetric, with all direct bond distances and angles being within $\sim 0.02\text{ \AA}$ and $\sim 3^\circ$ of the DFT values, respectively (Fig. 9–3). Differences between the carbon–carbon distances (0.084 \AA) and carbon–oxygen distances (0.059 \AA) are far greater than the corresponding standard deviations and clearly distinguish between single and double bonds—a manifestation of structural asymmetry. The $\text{O}\cdots\text{O}$ distance of $\sim 2.592\text{ \AA}$ in this structure is longer than those previously reported by electron diffraction at room temperature (2.512 \AA ⁸) and X-ray crystallography (2.535 \AA ¹⁰ and 2.547 \AA ¹¹). These studies, along with neutron scattering in crystals,⁹ liquid-phase NMR¹⁸ and gas-phase vibrational spectroscopy,¹⁷ are consistent with an asymmetric structure. Due to the relatively weak scattering of the hydrogen atom, in our fit, the O–H , $\text{H}\cdots\text{O}$ distances and the $\text{O–H}\cdots\text{O}$ angle were held at DFT values

(1.003 Å, 1.683 Å, and 148.4°, respectively). In light of the insensitivity of electron diffraction to hydrogen, it is surprising that Iijima *et al.*⁸ report a significantly out-of-plane H-atom ($\angle\text{HOCC}=26^\circ$), which, though in reasonable agreement with a then-available crystal structure,¹⁰ manifests as unusually large error bars (0.016 Å) in their fit O–H distance. A more recent x-ray crystal structure¹¹ supports the H-atom to be nearly in the molecular plane; $\angle\text{HOCC} \sim 4^\circ$.

The diffraction results reported here shed new light on the nature of the hydrogen bond in resonant and tautomeric structures. The keto structure with its large internal rotation exhibits a rotation-averaged dihedral angle of $\sim 105^\circ$ between the carbonyls at the reported temperature. The enolic structure clearly indicates that AcAc does exhibit some π -delocalization leading to shorter C–C, C–O and longer C=C, C=O bonds compared to ‘unperturbed’ distances in enols.³⁻⁵ However, this delocalization is not strong enough to give a symmetric skeletal geometry. The resulting long O \cdots O distance is significant in making the homonuclear O–H \cdots O hydrogen bond localized and asymmetric.

The dynamics of hydrogen motion (O–H \cdots O) involves not only the O \cdots O coordinate but also changes in skeletal geometry. In a symmetric double-well picture with ‘left’ and ‘right’ structures, there are two (\pm) states (symmetric and anti-symmetric), and the probability of finding the structure

in either is 50%, independent of the interaction. The time scale for hydrogen motion depends on the total internal energy and the height of the barrier, which in turn depends on the O...O separation—for short enough values, the structure becomes that of a single well. On the ultrashort timescale, the potential is asymmetric.^{22, 27} It would be interesting to resolve the dynamics in real time using the new developments of UED on this and higher energy structures.

9.4 Structural Dynamics

In reactions involving conjugated hydrogen-bonded structures, the effects of electron delocalization and resonance can lead to multiple pathways that are determined by the nature of the initial structure(s) involved. While the nature of the ground-state structure is now resolved, less is known about the excited states and their reactions. The ultraviolet spectrum of vapor phase AcAc shows a broad structureless absorption that peaks at ~266 nm and is assigned to the first $\pi\pi^*$ transition (S_2 state) of the enol tautomer.^{14, 28} The photochemistry has been studied spectroscopically in matrices,²⁹⁻³¹ solutions,³² and in the gas phase.³³⁻³⁵ Whereas spectroscopic techniques rely on selectivity to monitor state dynamics, UED resolves the ultrafast structural dynamics of the reaction, as demonstrated earlier for thermal, fragmentation, and ring opening reactions.

The possible reaction pathways of isolated, gas-phase AcAc upon 266 nm excitation are shown in Scheme 9–3.

We elucidated the dominance of the OH-loss pathway, the structure of the resulting OH elimination product, and the relevant timescale.

9.5 Results and Discussion

Two dimensional time-resolved diffraction frames were collected for a range of time delays from -77 to $+1273$ ps with respect to the arrival of the initiating laser pulse. Frames recorded at each time point were converted to the modified molecular scattering curves, $sM(s)$, for electron diffraction structural analysis. The radial distribution curves, $f(r)$, were obtained by Fourier transform of the $sM(s)$ curves. Frames obtained before time-zero contain information only on the ground-state structure of AcAc. For the time-resolved diffraction analysis, the ground-state data before time-zero was used as a reference and differenced from post-time-zero data to create difference curves, $\Delta sM(s)$ and $\Delta f(r)$, thereby obtaining the net structural change from reactants to products.²⁶ Figure 9–4 shows the time-resolved difference radial distribution curves using -77 ps as the reference. The curves clearly map out the reaction—the time-dependent depletion of old bonds and formation of new bonds.

In order to reveal the reaction pathway(s), the experimental $\Delta sM(s)$ and $\Delta f(r)$ curves at the +1273 ps delay (reference = -77 ps) are compared with theoretical $\Delta sM(s)$ and $\Delta f(r)$ curves of several reaction channels: isomerization, Norrish cleavage, and elimination, as shown in Fig. 9-5. This visual comparison provides an intuitive way of choosing an appropriate starting point for structural refinement. Although some isomerization of the chelated (H-bond intact) enol into non-chelated enol in matrices²⁹⁻³¹ and in solution³² has been studied, the poor match ($R = 1.103$) between this model and the data (see Fig. 9-5) indicates that the pathway is not significant in the isolated reaction; the experimental $\Delta f(r)$ shows high-amplitude peaks corresponding to bond scission that are not provided by the theoretical model. Norrish Type-I reactions, such as the loss of the acetyl or methyl groups were considered and discarded as poor models for the data (see Fig. 9-5). This is consistent with the structural dynamics discussed below.

The tautomerization channel, i.e., formation of keto and enol tautomers after internal conversion to the “hot” ground-state, also studied by spectroscopy in matrices,³⁰ appeared to fit the data ($R = 0.508$; not shown) when utilizing quantum chemically determined structures. A mixture of the structures of both keto and enol tautomers in their ground states at 2256 K

was used.‡ AcAc with this internal energy will consist of enol and keto tautomers in a 1:2 ratio. Structural refinement for this channel did not greatly improve the quality of the fit. Moreover, fitting the fractions of keto and enol tautomers eliminated the enol contribution completely, in contradiction to the thermodynamics of population distribution.

Superior structural refinement results were obtained with the use of the OH loss model ($R = 0.533$, see Fig. 9–5). OH loss has been observed by laser-induced fluorescence (LIF) spectroscopy of gas-phase AcAc.³³⁻³⁵ In our UED study, combinations of the previously mentioned channels were tested by comparing the data with mixtures of several theoretical models. This produced slightly improved fits (as more degrees of freedom are present). However, since the OH loss channel always remained the dominant component, structural refinement was carried out with this channel being the reaction pathway.

Having identified the reaction channel, the structure of its corresponding product, the 3-penten-2-on-4-yl radical, was then refined as shown in Fig. 9–6. The final refined structure is shown in Fig. 9–7 ($R =$

‡ This temperature was calculated considering a statistical distribution of the absorbed energy of a single photon among all modes in the ground state.

0.338). The refined covalent bond distances and angles show some deviations from the equilibrium structures predicted by quantum chemical calculations. The bonds connecting the methyl groups to the remainder of the carbon skeleton, $r(\text{C1-C2})$ and $r(\text{C4-C5})$, are longer by 0.080 and 0.045 Å, respectively. Also at variance from theory, the acetyl group is rotated out of the plane of the molecule by $\sim 20^\circ$ instead of being coplanar. This indicates that the radical is able to rotate around the C–C single bond. The fitted value reflects an average over all the rotations present in the products.

Structurally, due to the loss of intramolecular hydrogen bonding, the resonance of the conjugated system is disrupted, and the bonds revert to a more unperturbed state. The skeletal distances in the ground state enol, $r(\text{C2-C3}) = 1.359$ Å, $r(\text{C3-C4}) = 1.443$ Å, and $r(\text{C4-O4}) = 1.262$ Å,³⁶ become 1.304 ± 0.025 Å, 1.482 ± 0.023 Å, and 1.202 ± 0.017 Å, respectively, in the product radical where the hydrogen bond is severed and resonance stabilization is lost. Mean amplitudes of vibration were deduced to be consistent with a somewhat cold structure in agreement with a previous finding³⁵ that a significant fraction of internal energy is released into translational motion of the fragments (note that our initial thermal energy is higher than the temperature of the supersonic expansion³⁵).

Using the refined product structure shown in Fig. 9–7, its fractional contribution to each of the other time points was obtained. The plot of the

product fraction versus time is shown in Fig. 9–8. Over the entire time scale, a time constant of 247 ± 34 ps was obtained from nonlinear fitting using a first-order reaction model. In order to test the validity of a direct first order reaction (without intermediates), new diffraction-difference data were obtained by using a frame after time-zero as the reference. This alternative difference data (referred to hereafter as $\Delta\Delta sM(s)$ or difference-difference data) are shown in Fig. 9–9 for the +1273 ps frame with the +73 ps frame as the reference. In a first order reaction, the resulting data would be lower in amplitude yet still correspond to the parent→product reaction scheme. Conversely, if the reaction has multiple steps, the entire parent contribution will be removed in the difference-difference data. This data will then contain information on the intermediate→product reaction. The data shown in Fig. 9–9 suggests the latter case and the presence of an intermediate structure.

Elimination of OH from the T_1 ($\pi\pi^*$) state of AcAc has been suggested in the literature.³⁵ The possibility of the T_1 structure as the intermediate is tested by comparing theoretical $\Delta\Delta sM(s)$ and $\Delta\Delta f(r)$ with experimental data (see Fig. 9–9). The T_1 state possesses a non-planar structure with the C–O moiety twisted 66° out of the skeletal plane resulting in internuclear distances drastically different from S_0 ; for example, the O··O separation is 3.426 Å for the T_1 structure, compared to 2.592 Å for the S_0 structure.³⁶ The T_1 structure does not fit the experimental $\Delta\Delta sM(s)$ as the intermediate, ruling

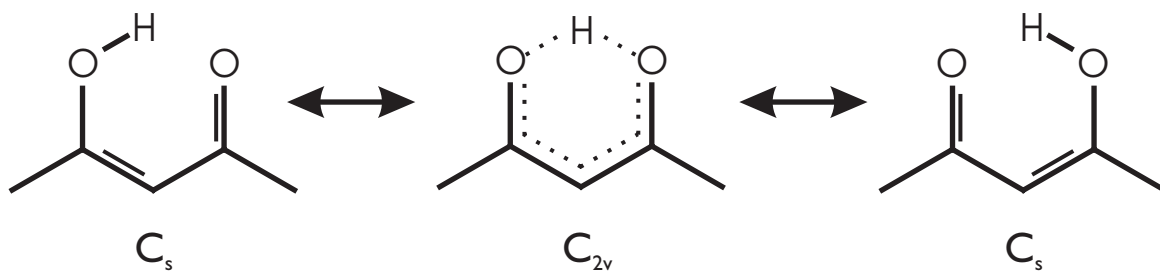
out a slow dissociation from T_1 as the rate determining step of the reaction. Figure 9–9 suggests that the intermediate structure is of singlet character, manifested as a combination of S_1 and S_2 structures because of their proximity in energy.³⁷ Furthermore, the structureless absorption band^{14, 28, 34} and absence of fluorescence^{33, 35} suggest that the S_2 state is very short-lived. Consequently, the observed rise is the rate determining step, the intersystem crossing (ISC) from S_1 to T_1 ; this long lifetime of S_1 has also been observed for malonaldehyde.³⁸ The appearance of pseudo-first order behavior is consistent with ISC as the rate-determining step for the overall elimination reaction.

Structural dynamics can now be related to the reaction pathway(s) involving different electronic states. The transition from S_2 to S_1 is ultrafast (fluorescence was not observed^{33, 35}), as discussed above. In the S_1 ($n\pi^*$) state, the structure is planar and the lifetime of molecules in this state is determined by the ISC to the T_1 ($\pi\pi^*$) state. The structure in the T_1 state is non-planar (C–O moiety twisted 66° out of the skeletal plane), and as such, it promotes the cleavage of the OH radical in order to reform the double bond present in the final radical. It is now easy to understand why the dominant reaction channel is not a Norrish-type cleavage as would be prompted by a T_1 structure of $n\pi^*$ excitation. The structures involved in the dynamics of this elimination are pictured in Fig. 9–10. Figure 9–11 confirms that the observed

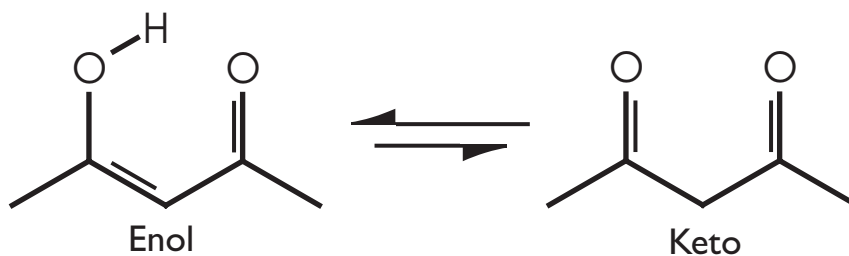
structural dynamics is not due to multi-photon processes but rather is the result of a one-photon process.

9.6 Conclusions

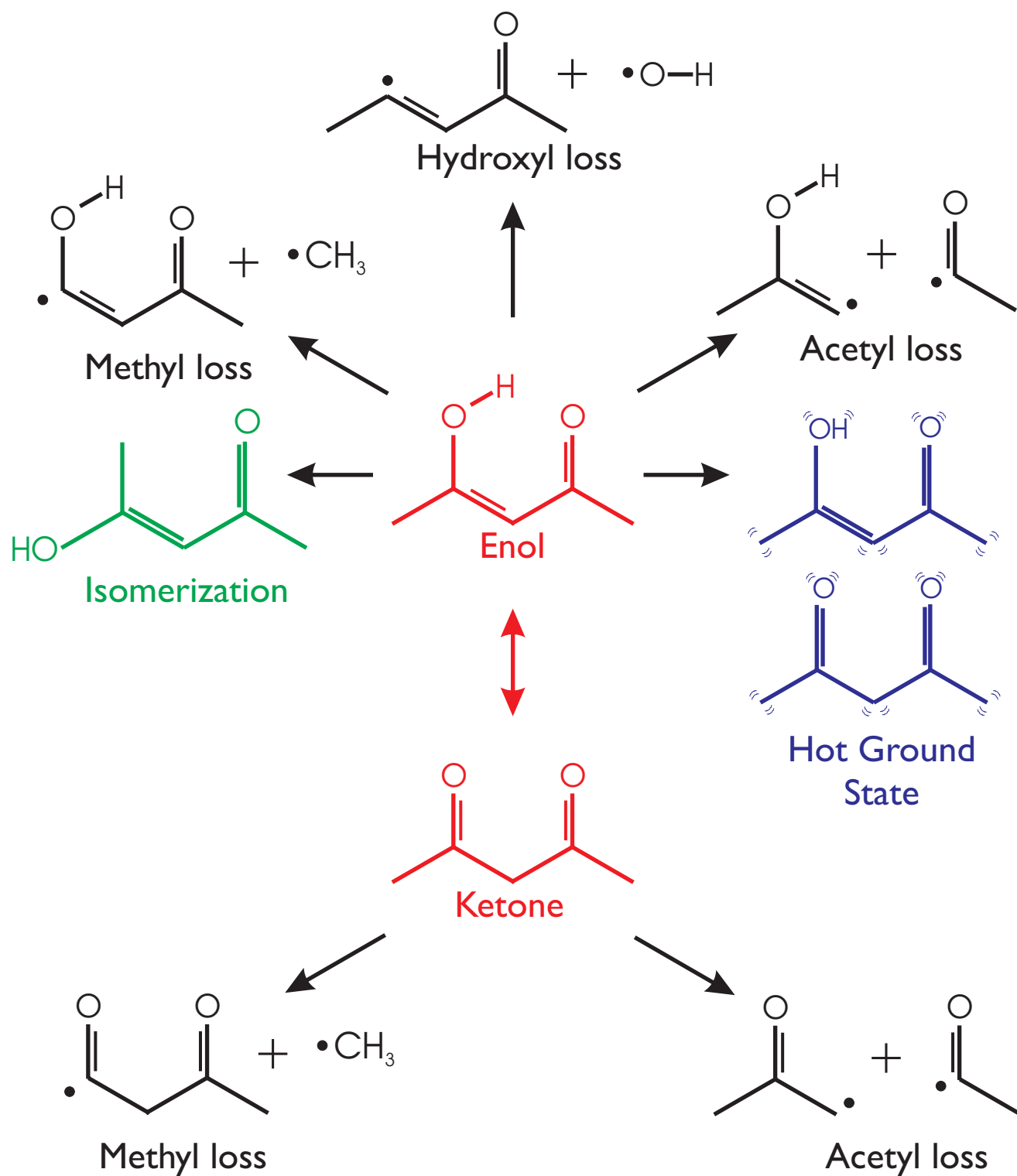
The sensitivity of UED to all nuclear positions reveals that the ground state of AcAc is of C_s asymmetric structure. The OH loss is the dominant channel after 266 nm excitation, but transient structures are found to precede the final product. The overall time constant for OH formation is determined to be 247 ± 34 ps. The influence of resonance stabilization on the molecular structure of the ground state is lost in the T_1 state, and the OH moiety is no longer co-planar with the conjugated bonds, aiding in efficient OH elimination. The $\pi\pi^*$ nature of this structure facilitates reaction pathways that are not typical among ketones—OH-elimination from the β carbon as opposed to a Norrish Type-I cleavage. The absence of resonance stabilization results in the more “electron-localized” structure of the 3-penten-2-on-4-yl radical, and the change in bond distances is directly observed. With ultrafast electron diffraction it was possible to map out changes of structures with time on the energy/state landscape of the reaction.



Scheme 9-1. Structures of enolic acetylacetone.



Scheme 9-2. Enol-keto tautomerization by hydrogen shift.



Scheme 9-3. Possible reaction pathways of acetylacetone following UV excitation. The fragmentation channels are all indicated in black.

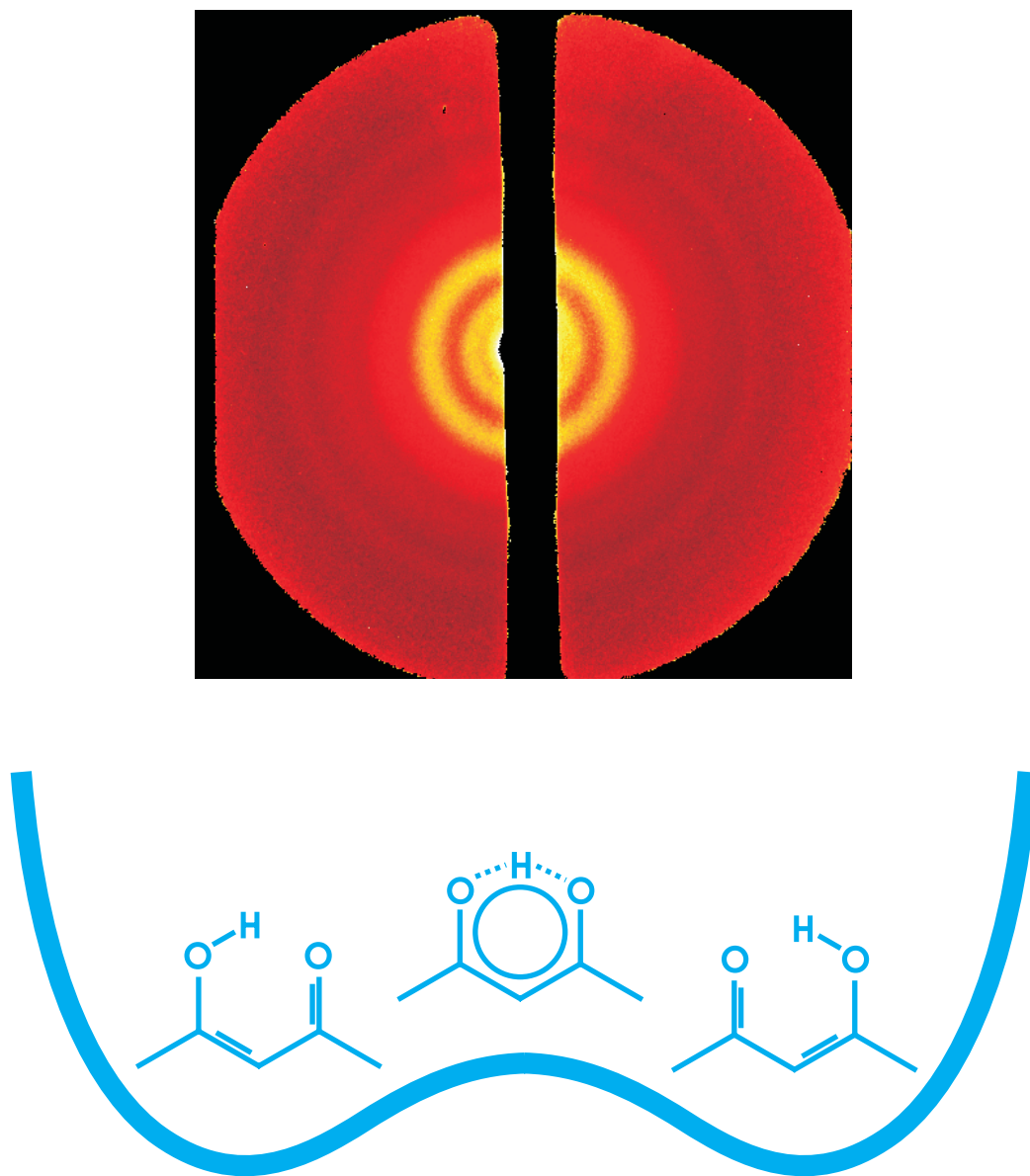


Figure 9-1. 2D ground-state diffraction image of acetylacetonone. Also shown schematically is the symmetric potential for the hydrogen motion between the two oxygen atoms in enolic acetylacetonone.

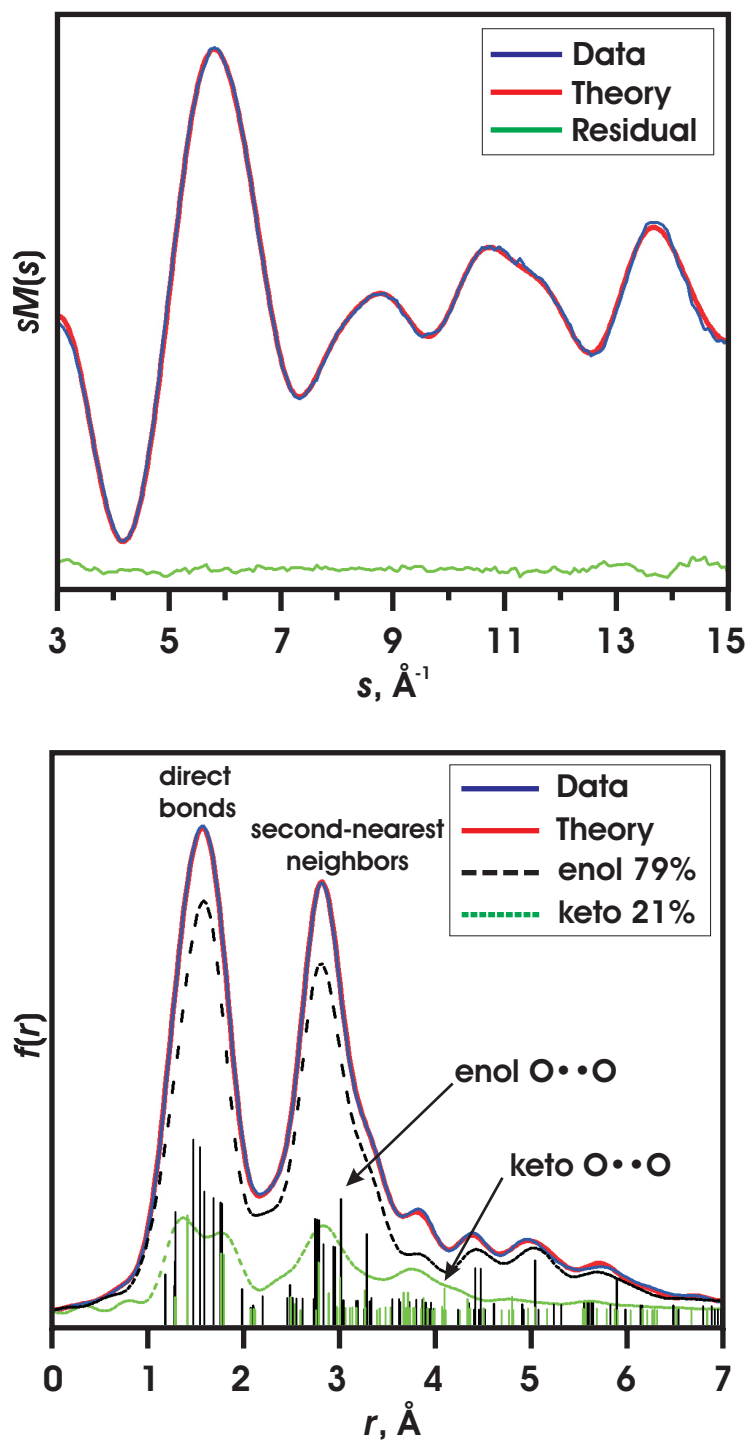
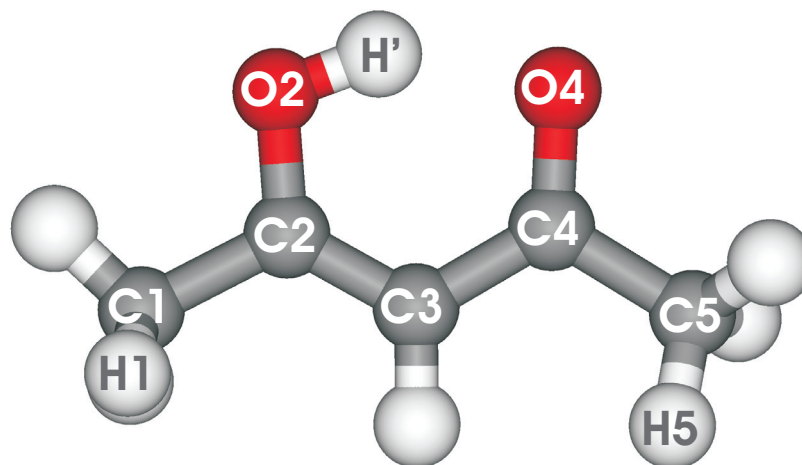


Figure 9-2. Diffraction data and structural refinement of acetylacetonone. (Top) Modified molecular scattering intensity, $sM(s)$. (Bottom) Total and species radial distribution curves, $f(r)$.



Distances

$r(\text{C1-C2}) = 1.504 \pm 0.021$ (1.495)
$r(\text{C2-C3}) = 1.359 \pm 0.034$ (1.370)
$r(\text{C3-C4}) = 1.443 \pm 0.019$ (1.444)
$r(\text{C4-C5}) = 1.518 \pm 0.023$ (1.513)
$r(\text{C2-O2}) = 1.321 \pm 0.021$ (1.325)
$r(\text{C4-O4}) = 1.262 \pm 0.005$ (1.244)

Angles

$\alpha(\text{C1-C2-C3}) = 123.6 \pm 1.1$ (124.1)
$\alpha(\text{C2-C3-C4}) = 120.4 \pm 1.0$ (120.4)
$\alpha(\text{C3-C4-C5}) = 118.2 \pm 1.0$ (118.6)
$\alpha(\text{C1-C2-O2}) = 112.9 \pm 2.7$ (113.7)
$\alpha(\text{C5-C4-O4}) = 118.7 \pm 3.1$ (119.7)
$\phi(\text{H1C1-C2C3}) = -57.2 \pm 16.5$ (-0.1)
$\phi(\text{H5C5-C4C3}) = -19.3 \pm 4.8$ (-63.2)

Figure 9-3. Final refined structure of the enol tautomer of acetylacetone. Distances are in ångströms and angles are in degrees.

Structural Dynamics

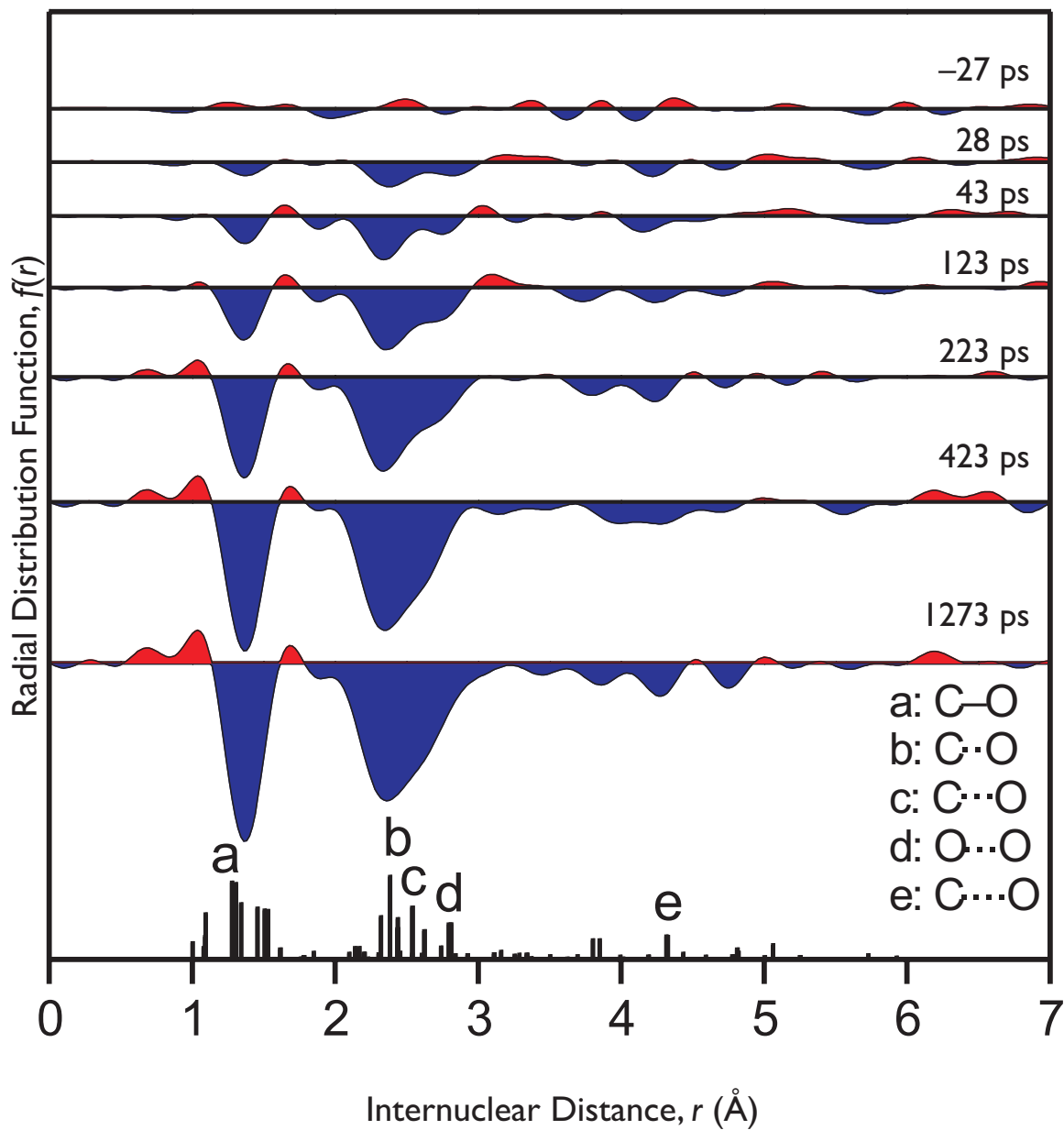


Figure 9-4. Observed structural dynamics of acetylacetonone. Shown are the time-resolved radial distribution curves, $\Delta f(r;t)$. The blue highlighted regions represent net depletion of internuclear pairs (“old bonds”). Red highlighting represents the formation of new distances. The vertical lines at the bottom indicate their relative contributions, proportional to nZ_iZ_j/r_{ij} . Z is the atomic number and r is the internuclear distance. Distances are in ångströms and angles are in degrees.

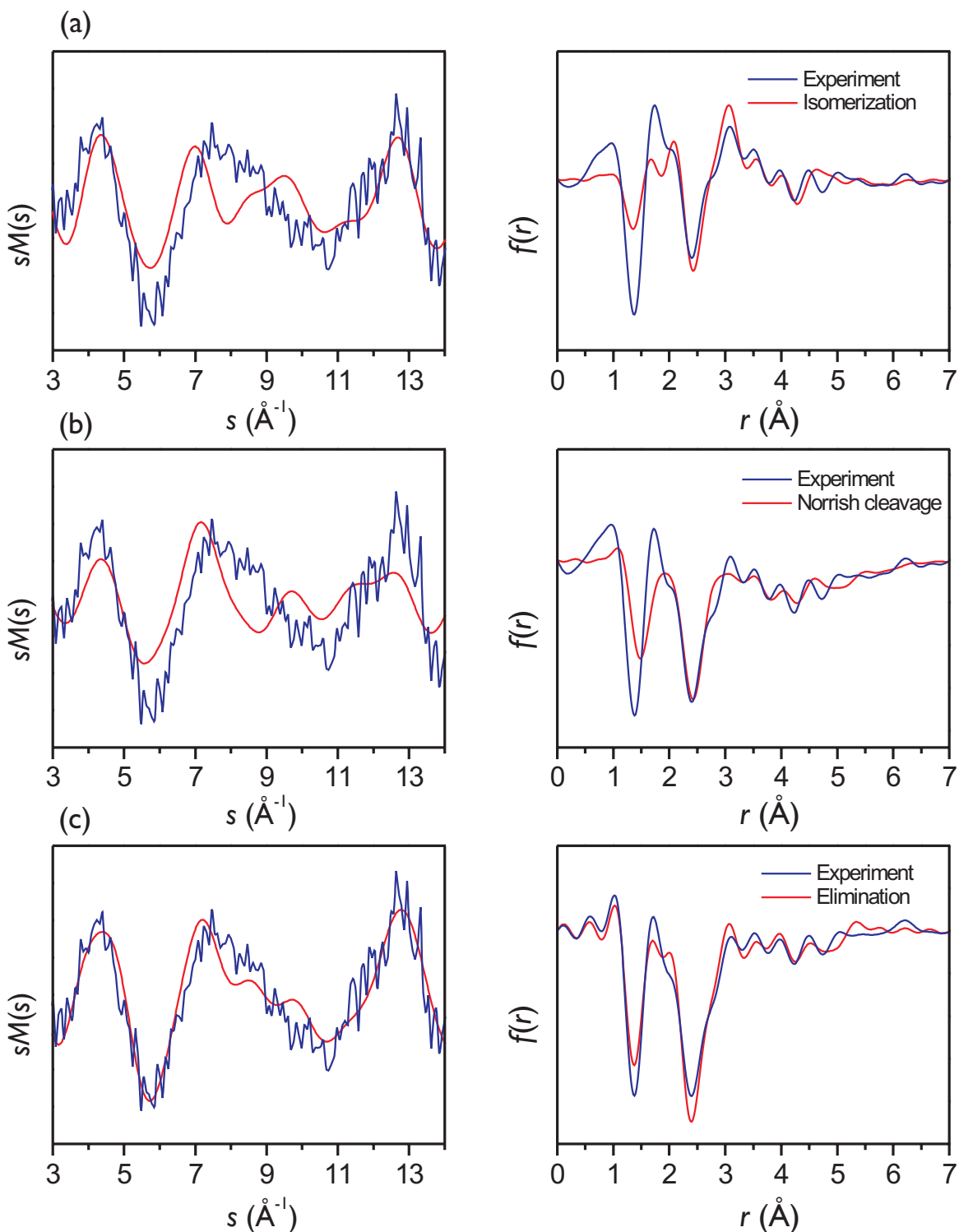


Figure 9-5. Experimental and theoretical diffraction-difference data ($\Delta sM(s)$ and $\Delta f(r)$); +1273 ps (reference = -77 ps) for different pathways. (a) Isomerization to *cis-trans-cis* enol. $R = 1.103$. (b) Norrish Type-I cleavage of the methyl group. $R = 1.222$. (c) Loss of the OH radical. $R = 0.533$. The minor difference in appearance of the experimental data is an effect of different background curves.

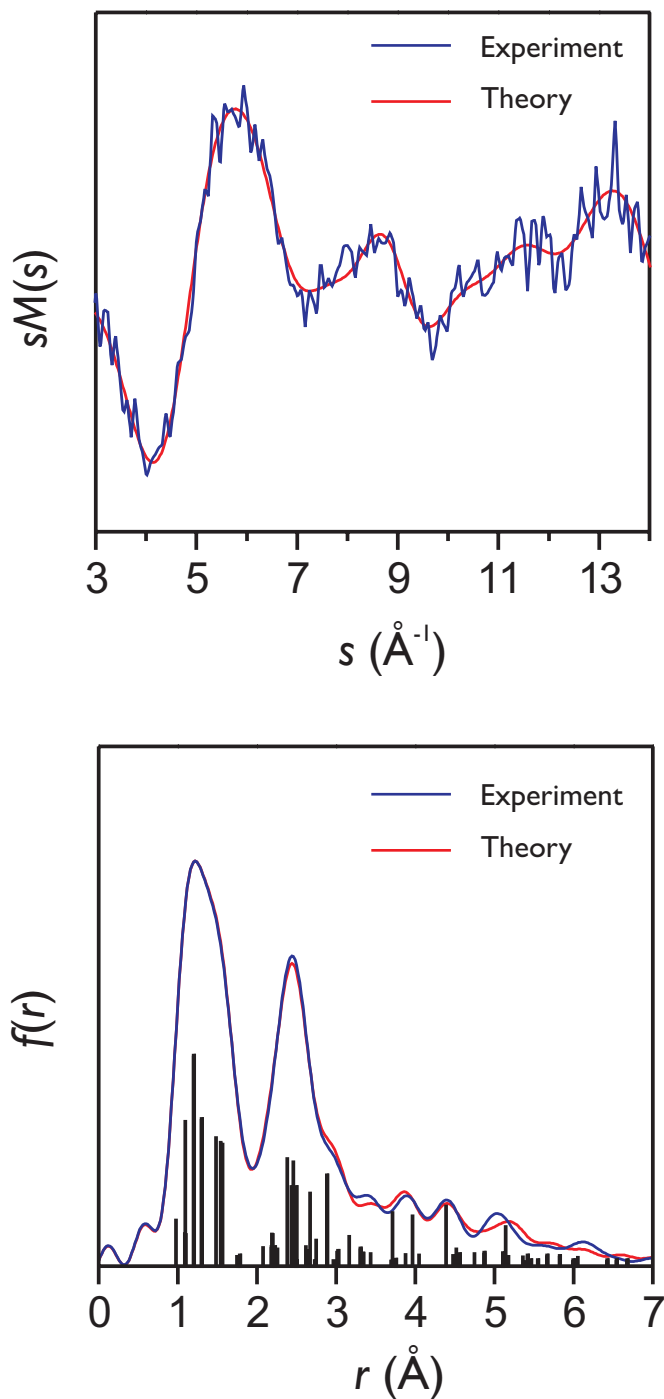
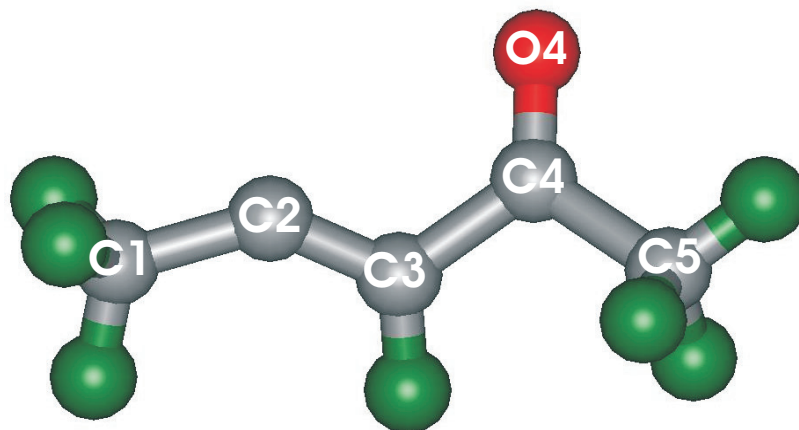


Figure 9-6. The refined theoretical $sM(s)$ and $f(r)$ curves and the +1273 ps “product only” data. $R = 0.273$. The bars below $f(r)$ show the intensity contributed by each internuclear separation in the molecule, proportional to nZ_iZ_j/r_{ij} . In “product-only” format the fitted parent contribution to the reaction is added to the difference data leaving only the product signal.



Distances		
	<i>experiment</i>	<i>DFT</i>
$r_1(\text{C1-C2})$	1.542 ± 0.023	1.462
$r_2(\text{C2-C3})$	1.304 ± 0.025	1.316
$r_3(\text{C3-C4})$	1.482 ± 0.023	1.499
$r_4(\text{C4-C5})$	1.564 ± 0.047	1.519
$r_5(\text{C4-O4})$	1.202 ± 0.017	1.212

Angles		
	<i>experiment</i>	<i>DFT</i>
$\angle_1(\text{C1-C2-C3})$	139.4 ± 5.9	141.5
$\angle_2(\text{C2-C3-C4})$	121.8 ± 1.7	123.8
$\angle_3(\text{C3-C4-C5})$	110.3 ± 2.8	115.4
$\angle(\text{C2C3-C4C5})$	-159.8 ± 14.2	180

Figure 9-7. The refined structure of the 2-penten-4-on-3-yl radical. Also shown are the refined parameters of the fitted structure compared with starting values obtained by DFT. Distances are in ångströms and angles are in degrees.

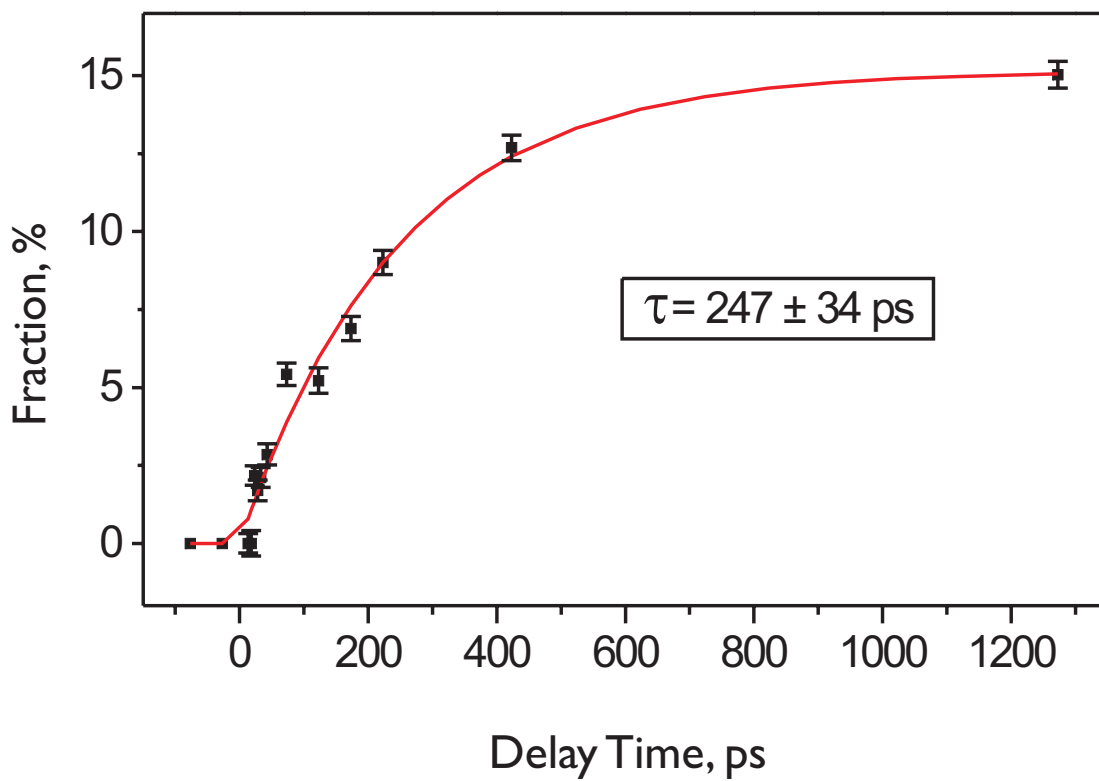


Figure 9-8. Fraction of OH loss products for all experimental time slices, showing a rise time of 247 ± 34 ps.

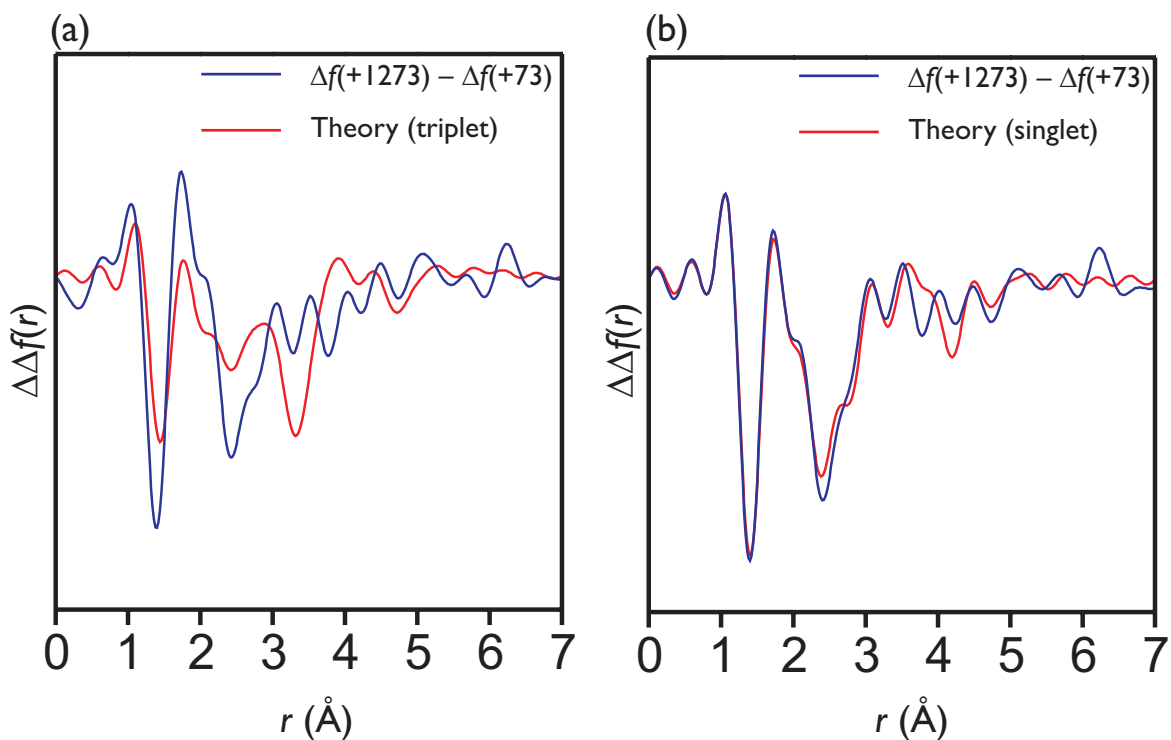


Figure 9-9. Difference-difference data. (a) +1273 ps frame–reference frame (+73 ps), and the theoretical model corresponding to $T_1(\text{DFT}) \rightarrow \text{OH}$ loss products. (b) +1273 ps frame–reference frame (+73 ps), and the theoretical model corresponding to $S \rightarrow \text{OH}$ loss products. S is an approximation of the singlet manifold structure made using a combination of S_1 and S_2 geometries (CASSCF) in $\sim 1:3$ ratio (see text).

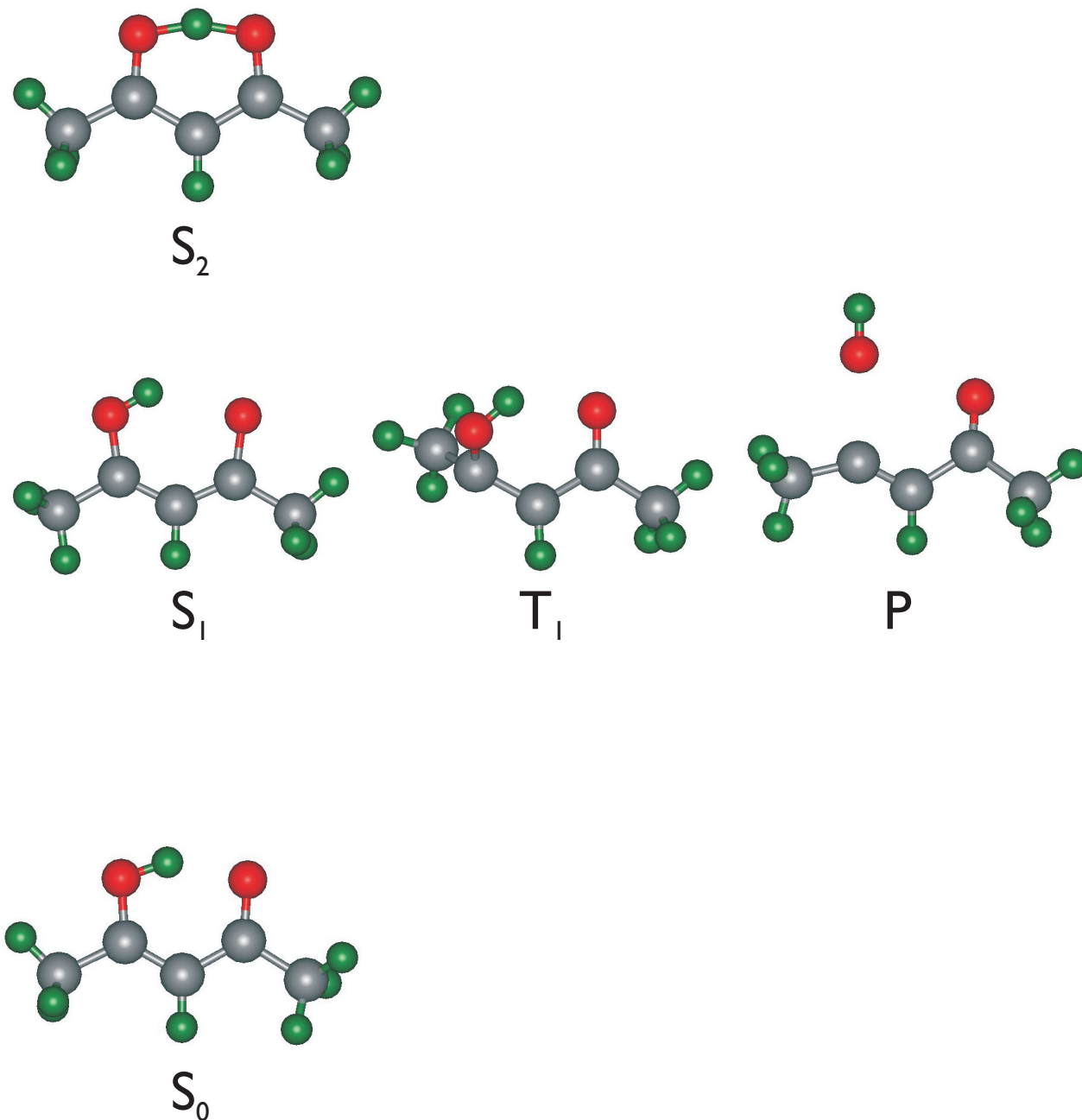


Figure 9-10. Structures involved in the dynamics of the OH elimination reaction. Ground-state (S_0) and OH elimination product (P) structures were experimentally obtained using UED (see text). Excited state structures (S_1 , S_2 , T_1) were obtained by *ab initio* methods at the CASSCF(10,9)/6-31G(d,p) level.

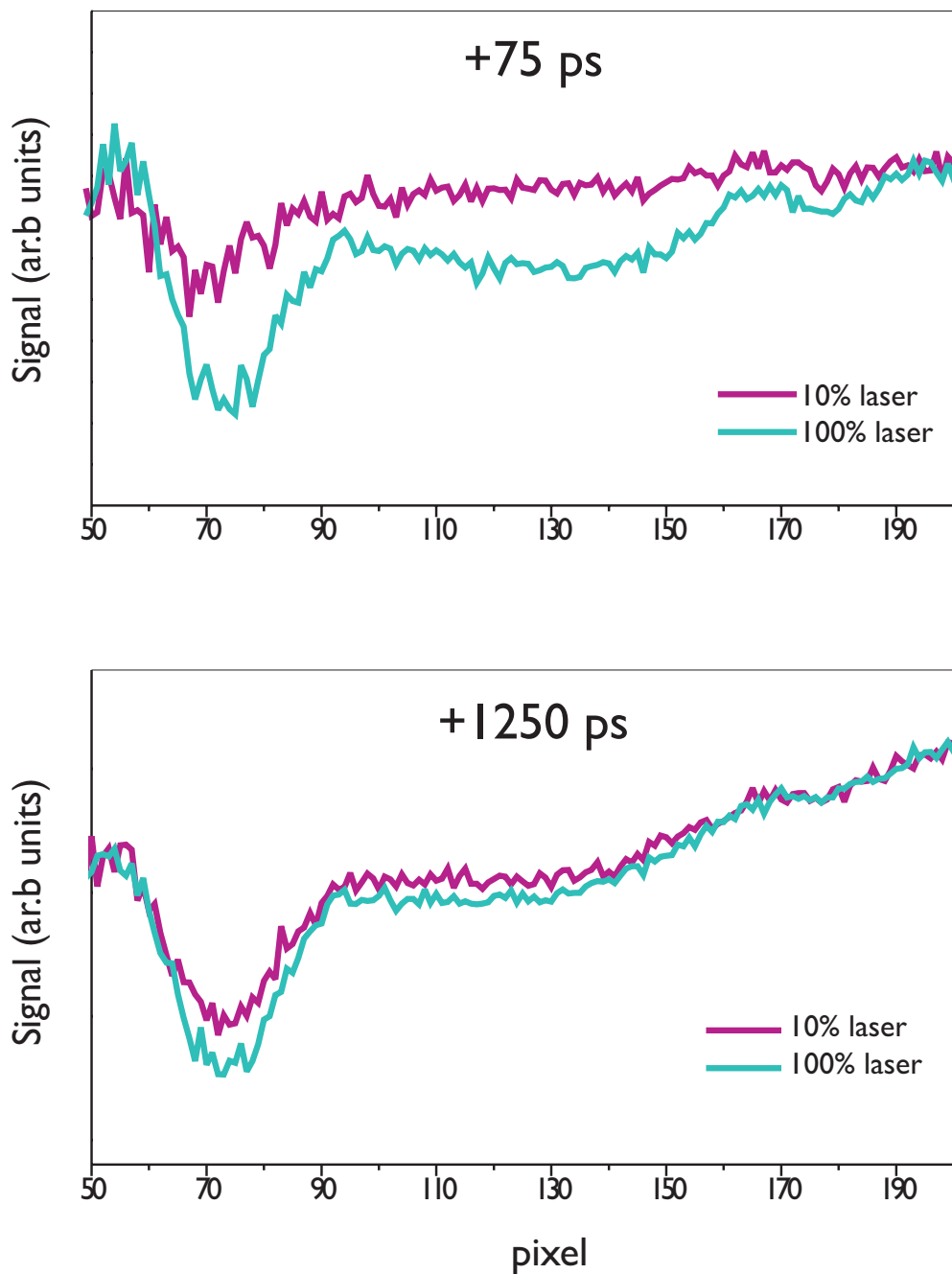


Figure 9-11. Power-dependence studies of UED observation of acetylacetone photochemistry. The comparison of the diffraction-difference signal at the two time slices indicates that the photochemistry is unaffected, except for an expected enhancement in the amplitude of the difference signal due to greater fractional change.

References

1. Steiner, T., *Angew. Chem.* **2002**, *41*, 48.
2. Perrin, C. L.; Nielson, J. B., *Annu. Rev. Phys. Chem.* **1997**, *48*, 511.
3. Gilli, G.; Bellucci, F.; Ferretti, V.; Bertolasi, V., *J. Am. Chem. Soc.* **1989**, *111*, 1023.
4. Gilli, P.; Bertolasi, V.; Ferretti, V.; Gilli, G., *J. Am. Chem. Soc.* **1994**, *116*, 909.
5. Gilli, P.; Bertolasi, V.; Pretto, L.; Ferretti, V.; Gilli, G., *J. Am. Chem. Soc.* **2004**, *126*, 3845.
6. Lowrey, A. H.; George, C.; D'Antonio, P.; Karle, J., *J. Am. Chem. Soc.* **1971**, *93*, 6399.
7. Andreassen, A. L.; Bauer, S. H., *J. Mol. Struct.* **1972**, *12*, 381.
8. Iijima, K.; Ohnogi, A.; Shibata, S., *J. Mol. Struct.* **1987**, *156*, 111.
9. Johnson, M. R.; Jones, N. H.; Geis, A.; Horsewill, A. J.; Trommsdorff, H. P., *J. Chem. Phys.* **2002**, *116*, 5694.
10. Camerman, A.; Mastropaolo, D.; Camerman, N., *J. Am. Chem. Soc.* **1983**, *105*, 1584.
11. Boese, R.; Antipin, M. Y.; Blaser, D.; Lyssenko, K. A., *J. Phys. Chem. B* **1998**, *102*, 8654.
12. Harris, R. K.; Rao, R. C., *Org. Magn. Reson.* **1983**, *21*, 580.

13. Folkendt, M. M.; Weiss-Lopez, B. E.; Chauvel Jr., J. P.; True, N. S., *J. Phys. Chem.* **1985**, *89*, 3347.
14. Nakanishi, H.; Morita, H.; Nagakura, S., *Bull. Chem. Soc. Jpn.* **1977**, *50*, 2255.
15. Hush, N. S.; Livett, M. K.; Peel, J. B.; Willett, G. D., *Aust. J. Chem.* **1987**, *40*, 599.
16. Powling, J.; Bernstein, H. J., *J. Am. Chem. Soc.* **1951**, *73*, 4353.
17. Tayyari, S. F.; Zeegers-Huyskens, T.; Wood, J. L., *Spectrochimica Acta* **1979**, *35A*, 1289.
18. Egan, W.; Gunnarsson, G.; Bull, T. E.; Forsen, S., *J. Am. Chem. Soc.* **1977**, *99*, 4568.
19. Dannenberg, J. J.; Rios, R., *J. Phys. Chem.* **1994**, *98*, 6714.
20. Ishida, T.; Hirata, F.; Kato, S., *J. Chem. Phys.* **1999**, *110*, 3938.
21. Bauer, S. H.; Wilcox, C. F., *Chem. Phys. Lett.* **1997**, *279*, 122.
22. Sharafeddin, O. A.; Hinsien, K.; Carrington, T.; Roux, B., *J. Comput. Chem.* **1997**, *18*, 1760.
23. Mavri, J.; Grdadolnik, J., *J. Phys. Chem. A* **2001**, *105*, 2039.
24. Grabowski, S. J., *J. Phys. Org. Chem.* **2003**, *16*, 797.
25. Delchev, V. B.; Mikosch, H.; St. Nikolov, G., *Monatsh. Chem.* **2001**, *132*, 339.

-
26. Srinivasan, R.; Lobastov, V. A.; Ruan, C. Y.; Zewail, A. H., *Helv. Chim. Acta* **2003**, *86*, 1763.
27. Ando, K.; Hynes, J. T., *J. Phys. Chem. B* **1997**, *101*, 10464.
28. Walzl, K. N.; Xavier Jr., I. M.; Kuppermann, A., *J. Chem. Phys.* **1987**, *86*, 6701.
29. Roubin, P.; Chiavassa, T.; Verlaque, P.; Pizzala, L.; Bodot, H., *Chem. Phys. Lett.* **1990**, *175*, 655.
30. Nagashima, N.; Kudoh, S.; Takayanagi, M.; Nakata, M., *J. Phys. Chem. A* **2001**, *105*, 10832.
31. Coussan, S.; Manca, C.; Ferro, Y.; Roubin, P., *Chem. Phys. Lett.* **2003**, *370*, 118.
32. Veierov, D.; Bercovici, T.; Fischer, E.; Mazur, Y.; Yogev, A., *J. Am. Chem. Soc.* **1977**, *99*, 2723.
33. Yoon, M.-C.; Choi, Y. S.; Kim, S. K., *J. Chem. Phys.* **1999**, *110*, 11850.
34. Yoon, M.-C.; Choi, Y. S.; Kim, S. K., *Chem. Phys. Lett.* **1999**, *300*, 207.
35. Upadhyaya, H. P.; Kumar, A.; Naik, P. D., *J. Chem. Phys.* **2003**, *118*, 2590.
36. Srinivasan, R.; Feenstra, J. S.; Park, S. T.; Xu, S. J.; Zewail, A. H., *J. Am. Chem. Soc.* **2004**, *126*, 2266.
37. Lim, E. C., *J. Phys. Chem.* **1986**, *90*, 6770.

-
38. Arias, A. A.; Wasserman, T. A. W.; Vaccaro, P. H., *J. Chem. Phys.* **1997**, *107*, 5617.

10

CONCLUSIONS AND FUTURE DIRECTIONS*

In 1937, Davisson and Thomson received the Nobel Prize 'for their experimental discoveries of the diffraction of electrons by crystals'. Earlier in the century, X-ray diffraction from crystals had been discovered; but, for gases, it was Debye and co-workers^{1, 2} who showed that X-ray scattering patterns are rich with structural information, despite the randomness in the position and orientation of the gaseous molecular samples. Over the past 70 years, ever since the pioneering work of Mark and Wierl,³ gas phase *continuous-beam* electron diffraction has become a powerful tool for studying

* From Srinivasan, R.; Lobastov, V.A.; Ruan, C.-Y.; Zewail, A.H., *Helv. Chim. Acta*, **2003**, *86*, 1762.

the *static* nature of molecular structures. Within just five years of the first GED experiment, Brockway⁴ listed in his review the structures of 44 inorganic and 103 organic molecules determined by GED. Since then, thousands of *static* molecular structures have been reported in the literature.⁵ Aided by advances in instrumentation, theoretical insights, and computational analysis procedures, the field has witnessed several stages of evolution—the visual method, the sector-microphotometer method, and now, the ultrafast imaging of transient structures, as noted by Jerome Karle.⁶ The central theme in ultrafast electron diffraction (UED) is the elucidation of the structural dynamics of *transient* molecular entities.

Reaching the spatiotemporal resolution on the atomic scale is the driving force behind the development of UED, the subject of this thesis. The current state-of-the-art in resolutions and sensitivity of UED (0.01 Å, 1 ps, and 1%, resp.), together with the theoretical advances made, make possible the freezing of transient structures, leading to studies of diverse molecular phenomena hitherto not accessible to other techniques. Of particular significance is the ability to observe evolution of structures on complex energy landscapes, including those far from equilibrium and with no heavy atoms.

This work has detailed the temporally and spatially resolved molecular structures, elucidated by UED, in diverse chemical phenomena. These

include structures in radiationless transitions, structures in non-concerted organic reactions, structures in non-concerted organometallic reactions, structures of carbene intermediates, dynamic pseudorotary structures, non-equilibrium structures, and conformational dynamics on complex energy landscapes. Figure 10–1 shows the scope of UED applications that has been achieved in our laboratory at Caltech.

On the ultrashort timescale, both the rotational and vibrational motions of molecules are coherent; a degree of order is imposed on the otherwise isotropic sample at equilibrium. It is, therefore, necessary to consider the structural changes, both in this regime of coherent dynamics, and when coherence is subsequently lost. The current time resolution allows us to determine both the *structure* and the *population* of transient intermediates at each instant in time. It is also possible to exploit the coherent motion of atoms to observe new structural features as revealed by previous theoretical studies on the impact of rotational and vibrational coherences on the scattering pattern.⁷ It has been shown that an additional dimension of imaging can be achieved at times when coherence is induced or recovered—in a sense, Debye’s ring pattern begins to approach the diffraction from a crystalline sample. The X-ray crystallography method of using different crystal orientations to map out the structure of the unit-cell can be imitated in UED by exciting different orientations.⁸

The first three generations of UED have been devoted to studies of isolated, complex structures. Currently, in this laboratory, a major step forward in the evolution of UED is the development of the fourth-generation apparatus (UED-4)⁹⁻¹¹ designed for diffraction studies of surfaces and macromolecules on the ultrafast timescale, thus opening up the world of condensed phases and biology. With the electron-pulse sequencing of the diffraction-difference method, the six-orders-of-magnitude higher cross-section of electron scattering (compared to X-rays), and the development of femtosecond pulsed-electron sources,¹²⁻¹⁴ the technique is poised to reach single molecule studies of complex structures.¹⁵⁻¹⁷

In December 1999, Philip Ball of *Nature* observed,¹⁸ “Diffraction on the ‘molecular’ timescale of femtoseconds is an infant discipline which promises wonders once perfected, but which is capable right now of only the crudest of impressionistic sketches: blurred images of lattice dynamics, showing evidence of rapid change but without a single molecule (let alone an atom) in focus. The static photography of the Braggs has yet to produce its first movie.” UED-3 has not only succeeded in bringing isolated molecules into sharp focus but has also captured the crucial ‘freeze frames’ in these movies. As noted by several colleagues,¹⁹⁻²⁷ the recent triumphs of UED have generated much excitement for the burgeoning field of ‘structural dynamics’.

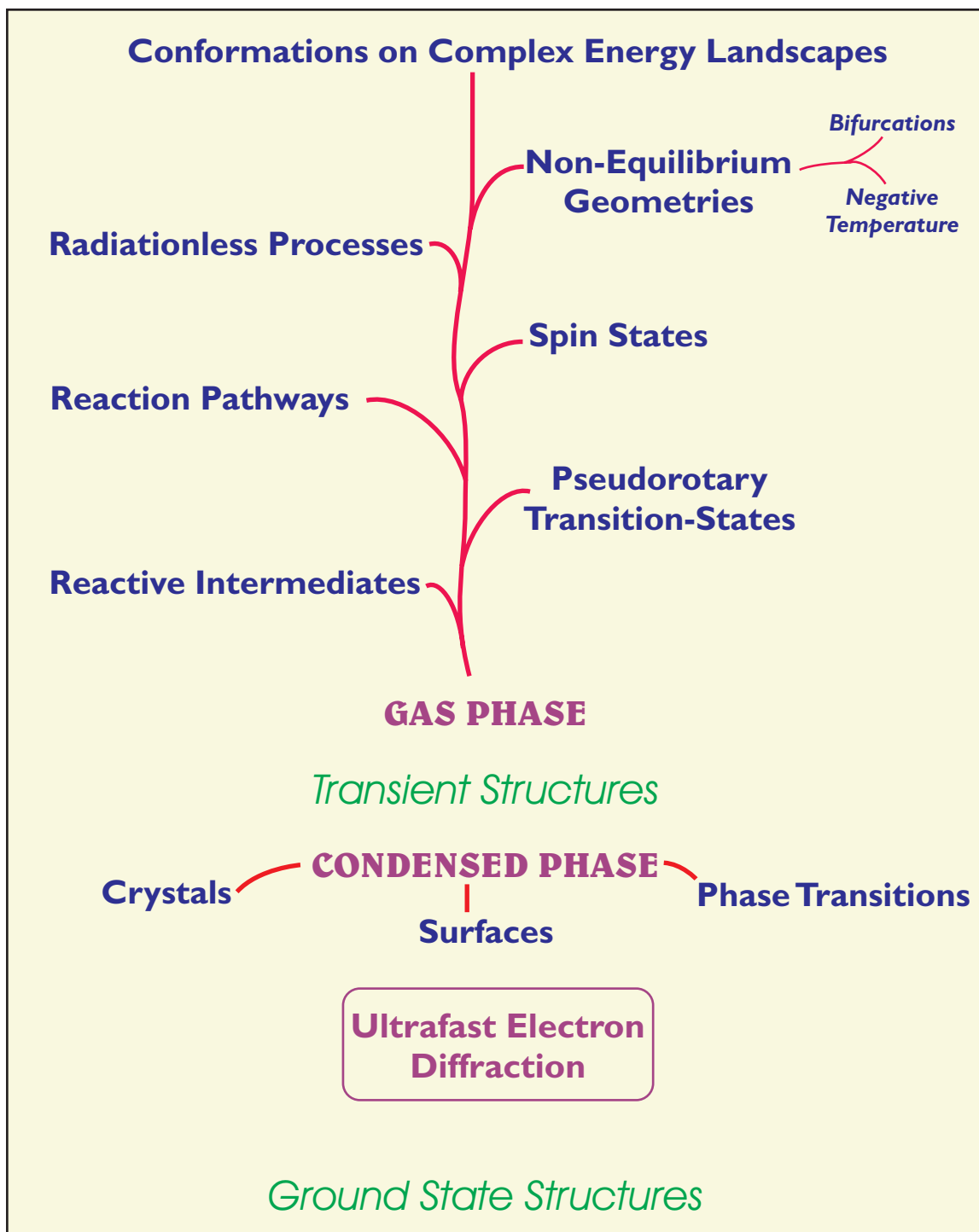


Figure 10-1. The scope of phenomena and concepts elucidated by UED via the determination of ground-state and transient molecular structures.

References

1. Debye, P.; Bewilogua, L.; Ehrhardt, F., *Phys. Z.* **1929**, *30*, 84.
2. Debye, P., *Ann. Phys.* **1915**, *46*, 809.
3. Mark, H.; Wierl, R., *Naturwissenschaften* **1930**, *18*, 205.
4. Brockway, L. O., *Rev. Mod. Phys.* **1936**, *8*, 231.
5. Hargittai, I.; Hargittai, M., *Stereochemical Applications Of Gas-Phase Electron Diffraction*. VCH: New York, 1988.
6. Karle, J., *Structural Chem.* **2000**, *11*, 91.
7. Williamson, J. C.; Zewail, A. H., *J. Phys. Chem.* **1994**, *98*, 2766.
8. Hoshina, K.; Yamanouchi, K.; Ohshima, T.; Ose, Y.; Todokoro, H., *J. Chem. Phys.* **2003**, *118*, 6211.
9. Ruan, C. Y.; Vigliotti, F.; Lobastov, V. A.; Chen, S. Y.; Zewail, A. H., *Proc. Natl. Acad. Sci. USA* **2004**, *101*, 1123.
10. Ruan, C. Y.; Lobastov, V. A.; Vigliotti, F.; Chen, S. Y.; Zewail, A. H., *Science* **2004**, *304*, 80.
11. Vigliotti, F.; Chen, S. Y.; Ruan, C. Y.; Lobastov, V. A.; Zewail, A. H., *Angew. Chem.-Int. Edit.* **2004**, *43*, 2705.
12. Schelev, M. Y.; Bryukhnevich, G. I.; Monastyrski, M. A.; Prokhorov, A. M.; Smirnov, A. V.; Vorobiev, N. S., *Opt. Eng.* **1998**, *37*, 2249.
13. Qian, B.-L.; Elsayed-Ali, H. E., *Rev. Sci. Instrum.* **2001**, *72*, 3507.
14. Qian, B.-L.; Elsayed-Ali, H. E., *Phys. Rev. E* **2002**, *65*, 046502.

-
15. Hajdu, J., *Curr. Opin. Struc. Biol.* **2000**, *10*, 569.
 16. Miao, J.; Hodgson, K. O.; Sayre, D., *Proc. Natl. Acad. Sci. USA* **2001**, *98*, 6641.
 17. Webster, G.; Hilgenfeld, R., *Single Mol.* **2002**, *3*, 63.
 18. Ball, P., *Nature* **1999**, *402*, C30 Suppl.
 19. Poliakoff, M.; Turner, J. J., *Angew. Chem. Int. Ed.* **2001**, *40*, 2809.
 20. Thomas, J. M., *Nature* **1991**, *351*, 694.
 21. Hoffmann, R., *Am. Scientist* **1999**, *87*, 308.
 22. Helliwell, J. R., *Phys. World* **2001**, *14*, 25.
 23. Wilson, E., *Chem. Eng. News* **2001**, *79*, 10.
 24. Hall, N., *Chem. Commun.* **2002**, 2185.
 25. Thomas, J. M., *Faraday Discuss.* **2002**, *122*, 395.
 26. Coppens, P.; Novozhilova, I. V., *Faraday Discuss.* **2002**, *122*, 1.
 27. Thomas, J. M., *Angew. Chem.-Int. Edit.* **2004**, *43*, 2606.